THREE-DIMENSIONAL NUMERICAL AND PHYSICAL MODELLING OF COASTAL HYDRO-ENVIRONMENTS

TURBULENT STRATIFIED FLOWS IN ESTUARINE HARBOURS AND BARRAGES

KOUROSH HEJAZI

OCTOBER 2014

In the Name of God

The Almighty, the Merciful, the Compassionate

... And we have made from water every living thing ...

Surah Al-Anbiya (21), Verse 30

The Quran

To My Parents

ACKNOWLEDGEMENTS

I would like to express my deepest gratitude to my supervisor Professor Roger A. Falconer for his continuous advice, support and encouragement throughout the long period of this research project, which would not be finalised without his sincere help, consideration and goodwill.

My parents have patiently supported me in all aspects of life details of which have been associated with every moment of thinking and working on this project. The support I have received from my beloved sister both emotionally and financially cannot be expressed in few words. Her support very much helped for the continuation of this project which would not be attained without her sincere and loving care. I would like to express my warmest appreciations to my sons Bardia and Dara who have so kindly and silently lived with my project with the least expectations and the utmost support and love. I would also like to thank Nazila during her stay and support in Cardiff.

Dr Farhad Yazadandoost encouraged me for doing this project and gave his support for the commencement of my studies in the UK. During the past ten years his sincere inspiration for finalising the project with all considerations are highly appreciated. Dr Masoud Montazeri Namin with a very friendly attitude gave professional guidance throughout the research along with very useful discussions which provided lots of contributions to the project. I also would like to thank Professor Amir Keyvan Khandani for his excellent guidance for signal processing and filtering the laboratory data.

I would like to thank Mr Paul Leach for very sincere help in the design, construction and set-up of the laboratory tidal basin and model harbour and providing assistance throughout the experiments. My acknowledgement goes to Mr Des Sanford for his professional help in the design of the electrical elements of the laboratory tidal basin and the design and set-up of the data acquisition and control software and the instrumentation. I would also like to express my appreciation to Mrs Chris Lee for her sincere help for the completion of my research project.

K. N. Toosi University of Technology has financially supported this research project and has been helpful in the past ten years for facilitating the continuation of the research, which I would like to express my appreciation. The financial support of the Ministry of Science, Research and Technology of Iran is highly appreciated.

In my last years of high school I was stimulated by the idea of the correlation between physics and philosophy. In the last year of high school I was passionately interested in jointly studying physics and philosophy at university. After the rejection of the recommendation I received from my beloved father to study medicine, and losing the opportunity for comprehension of the relationship between biology and philosophy and the pleasure of fulfilment of his desire, I decided to study civil engineering, which I have enjoyed very much ever since.

Now I am trying to understand and comprehend the physical phenomena, which govern the flow field and in particular water, and I am also trying to place a philosophy, which would provide a foundation for reasonably simulating the physical phenomena with the aid of mathematics, and possibly establish a logical correlation between them; of course, without a proper education in physics neither in philosophy.

Here and now after a quarter of a century I am still at the same point of the struggle to find the right correlation between the physics and the philosophy. So from my experience it is fair to say: it is physics and it is philosophy; in reality and in mind; that make the world go round.

Cardiff, May 2003

The submission of this thesis was delayed for a decade due to some very complicated unforeseen circumstances. The work needed to be renewed and updated to the most recent research, which consequently required some new research and the addition of the corresponding materials to the thesis.

Learning to take the positive side of everything in the past ten years, it might worth mentioning that during this period, a few features have been added to the numerical model and more engineering applications have been simulated and investigated. I also have had the opportunity to better understand the relevant physical phenomena and establish a more coherent relation between the philosophy of the research and the governing physical and mathematical relations. It was also an opportunity for me to connect the mathematical relations to more sensible physical and engineering applications. The numerical modelling has also received a clearer placement among physical phenomena, mathematical relations and engineering applications.

Tehran, November 2013

ABSTRACT

An arbitrary Lagrangian-Eulerian (ALE) three-dimensional hydrodynamic free-surface numerical model has been developed based on the time-dependent Reynolds-averaged Navier-Stokes (RANS) equations and the finite volume method (FVM). The model with non-hydrostatic pressure distribution and a structured non-orthogonal curvilinear staggered mesh is capable of simulating non-homogeneous stratified flows and problems involving complex bathymetry. A projection method is deployed for solving the set of the equations, and a buoyant k-ε turbulence model is included in the numerical model. Six new advection schemes are introduced, and a fifth-order-accurate upstream scheme was utilised in the numerical model. Extensive numerical tests showed the capability of the model in simulating free surface flows and non-linear terms in Navier-Stokes equations. To achieve a better understanding of hydrodynamics, mixing, and salt transport and stratification and their interactive mechanisms in estuarine harbours and barrages, a laboratory tidal basin was designed, set up and employed for velocity, water surface elevation and salinity measurements of an idealised vertically distorted model harbour. For despiking and denoising the velocity data a linear algorithm was established, which successfully lowered the noise level and removed the spikes. The measurements showed a horizontal circulation in the harbour and weak vertical circulations. The salinity suppressed the circulation across the water depth, resulting in less mixing in vertical direction and stronger flushing on the surface. Comparisons of the numerical model simulations against the experimental data showed that the velocities and flow patterns were in generally good agreement with the measured values. For the fresh water the model under-predicted the dominant velocity components for the areas with strong circulation and for the saline water the simulated results showed an over-prediction in lower layers and good agreements with the measured values for the top layer. The water elevations exhibited very close predictions compared with the measured data. The salinity simulated profiles showed good agreements with the measured values for lower layers and an over-prediction for the top layer. The investigations showed that the dominant velocities inside the harbour were increased for taller barriers, but with the increase of mean water depth the circulations weakened. The saline water flushing into the harbour flows underneath the fresh ambient water resulting in higher salinity concentration in the harbour over time.

CONTENTS

Chapter Four
Numerical Modelling
Scheme, Structure and the Solution Method

Chapter Six
Physical Model Studies
Design and Operation of the Laboratory Tidal Basin and Model Harbour

Chapter Seven
Physical Model Studies
Instrumentation, Test Arrangements, Data Acquisition and Signal Processing

TABLE OF FIGURES

TABLE OF TABLES

TABLE OF PICTURES

NOMENCLATURE

"A part of the secret of analysis is the art of using notation well."

Leibniz on Determinants (Langhaar, 1951)

All symbols which are used throughout the thesis have been listed herein. The symbols which have contributed to a calculation procedure for a particular section have been defined in the corresponding section.

A	Amplification factor
a	Amplitude of standing wave
BH	Barrier height
C	Scalar quantity; species concentration Chézy value Constant in velocity logarithmic law Wave celerity
C'	Fluctuating concentration
$\bar{C}$	Time-average of concentration
c_D	Empirical constant of ε-equation
C_r	Courant number
c_μ	Empirical constant in k-ε turbulence model
c'_μ	Empirical constant of Kolmogorov-Prandtl expression
$c_{1\varepsilon}$	Empirical constant in ε-equation of k-ε turbulence model
$c_{2\varepsilon}$	Empirical constant in ε-equation of k-ε turbulence model
$c_{3\varepsilon}$	Buoyancy parameter in ε-equation of k-ε turbulence model

D	Water depth
d	Distance from wall in velocity logarithmic law
$d\boldsymbol{S}$	Surface element vector
d_0	Constant in velocity logarithmic law
E	Roughness parameter
$\boldsymbol{F}$	Body force per unit volume Flux vector
f	Dimensionless resistance coefficient Coriolis parameter
$\boldsymbol{F_A}$	Advective flux vector
$\boldsymbol{F_D}$	Diffusive flux vector
F_r	Froude number
Fr_D	Densimetric Froude number
FW	Fresh water
G	Buoyancy term of k-equation Distortion ratio
g	Gravitational acceleration
g'	Reduced gravity
H	Water depth
$H(f)$	Frequency response of the infinite Wiener filter
H_W	Wave height
I	Plane number for planes perpendicular to x-direction
i	Cell number in x-direction
$\boldsymbol{i}$	x-direction unit vector
J	Plane number for planes perpendicular to y-direction
j	Cell number in y-direction
$\boldsymbol{j}$	y-direction unit vector
k	Cell number in z-direction Wave number Kinetic energy per unit mass k turbulence model
$\boldsymbol{k}$	z-direction unit vector
k-kl	k-kl turbulence model
k-l	k-l turbulence model
K_p	Pressure response factor
k_s	Length parameter characteristic of the surface roughness (roughness length scale)
k-ε	k-ε turbulence model

k-v_t	k-v_t turbulence model
k-τ	k-τ turbulence model
k-ω	k-ω turbulence model
L	Length scale Wave length Length
L	Layer of water column
N	Number of grid intervals over one wavelength Buoyancy frequency (Brunt-Väisälä frequency)
n	n^{th} time level Number of layers in z-direction
$\boldsymbol{n}$	Unit vector normal to surface
P	Dynamic pressure Production term of k-equation
$\boldsymbol{P}$	Surface force per unit volume
p	Pressure
p'	Fluctuating pressure
$\bar{p}$	Time-average of pressure
P_a	Atmospheric pressure
P_x	x-direction surface force per unit volume
P_y	y-direction surface force per unit volume
P_z	z-direction surface force per unit volume
p_0	Reference pressure
Q	Celerity ratio Sources
$Q_{\Re}$	Volume of Q associated with finite volume $\Re$
$\boldsymbol{Q}_S$	Surface sources
Q_V	Volume sources
Re	Reynolds number
$\boldsymbol{R}_{eo}$	Vector of correlation between odd and even indexed velocity points
R_f	Flux Richardson number
R_h	Hydraulic radius
R_i	Gradient Richardson number
$\overline{\boldsymbol{R}}_{nn}$	Autocorrelation matrix for Doppler noise
$\overline{\boldsymbol{R}}_{oo}$	Correlation matrix of odd time indexed velocity points
$\overline{\boldsymbol{R}}_{vv}$	Autocorrelation matrix for true velocity
$\overline{\boldsymbol{R}}_{xx}$	Autocorrelation matrix for noisy recorded velocity signal

S	Slope Closed surface
S_c	Volumetric source term
S_e	Slope of the energy gradient of flow
S_r	Slope scale
SW	Saline water
$S_0/2$	Stroke amplitude of wave-maker
T	Tidal period Wave period
t	Time
TP	Tidal period
TR	Tidal range
t_{xr}	Horizontal motion time scale
t_{zr}	Vertical motion time scale
u	x-direction velocity component
u'	Fluctuating velocity of u-component
$\overline{u}$	Time-average of u-component of velocity
u_{res}	Resultant velocity in distance d from the wall
u_τ	Resultant shear velocity in velocity logarithmic law
V	Water velocity
$\boldsymbol{V}$	Velocity vector
v	y-direction velocity component
v'	Fluctuating velocity of v-component
$\overline{v}$	Time-average of v-component of velocity
$\hat{V}$	Velocity scale
V^*	Provisional velocity
$\boldsymbol{V}_g$	Grid velocity
V_n	Normal component of velocity
v_n	Normal component of velocity
$V_{\Re}$	Volume of V associated with finite volume $\Re$
V_r	Velocity scale
V_s	Surface fluid speed
v_t	Tangential component of velocity
V_τ	Tangential component of velocity
w	z-direction velocity component

w'	Fluctuating velocity of *w*-component
$\overline{\overline{W}}$	Matrix of Wiener filter coefficients
$\overline{w}$	Time-average of *w*-component of velocity
w_g	*z*-direction grid velocity
$w_{i,j}$	Wiener filter coefficients
X	*x*-direction body force per unit volume
x	*x*-direction
X_r	Horizontal length scale
Y	*y*-direction body force per unit volume
y	*y*-direction
y^+	Dimensionless wall distance
Z	*z*-direction body force per unit volume
z	*z*-direction
z_b	Bed elevation above datum
Z_r	Vertical length scale
β	Rate of change of density due to concentration
Γ	Turbulent diffusivity of mass
Δt	Time step interval
Δx	*x*-direction grid size
Δy	*y*-direction grid size
Δz	*z*-direction grid size
ε	Viscous dissipation
$\dot{\varepsilon}_{ij}$	Rate-of-strain tensor
η	Surface elevation
θ	Implicit weighting factor Angle of latitude
θ_D	Implicit weighting factor for diffusion
θ_P	Implicit weighting factor for pressure
θ_η	Implicit weighting factor for velocity on free surface
κ	von Kármán's constant
λ	Diffusion coefficient Molecular diffusivity
$\mathfrak{\lambda}$	Diffusivity constant
μ	Coefficient of viscosity
ν	Kinematic viscosity

ν_T	Turbulent or eddy viscosity
ξ_k^n	Fourier coefficient for wave number *k* at time level *n*
ρ	Density
ρ_r	Reference density
σ_k	Empirical diffusion constant
σ_n^2	Noise variance
σ_T	Turbulent Schmidt number
σ'_x	*x*-direction deviatoric normal stress *x* Reynolds normal stress
σ'_y	*y*-direction deviatoric normal stress *y* Reynolds normal stress
σ'_z	*z*-direction deviatoric normal stress *z* Reynolds normal stress
σ_ε	Empirical constant in ε-equation of k-ε turbulence model
$\boldsymbol{\tau}$	Unit vector tangential to surface
τ_b	Solid boundary shear stress
τ'_{ij}	*i*-*j* Reynolds shearing stress
τ_{ij}	Shear stress on a plane perpendicular to *i*/*j*-direction and in *j*/*i*-direction
Φ	Scalar quantity per unit volume
ϕ	Quantity Φ per unit mass
Ω	Value of volume
ω	Angular speed of the earth's rotation
ϖ	Angular frequency
$\Omega_{\Re}$	Value of volume of finite volume $\Re$

CHAPTER ONE

INTRODUCTION

"Reason only perceives that which it produces after its own design."
Immanuel Kant, Critique of Pure Reason (Abbott, 1979)

1.1 ESTUARINE HYDRO-ENVIRONMENTS

Estuaries are water bodies of global significance where inland fresh water meets saline water from the marine environment. The estuarine hydrodynamics is governed by tides, fresh water discharges, density driven currents and winds. Freshwater discharge variations as a result of freshets and droughts and surges might cause a stochastic character in such regions. Complex bathymetry inherently associated with estuaries in combination with the complicated hydrodynamics makes them one of the attractive and most challenging hydro-environments. Many ports are constructed in estuaries providing sheltered basins and access to inland waterways, and many major populated cities are located on estuaries.

The down-estuary direction experiences a fairly rapid change of water density. The vertical variation of density distributions also may range from well mixed, with no significant density variations, to highly stratified conditions. The vertical structure changes on sub-tidal timescales as a result of variations in neap-spring tidal velocities

or variations of the fresh-water discharges (Allen et al., 1980; Jay and Smith, 1990). The along-channel baroclinic pressure gradient and stratification are caused by buoyancy forces as a result of horizontal and vertical density gradients. The gravitational circulation is characterised by seaward flows at the surface and landward flows at the bottom. In many estuaries the dominant components in the salt balance are export of salinity by the fresh-water discharge and import by the gravitational flow, leading to salinity distributions which may take the form of a salt wedge (de Nijs, 2012). On sub-tidal timescales, the forcing conditions at the boundaries may cause excursions of saline water larger than the tidal excursion. Periods of low fresh water discharges or meteorological events such as storms or a combination of both, may cause saline water to penetrate far into the estuary. In ocean dynamics, due to three-dimensional circulation, the advection terms take on considerable importance for the equations of motion as well as the salinity equations, and are known to play a key role in the evolution of stratification.

The water quality in an estuary may be adversely or beneficially affected by a barrage. Potentially the worst water quality effects arise in the case of tidal penetrating amenity barrages. In conditions of low fluvial flow, the upstream pool can become highly stratified with a stagnant layer of saline water remaining for long periods (Reilly, 1993).

1.2 STRATIFIED FLOWS

Horizontal flows driven by buoyancy forces in the presence of a surface or interface, known as gravity currents or density currents, are a common occurrence in many environmental contexts. Stratified flows occur in the atmosphere, oceans, estuaries and lakes. The sea-breeze turbidity currents and saltwater intrusions in estuaries are typical examples (Brown, 1999).

The gravitational flows are often many times larger than the fresh water discharge and therefore have a big impact on the rate of flushing of an estuary. The gravitational circulation is reduced by vertical mixing, which is usually heavily damped in stratified flows, and by energy dissipation at the bed. The latter is increased by the occurrence of high tidal velocities in the low layers. The strength of a gravitational circulation may vary according to the degree of stratification, but it is not dependent on the existence of vertical density stratification. Many deep estuaries with weak or negligible vertical stratification have strong gravitational circulations

(HR Wallingford, 1999). The gravitational flow is normally strongest in deep estuaries with weak tidal currents.

The net effect of stable stratification is to reduce the internal shear stresses and the linkage between overlying layers of water, thereby increasing velocity gradients. At the same time, it has an even bigger effect on reducing the vertical mixing of saline water, heat, suspended sediments and pollutants in an estuary (HR Wallingford, 1999). The presence of stratification can trap a rising plume, if dilution is so great that it prevents it bursting through the interface. Stratification also prevents dissolved oxygen diffusion downwards into the lower layers and it prevents suspended sediment being mixed into upper layers (HR Wallingford, 1999). Transient stratification in estuaries reflects competition between the stratifying influences of the vertical gravitational circulation and longitudinal density gradient by vertical shear, set against the mixing influence of, principally, tidally generated turbulence (Liu et al., 2002). The presence of the buoyancy force due to the stratification may have a substantial effect on the flow development and mixing processes, and hence influence the distribution of scalar substances such as pollutants and suspended sediments in the environment.

1.3 TURBULENT TIDAL FLOW MODELLING IN STRATIFIED ESTUARIES, HARBOURS AND BARRAGES

Estuaries inherently exhibit unsteady, non-uniform, periodically reversal direction, stratified flows with complex vertical salinity and velocity distributions, and provide suitable zones for sediment deposition which may comprise fluid-like muddy beds. Salinity intrusion in estuaries, harbours and barrages is a potentially serious problem. Buoyancy forces, due to salinity intrusion and through their effect on mixing, may strongly impact water quality and contaminant transport. They can suppress vertical mixing and degrade water quality of stable density stratified flows of coastal waters, estuaries, harbours and barrages.

The turbulent transfer of momentum and salinity are strongly affected by buoyancy forces. Consequently, knowledge of turbulent mixing is essential to the comprehension of mechanism of stratified flows (de Nijs and Peitrzak, 2011). Turbulent Prandtl numbers are found to increase with stratification to values larger than one. Consequently, the vertical turbulent mass transport is suppressed by buoyancy forces, before the turbulent kinetic energy and vertical turbulent

momentum exchange are inhibited. With increasing stratification, the buoyancy fluxes do not cease; instead they become counter-gradient. Buoyancy driven motions play an active role in the transfer of mass (de Nijs and Peitrzak, 2012a). Realising the competition between turbulent mixing and stratification processes due to barotropic and baroclinic forcing is of fundamental importance to studies of estuarine and costal dynamics. This competition determines the resulting stratification and the estuarine salt balance (de Nijs and Peitrzak, 2012b).

It may be fair to say that modelling combines science, practice and art. This includes both physical and numerical models, each of which holds their advantages, drawbacks and inadequacies. Hydraulic models of estuaries are very useful in comparing alternative designs or operational strategies. However, the complexity of the flow and transport processes in coastal and estuarine regions, make estuarine models prone to scale effects (e.g. incorrect scaling of influence of viscosity), and laboratory effects due to simplification of input conditions as well as limitations of measuring devices and proper implementation of real world phenomena. On the other hand, for some situations where the processes are too complex to be replicated at model scale, a numerical model may be more appropriate than a hydraulic model.

Barrage schemes need to embrace the principles of sustainable development, integrating economic investment and environmental improvement. They may offer solutions to a number of problems. At the same time, estuaries have a high conservation, environmental and amenity value and are a limited natural resource (Walker et al., 1999). The most immediate impact of a barrage is on the hydrodynamics regime of the estuary which is likely to fundamentally modify salinity and other water quality parameters in the estuary (HR Wallingford, 1999).

1.4 SCOPE OF THE RESEARCH

The studies reported in the literature do not provide a conclusion on the following subjects:

- A portrait of the precise processes that govern the complex turbulent flow pattern and vertical mixing in a harbour mouth and basin;
- A detailed picture of the processes involved in transport and stratification of salt in estuarine harbours and barrages on tidal and sub-tidal timescales;
- A description of the spatial structure of currents and salinity and their mutual relationship in harbours and barrages;

- A formulated relation between harbour mixing and stratification.

The principal aim of this study is to achieve a better understanding of hydrodynamics of estuarine harbours, salt transport and stratification and their relation to harbour mixing. The scope of the research is aimed to address the following questions:

- What are the dominant processes that determine the transport and distribution of salt in harbours?
- What are the interactive mechanisms of hydrodynamics, stratification and mixing in harbours?
- How do the geometry and hydrodynamic forcing conditions influence the above mechanisms and the nature of stratification in harbours?
- How accurately is a three-dimensional numerical model able to predict the hydrodynamics governing the harbour mixing and stratification?
- What is the influence of stratification on flow and turbulence in harbours and barrages?

The following tasks have been left for further research in the field:

- The comparison of aforementioned mechanisms and simulations with real estuaries, harbours and barrages;
- The study of the effect of wave-current interaction on hydrodynamics and mechanisms of the interest of this research project.

1.5 RESEARCH METHODOLOGY

A hydraulic model has been employed in concert with a numerical model, utilising the strengths of both modelling methods. The numerical model with non-hydrostatic pressure distribution and variable density was developed to predict the flow field and salinity stratification in a three-dimensional environment. The laboratory-measured values of velocities, water elevations and salinity concentrations were used for calibration and verification of the numerical model.

To account for the non-isotropic behaviour of stratified flow inside the harbour, investigations were carried out on different turbulence model closures so as to examine the stratification-turbulence interaction on a 2DV module of the numerical model. The primary aim was to obtain improved understanding of the effects of buoyancy forces caused by salinity on the turbulence structure and their mutual

relationship. Laboratory measured data reported in the literature of a number of lock-release, buoyant jet and intrusive gravity currents were compared against numerical predictions to investigate the suitability of the turbulence model closures to characterise the hydrodynamics and mixing behaviour of the flow.

The numerical model also contributed to a distortion study for the model harbour to portray and emphasise the potential misinterpretation of measured values due to vertical distortion used in laboratory scaled models and the discrepancies of simulated values of numerical models compared to the corresponding data.

The numerical model was further employed for analysing applications of different mean water depths and barrier heights to examine the influence of these parameters on hydrodynamics and stratification in harbours.

A laboratory tidal basin was designed, set up and employed for velocity, water elevation and salinity measurements of the model harbour for fresh water and salinity stratified conditions with various barrier heights and mean water depths. The measurements were designed to serve the following goals:

- To improve the knowledge regarding the dominant mechanisms responsible for the evolution of the internal flow structure in the model harbour.
- To improve the knowledge regarding the dominant mechanisms determining the exchange of saline water behind a barrier.
- To provide data for the calibration and verification of the newly developed three-dimensional numerical model.

An extensive signal procedure was carried out to minimise the noise and spikes of the measured velocity and salinity concentration data by establishing suitable correlations for the collected digital signals.

1.6 OUTLINE OF THE THESIS

The research questions are addressed in Chapters Two, Five, Eight and Nine. Overall conclusions are presented in Chapter Ten. A short description of the chapters has been outlined in the next paragraphs.

Chapter Two brings together the literature on modelling of coastal flow fields and the phenomena caused by salt intrusion and the corresponding stratification in estuarine harbours and barrages, discussing the requirements for a numerical model to accurately prediction of combined turbulent tidal and gravity currents, their mixing and nature of their stratification.

The chapter provides a review of hydrodynamic and turbulence numerical and physical modelling of tidal flows in estuarine waters, harbours and barrages. Numerical modelling has received more attention with focusing on the projection method. Mechanisms of salinity stratified estuaries, harbours and barrages and their three-dimensional numerical modelling have been discussed. Turbulence modelling of estuarine harbours and barrages has been investigated and a review of some k-ε turbulence models is presented. Non-isotropy of turbulence stresses along with turbulence-stratification interaction is discussed. A review on the relevant literature of data acquisition and signal processing of laboratory measured values also has been included in the survey.

Chapter Three introduces the governing hydrodynamic equations of motion and mixing and outlines some of turbulence models including the models utilised in this research project.

Chapter Four provides a comprehensive description of the three-dimensional non-hydrostatic free surface numerical model with density variation developed herein and presents the solution method in arbitrary Lagrangian-Eulerian (ALE) coordinate system.

Chapter Five examines the ability of the numerical model in simulating advection, diffusion and wave propagation in complex bathymetries and with various temporal and spatial boundary conditions. The test cases also include the simulation of gravity flows in a number of lock-release, buoyant jet and salinity intrusion hydrodynamics. Different turbulence closures have been implemented to examine the suitability of each of them for stratified environments of interest. The chapter also discusses the changes in the turbulence structure and the effects on vertical transport of momentum and buoyant mass of stratified flows with the consideration of either isotropic or non-isotropic turbulence closures.

Chapter Six introduces the governing equations for physical modelling and illustrates a comprehensive description of the laboratory tidal basin and the model harbour design and set-up.

Chapter Seven is dedicated to description of test arrangements, instrumentation, calibration, data acquisition and signal processing and digital filtering of the measured values. A linear method has been introduced for minimising the noise and spikes by the establishment of temporal correlations for the flow field.

For the salinity concentrations recorded in the model harbour, a moving average strategy has been utilised to eliminate the noise from the signals.

Chapter Eight presents the measurement results and investigates the mechanisms that govern the hydrodynamics and dominate the advection of salinity, salt exchange, stratification and evolution of the internal flow structure of the model harbour in the laboratory tidal basin. This has been covered by analysing the measured values of velocities, water elevations and salinity concentrations for different laboratory set-ups. The spatial extent of the measurements served to determine whether the stratification remained stable during the ebb and flood tidal excursions along the entrance and harbour axes. Moreover the effect of salinity on hydrodynamics has been discussed and the effect of different barrier heights on the hydrodynamics has been investigated.

Chapter Nine further addresses the concepts developed in the previous chapters by the simulated values of the three-dimensional model. The data and analyses in the previous chapters provide requisite information to assess the predictive capability of the model. The data sets have been used for the calibration and verification of the three-dimensional numerical model to examine the accurately prediction of the hydrodynamics and stratification pattern of the tidal flow regime at the entrance and inside the model harbour. A discussion is provided on the discrepancies between the numerical model results and measurements. A distortion study has been conducted to emphasise the scale effects of vertically distorted models on the interpretation of the measured laboratory values and their comparisons with the numerical model predictions. As a part of the numerical investigations, different salinity contents and barrier heights for a range of mean water levels are simulated and the predicted results are compared. This served to study the relation between the advection of the salt and the spatial and temporal variability of the vertical structure of the tidal currents along the entrance and centreline axes of the model harbour.

Chapter Ten discusses and integrates the main concluding remarks of all chapters, and offers some recommendations for further research in the area.

CHAPTER TWO

LITERATURE REVIEW

"Water is the principle, or the element, of things. All things are water."
Thales of Miletus (Plutarch, Placita Philosophorum)
(O'Connor and Robertson, 1999)

2.1 INTRODUCTION

This chapter has been aimed to address the relevant literature corresponding to the research questions posed in Chapter One, and affords evidence to the pertinent subjects of fundamental importance in a limited framework.

As the central part of this research project is the numerical and physical modelling of tidal flows in estuarine harbours, these two, with the dominance of numerical modelling, have received most of the attention. Three-dimensional numerical models are the focal point followed by two-dimensional laterally-averaged models, as the latter is the core of the three-dimensional model developed herein. The projection method, which has been deployed in the solution algorithm of the numerical model, has been also discussed in some detail.

Although the two-dimensional horizontal models are not in the area of interest of this research project, they have been reviewed as they still are powerful tools for shallow-water simulations, and provide valuable insight about the effects of

impoundment geometry, harbour flushing and overall water quality processes. However they are not capable of accurately modelling mixing and stratification as the vertical density gradients and vertical turbulence play a significant role in the dynamics of estuarine water bodies.

Physical models, on the other hand, have been the focus of many research projects, as they provide very useful means for a better comprehension of physical phenomena and clarification of the hydrodynamics and mechanisms of interest. They also provide invaluable data for calibration and validation of numerical models. However, they appear in a smaller number of publications in recent literature.

The velocity data recorded by acoustic Doppler velocity meters (ADVs) and the conductivity data are noticeably noisy. Data acquisition and signal processing procedures of the studies in the similar fields have been reviewed to provide the basics for the corresponding studies carried out in this thesis.

Stratified flows are of prime importance in estuarine studies, as salt intrusion is almost always present in harbours and barrages located in these areas. Their attractive and complicated hydrodynamics has been the reason for many analytical, physical and numerical studies. Their principal vertical behaviour makes the two-dimensional vertical models of major utilisation for such physical structures. However, it has to be emphasised that the hydrodynamics of stratification in a tidally-influenced harbour is fully three-dimensional, and therefore the relevant 3D models have been covered even if they have not fulfilled the expectations according to simulated results reported in the literature.

Turbulence modelling in conjunction with dynamics of estuaries and harbours and in combination and interaction with buoyant stratified flows makes it the most challenging subject of the detailed studies of estuarine hydrodynamics. Its inclusion in the numerical model as an important part of the predictive means of hydrodynamics of estuarine hydro-environments, even in the absence of salinity and stratification, is of prime importance.

The complicated nature of salinity-stratified hydrodynamics and non-isotropic behaviour of turbulence and mixing associated with such conditions, leads to the review of the relevant turbulence closures in the field.

A conclusion of the chapter provides the necessary information of an outlook for the fields of the interest of this research project.

2.2 HYDRODYNAMIC AND TURBULENCE MODELLING OF TIDAL FLOWS IN ESTUARINE WATERS, HARBOURS AND BARRAGES

"The sciences do not try to explain, they hardly even try to interpret, they mainly make models" (von Neumann: O'Connor and Robertson, 1999).

Dalrymple (1985) pointed out that field studies provide the best data, but they are usually expensive and too many variables of nature are present, making data interpretation difficult. In contrast, physical models are smaller, less expensive, easily studied, and simpler than nature, yet they include most important aspects of the problem. In addition, physical and numerical model input conditions can be controlled and systematically varied, whereas field studies have no such control (Kamphuis, 1991). Mathematical models point out the most important deficiencies, and physical models offer the chance to monitor and measure the physics in a controlled environment (Hughes, 1993).

Tidal motion is sensitive to the length, depth and roughness of an estuary (Bowden, 1983). The rate of longitudinal mixing is governed by the strength of the tidal velocities, shape of the channel cross-section and by gravitational circulations induced by longitudinal salinity gradients (HR Wallingford, 1999). Vertical mixing is caused by turbulent eddies which generate internal stresses in the flow by interchanging momentum of the fast flowing and slower flowing layers. Turbulence also mixes salt, heat, sediment and pollutants through the water column. Stable stratification damps the vertical turbulent eddies and reduces vertical mixing drastically (Odd and Rodger, 1978). The degree of stratification is quantified by the local gradient Richardson number, that usually peaks at a level at which the density gradient is largest. In vertically well-mixed estuaries with a tidal range to mean tide depth ratio, 0.5-2.0, the pattern of saline intrusion and mud and sand transport is governed by the inequality of the flood and ebb tides caused by shallow effects (HR Wallingford, 1999). This usually results in a short strong flood current and a long period of weaker currents on the ebb tide. The turbulence in estuarine environments generally occurs at higher values for shear and stratification than the turbulence in the ocean and shelf seas (de Nijs and Pietrzak, 2012a).

HR Wallingford (1999) defines a barrage as a structure built in an estuary, at a point where it is not less than 15 m wide, with the specific intention of preventing, or in some way modifying tidal propagation, including barrages designed to retain a

minimum upstream water level. Part-tide barrages, which allow the intrusion of seawater, give rise to a whole class of problems in the upstream pool. The intruding seawater is likely to form a stable two-layer system with little or no vertical turbulent exchange, especially during neap tides and low river inflows (HR Wallingford, 1999). Mud and polluted particulate matter tend to be trapped in the lower layer causing major water quality problems. HR Wallingford (1999) comments on the hydraulic impacts of barrages in order to assess whether the barrage would change the pattern of saline intrusion, stratification and gravitational circulation so as to have an adverse effect on flushing of pollutants, cooling water, water quality, sedimentation or the ecosystem in the estuary. If the barrage is overtopped by the tide, the issue of whether the polluted saline water would be trapped upstream should be noticed.

The tidal barrage in the Tees estuary restricts the upstream movement of the salt resulting in the formation of a new freshwater region to landward. The blocking of the tidal flow at the barrage has resulted in a marked increase in stratification due to reduction in tidal current speed and in the rate of vertical transfer of salt. The time of the most intensive mixing has changed from the ebb tide to the flood tide (Riddle and Lewis, 1999). The modelling studies have indicated that the changes in the stratification on the flood tide for the post barrage situation are principally associated with vertical mixing, rather than differential advection of the longitudinal distribution of salt. Xia et al. (2010) investigated the impact of constructing a tidal barrage on the hydro-environmental aspects of the Severn estuary, using a numerical model. They reported that at some cross-sections, the maximum discharges were predicted to decrease by 30-50%, as compared with the corresponding discharges predicted without the barrage. The model also predicted that with the barrage, the maximum water levels upstream of the barrage would decrease by 0.5-1.5 m, with the peak tidal currents also being reduced considerably. For different operating modes, complex velocity fields were predicted to occur in the vicinity of the barrage.

2.2.1 *Numerical Models*

A comprehensive classification for a wide range of tidal flow modelling can be found in Abbott (1997). Categorising the coastal modelling and its development, based on the generations of the models, has been provided by Abbott (1989). Abbott (1993) also provides a review on reliability and applicability of the full three-

dimensional, intermediate models of the two- and three-dimensional and one- and two-dimensional nearly-horizontal flow models. Here only a brief review on the levels of tidal flow modelling is presented. The hydrodynamic stages are usually characterised by the dimensionality of the flows that the models simulate (Abbott, 1997). The classification presented herein (HR Wallingford, 1999), classifies the tidal flow models according to their dimensions:

- 1D: Cross-sectionally averaged;
  - Applications: Adequate for predicting tidal and surge propagation and fluvial flooding in narrow estuaries (width <10% length).
  - Limitations: Cannot simulate stratification, gravitational circulation or secondary or residual currents.
- 2D Horizontal: Depth-averaged;
  - Applications: Adequate for predicting tidal and surge propagation and fluvial flooding in wide, relatively shallow vertically well-mixed estuaries (width >10% length).
  - Limitations: Cannot simulate stratification, gravitational circulation or secondary currents.
- 2D Vertical: Width-averaged;
  - Applications: Adequate for predicting tidal levels, currents, salinity, water quality and suspended sediment in a relatively narrow (width <10% length) stratified or deep estuary.
  - Limitations: Cannot simulate variation of currents across an estuary.
- 3D Hydrostatic: Assumes hydrostatic pressure distribution;
  - Applications: Adequate for predicting tidal currents, salinity, water quality and suspended sediment in a wide stratified estuary.
  - Limitations: Cannot simulate flows in zones with large vertical acceleration.
- Full 3D: Complicated unsteady non-hydrostatic pressure distribution;
  - Applications: Adequate for predicting detailed 3D flows.

2.2.2 *Physical models*

Although hydraulic models may be more expensive than computer models, they have a very great advantage for some situations, especially for three-dimensional density-stratified flows (Fischer et al., 1979). The influence of the planform geometry, entrance width and tidal range on the exchange characteristics of

a simple rectangular harbour, having a constant depth and planform area, with a single asymmetric entrance and vertical sides, was investigated in the studies of Jiang and Falconer (1983). The laboratory results confirmed that the optimum gross tidal flushing occurs for a rectangular harbour when the length to breadth ratio is between 0.5 and 2, and for lower tidal ranges ideally the harbour should be square. Tidal circulation and flushing for a square harbour with a single asymmetric entrance has been investigated extensively in a number of studies conducted by Nece and Falconer (1989a, 1989b), Falconer and Yu (1991), and Falconer and Chapman (1996). More specifically, mean water level velocity distributions along the centreline axes of the model harbour were presented and compared for flood and ebb tide conditions. In the studies of Nece and Falconer (1989b) also the influence of different distortion ratios was investigated on velocity distributions, with the results indicating little variation for both the flood and ebb tide at mean water level. In another set of experiments (Falconer and Yu, 1991) emphasis was placed on determining the influence of the mean depth, bed slope and vertical scale distortion on the tidal current structure at mean water level, and on the tidal exchange characteristics. The results showed that the tidal exchange coefficient decreased with increasing mean depths and increased for increasing distortion. Transport in these types of water bodies is advection dominated, and vertical distortion and low Reynolds numbers in the model rule out equivalence of local diffusion characteristics in the model and prototype (Nece, 1984). In a study of tidal circulation and flushing in five western Washington marinas Nece et al. (1980) used distorted hydraulic models with distortion ratios equal to 10 and 12.5.

Langendoen (1992) studied the influence of the harbour entrance geometry on the velocity and density fields in the entrance of a tidal harbour by means of laboratory experiments and field measurements. Ohle et al. (2000) used undistorted physical models for the extension of Altenwerder harbour, and the reconstruction of Hansahafen harbour in Hamburg, for two-dimensional flow simulations and analysis of different designs of harbour geometries with respect to flow characteristics and sedimentation conditions. Hassan et al. (2012) used a physical scale model to study wave propagation during various storm wave conditions into the harbour of Ostend.

Cuthbertson et al. (2006) modelled the relative influence of tidal and fluvial forcing on the density-driven exchange across a submerged barrier, with particular emphasis on the relative importance of these agencies in controlling the temporal and

spatial development of the brackish layer formed behind the barrier. They reported that the intrusion experiments indicated that the formation, growth, and stabilisation of the brackish pool during its early stages of development are dependent upon the tidal conditions and the geometrical details of the impoundment volume. They concluded that as far as the water quality of the impounded volume is concerned, the dimensions and structure of the trapped brackish water pool are of fundamental importance.

2.2.2.1 Data Acquisition and Signal Processing

The ADV is a remote-sensing, three-dimensional velocity sensor, originally developed and tested for use in physical model facilities (Kraus et al., 1994; Lohrmann et al., 1994), and its operation is based on the Doppler shift effect.

High levels of noise and spikes have been reported in measurements with ADV velocimeter (Nikora and Goring, 1998; McLelland and Nicholas, 2000). In turbulent flows, the ADV velocity fluctuations characterise the combined effects of the Doppler noise, signal aliasing, velocity fluctuations, installation vibrations and other disturbances (Chanson et al., 2008). Both the spectra and the probability distributions indicate that as a first approximation, the Doppler noise is Gaussian white noise (Nikora and Goring, 1998). Chanson et al. (2002) discussed the noise of an ADV system. The main source of Doppler noise is the random target distribution in the sampling volume, which induces an instantaneous Lagrangian deviation of the position of the target from the mean position determined by the spatially averaged velocity. This creates instantaneous random Doppler-phase noise that is added to the spatially averaged Doppler phase (Doroudian et al., 2010). McLelland and Nicholas (2000) explained the physical processes causing spikes by aliasing of the Doppler signal. For steady flow situations a few techniques to eliminate the spikes have been developed (Nikora and Goring, 1998; Goring and Nikora, 2002; Wahl, 2003). Wahl (2000) also developed the WinADV program for post-processing and analysis of ADV data. Due to the presence of intermittent spikes contaminating time series measured by acoustic Doppler velocimetry, statistical properties, and power spectral density of such data sets can have unrealistic values (Parsheh et al., 2010). These spikes appear when the flow velocity exceeds the preset velocity range of the equipment, the turbulence intensities are high, or there are contaminations from previous pulses reflected from the flow boundaries.

Voulgaris and Trowbridge (1998) evaluated accuracy of the acoustic Doppler velocimeter (ADV) by measurements of open channel flow using an ADV and a laser Doppler velocimeter. The results were qualitative and showed a good agreement between the mean values obtained by the two sensors. They examined the degree of accuracy in measuring mean velocity, variance, and covariance of the flow field together with the effect of the proximity to the boundary in flow measurements. The types and magnitudes of noise involved in flow measurements using an ADV sensor were also examined. They concluded that ADV is suitable for accurate measurements of mean flow even at positions close to the boundary. However, Dombroski and Crimaldi (2007) stated that the accuracy of ADVs is limited when making measurements close to the bed or in flows where large spatial gradients are present. To validate the use of ADVs for the measurement of turbulent flows, Khorsandi et al. (2012) conducted experiments in an axisymmetric turbulent jet and in approximately homogenous isotropic turbulence with zero mean flow. The jet experiments showed that the horizontal RMS velocities measured by the ADV were overestimated compared to both flying hot-film anemometry measurements and the accepted values in the literature. However, the vertical component of the RMS velocity agreed well with those of other studies. To correct the data, post-processing filters and a Doppler noise-reduction method were applied to the jet data. Despite decreasing the RMS velocities, they remained erroneously higher than the accepted values. Their results showed no clear relationship between the Doppler noise and the mean flow.

Goring and Nikora (2002) assumed that good data can be found within a cluster and that points located outside the cluster are spikes. They suggested a method based on iterative phase-space thresholding as the most suitable solution for spike detection. They reported that the method worked extremely well confirmed by successful application of the method to numerous ADV data. Doroudian et al. (2010) combined a spike-removal procedure on the beam velocities with a noise-reduction method on the flow velocities to improve turbulence measurements with ADVs. It was shown that spikes were best removed from ADV beam velocity data before calculating flow velocities, thereby correcting all three flow velocity components at the source. Yin et al. (2001) developed a method to analyse a time series of velocity signals in order to obtain a time series of a moving-averaged velocity. They described the turbulent velocity fluctuations with a Gaussian probability distribution,

and the method was developed to calculate the local mean velocity of unsteady tidal flow from the experimental data using ADV with noisy signals. de Nijs et al. (2009) used a 10 minute moving average filter to determine the main flow and turbulence statistics.

Snyder and Castro (1999) assessed the use of ADVs in a stratified tank with variable density of saltwater over the transmitting path of the probe. The tests showed that the indicated distance to the boundary was directly proportional to the specific gravity of the saltwater. A correction scheme was developed for highly concentrated saltwater, and its suitability was verified in homogeneous saltwater solutions.

2.3 NUMERICAL MODELLING OF COASTAL FLOW FIELDS, ESTUARIES AND HARBOURS

If a model is only to be applied for a strongly stratified water body, so that it maintains a two-layer system of flow throughout the simulation, a two-layer system, which represents the simplest case of a stratified flow (Harleman, 1961), may be considered. The flow in a two-layer system is divided into two homogenous layers with only a density difference at the interface (Karelse et al., 1974). Multi-layer systems have been discussed in Vreugdenhil (1994). However, these models cannot simulate problems involving three-dimensionality and vertical eddies or flows with continuous-density gradients. In two-layer numerical model simulations of saline intrusion and sediment transport in the Rotterdam Waterways, HR Wallingford (1979) concluded that tidal processes in the waterways can be simulated satisfactorily for engineering purposes by schematising the flow into two layers. The main process, which determines the longitudinal and vertical distribution of salt within the layered system, is the vertical turbulent exchange of salt across the interface. Castro et al. (2007) used a two-layer, finite volume model for simulations of stratified flows through channels with irregular geometries. The flow was assumed to be composed of two shallow layers of immiscible fluids with constant densities, and was presumed to be one dimensional. In a similar study, Castro et al. (2004) investigated maximal and tidally induced two-layer exchange flows through the Strait of Gibraltar. Chen and Peng (2006) applied a two-dimensional explicit finite volume method for solving the two-layer shallow water equations for confluence simulation.

A successful modelling of strong advection is one of the most challenging problems. Although traditional first-order finite difference methods are monotonic and stable, they are also strongly dissipative, and suffer from severe inaccuracies due to truncation error. On the other hand, traditional high-order difference methods are less dissipative but are susceptible to numerical instabilities, which cause non-physical oscillations in advection-dominated regions and zones of large gradient of the variables. Incorporating artificial diffusion into the numerical scheme to dampen spurious oscillations in regions of large gradients, results in smearing out the solution elsewhere. The ULTIMATE QUICKEST scheme (Leonard, 1991) gives results which are probably entirely adequate for most practical situations (Fig. 2.1). In a study of comparing a series of numerical schemes for one-dimensional advection-diffusion problems, Wang and Hutter (2001) concluded that the modified TVD Lax-Friedrichs method is the most competent method for advectively-dominated problems with a steep spatial gradient of the variables. However, they are at most first-order accurate at local extrema and highly dependent on the slope limiters used in the model in some cases. Bruneau et al. (1997) also proposed TVD schemes from a family of second- and third-order Lax-Wendroff-type schemes.

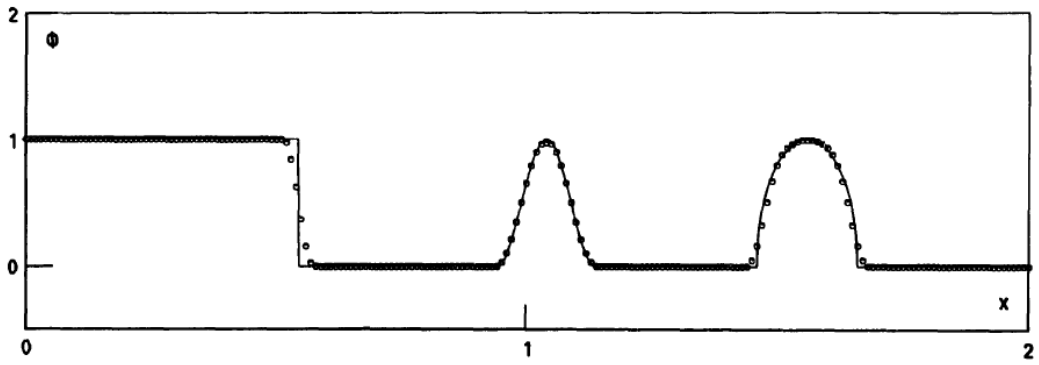

Figure (2.1) - ULTIMATE QUICKEST results (adapted from Leonard, 1991)

Finite difference method has been deployed in a number of numerical models using structured grids (POM, Blumberg and Mellor, 1987; TRIM, Casulli and Cheng, 1992; Lin and Falconer, 1996; ECOMSED, HydroQual, Inc., 2004; ROMS, Shchepetkin and McWilliams, 2005; NCOM, Barron et al., 2006; Anthonio and Hall, 2006). Unstructured grids have also been employed in a number of studies deploying finite element method (ADCIRC, Luettich et al., 1991; QUODDY, Lynch and Werner, 1991; SEOM, Iskandarani et al., 2003), or using hybrid approaches involving finite volume method (UnTRIM, Casulli and Walters, 2000; FVCOM, Chen et al., 2003; ELCIRC, Zhang et al., 2004).

2.3.1 *2DH Models*

Two-dimensional horizontal (2DH) numerical models are very popular due to their acceptable accuracy and high efficiency. There is a wide variety of numerical models developed on the basis of depth-averaged Navier-Stokes equations, for simulating the tidal circulation and flushing in harbours (Falconer, 1980b), for steady shallow water flows (Zhou, 1995), and for modelling water quality processes and fate and transport of oil spills (Sarhadi Zadeh and Hejazi, 2010, 2012). Estuaries are transitional areas which trap significant quantities of particulate and dissolved matter through a wide variety of physical and biogeochemical processes. Harbour planform effects and investigation of effective harbour geometry parameters on cohesive sediment transport and sedimentation has also been studied by means of 2DH models (Mojabi and Hejazi, 2011; Mojabi et al., 2011, 2013). Karimi et al. (2012) presented an integrated 2DH numerical model for interactive simulations of oil spills, sedimentation and transport of oil in sediment laden marine waters. In some cases depth integrated models are preferred as they are computationally economical, easier to program and provide sufficiently accurate results. In depth-averaged models, however, the vertical distribution of currents is not known and the bed friction is expressed in terms of the mean velocity rather than the velocity near the bottom.

In addition to employing high-order numerical methods to increase the accuracy of solution of shallow-water equations, nested grid refinement may be implemented in order to improve the solution through resolution of computational grids. Peng et al. (2010) developed a nested-block, finite volume based Cartesian grid, method for simulating the unsteady viscous incompressible flows with complex immersed boundaries using a two-step fractional step procedure. Hadaeghi and Hejazi (2013) developed a 2DH finite volume nested model to solve vorticity transport in viscous fluid flows. The solution was based on a fractional step method and an iterative successive-over-relaxation (SOR) scheme was employed to solve the two-way nested grid normalised equations. The discretisation scheme provided second-order accuracy in space and time.

Attempting to obtain higher efficiency and affording accuracy, three-dimensional Reynolds averaged Navier-Stokes equations may be depth-averaged but retain the non-hydrostatic pressure terms (Stelling and Zijlema, 2003; Walters, 2005; Bai and Cheung, 2013). Marshall et al. (1997) discussed the use of ocean models based on hydrostatic, quasi-hydrostatic, and non-hydrostatic equation sets.

Nece and Falconer (1989a) stated that in complex studies where vertical density gradients are important and single-fluid models are not appropriate, then the three-dimensional equations should be solved directly. Lin and Falconer (1997) presented a three-dimensional layer-integrated model with flooding and drying, and studied the tidal motion in lower reaches of the Humber estuary.

2.3.2 *2DV Models*

Perrels and Karelse (1982) introduced a finite difference two-dimensional, laterally averaged model with hydrostatic pressure assumption, for salt intrusion simulations in estuaries. Daubert et al. (1982) and Daubert and Cahouet (1984) developed 2DV models using a three-step fractional method. Haque and Berlamont (1998) developed a 2DV finite element model to predict the flow, density, and turbulence fields of a stratified tidal medium. Zhou and Stansby (1999) developed a 2DV numerical model based on arbitrary Lagrangian-Eulerian (ALE) description and in the σ-coordinate system, using a semi-implicit time-stepping method for solving unsteady Navier-Stokes equations. Yuan and Wu (2004a) developed an implicit finite difference model in the σ-coordinate system for non-hydrostatic, two-dimensional vertical plane free surface flows using the solution method presented in Namin et al. (2001). Zijlema and Stelling (2005) introduced a semi-implicit 2DV numerical model which solves the incompressible Euler equations with the aid of a projection method and splitting the pressure into hydrostatic and non-hydrostatic components by the finite volume technique. More 2DV models were developed by Stelling and Busnelli (2001), Stansby and Zhou (1998), and Memarzadeh and Hejazi (2012). Hejazi et al. (2013) introduced a 2DV numerical model to simulate wave-mud interaction. The fully non-linear Navier-Stokes equations with complete set of kinematic and dynamic boundary conditions at free surface and interface with the two-equation k-ε turbulence model with buoyancy terms were solved. A finite volume method based on an ALE description was utilised for the simulation of wave motion in a combined system of water and viscous mud layer. The propagation of irregular waves in a two-layer viscous fluid system and interaction of water waves with a muddy bed bounded below by a horizontal rigid plane was also investigated by the model and spectral method (Hejazi et al., 2014b). The model was further modified to study the interaction between wave, current and mud bed (Hejazi et al., 2014a).

2.3.3 *3D Models*

Undoubtedly the vast variety of the three-dimensional models developed to date and extensive features of their groups and each cannot be distinctly categorised. However, to formulate the present review, and to have more useful conclusions, this section follows the main parts of the structure of the numerical model developed herein which have been identified to be the solution method, the pressure treatment approach, and the coordinate system.

2.3.3.1 Solution Method

To optimise stability and economy, Wolf (1983) developed a fully nonlinear three-dimensional model, using the Galerkin method in the vertical dimension, in which the gravity wave terms were treated by an alternating-direction implicit (ADI) scheme, while the friction, viscous and advective terms were treated explicitly. The 3D hydrodynamic model MOHID (Fossati and Pierdra-Cueva, 2013) encompasses a finite-volume approach, using a semi-implicit ADI algorithm for the horizontal advection-diffusion schemes. Hydrostatic equilibrium and Boussinesq approximation have been assumed in the model. Despite its advantages, ADI scheme encounters problems at corner boundaries. Closed boundaries, or the boundaries whereon the velocity is specified, also introduce instabilities due to the loss of symmetry in the ADI scheme (Wolf, 1983). Weare (1979) showed the effect of corner boundary condition on accuracy as it imposes zero tangential and normal flow. He also showed how this inaccuracy is diffused throughout the flow by the ADI scheme.

MIKE 3 (DHI, 2009a) is a fully three-dimensional model which simulates unsteady flows with the consideration of density and bathymetry variations and external forcing, with the application of Boussinesq approximation. The software includes two models of hydrostatic assumption and non-hydrostatic pressure distribution. The artificial compressibility method has been adopted in the non-hydrostatic version of MIKE 3. The governing equations are discretised in an implicit, finite difference fashion on a rectangular, staggered grid and are solved non-iteratively by the use of an alternating direction implicit algorithm, employing a fractional-step technique. The equations are solved in one-dimensional sweeps, alternating between x, y and z directions providing a time-centred scheme. Time centring of the hydrodynamic equations is achieved by defining the pressure at one-

third time step intervals and the velocity components at one time step intervals differing one-third time step for each component, in an arrangement that the pressures are located in the mid-way of temporal series of velocity components (Fig. 2.2). The partial differential equations are then formulated as a system of implicit expressions, and the resulting tri-diagonal system of equations is solved by the double sweep algorithm. Alternative advection-dispersion schemes, which somehow form a QUICKEST (quadratic upstream interpolation for convective kinematics with estimated streaming terms; Leonard, 1979) family of schemes, are provided in the model. The eddy viscosity may be determined by one of the closure models of a constant eddy viscosity, the zero-equation Smagorinsky sub-grid model, the one-equation k model, the two-equation standard k-ε model, or a combination of the Smagorinsky model for the horizontal direction and a k-ε model for the vertical direction.

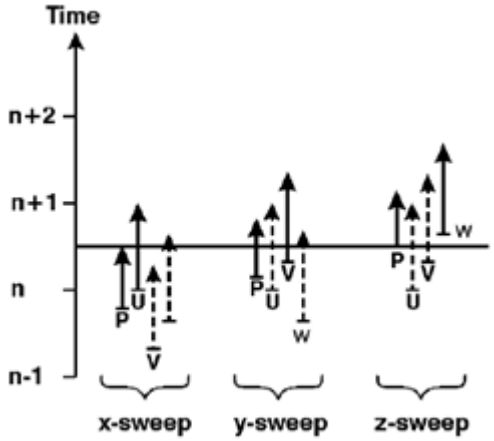

Figure (2.2) - Time centring of MIKE 3 (adapted from DHI, 2009a)

Zhang and Gin (2000) developed a three-dimensional multi-level hydrodynamic model. The model assumes hydrostatic pressure distribution, applies the Boussinesq approximation, and the water density has been considered to be constant. A finite difference method in a non-uniform rectangular staggered grid system has been utilized. A two-step Euler predictor-corrector algorithm is introduced to predict and correct the free surface water elevation. Three time-levels are involved in predictor equation. The central and forward differences for the time derivative terms and the central differences for the space derivative terms are adopted. The momentum equations in the horizontal direction are discretised by explicit schemes, and the continuity equation is discretised by an implicit scheme for the vertical velocity. Chen (2003) used a two-step predictor-corrector algorithm for

solving three-dimensional free surface equations without hydrostatic pressure assumption. Yuan and Wu (2004b) presented an implicit method for solving the complete three-dimensional Navier-Stokes equations. They introduced a top-layer pressure treatment and a partial cell bottom treatment. A domain decomposition method was used to segregate the resulting 3D matrix system into a series of two-dimensional vertical plane problems, for each of which a block tri-diagonal system was directly solved for the unknown horizontal velocity. Using an ADI method in the horizontal plane, also Hejazi (2005) directly solved the block tri-diagonal matrices of the vertical planes of the 3D model to compute pressures of the corresponding Poisson equation of each vertical plane.

TELEMAC-3D (LNHE, 2013) solves three-dimensional flow equations, with or without the hydrostatic pressure hypothesis, and the transport diffusion equations of intrinsic quantities. The mesh structure is made of prisms and the Boussinesq approximation has been applied. The TELEMAC-3D basic algorithm can be split up in three fractional steps. The first step consists of solving the advection terms in the momentum equations to find the advected velocity components. In the second step the new velocity components are updated from the advected velocities taking into account the diffusion and source terms in the momentum equations, providing an intermediate velocity field. The third step then computes the water depth from the vertical integration of the continuity equation and solves the momentum equations by only including the pressure terms. The algorithm, for the non-hydrostatic pressure, employs the same procedure as in the hydrostatic pressure assumption, but for the computation of the dynamic pressure and free surface, in the projection step, the pressure gradient changes the velocity field in order to provide the required zero divergence of velocity. The turbulent viscosity may be taken constant, or determined either from a mixing length, Smagorinsky, or a k-ε model.

Flow-3D (Flow Science, Inc., 2008) uses finite difference or finite volume approximations by the method of volume of fluid (VOF). The flow region is subdivided into a mesh of fixed rectangular staggered cells. Pressures and velocities are coupled implicitly by using time-advanced pressures in the momentum equations and time-advanced velocities in the continuity equation. The semi-implicit formulation results in coupled sets of equations that are solved by an iterative technique. Successive over relaxation (SOR) or special alternating-direction, line implicit methods (SADI) are available for iterations. The SADI technique may be

used in one, two, or three directions depending on the characteristics of the problem to be solved. The basic numerical method has first-order accuracy with respect to time and space increments. Internal viscous shear and the diffusion of fluid fraction, fluid density, turbulence energy, and turbulence dissipation are all treated in analogous ways. The diffusion coefficient for each process is proportional to the dynamic viscosity, which may vary in space and time as a result of the turbulence models. All quantities are evaluated explicitly in these calculations.

SELFE (Zhang and Baptista, 2008) solves the 3D shallow water equations, with hydrostatic and Boussinesq approximations, and transport equations for salt and heat based on finite element and finite volume methods in a semi-implicit fashion. Unstructured triangular grids and hybrid vertical coordinates are used in the horizontal and vertical directions respectively. The barotropic equations are solved first, and the transport and turbulent closure equations lag one time step behind, which treats the baroclinic pressure gradient term in the momentum equation explicitly. Kanarska et al. (2007) studied the degeneration of an initially large-scale wave into solitons. Their simulated results are shown for hydrostatic and non-hydrostatic conditions in Fig. (2.3). Their comparisons showed that the non-hydrostatic pressure distribution exhibits good agreements with the experimental data, but the degeneration process is not described correctly in a hydrostatic model. The bottom figure shows the regions where non-hydrostatic pressure is large; these are zones of waveform transformation into higher frequency solitons. The energy dissipation is different in hydrostatic and non-hydrostatic models. In the hydrostatic model the energy is dissipated across the overly sharp front, whereas in the non-hydrostatic model the energy is transferred to higher horizontal wavenumbers due to dispersion and nonlinearity.

2.3.3.2 Pressure Treatment Approach

Hydrostatic pressure assumption and Boussinesq approximation have been applied in a vast variety of numerical models (Stansby, 1997; Delft3D, Delft Hydraulics, 2013; ECOMSED, HydroQual, Inc., 2004; GETM, Burchard and Bolding, 2002; Herzfeld, 2009; ROMS, Shchepetkin and McWilliams, 2005; Sankaranarayanan and Ward, 2006). However, for applications involving short period waves, abruptly changing bed topographies, and stratification due to strong density gradients, the hydrostatic assumption is no longer valid.

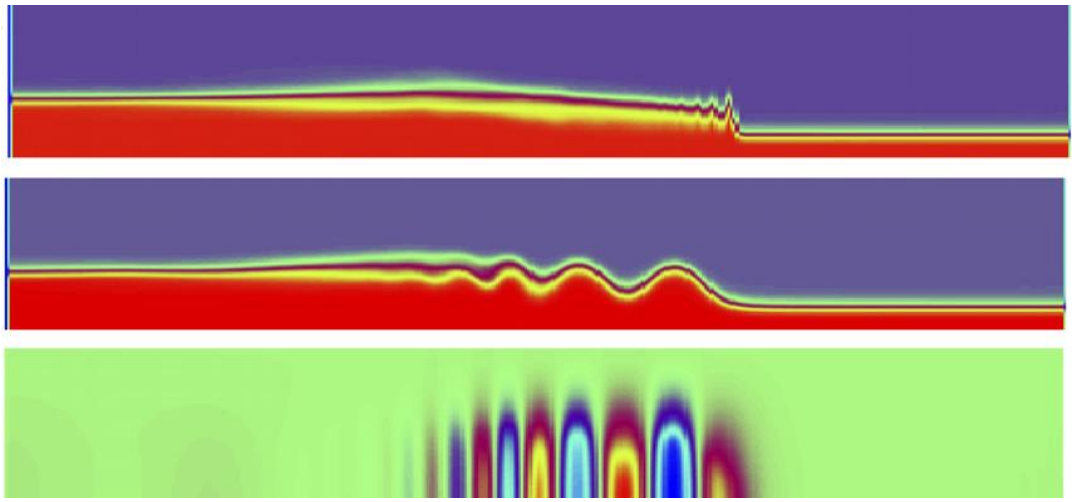

Figure (2.3) - Density distribution for hydrostatic (top) and non-hydrostatic (middle) simulations and non-hydrostatic pressure distribution (bottom) (adapted from Kanarska et al., 2007)

For simulating free surface evolution, the marker-and-cell (MAC) method (Harlow and Welch, 1965), the volume of fluid (VOF) method (Hirt and Nichols, 1981), and the arbitrary Lagrangian-Eulerian (ALE) method (Chan, 1975) have been broadly used. Depending on the treatment of density gradient in the governing equations, numerical models may be classified as barotropic or baroclinic. 2D and 3D baroclinic models have been widely developed (Casulli and Cheng, 1992; Casulli and Stelling, 1998; Casulli, 1999; Stelling and Busnelli, 2001; Namin et al., 2001; Kanarska and Maderich, 2002; Pandoe and Edge, 2003; Choi and Wu, 2006; Zhong and Li, 2006; Young et al., 2007; Kanarska et al., 2007). Development of non-hydrostatic free surface flow models, based on explicit projection method (Chorin, 1968; Li and Fleming, 2001; Lin and Li, 2002), semi-implicit fractional step method (Casulli, 1999; Casulli and Zanolli, 2002; Hejazi, 2005; Zijlema and Stelling, 2005; Deponti et al., 2006; Hejazi et al. 2013), and fully implicit method (Namin et al., 2001) is an ongoing research.

Finite volume formulation has been utilised in SUNTANS (Fringer et al., 2006) to solve the three-dimensional, non-hydrostatic Navier-Stokes equations with the Boussinesq approximation on an unstructured, staggered, z-level grid. The method is based on a semi-implicit scheme for the free surface and vertical diffusion. The remaining terms in the momentum equations are discretised explicitly with the second-order Adams-Bashforth method, while the pressure-correction method is employed for the non-hydrostatic pressure in order to achieve overall second-order

temporal accuracy. The method of SUNTANS incorporates a pressure-split algorithm and this is inherently quasi-hydrostatic from the point of view that the non-hydrostatic pressure does not directly affect the free-surface at a given time step. Fringer et al. (2006) explain that the algorithm is fully non-hydrostatic regarding the temporal accuracy of the solution method, as the effect of the non-hydrostatic pressure on the free surface at a given time step is negligible since it is the same order of magnitude as the error associated with the global second-order temporal accuracy of the overall solution procedure. Lee et al. (2006) presented a three-dimensional, non-hydrostatic model with the inclusion of k-ε turbulence closure equations for small amplitude free surface flows. By decomposing the pressure into hydrostatic and non-hydrostatic parts, the numerical model uses an integrated time step with two fractional steps. The non-hydrostatic numerical model developed by Anthonio and Hall (2006) for free surface flows, requires the solution of two Poisson equations at each time step. The simulation of a solitary wave travelling in a channel was carried out for a water depth of 10 m. Contours of the distribution of dynamic pressure, horizontal and vertical velocities are presented in Fig. (2.4).

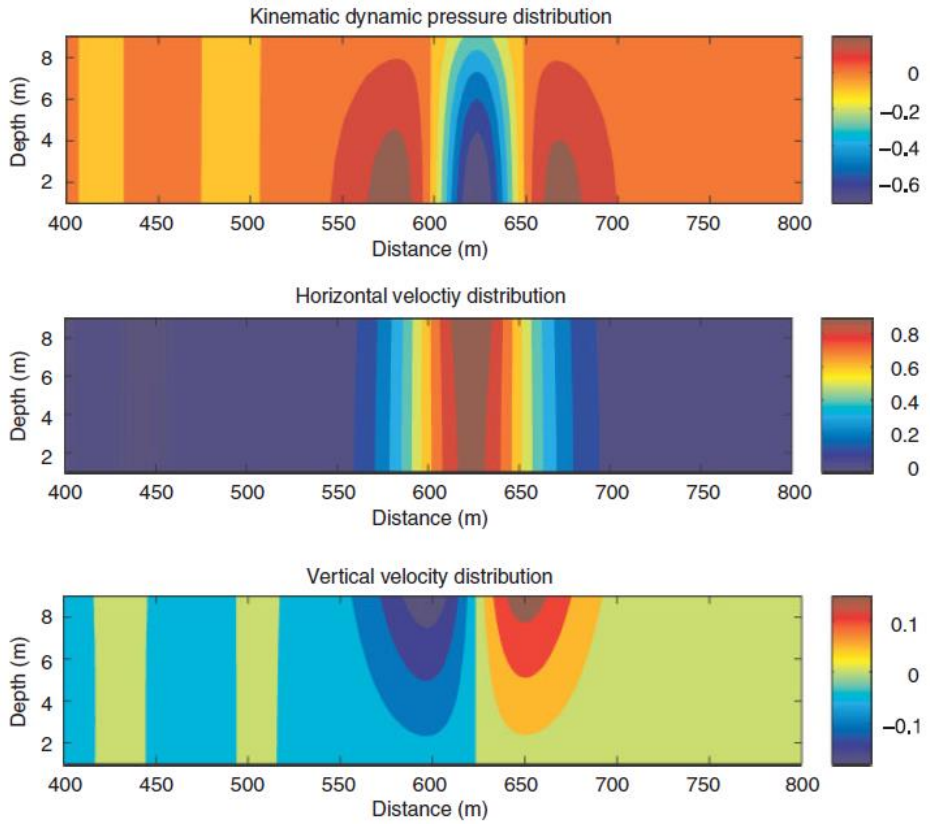

Figure (2.4) - Distribution of kinematic dynamic pressure (m) and velocities (m/s) under solitary wave (adapted from Anthonio and Hall, 2006)

The FLUENT software (Fluent Inc., 2006) employs finite volume method, supports a variety of mesh types and incorporates solution-adaptive refinement of the mesh. A fully segregated pressure based solver, a coupled pressure based solver with pseudo-transient option, and implicit and explicit density based solvers are included in the software. The pressure-based solver employs an algorithm which belongs to a general class of the projection methods. In the projection method, the constraint of continuity of the velocity field is achieved by solving a pressure, or a pressure correction equation. The pressure equation is derived from the continuity and the momentum equations, so that the velocity field, corrected by the pressure, satisfies continuity. The solution process involves iterations wherein the entire set of governing equations is solved repeatedly until the solution converges. Two pressure-based solver algorithms, segregated algorithm and coupled algorithm, are available. In the pressure-based segregated algorithm the governing equations are solved sequentially. Because the governing equations are non-linear and coupled, the solution loop must be carried out iteratively in order to obtain a converged numerical solution. The segregated algorithm is memory-efficient, but the solution convergence is relatively slow. The pressure-based coupled algorithm solves a coupled system of equations comprising the momentum equations and the continuity equation. Pressure-velocity coupling algorithms, SIMPLE (Semi-Implicit Method for Pressure-Linked Equations), SIMPLEC (SIMPLE-Consistent), PISO (Pressure Implicit with Splitting of Operators), Coupled, and fractional step method for unsteady flows using the non-iterative time advancement scheme (NITA) are included in the model. All schemes, except the coupled, use the pressure-based segregated algorithm and are based on the predictor-corrector approach. Several upwind schemes, first-order, second-order, power law and QUICK, are available. The diffusion terms are central-differenced and are second-order accurate. The adaptive central bounded numeric scheme locally adjusts the discretisation to be as close to second order as possible while ensuring stable simulation. FLUENT provides a large variety of turbulence models, including k-ε family and k-ω family models, alternative Reynolds stress (RSM) and large eddy simulation (LES) models.

2.3.3.3 Coordinate System

Within different approaches used for the construction of three-dimensional models, the most popular ones are the multi-layer, the multi-level and the fully 3D

systems. The multi-layer and multi-level approaches are generally used for flows in coastal waters where vertical acceleration is often negligible. A number of three-dimensional hydrodynamic multi-layer and multi-level models have been developed (Kawahara et al., 1983; Tomoya and Pun, 1992; Kim and Lee, 1994). The multi-layer and the multi-level models differ in the construction of the interfacial layer. In a multi-layer model, the interfacial layers, without mass transport across the layers, can freely displace vertically to maintain continuity. The application of a multi-layer model to tidal currents, therefore, requires the strict specification of open boundary conditions at the layer interfaces, which encounters some difficulty in practice. In the multi-level models, on the other hand, it is assumed that the interfacial layers are fixed in space and continuity is maintained through the vertical transport between layers.

The terrain-following σ-coordinate system is widely used for modelling free surface flows over irregular bottoms (Blumberg and Mellor, 1987; Mahadevan et al., 1996; Stansby, 1997; Zhou and Stansby, 1999; Li and Fleming, 2001; Lin and Li, 2002; Li and Zhu, 2002). Two-dimensional and three-dimensional σ-coordinate non-hydrostatic models with the semi-implicit fractional step method were developed by Zhou and Stansby (1999) and Kocyigit et al. (2002) respectively. The explicit projection method was also incorporated into the σ-coordinate non-hydrostatic model for water wave simulations (Chorin, 1968; Lin and Li, 2002). In the case of flows over a steep topography, however, the σ-coordinate transformation could introduce numerical errors in calculating the horizontal pressure gradient and the horizontal diffusion (Haney, 1991; Stelling and Kester, 1994; Song, 1998).

Drago and Iovenitti (2000) developed a three-dimensional finite difference model using σ-coordinate system for the vertical direction. An explicit scheme for temporal integration and a staggered grid for spatial discretisation were adopted. They explain that the use of the σ-coordinate transformation in multi-level models has the advantage of transforming a physical uneven domain into a flat domain so that the difficulties of common multi-level approach for sharp depth variations are overcome. In σ-coordinate, the transport across layers is allowed, but it is due only to upwelling or downwelling, and not to bathymetry and free surface variations as in common multi-level models. Compared to fully three-dimensional models, multi-level modelling does not afford convenience in areas where high vertical gradients of density are present. ECOM (Blumberg and Mellor, 1980, 1987) also uses σ-

coordinate in vertical plane and orthogonal curvilinear system in horizontal plane, and applies hydrostatic approximation. The model recognises fast, barotropic external waves and slow, baroclinic internal waves, and solves corresponding equations with different time steps. Herzfeld (2009) introduced a three-dimensional finite difference free surface hydrodynamic model, based on the primitive equations. The model uses a curvilinear orthogonal grid in the horizontal and a choice of fixed z-coordinates or terrain following σ-coordinates in the vertical. A one-way nesting strategy was used to propagate the large-scale circulation into the regional domain.

The version of MIKE 3 with the hydrostatic pressure assumption (DHI, 2009b) deploys the finite volume method. The spatial domain is discretised into non-overlapping cells. An unstructured mesh is used in the horizontal domain while the vertical domain consists of a structured mesh. The vertical mesh is based on either sigma or combined sigma and z-level coordinates. Sigma coordinates have the advantage of accurately representing the bathymetry and providing consistent resolution near the bed. However, they can suffer from significant errors in the horizontal pressure gradients, advection and mixing terms in areas with sharp bathymetry changes. The use of z-level coordinates facilitates the calculation of the horizontal pressure gradients, advection and mixing terms at the expense of inaccurately representing the bathymetry and resulting in unrealistic predictions of flow velocities near the bottom due to the stair-step representation of the bathymetry.

Cancino and Neves (1999) described a fully three-dimensional finite difference baroclinic model for hydrodynamics and fine suspended sediment transport, based on the hydrostatic and Boussinesq approximations. The model uses a vertical double sigma coordinate system with a staggered grid and a semi-implicit two-time level scheme. The horizontal transport and the Coriolis terms are solved explicitly, while an implicit algorithm for the pressure terms and for the vertical transport is used. The horizontal and vertical viscosity calculations are based on Kolmogorov and mixing length approaches respectively. For the bottom friction shear stress, a logarithmic velocity profile has been assumed. They state that despite the advantage of the sigma coordinate in regions with complex bathymetry, this convenience is not maintained where density is a major forcing. A double sigma coordinate uses a horizontal plane to split the water column into two vertical domains and considers a sigma transformation in each of them. They also emphasise the advantage of double sigma

coordinate system in stratified flows. In these flows, pycnoclines, in general, are quasi-horizontal and do not follow the bottom topography.

Ushijima (1998) predicted the profile of a liquid surface by means of three-dimensional curvilinear coordinates which were regenerated in each computational step on the basis of the arbitrary Lagrangian-Eulerian (ALE) formulation. The calculation of pressure and velocity correction substantially followed the SMAC method (Amsden, 1970). Three-dimensional numerical simulation of a splashing drop (Fig. 2.5) using a SMAC method is presented by McKee et al. (2008). Mayer et al. (1998) developed a fractional step method for solving the time dependent two-dimensional Euler equations in a system of time-varying curvilinear grid by finite volume method. The geometry of the free surface was described by a height function, and its evolution was tracked by integrating in time the kinematic boundary conditions based on the free surface volume flux. Ai et al. (2011) employed a pressure correction technique to solve the incompressible Euler equations for simulating three-dimensional free surface flows with a non-hydrostatic pressure distribution on a vertical boundary-fitted coordinate system.

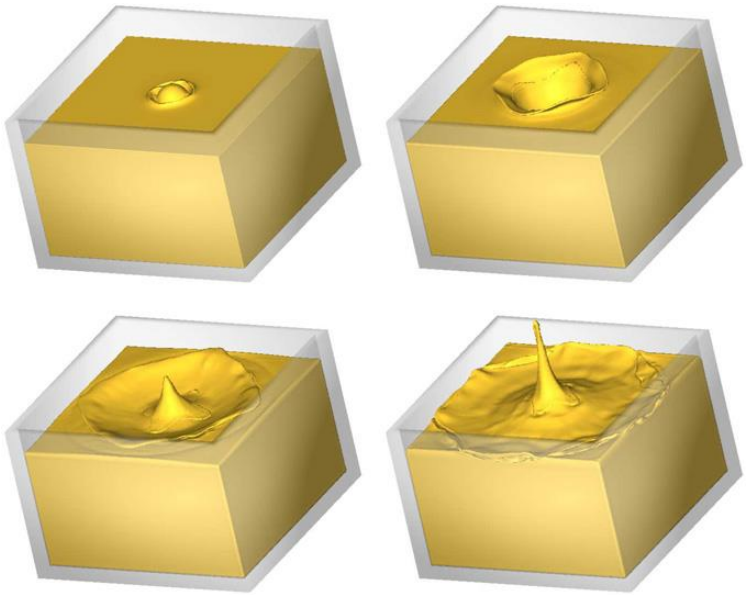

Figure (2.5) - Three-dimensional numerical simulation of a splashing drop at different times (adapted from McKee et al., 2008)

2.4 NUMERICAL SCHEMES FOR FREE SURFACE FLOWS

Numerical methods for simulating unsteady flows involving free surfaces may be classified into two general categories of fixed and moving-grid methods. Fixed-

grid methods include two categories of surface-tracking and surface-capturing methods. In the surface-tracking method the free surface is explicitly identified and tracked by means of pre-defined markers or interface-fitted grid cells. In the surface-capturing method the free surface is implicitly captured by a contour of a certain scalar function. In most surface-tracking methods the governing equations are solved only for the liquid and the free surface grid cells, while in the surface-capturing method the equations are solved on both the liquid and gas regions. The surface-tracking method has many variants including front-tracking methods and marker methods. The front-tracking methods represent the interface by a connected set of points. The marker methods include the marker-and-cell (MAC) method by Harlow and Welch (1965) and the volume of fluid (VOF) family of methods, and track the free surface with volume markers. There are a large class of numerical methods based on the surface-capturing approach. Among them are artificial compressibility method, phase field methods and level set method (Yue et al., 2003).

The free surface remains sharp and is computed precisely in the moving-grid method, which is basically a Lagrange-type method that treats the free surface as the boundary of a moving surface-fitted grid. The moving-grid method consists of either structured or unstructured grids, and includes strictly Lagrangian methods, free Lagrangian methods, and Lagrangian-Eulerian methods (Floryan and Rasmussen, 1989). In arbitrary Lagrangian-Eulerian (ALE) methods introduced by Hirt (1970) and Hirt et al. (1974), the distortion of grids due to free surface deformation requires reconstruction of mesh in each time step, which may induce numerical diffusion.

For development of non-hydrostatic free surface flow models, in general, two approaches, the projection method, proposed by Chorin (1968), Temam (1969) and Yanenko (1971) and the implicit method have been employed. The solution of the coupled set of governing equations in the implicit method benefits from the exclusion of decoupling errors (Namin et al., 2001). Nevertheless, the implicit discretisation results in the solution of large nonlinear algebraic systems which requires extensive computational effort. The projection method, on the other hand, decouples the computation of the velocity and pressure fields.

Yue et al. (2003) presented a numerical method that couples the incompressible Navier-Stokes equations with the level set method in a curvilinear coordinate system. The finite volume method was used to discretise the governing equations on a non-staggered grid with a four-step fractional step method. The free surface flow problem

was converted into a two-phase flow system on a fixed grid in which the free surface was implicitly captured by the zero level set. Puckett et al. (1997) presented a numerical model based on a second-order projection method for variable density flows using approximate projection formulation. The boundary between the fluids was tracked with a second-order, volume-of-fluid interface tracking algorithm. Memarzadeh and Hejazi (2012) utilised an incompressible smoothed particle hydrodynamics (ISPH) method for 2DV modelling of nonlinear wave run-up on steep slopes. SPH method is capable of high accurate modelling of free surface flows with large deformations. The equations were solved in a Lagrangian form using a two-step fractional method.

2.4.1 *Projection Method*

The projection method is based on the philosophy that in incompressible flows, pressure does not carry any thermodynamic meaning and is present only as a Lagrange multiplier for the incompressibility constraint (Chorin, 1968). This motivated a time-splitting discretisation scheme which decouples the computation of velocity and pressure, the core of the projection method (E and Liu, 1995). The projection method, which numerically may resemble a fractional step method, has been widely deployed for simulation of free surface flows with non-hydrostatic pressure distribution. The algorithm consists of two major steps. In the first step, ignoring the incompressibility constraint, the pressure terms in the momentum equations are excluded and the resultant transport equations are solved to compute an intermediate velocity field. Second step consists of calculating the pressure field by solving a Poisson equation and accounting for the continuity equation, so that the correction is applied by projecting the computed velocity field onto the space of divergence-free vector fields. The free surface is also calculated in the second step by coupling the kinematic free surface boundary equation to the Navier-Stokes equations.

The efficiency of the scheme is at the price of introducing a numerical boundary layer on the pressure approximations and the intermediate velocity fields. This also signifies the main difficulty in the design and implementation of more efficient projection methods, which is the treatment of the boundary conditions (E and Liu, 1995). A detailed review of different projection methods based on the time accuracy of the procedures is given by Armfield and Street (2002). Armfield and

Street (2003) also carried out an analysis of the pressure accuracy of different fractional step methods. An overview of boundary condition choices that give second-order convergence for all solution variables is presented in Brown (2001). Gresho and Sani (1987) discussed different pressure boundary conditions for the incompressible Navier-Stokes equations. Brown et al. (2001) studied accurate projection methods for the incompressible Navier-Stokes equations. Kim and Moin (1985) showed that the use of velocity boundary conditions for the intermediate velocity field can lead to inconsistent numerical solutions. Perot (1993) stated that the poor temporal accuracy of fractional step method is not due to boundary conditions, but due to the method itself.

Guermond et al. (2006) reviewed stability and convergence results for a broad range of projection schemes which were classified into three classes, namely the pressure-correction methods, the velocity-correction methods, and the consistent splitting methods. Van Kan (1986) presented an ADI scheme with pressure correction method which was second order accurate in space and time. Bell et al. (1989) presented a second-order projection method.

2.5 STRATIFIED FLOWS

Gravity currents, which result whenever fluid of one density flows horizontally into fluid of a different density, are frequent occurrences in both natural and man-made situations (Huppert and Simpson, 1980). Many oceanic fronts, especially those created by tidal processes, appear to be governed by simple gravity current frontal dynamics (D'Alessio et al., 1996). Benjamin (1968) presented a broad investigation into the properties of steady gravity currents. In most practical situations, gravity current flows are not steady. Consequently, the propagation velocity of the front, the height and length of the head, and the density difference all vary as the flow evolves (Alahyari and Longmire, 1996).

Natural and artificial gravity currents have been extensively investigated by Simpson (1997). More recently Huppert (2006) and Ungarish (2009) provided inclusive reviews of gravity currents. D'Alessio et al. (1996) provided a review on the numerical work on density currents. Laboratory experiments have been widely conducted to investigate the mixing characteristics and propagation rates of gravity currents (Simpson and Britter, 1979; Huppert and Simpson, 1980; Hallworth et al. 1993; Kneller et al., 1997, 1999).

From the experimental results of the release of a fixed volume of one homogeneous fluid into another of slightly different density, Huppert and Simpson (1980) argue that the resulting gravity current can pass through three states. There is first a slumping phase, during which the current is retarded by the counter flow in the fluid into which it is issuing. At this phase the head of the current travels at constant speed and maintains nearly constant depth (Hacker et al., 1996). The current remains in this slumping phase until the depth ratio of current to intruded fluid is reduced to less than about 0.075. This may be followed by a purely inertial phase, wherein the buoyancy force of the intruding fluid is balanced by the inertial force. Motion in the surrounding fluid plays a negligible role in this phase. Hacker et al. (1996) state that in the second stage, the similarity phase, the current decelerates, as $t^{-1/3}$ and decreases in depth. The transition between these two stages has been found to occur after the current has propagated approximately ten lock lengths. There then follows a viscous phase, wherein the buoyancy force is balanced by viscous forces. It is argued and confirmed by experiment that the inertial phase is absent if viscous effects become important before the slumping phase has been completed (Huppert and Simpson, 1980).

In the studies of Britter and Simpson (1978), mixing was observed to be a result of instability similar to the Kelvin Helmholtz instability at the interface between the two fluids. Alahyari and Longmire (1996) used axisymmetric laboratory gravity currents to study the structure and dynamics of gravity current heads during the inertia-buoyancy phase of the flow. They reported that during the early stages of the inertial phase, vertical velocity fields revealed a cyclic process of vortex formation. One cycle consists of three parts. There is first formation of a vortex due to baroclinic vorticity at the leading edge of the head, then formation of a vortex of opposite circulation along the bottom surface takes place, and the last part consists of the convection of heavy fluid forward by the vortex pair. The new heavy fluid at the leading edge then initiates a new cycle. Navier-Stokes simulations of a lock-release initial value problem show that long internal waves may be generated and propagate ahead of the gravity current (White and Helfrich, 2008). Lee and Kim (2012) compared the Boussinesq approximation and variable density models for the two-dimensional Rayleigh-Taylor instability with a phase-field method. Numerical experiments indicated that for an initially symmetric perturbation of the interface, the symmetry of the heavy and light fronts for the Boussinesq model can be seen for a

long time. However, for the variable density model, the symmetry is lost although the flow starts symmetrically.

The dynamics of inertial gravity currents that are initially stratified in density have been examined through systematic laboratory experiments by Gladstone et al. (2004). These experiments have identified that the initial vertical stratification may lead to significant stream-wise stratification of the flow if the density ratio between the layers is sufficiently large. Moreover, the experiments have identified that the layer containing the greatest buoyancy will propagate to the nose of the flow and drive the current. This may, in some circumstances, be the upper, less dense layer. The experiments also show that the layers propagate forward by intruding along a density interface between the body and wake regions of the current. The degree of mixing between the two layers during this process depends on the initial density ratio, the strength of the stratification, between the layers. The intrusion of fluid in such stratified flows leads to a more complicated vertical profile than that initially imposed on the flow. The competition is described between the early separation of the layers owing to their velocity differences and the vertical mixing at the interface between the layers. Interpretation from the experiments suggests that the buoyancy contrast controls separation while the density contrast controls mixing. From the experimental observations Gladstone et al. (2004) summarised the flow behaviours of two-layer density-stratified inertial currents. Figure (2.6) shows the schematic cartoons of the flow behaviour.

When a turbulent gravity current propagates over a rigid surface, there are two main processes which contribute to the mixing. Wave breaking behind the head due to shear instability leads to the formation of Kelvin-Helmholtz billows and a mixed layer above the flowing current. Additionally, the front of the current is broken up into a complex structure of lobes and clefts (Brown, 1999). The excitation of internal gravity waves by fluid intrusions that propagate along the interface of a two-layer fluid also has been investigated by way of laboratory experiments (Flynn and Sutherland, 2004).

On the experimental observations of gravity currents, Garcla and Parsons (1996) concluded that the magnitude of the current Reynolds number has a strong influence on mixing rates. Low mixing rates are associated with fronts in relatively shallow fresh water depths and low Reynolds numbers. Mixing rates increase more rapidly as the ratio of current thickness to fresh water depth increases. The pattern of

fluid motion within turbulent density currents has been described and discussed by several authors (Middleton, 1966a, 1966b; Allen, 1982; Simpson, 1987).

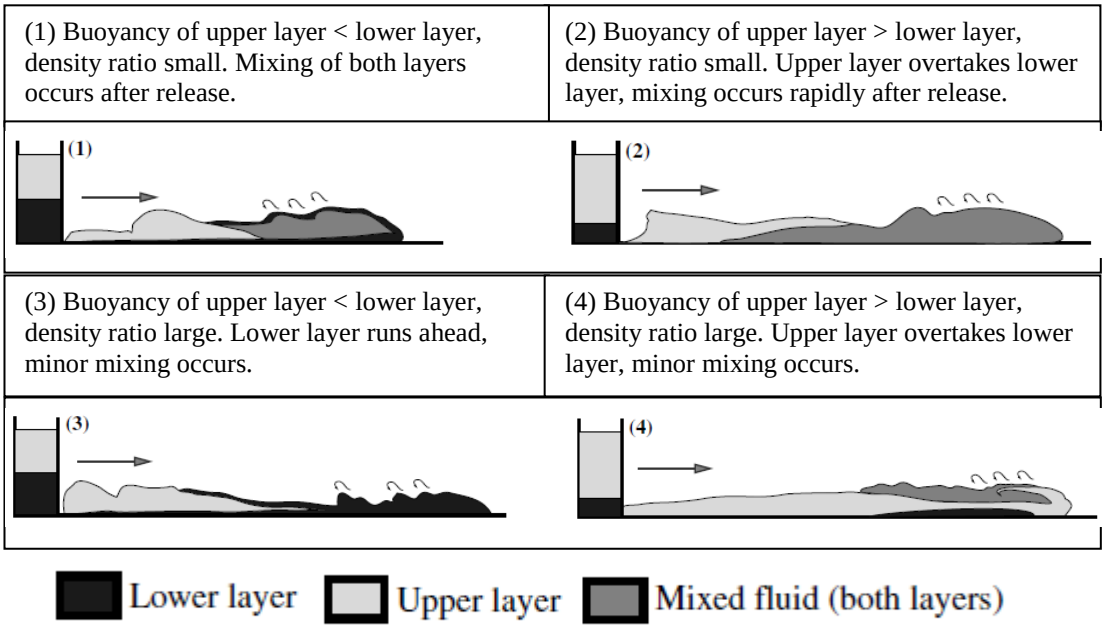

Figure (2.6) - Schematic cartoons of the flow behaviour of two-layer density stratified inertial currents (adapted from Gladstone et al., 2004)

Entrainment is one of the most important features of gravity currents, increasing the total volume of dense fluid and simultaneously decreasing its density (Cheong and Han, 1997). It is known that the gravity current made by sudden release of dense fluid on a horizontal surface entrains nearly twice of initial volume before losing its identity as a gravity current (Hallworth et al., 1993). De Nijs et al. (2009) concluded that salinity-induced density currents govern the exchange of suspended particulate matter between the Rotterdam Waterway and the Botlek Harbour and cause high siltation rates in Botlek Harbour. Their analysis revealed the dominant role played by the lock-exchange mechanism. In a study for a contamination event in the Flix reservoir in Spain, La Rocca and Bateman Pinzon (2010) claim that density and turbidity currents can be responsible for contamination of water bodies.

Relatively few investigations of gravity currents have accounted for non-Boussinesq effects (Birman et al., 2005; Lowe et al., 2005; Birman and Meiburg, 2006). Birman et al. (2005) investigated the unsteady dynamics of large density contrast non-Boussinesq lock-exchange flows by means of high-resolution two-dimensional simulations of the incompressible variable-density Navier-Stokes equations, employing a combination of spectral and compact finite difference

methods. They concluded that for both slip and no-slip boundary conditions, and for all Reynolds values, for larger density contrasts, the dense front dissipates an increasing amount of energy. In contrast, the energy dissipated by the light front remains near its Boussinesq level for all values of the density ratio. In addition, the height of the light front is very close to half the channel height, and it propagates with a non-dimensional velocity very close to a half.

Boñgolan-Walsh et al. (2007) studied the impact of boundary conditions on gravity currents using direct numerical simulations. The effect of the Neumann and Dirichlet boundary conditions for the bottom continental shelf on the entrainment and transport of gravity currents was investigated. The finding was that gravity currents under these two different boundary conditions differ most in the way they transport heat from the top towards the bottom.

2.5.1 *Salt Intrusion in Estuaries, Harbours and Tidal Barrages*

Measurements in the Rotterdam Waterway (de Nijs, 2012) show that the along-channel pressure gradient causes lock-exchange type flows near slack water at the limit of saltwater intrusion. During the ebb, the baroclinic pressure gradient causes relatively more shear higher in the water column than during the flood, while during the flood the combined effect of the baroclinic pressure gradient and damping of turbulence cause maximal velocities at the pycnocline at mid depth.

All barrages for various reasons are designed to modify or totally prevent the progression of the tide up an estuary or inlet. Many urban waterfront developments such as the Cardiff Bay and Tees barrages in the United Kingdom have incorporated full tidal barriers to exclude completely any tidal incursions and to create freshwater impoundments in which the water elevation is maintained permanently at a controlled level. Partially or fully submerged tidal weirs, permit a degree of exchange and mixing to occur between the tidally forced, saline, coastal waters and the freshwater river inflow (Cuthbertson et al., 2006). The degree of mixing and entrainment to a large extent depends on the size and depth of the impoundments. In small impoundments, with rapid mixing, the effects of stratifications and concentration gradients of various parts of the impoundment can be ignored (Wearing, 2000). The implementation of an estuarine tidal barrier scheme results in the inhibition of the natural tidal intrusion, mixing, and flushing processes (Cuthbertson et al., 2006). These changes have important repercussions (Burt and

Rees, 2001) for the water quality of the impounded volume (Coates et al., 2001). In most tidal barrages, saltwater flows over the barriers during high tide creating heavily stratified saline layer under the fresh water. The conditions of slight mixing of the lower layers leads to low levels of dissolved oxygen (Whyte and Ali, 2003).

2.5.2 *3D Numerical Modelling of Stratified Flows*

In comparison with 2D and axisymmetric gravity currents, fully 3D gravity currents have been investigated more rarely in the literature. Shen et al. (1995) developed a three-dimensional hydrodynamic and pollutant transport quality model by using the shallow water assumption and the Boussinesq approximation to simulate wind-induced circulation under isothermal and stratified conditions in Lake Ontario and its nearshore areas. A nested model approach was used to study the currents and pollutant transport. For the barotropic pressure, the semi-implicit difference scheme SIMPLER (Semi-Implicit Method for Pressure-Linked Equations Revised) method (Patankar, 1980) was used. The Poisson equation of the water elevation was solved by the SOR method (Roache, 1972). The Adams-Bashforth scheme was used for the temporal terms and the weight averaged donor-cell scheme for the advective terms (Shen, 1991). The central difference scheme of second order accuracy in space was used for the diffusive term. They concluded that the vertical temperature distribution had a strong influence on pollutant transport and a three-dimensional stratified model was necessary for the simulation of currents and pollutant transport in that nearshore area during the summer period.

Huang and Spaulding (1995) developed a three-dimensional finite difference model to predict circulation and water quality induced by surface discharges in estuarine and coastal waters. The model employed a vertical γ-coordinate, using an algebraic transformation within the σ-coordinate transformation system. The model was tested against laboratory experiments of a surface freshwater discharge into saline quiescent receiving water in a constant depth basin. They reported that the predictions realistically reproduced the strong currents and freshwater transport near the surface. Simulations of the Rotterdam Waterway by Delft3D (Delft Hydraulics, 2006) three-dimensional hydrostatic numerical model conducted by de Nijs (2012), showed underprediction of the saline water intrusion, stratification and the height of the pycnocline above the bed. de Nijs (2012) concluded that the model is not capable of adequately predicting the distribution of salinity, and therefore the effect of

salinity stratification on turbulent mixing should be further investigated and implemented in further model developments.

Patterson et al. (2005b) compared the experimental results of three-dimensional releases of fixed volumes of saline fluids into fresh water and their radial spread to 2D and 3D numerical simulations. They concluded that shallow water modelling is not suitable for axisymmetric lock-releases. La Rocca et al. (2008) investigated the dynamics of a three-dimensional gravity current by both laboratory experiments and numerical simulations with either smooth or rough flat bottoms. The gravity current was generated by lock-exchange mechanism and the mathematical model was a finite volume single layer model based on shallow water equations. They reported a systematic discrepancy between the numerical and experimental results, mainly during the first phase of the gravity current evolution, and concluded that this discrepancy was attributed to the limits of the mathematical formulation, in particular, the neglect of entrainment in the numerical model. La Rocca and Bateman Pinzon (2010) compared the experimental results and numerical simulations conducted by their proposed model for 3D gravity currents. They concluded that in the case of constant density, the two-layer mathematical formulation reproduces correctly the key features of the dynamics of the three-dimensional lock-exchange-release phenomenon. Numerical results obtained for the variable density case make sense and are in qualitative agreement with the experimental observations found in literature. Hydrostatic pressure assumption and Boussinesq approximation were applied in the numerical formulations. Cuthberston et al. (2006) reported that numerical models (e.g. Maskell and Ng, 1999) replicate qualitatively the formation of the stratified water behind the barrage but significant quantitative discrepancies remain between the model predictions and field measurements.

2.6 TURBULENCE MODELLING

Rodi (1984) provides a comprehensive review of turbulence modelling. A general review of turbulence models is presented by ASCE Task Committee on Turbulence Models in Hydraulic Computations (1988). Turbulence models may range from the simple eddy viscosity models to the more detailed large eddy simulations (LES) and direct numerical simulations (DNS). However, DNS and LES can be computationally expensive and often idealised for most geophysical and engineering applications. These limitations have led to the use of RANS approaches

commonly based on turbulent kinetic energy (TKE) closure schemes. The most widely used RANS models are two equation models, like the well-known *k*-ε model which requires the solutions of the turbulent kinetic energy equation and the dissipation of it (Venayagamoorthy et al., 2003).

Schmitt (2007) states that, the DNS or LES results or experimental data are very consistent in indicating the non-validity of the hypothesis of Boussinesq, which is at the heart of many turbulent viscosity models. However, eddy-viscosity turbulence models such as the *k*-ε model are widely used for many applications, and seem to provide satisfactory predictions which may be seen as a contradiction. Schmitt (2007) further explains that these models predict rather closely only simple flows, and only as far as mean fields are concerned. The inaccuracies come from the transport equations and the linear constitutive equation. The main limitation of this linear closure is that it rests on an analogy with kinetic theory, an analogy that can be criticised on theoretical grounds.

Tsanis (1989) compared different turbulence models and concluded that the mixing length model (Reid, 1957), the *k*-ε model (Svensson, 1978), and the eddy viscosity model (Pearce and Cooper, 1981) had very similar vertical current structures. Due to its simplicity, the eddy viscosity model proposed by Pearce and Cooper (1981) was used in the study of Shen et al. (1995). The vertical eddy viscosity coefficient was taken as zero at the water surface, increasing linearly to a depth of 1 meter, and set constant for the remainder of the depth. The horizontal eddy viscosity was calculated by a grid-size-dependent equation.

A major part of industrial CFD is carried out with eddy-viscosity-based two-equation models. Standard eddy-viscosity models tend to under-predict separation tendency. The modelling of the production resulting from the Boussinesq hypothesis is rather crude (Johansson, 2000). Algebraic approximations of the Reynolds stress transport equations are typically used to replace the eddy-viscosity based relation to determine the energy distribution among the components. In algebraic Reynolds stress models the aim is to replace that hypothesis with a more general, still local and algebraic, anisotropy relation. Hybrid methods that combine RANS and LES methods in different regions of the same flow form a possibility that still needs development (Johansson, 2000).

The algebraic Reynolds stress model (ARSM) more accurately represents the anisotropy of the Reynolds stresses than the linear gradient model commonly used in

the *k-ε* model (Taulbee, 1992). Some of the algebraic Reynolds stress models are implicit (Pope, 1975; Rodi, 1976; Gatski and Speziale, 1993), while others are explicit (Taulbee, 1992; Girimaji, 1996; Jongen and Gatski, 1998; Wallin and Johansson, 2000; So et al., 2002, 2004a, 2004b; Violeau, 2009; Pham and Nguyen, 2012).

2.6.1 *Turbulence Modelling of Tidal Flow Fields and Estuarine Harbours*

An ideal model should introduce the minimum amount of complexity while capturing the essence of the relevant physics (Wilcox, 2006). Turbulent schemes in a range of simple flow-dependent eddy viscosity models (Aldridge and Davies, 1993), one equation turbulent kinetic energy models (Davies and Jones, 1990; Muin and Spaulding, 1997), and two equation turbulence closure models using an equation each for turbulent kinetic energy and mixing length (Blumberg and Mellor, 1987; Blumberg et al., 1992) are used in three-dimensional hydrodynamic models. Xing and Davies (1996) showed that there are no significant differences between the predictions of tidal currents and mixing intensities obtained using a simple eddy viscosity model and various turbulence closure models.

de Nijs et al. (2010) argued that asymmetric turbulent mixing processes can be induced by straining of the salinity field causing stronger stratification on the ebb tide than on the flood tide, or unstable stratification on flood tide and stable stratification on ebb tide. Regarding work of Geyer et al. (2000), de Nijs et al. (2010) also concluded that in the case of strong stratification it may be anticipated that the characteristic advection timescales are smaller than the turbulent diffusion timescales. Then, on a tidal timescale, advection driven processes may govern the rate of change of the vertical density structure. They proposed that the growth of the pycnocline height along the estuary be analysed to help to determine the processes influencing the evolution of the salt wedge structure.

Falconer and Li (1994) used a *k-ε* turbulence model for modelling tidal eddies in coastal basins. de Nijs and Pietrzak (2012b) concluded that the choice of turbulence model has a larger effect on predictions of saltwater intrusion compared to the variation of the grid resolution, background viscosities and bed friction. They obtained best results with the *k-ε* turbulence model.

2.6.2 *Turbulence Modelling of Stratified Flows*

Rodi (1987) provides a general review of turbulence modelling in stratified fluids. Stably stratified flows in large water bodies such as the ocean and estuaries are prevalent in the natural environment. Mixing at the front of a gravity current such as a saline flow depends on two main processes: Kelvin-Helmholtz billows which roll up in the region of velocity shear above the front of the dense current, and a complex shifting pattern of lobes and clefts which form near the bottom at the lower part of the leading edge (Simpson, 1987). It has been suggested that mixing at the front of turbidity currents plays an important role in the dynamics of such flows (Allen, 1971).

If the density gradient peaks near the mid-depth of the flow it may control the level of turbulence throughout the flow to a level similar to that at the interface. The damping effect of stratification is very sensitive to even small values of Richardson number (HR Wallingford, 1999). The turbulent structure of tidal bottom boundary layers may be strongly influenced by horizontal density gradients. Due to tidal straining, turbulence is enhanced when the flow is towards water of lower density, and vice versa. In sufficiently deep shelf seas, well-mixed surface and bottom boundary layers may be separated by stable vertical density stratification (Burchard et al., 2008). A laboratory study by Kranenburg and Pietrzak (1989) of a turbulent two layer fluid, found that near the pycnocline there was a significant reduction in turbulence. They also demonstrated that while internal waves can contribute to turbulence production in the lower layer, negligible mixing was observed between the layers. de Nijs and Pietrzak (2012a) state that in conventional Reynolds averaged Navier Stokes (RANS) models, it is assumed that the turbulence is down-gradient and the influence of buoyancy forces, in the case of stable stratification, is typically taken into account as a sink of turbulent kinetic energy, which reduces the value of the eddy viscosity compared to neutral conditions. Their work includes turbulence closures with counter-gradient transport for RANS models.

The dynamics of gravity currents are believed to be strongly influenced by dissipation due to turbulence and mixing between the current and the surrounding ambient fluid. Shin et al. (2004) presented a new theory suggesting that dissipation is unimportant when the Reynolds number is sufficiently high. However, Benjamin (1968) suggests that dissipation is an essential ingredient in gravity current

dynamics. They predicted that in a deep ambient water the front Froude number is 1, rather than the previously accepted value of $\sqrt{2}$.

Venayagamoorthy et al. (2003) investigated proposed changes to RANS turbulence models for the regimes of weak to moderate stratification. Modifications were made to the *k*-ε model to account for stratification. Simulations of the stratified open channel flow highlighted the importance of correctly modelling the turbulent Prandtl number as well as the buoyancy parameter $c_{3\varepsilon}$. The results suggested that the turbulent Prandtl number should be close to unity for the neutrally stable flows. Further, it appeared that the buoyancy parameter $c_{3\varepsilon}$ has to be prescribed as a value of the order of $c_{1\varepsilon}$ in order to correctly model the effects of the buoyancy force in the dissipation equation.

Non-hydrostatic, high-resolution, two-dimensional simulations of bottom gravity currents were conducted in the studies of Özgökmen et al. (2004). They concluded that an explicit representation of mixing in overflows in numerical models requires not only a small vertical grid scale, but also a horizontal grid scale that is small enough to capture the billows forming near the density interface. Oceanic observations indicate that the typical height-to-length ratio of Kelvin-Helmholtz billows is about 0.1. Bombardelli et al. (2004) presented numerical simulations of saline, discontinuous density currents, in two and three dimensions. They reported that the currents presented characteristic flow instabilities at the interface which were constituted by small spatial scales. They concluded that a very fine resolution of these scales is needed to adequately capture the instabilities.

Wall-jet flow, lock-exchange and intrusive gravity currents were simulated to investigate the effects of using two different turbulence closures, a two-equation standard *k*-ε model with buoyancy terms and an explicit algebraic Reynolds stress model (EARSM) along with an explicit algebraic scalar flux model (EASFM) developed by Sharifian and Hejazi (2014). Results showed that the EARSM provides better predictions for velocity profiles especially in the far zone from the bed, and also for the front head position. However, using appropriate wall functions for Reynolds stresses could augment accuracy of model in boundary layers. They also concluded that a distinct turbulence model cannot satisfactorily predict all turbulent flow cases, and especial calibration for constants and consideration for source terms are needed**.**

Özgökmen et al. (2009) evaluated LES in a 3D lock-exchange problem, which contained shear-driven mixing, internal waves, interactions with boundaries and convective motions while having a simple domain, initial and boundary conditions, and forcing. Jacobitz (2000) studied the evolution of the velocity field and scalar concentration fields in stably stratified shear flow using direct numerical simulations. Two cases with vertical and horizontal mean shear were compared. In both cases, the growth of the turbulent kinetic energy weakened as the Richardson number was increased. However, the horizontal shear case showed a stronger growth of the turbulent kinetic energy than the vertical shear case for a given Richardson number. The ordering of the velocity components were found to change from stream-wise > horizontal > vertical in the vertical shear case to stream-wise > vertical > horizontal in the horizontal shear case. Two-dimensional results of numerical simulations of Patterson et al. (2005a) showed that the large eddy model was successful in modelling the large scale structure of gravity currents. Examination of the three-dimensional results showed that macroscopic features of the flow observed at the interface between the light and dense fluid were also modelled well.

2.6.3 *Effects of Stratification on Turbulence and Mixing*

Many problems in mixing in the estuaries are often complicated by density stratifications due to salinity profiles. This internal structure has a very great effect on both mean flow fields and the turbulent mixing and dispersion. But since often stratification results from transport processes, mixing depends on the flow field and the density stratification, while on the other hand, the flow and stratification depend on the mixing (Fischer et al., 1979). Stable stratification affects the flow in several ways. Vertical mixing of the stratification provides an additional sink of energy. The stratification also influences the structure of the turbulence, since vertical motions are directly affected by buoyancy forces (Holford and Linden, 1999). Turbulence in a stratified fluid is typically anisotropic, with reduced vertical velocities and vertical length-scales, and a reduced correlation between the density perturbation and the vertical velocity component. Propagating internal gravity waves owe their existence to the presence of a restoring buoyancy force, and turbulence, especially in its later stages of decay, can be dominated by the presence of a stabilising stratification (Riley and Lelon, 2000). In the oceans, flows on intermediate scales are usually strongly influenced by stable stratification.

de Nijs and Pietrzak (2011) have listed a number of studies on the effects of buoyancy forces on the turbulent transfer of momentum, heat and mass, which have been conducted using algebraic and numerical models, laboratory facilities and field surveys. de Nijs (2012) describes transport and sedimentation processes of suspended particulate matter in a stratified tidally energetic estuary, which has been investigated using field data and simulated values of a 3D hydrostatic numerical model. The strong salinity stratification of the basin largely suppresses turbulence. Regarding the field measurements that show the salt wedge remains stable during tidal excursions, he concludes that advection in combination with tidal phase differences must play an important role in transport and change of the salinity structure. de Nijs (2012) has applied the concept of total turbulent kinetic energy to analyse the effects of stratification on damping of vertical turbulent transports of mass and momentum. This concept distinguishes between vertical and horizontal turbulent kinetic energy and turbulent conversions of energy between the vertical turbulent kinetic energy balance and the turbulent potential energy balance.

For down-gradient transports the turbulent Prandtl-Schmidt number increases with stratification. This behaviour implies that the vertical turbulent mass transports are damped before the turbulent kinetic energy and vertical turbulent transport of momentum are suppressed by the effects of stratification. However, counter-gradient buoyancy fluxes are observed when the available turbulent potential energy is larger than the vertical kinetic energy. Turbulence remains active far beyond critical stratification numbers reported in the literature, which means stratification plays an important role in the decay of the turbulence (de Nijs and Pietrzak, 2012a). In turbulent flows, the signs of the ensemble mean vertical turbulent transports of salinity are usually opposite to those of the mean gradients of salinity (de Nijs and Pietrzak, 2011). These fluxes are referred to as down-gradient fluxes and modelled as diffusion. However, in stratified flows gravity oscillations can develop, which cause oscillating fluxes at a buoyancy frequency of about $(2\pi)^{-1} N$ where N is the Brunt-Väisälä frequency. These oscillations become counter-gradient when potential energy is transferred to kinetic energy.

2.6.4 *k-ε Turbulence Models*

The most frequent employed turbulence models are the eddy-viscosity models (EVMs). Despite the rapidly increasing computer power, the simplistic EVMs still

dominate the CFD community. Bredberg (2001) makes a thorough analysis of the EVMs. Following the *k*-ε model of Jones and Launder (1972), numerous EVMs, most of them based on the *k*-equation and an additional transport equation, such as the *k*-*kl* (Mellor and Yamada, 1982), the *k*-ω (Wilcox, 1988), the *k*-τ (Speziale et al., 1992), and the *k*-v_t (Peng and Davidson, 2000) models have been presented. Speziale (1987) developed nonlinear *k*-*l* and *k*-ε models. de Nijs (2012) recommends developing turbulence closure schemes within the total turbulent energy concept, as the *k*-ε turbulence models do not account for energy transfers between the turbulent potential and kinetic energy balances and assume a constant Prandtl number. Moreover, they do not account for other sources of turbulence than shear such as production of turbulence by unstable stratification and unstable internal waves.

Bahari and Hejazi (2009a) utilised different variants for buoyancy-affected terms in *k*-ε turbulence model to predict the flow parameters more accurately, and to investigate applicability of alternative *k*-ε turbulence buoyant closures in numerical simulation of horizontal gravity currents. The additional non-isotropic turbulent stress due to buoyancy was considered in production term, based on an algebraic stress model. In order to account for the turbulent scalar fluxes, general gradient diffusion hypothesis was used along with Boussinesq gradient diffusion hypothesis with a variable turbulent Schmidt number and the suggestion of Henkes and LeQuere (1996) for controversial empirical constant, $c_{3\varepsilon}$, in ε equation. Shams Nia and Hejazi (2012) implemented a nonlinear *k*-ε turbulence model firstly presented by Speziale (1987) in a 2DV numerical model (Hejazi, 2005). The simulations of lock-release type gravity currents and heated impinging jets into horizontal cross flows were compared with measured values and results of the buoyant standard *k*-ε turbulence model. They concluded that both models provided acceptable predictions for the front head position. However, in stratified saline water of lock-release types, the nonlinear model provided better results for velocity profiles especially near the bed. Davidson (1990) combined ASM and *k*-ε formulae for Reynolds stress, and proposed a second closure correction method to account for Reynolds stress components. This model takes from an ASM that part of the non-isotropic Reynolds stress which is due to buoyancy, and the remaining part from the *k*-ε model. Verdier-Bonnet et al. (1999) and Kun et al. (2000) used this hybrid model in their studies of coastal circulation modelling and vertical planar buoyant jets respectively, and came to more realistic results.

2.6.5 *Turbulence-stratification Interaction*

Monismith and Fong (1996) used a simple model of vertical mixing in a stratified tidal flow, which incorporated two means for accomplishing vertical mixing; shear instability and bottom mixed-layer deepening by turbulence produced at the estuary bottom and in the shear layer at the top of the mixed layer. Rotation and longitudinal salinity gradients were not included in the model. They reported that when the Richardson number was less than critical, periodic stratification developed, whereas when it was greater than the critical value, nearly constant stratification consisted of a fresh layer overlying an ocean layer. The model showed that shear arising from bottom friction can significantly enhance the rate of mixing in stratified tidal flows.

Studies on counter-gradient transport in the coastal and estuarine context are scarce. While it has been indicated that buoyancy fluxes can become counter-gradient, little direct observational evidence in the estuarine and coastal context can be found in the literature. de Nijs and Pietrzak (2011) reported that measurements of turbulent fluctuations of velocity and salinity show persistent counter-gradient buoyancy fluxes. These counter-gradient fluxes are controlled by the ratio of vertical turbulent kinetic energy and available potential energy. The onset of counter-gradient fluxes is found to approximately coincide with larger available potential energy than vertical turbulent kinetic energy. The near-bed stratification and pycnocline confine the bed-generated turbulence to the lower part of the water column (de Nijs and Pietrzak, 2012a).

From a phenomenological view point, de Nijs and Pietrzak (2011) explain counter-gradient flux as incompletely mixed or dissipated parcels of rising water of lower density and descending water of higher density, which have retained a certain memory of their mixing history or turbulent properties. This memory lasts longer for salinity-induced density fluctuations than for velocity fluctuations, because momentum can be transferred more quickly with the surrounding fluid through pressure fluctuation forces than mass, which requires mixing. It is anticipated that the memory effects induced by the density fluctuations, increase with increasing stratification. While turbulence remains active at strong stratification, mass transports are strongly damped and counter-gradient mass transports indicate restratification.

2.7 CONCLUSIONS

The complicated hydrodynamics associated with complex bathymetry of estuarine environments in combination with salinity stratified flows present in most estuaries requires a three-dimensional model with flexible coordinate system for capturing the elevation changes near the boundaries of sharp gradients, including bed topography, interfaces of stratified layers, and the free surface. The hydrostatic pressure assumption is not capable of accurate prediction of free surface and density profiles, especially in the presence of stratification and considerable baroclinic pressures; hence a non-hydrostatic model is required. Advection is the dominant forcing in such environments and for the flows of the interest of this research project. Therefore, special treatment is needed for implementation of high-accurate advection schemes in the numerical model.

The projection method optimises accuracy, ease of implementation of different schemes for the Navier-Stokes equations components, appropriate for the importance of their role and the desirable degree of accuracy for each term, as well as the computational time. The accuracy of the projection method places this technique far above the explicit approaches and almost as accurate as the methods using fully coupled algorithms which require much more computational effort. The turbulence model choice for predicting the detailed vertical mixing, especially when the stratified advective flows govern the flow field, becomes an important issue in line with preserving the functionality of the projection method. The combination of these features is not present in the existing numerical models.

The physical model of this study, which may be classified as a validation model and, to some extent, a process model, should determine the three-dimensional velocity field as well as three-dimensional stratification features. However, the modelling cannot include the proper consideration of all elements of real problems of the hydro-environments of the interest of the current research project, due to the limitations of experimental procedures. A conclusion on the stratification processes in harbours has not been provided in the literature, and the influence of different heights of the entrance-barriers for simplified model harbours and barrages on the hydrodynamics and stratification has yet to be determined. A signal procedure is necessary for the measured data to provide trustable means for the validation of the numerical model as well as interpretation of the hydrodynamic phenomena.

CHAPTER THREE

GOVERNING HYDRODYNAMIC EQUATIONS
AND
TURBULENCE MODELLING

"Turbulent motion, it remains to call attention to
the chief outstanding difficulty of our subject."
Horace Lamb, Hydrodynamics, 1932 (Reynolds, 1974)

3.1 INTRODUCTION

This chapter has been devoted to set out the fundamental concepts, definitions, and assumptions, and to establish the governing equations of fluid flow with particular reference to the flow associated with tidal, or long-period wave propagation. It also provides the background material for the research carried out in this study and presented in the thesis. The main topics which are covered in this chapter are outlined in the following paragraphs.

Firstly, although there is a wide acceptance and use of the basic concepts and definitions, they have been clarified, together with the assumptions made for the establishment of the equations of fluid flow. Then, since fluid dynamics provides the relationships between the fluid motion and the forces acting in the fluid, the subjects discussed are the kinematics of fluid motion, the origin of forces in fluid, and ultimately the dynamical equations of motion. In addition to the latter, the principles of mass conservation (continuity equation), and momentum (Newton's second law of

motion), are introduced as governing relationships, which the fluid must also obey. Attention has been given to the effect of variable density due to salinity as the salt intrusion is part of the numerical and hydraulic model studies. This adds the species concentration conservation equation to the set of the equations to be solved.

A turbulence modelling discussion follows the derivation of the turbulent Navier-Stokes equations. The task of turbulence models is to determine the turbulent transport terms, which appear in the mean-flow equations. Therefore the equations can be solved and the velocity, and concentration fields be obtained. A wide-spectrum of turbulence models is available, ranging from the simple mixing length hypothesis to rather complex models employing differential transport equations for the turbulent stresses and heat or concentration fluxes. The discussion about turbulence modelling is concentrated on the buoyant k-ε turbulent model.

The chapter is organised in three main parts:

- Basic concepts, definitions, and assumptions together with the laws of fluid dynamics, which lead to the establishment of the general form of the Navier-Stokes equations;
- Introducing turbulence, the mean-flow equations, and the Navier-Stokes equations for incompressible turbulent flow, which are used in this study;
- Following introductory remarks about turbulence modelling and basic concepts, buoyant k-ε turbulence model, which has been included in the numerical model developed herein, has been discussed.

In each part boundary conditions are presented and discussed in some detail. The division of the chapter into three parts is for convenience of covering the relevant topics and the substantial consistency of the nature of the subjects itself cannot be altered.

3.2 BASIC CONCEPTS, DEFINITIONS AND ASSUMPTIONS

Having a minimum compressibility at about 50˚C (Daugherty, 1961), water is considered as an incompressible fluid for most practical purposes and in the present study. It is assumed that water is a Newtonian fluid in character, for which the viscosity does not change with the rate of deformation. It is also treated as an isotropic substance, which considers that the relation between the components of stress and those of the rate-of-strain is the same in all directions. In a Newtonian fluid this relation is linear, which means the fluid obeys Stoke's law of friction. It is

also assumed that the dimensions of the problem are large enough compared with molecular distances so that the fluid may be treated as a continuous medium without loss of essential detail. So the fluid particle, which is the infinitesimal used for deriving the equations, is the smallest lump of material having sufficient molecules to allow a continuum interpretation. For incompressible fluids, the continuum properties necessary to describe the kinematical and dynamical behaviour are the density, the velocity, the internal stresses, and the viscosity.

3.3 EQUATIONS OF CONTINUITY AND MOTION OF FLOW

The equations of motion for an incompressible, viscous, Newtonian fluid have been concisely presented in this section. In the general case of three-dimensional motion, the flow field is specified by the velocity vector $\boldsymbol{V}$, which according to the definition given for the fluid particle, is the appropriate mean quantity in the dynamical sense required by Newton's laws of motion;

$$\boldsymbol{V} = \boldsymbol{i}\, u + \boldsymbol{j}\, v + \boldsymbol{k}\, w \tag{3.1}$$

where u, v, and w are the three orthogonal instantaneous components. The velocity components, the pressure, p, and the density, ρ, all are functions of the coordinates x, y, z, and time t. For the determination of these five quantities there exist five equations: the continuity equation (conservation of mass), the three components of the equation of motion (conservation of momentum) and the conservation equation of species concentration.

In this study, the variation of density is not due to compressibility. It is only attributed to density stratification and therefore the change in the concentration of species, with the particular interest in salinity due to salt intrusion. Hence, the assumption of incompressibility for water remains as valid.

The equation of continuity expresses the fact that for a unit volume there is a balance between the masses entering and leaving per unit time. In the case of non-steady flow of an incompressible fluid, this condition leads to the equation:

$$\operatorname{div} \boldsymbol{V} = 0 \tag{3.2}$$

The equations of motion are derived from Newton’s second law, which states that the product of mass and acceleration is equal to the sum of external forces acting on the body. In fluid motion two classes of forces are considered; gravitational forces

acting through the mass of the body, and pressure and friction acting on the boundary. The equation of motion is written in the following form:

$$\rho \frac{\mathrm{D}\boldsymbol{V}}{\mathrm{D}t} = \boldsymbol{F} + \boldsymbol{P} \tag{3.3}$$

In this equation $\boldsymbol{F} = \rho \boldsymbol{g}$ is the body force and denotes the gravitational force per unit volume and $\boldsymbol{P}$ is the surface force and denotes the force on the boundary per unit volume.

$$\boldsymbol{F} = \boldsymbol{i}\, X + \boldsymbol{j}\, Y + \boldsymbol{k}\, Z \tag{3.4}$$

$$\boldsymbol{P} = \boldsymbol{i}\, P_x + \boldsymbol{j}\, P_y + \boldsymbol{k}\, P_z \tag{3.5}$$

$\frac{\mathrm{D}\boldsymbol{V}}{\mathrm{D}t}$ in equation (3.3) denotes the substantive acceleration, which consists of the local acceleration $\partial \boldsymbol{V}/\partial t$, and the advective acceleration $\mathrm{d}\boldsymbol{V}/\mathrm{d}t$. The body forces are considered as given external forces. The surface forces depend on the rate of strain caused by the velocity in fluid. The system of forces determines a state of stress, whose relation with the rate of strain can only be given empirically. For isotropic, Newtonian fluids it may be assumed that this relation is a linear one.

3.3.1 *Stress Tensor*

For an infinitesimal parallelepiped control volume, $\mathrm{d}V = \mathrm{d}x\, \mathrm{d}y\, \mathrm{d}z$, the stress tensor of an inhomogeneous stress system, in the absence of a volumetric distribution of local moments, requires nine scalar quantities for its description. The stress tensor and the corresponding matrix are symmetric with respect to the principal diagonal (Chou and Pagano, 1967). The stress tensor is represented by τ_{ij}, where the first subscript indicates the axis to which the surface containing the stress is perpendicular, and the second subscript indicates the direction to which the stress is parallel. The surface force per unit volume is then given by derivatives of the stresses as has been presented in equation (3.6):

$$\boldsymbol{P} = \boldsymbol{i}\, \frac{\partial \tau_{xj}}{\partial x_j} + \boldsymbol{j}\, \frac{\partial \tau_{yj}}{\partial x_j} + \boldsymbol{k}\, \frac{\partial \tau_{zj}}{\partial x_j} \tag{3.6}$$

When a state of hydrostatic stress prevails, the surface force per unit volume becomes simply the negative of the pressure gradient:

$$\boldsymbol{P} = -\,\mathrm{grad}\; p \tag{3.7}$$

in which p is the uniform hydrostatic pressure. In a fluid at rest, or in the absence of deformation of fluid particles, all the shearing stresses vanish. Introducing the expression (3.6) into the equation of motion (3.3), and resolving into components leads to equation (3.8).

$$\rho \frac{\mathrm{D}u_i}{\mathrm{D}t} = F_i + \frac{\partial \tau_{ij}}{\partial x_j} \tag{3.8}$$

3.3.2 *Rate-of-strain Tensor*

Since the motion of the fluid is completely determined when the velocity vector $\boldsymbol{V}$ is given as a function of time and position, $\boldsymbol{V} = \boldsymbol{V}(x, y, z, t)$, there exist kinematic relations between the components of the rate of strain and this function. The rate-of-strain tensor, $\dot{\varepsilon}_{ij}$, is symmetric, thus six, rather nine, quantities suffice to determine the state of strain at a point. The mathematical properties of this tensor are analogous to those of the equally symmetric stress tensor.

When the fluid is at rest, it develops a uniform field of hydrostatic stress, which is identical with the thermodynamic pressure. When the fluid is in motion, the equation of state still determines a pressure at every point (principal of local state), and it is convenient to consider the deviatoric normal stresses together with the unchanged shearing stresses (Schlichting, 1979):

$$\sigma'_j = \sigma_j + p \tag{3.9}$$

where σ_j s are the normal stresses. The six quantities so obtained constitute a symmetric stress tensor the existence of which is due to the motion because at rest all its components vanish identically.

With the aid of equation (3.9) the non-viscous pressure terms can be separated in the equation of motion (3.8) so that they become as follows:

$$\left.\begin{aligned}
\rho \frac{\mathrm{D}u}{\mathrm{D}t} &= X - \frac{\partial p}{\partial x} + \left(\frac{\partial \sigma'_x}{\partial x} + \frac{\partial \tau_{xy}}{\partial y} + \frac{\partial \tau_{xz}}{\partial z} \right) \\
\rho \frac{\mathrm{D}v}{\mathrm{D}t} &= Y - \frac{\partial p}{\partial y} + \left(\frac{\partial \tau_{xy}}{\partial x} + \frac{\partial \sigma'_y}{\partial y} + \frac{\partial \tau_{yz}}{\partial z} \right) \\
\rho \frac{\mathrm{D}w}{\mathrm{D}t} &= Z - \frac{\partial p}{\partial z} + \left(\frac{\partial \tau_{xz}}{\partial x} + \frac{\partial \tau_{yz}}{\partial y} + \frac{\partial \sigma'_z}{\partial z} \right)
\end{aligned}\right\} \tag{3.10}$$

3.3.3 *The Stress-strain Law of a Newton-Stokes Fluid*

The stress tensor is connected with the rate-of-strain tensor through the coefficient of viscosity, μ. Newton hypothesised that the viscous force resisting the shearing strain of a fluid is linearly proportional to the rate of shear. The present generalisation of Newton's formulation is due to Stokes. Four premises underline the Stokesian formulation (Shapiro, 1961):

i. The fluid is isotropic. Hence the principal axes of stress and strain must coincide.

ii. Mere translation and rotation do not induce resisting stresses, but any deformation is resisted by viscous stresses. Each of the six components of viscous stress is assumed to be linearly proportional to a linear sum of the six deformation rates (three ε's and three γ's).

iii. The linear stress-strain law must have the same form for any orientation of the coordinate system.

iv. In the absence of deformation, the stress tensor must reduce to the hydrostatic pressure.

3.3.4 *Navier-Stokes Equations*

By satisfying premises (i) to (iv) and introducing the resultant constitutive stress-strain relations, the resultant surface force in terms of velocity components is obtained (Shapiro, 1961; Schlichting, 1979). By introducing the surface-force expressions into the fundamental equation (3.8), for incompressible flows with constant viscosity, the Navier-Stokes equations assume the following vectorial form:

$$\rho \frac{\mathrm{D}\boldsymbol{V}}{\mathrm{D}t} = \boldsymbol{F} - \text{grad } p + \mu \nabla^2 \boldsymbol{V} \tag{3.11}$$

These equations differ from Euler's equations by the viscous terms $\mu \nabla^2 \boldsymbol{V}$. The equation of continuity reads:

$$\frac{\partial u}{\partial x} + \frac{\partial v}{\partial y} + \frac{\partial w}{\partial z} = 0 \tag{3.12}$$

The conservation equation of species concentration is added to the above set of the equations, which with the known body forces form a closed set of five equations for the five unknowns, *u*, *v*, *w*, *p*, and ρ. The species concentration conservation equation reads as follows:

$$\frac{\partial C}{\partial t} + u\frac{\partial C}{\partial x} + v\frac{\partial C}{\partial y} + w\frac{\partial C}{\partial z} = \lambda\left(\frac{\partial^2 C}{\partial x^2} + \frac{\partial^2 C}{\partial y^2} + \frac{\partial^2 C}{\partial z^2}\right) + S_c \tag{3.13}$$

where C is a scalar quantity which may stand for species concentration (salt in this study), S_c is a volumetric source term, and λ is the molecular diffusivity of C.

3.3.5 *Boundary and Initial Conditions*

The solutions of the equations of motion of flow become fully determined physically when the boundary and initial conditions are specified. In the case of viscous fluids the condition of no slip on solid boundaries must be satisfied, i.e., on a wall both the normal and tangential components of the velocity must vanish:

$$v_n = 0 \tag{3.14}$$

$$v_t = 0 \tag{3.15}$$

In the equations (3.14) and (3.15) v_n and v_t represent normal and tangential components of the velocity respectively. For the no-slip condition to apply to any boundary this requires the velocity immediately adjacent to the boundary to be zero, with the velocity having to increase with distance from the boundary until the free stream velocity is achieved. The distance between the boundary and the elevation where the free stream temporal mean velocity occurs (or nearly occurs) defines the boundary layer thickness. Part of the boundary layer is laminar; termed the laminar sub-layer for turbulent flow (Falconer, 1993).

More details on boundary conditions are given in the following sections of this chapter. The boundary and initial conditions for solving the set of the equations have been thoroughly discussed in Chapter Four.

3.4 TURBULENCE

In estuaries and coastal areas the flows of practical relevance are almost always turbulent; this means that the fluid motion is highly random, unsteady and three-dimensional. Turbulent motions contribute significantly to the transport of momentum and mass and therefore have a determining influence on the distribution of velocity and species concentration over the flow field.

The largest eddies, which are associated with the low frequency fluctuations, are determined by the boundary conditions of the flow and their size is of the same order of magnitude as the flow domain. The smallest eddies, associated with the high

frequency fluctuations, are determined by viscous forces. The width of the spectrum, and thus the difference between the largest and the smallest eddies, increases with the Reynolds number.

In spite of all the recent advances in computer technology, turbulent flows cannot at present be calculated with an exact method. In the succeeding section problems involving fully developed turbulent motion are discussed, and a restriction of considering the time-averages of turbulent motion due to the complexity of turbulence fluctuations is imposed.

Therefore by a statistical approach, which was first suggested by Osborne Reynolds, the equations are averaged over a time scale which is long compared with that of the turbulent motion. The resulting equations describe the distribution of mean velocity, pressure, and species concentration in the flow. The system can be closed only with the aid of empirical input, whence the calculation methods based on the averaged flow equations are semi-empirical.

In describing a turbulent flow in mathematical terms the instantaneous values of the velocity, the pressure, and the scalar quantity of concentration are separated into mean and fluctuating quantities. Denoting the time-average of the *u*-component of velocity by $\overline{u}$, and its velocity of fluctuation by u' :

$$u = \overline{u} + u' \tag{3.16a}$$

This also may be applied for the other components of velocity. The following relations result in the same manner for pressure, and concentration:

$$p = \overline{p} + p' \tag{3.16b}$$

$$C = \overline{C} + C' \tag{3.16c}$$

The mean quantities are formed at a fixed point in space and are given, e.g. by:

$$\overline{C} = \frac{1}{t_2 - t_1} \int_{t_1}^{t_2} C \, \mathrm{d}t \tag{3.17}$$

Thus, by definition, the time-averages of all quantities describing the fluctuations are equal to zero. The fluctuations influence the mean motion in such a way that the latter exhibits an apparent increase in the resistance to deformation in the form of an apparent increase in the viscosity of the flow. This increased apparent viscosity of the mean stream forms the central concept of all theoretical considerations of turbulent motion.

3.4.1 *Turbulent Navier-Stokes Equations*

The Navier-Stokes equations for incompressible flow with the notion of Boussinesq approximation can be rewritten as follows:

$$\frac{\partial u_i}{\partial t} + \frac{\partial u_j u_i}{\partial x_j} = \frac{1}{\rho_r} X_i - \frac{1}{\rho_r}\frac{\partial p}{\partial x_i} + \nu \frac{\partial^2 u_i}{\partial x_j x_j} + g_i \frac{\rho - \rho_r}{\rho_r} \tag{3.18}$$

where p is the instantaneous pressure minus the hydrostatic pressure at reference density ρ_r. Due to the Boussinesq approximation the influence of variable density appears only in the buoyancy term (the last term on the right hand-side of equation 3.18) involving the reference density and the gravitational acceleration. A detailed implementation of Boussinesq approximation is presented in Chapter Six. The equations of continuity and species concentration conservation may be written as follows:

$$\frac{\partial u_i}{\partial x_i} = 0 \tag{3.19}$$

$$\frac{\partial C}{\partial t} + \frac{\partial C\, u_i}{\partial x_i} = \lambda \frac{\partial^2 C}{\partial x_i\, x_i} + S_c \tag{3.20}$$

Together with an equation relating the local density ρ to the local values of concentration (C), equations (3.18-3.20) form a closed set and are the exact equations, which describe all the details of the turbulent motion.

Introducing the hypotheses regarding the decompositions of velocity components and pressure into their time-averages and fluctuation terms from equations (3.16) into the equation of continuity (Eq. 3.12) and using the rules of operating on mean time-averages (see Schlichting, 1979) results in the following equations:

$$\frac{\partial \overline{u}}{\partial x} + \frac{\partial \overline{v}}{\partial y} + \frac{\partial \overline{w}}{\partial z} = 0 \tag{3.21}$$

$$\frac{\partial u'}{\partial x} + \frac{\partial v'}{\partial y} + \frac{\partial w'}{\partial z} = 0 \tag{3.22}$$

The time-averaged velocity components and the fluctuating components each satisfy the incompressible equation of continuity. Dropping the over-bars, indicating averaged values, for brevity, the continuity equation then reads:

$$\frac{\partial u_i}{\partial x_i} = 0 \tag{3.23}$$

Applying the same process into the equations of motion and species concentration results in the following system of equations:

$$\frac{\partial u_i}{\partial t}+\frac{\partial u_j u_i}{\partial x_j}=\frac{1}{\rho_r}X_i-\frac{1}{\rho_r}\frac{\partial p}{\partial x_i}+\nu\frac{\partial^2 u_i}{\partial x_j x_j}-\frac{\partial\overline{u_i' u_j'}}{\partial x_j}+g_i\frac{\rho-\rho_r}{\rho_r} \tag{3.24}$$

$$\frac{\partial C}{\partial t}+\frac{\partial C\,u_i}{\partial x_i}=\lambda\frac{\partial^2 C}{\partial x_i\,x_i}-\frac{\partial\overline{C' u_i'}}{\partial x_i}+S_c \tag{3.25}$$

Equations (3.23) to (3.25) determine the problem under consideration. Comparison of these equations with the original set of the Navier-Stokes equations (Eqs. 3.18-3.20), shows that the instantaneous values of velocity and pressure have been replaced by the corresponding temporal average values, and the new set of the equations in addition contains terms which depend on the turbulent fluctuations of the stream. These equations govern the mean-flow quantities. The equations are also exact since no assumptions has been introduced in deriving them, but they no longer form a closed set due to the non-linearity of equations (3.18) and (3.20), as the averaging process has introduced unknown correlations between fluctuating velocities (e.g. $\overline{u'v'}$), and between velocity and scalar fluctuations (e.g. $\overline{C'u'}$). The additional terms can be interpreted as components of a stress tensor due to the turbulent velocity components of the flow as follows:

$$\tau'_{ij}=-\rho\overline{u_i' u_j'} \tag{3.26}$$

These additional stresses are known as apparent or virtual stresses of turbulent flow or Reynolds stresses. Physically, these correlations, or according to Hinze (1975) double correlations between turbulence velocity components, multiplied by the density, represent the transport of momentum and mass due to the fluctuating motion. -ρ $\overline{u'v'}$ is the transport of *x* momentum in the direction of *y* (or vice versa); it acts as a stress on the fluid and is therefore called turbulent or Reynolds stress. -ρ $\overline{C'u'}$ is the transport of the scalar quantity *C* in the direction of *x* and is therefore a turbulent mass flux (for more on double-velocity correlation tensor see Reynolds, 1974). Since these stresses are added to the ordinary viscous terms in laminar flow and have a similar influence on the course of the flow, it is often said that they are caused by eddy viscosity. In most flow regions, the turbulent stresses and fluxes far outweigh their laminar counterparts and consequently, the latter may be omitted with a good degree of approximation.

Equations (3.23-3.25) can be solved for the mean values of velocity, pressure, and concentration only when the turbulence correlations can be determined. Exact transport equations can be derived for turbulent correlations (see Rodi, 1984), but the closure of the equations cannot be obtained due to correlations of higher order, so a turbulence model must be introduced to relate the correlations to mean flow quantities. The quality of the turbulence simulation necessary to obtain accurate predictions of the mean-flow quantities depends on the relative importance of the turbulent transport terms in equations (3.24) and (3.25). In certain flows or flow regions, the inertial terms on the left-hand side of the momentum equation (3.24) are balanced mainly by the pressure gradient or by the pressure gradient and buoyancy terms, even if the flow is turbulent. In such cases, the turbulence simulation may be relaxed and potential-flow solutions are sufficient. On the other hand, equation (3.25) for species concentration does not contain pressure-gradient and buoyancy terms, so that the turbulence terms are always important, except possibly in cases with large source terms. This equation shows that the transport of the species due to turbulence diffusion is independent of the transport due to the mean current (Harleman, 1961). Therefore, realistic modelling of the turbulent concentration-flux term is always necessary in order to obtain realistic concentration distribution by solving the equation of species concentration conservation (Rodi, 1984).

3.4.2 *Coriolis Effect*

In equation (3.24), X_i s, as were introduced in section 3.3, represent components of body force per unit volume, and therefore X_i/ρ_r s are in terms of acceleration, which if the effect of earth's acceleration is neglected, in the absence of any other body force and only the presence of earth's gravitational force, then the body force accelerations are simply expressed by the following:

$$X_i/\rho_r = g_i \tag{3.27}$$

However, in modelling large water bodies like estuarine and coastal flows the effects of the earth's rotation should be considered. Although this force may be included in the total body force, its effect, for convenience, is shown separately in the equations.

If the *x*-direction is assumed to be a straight line parallel to the equator, the *y*-direction to lie from south to north, and the *z*-direction to be upwards and normal to the earth's surface, then the earth's rotation gives rise to an acceleration due to the

relative motion, namely Coriolis acceleration, and therefore the body force accelerations are represented by:

$$\left.\frac{X}{\rho_r} = f\ v - 2\omega \boldsymbol{cos}\,\theta\, w, \qquad \frac{Y}{\rho_r} = -\,f\ u, \qquad \frac{Z}{\rho_r} = -\,g - 2\omega \boldsymbol{cos}\,\theta\, u\right\} \tag{3.28}$$

f is the Coriolis parameter and is equal to $2\omega\sin\theta$, in which ω is the angular speed of the earth's rotation ($\approx 7.27\times10^{-5}$ rad/s), and θ is the angle of latitude of the domain. The Coriolis terms may be simplified with two assumptions;

- The horizontal velocity scale is significantly larger than the vertical scale in the oceanic large water bodies, and with the hydrostatic approximation assumption, results in neglecting the second part of the X component.
- $2\omega\cos\theta$ is at least 4 orders of magnitude smaller than the acceleration due to gravity and is usually neglected.

Thus for practical purposes, these accelerations read (Falconer and Chen, 1996):

$$\left.\frac{X}{\rho_r} = f\ v, \qquad \frac{Y}{\rho_r} = -\,f\ u, \qquad \frac{Z}{\rho_r} = -\,g\right\} \tag{3.29}$$

Further details of the Coriolis acceleration have been given in Dronkers (1964).

3.4.3 *Boundary Conditions*

The boundary conditions to be satisfied by the mean velocity components are the same as in ordinary laminar flow, namely they all vanish at solid walls (no-slip condition). Moreover, all turbulent components must vanish at the walls and they are very small in their immediate neighbourhood. Therefore, all components of the tensor of apparent stresses vanish at the solid walls and the only stresses which act near them are the viscous stresses of laminar flow. As, in immediate neighbourhood of a wall the apparent stresses are small compared with the viscous stresses, in every turbulent flow there exists a very thin layer next to the wall which, in essence, behaves like one in laminar motion. It is known as the laminar sub-layer, and its velocities are so small that the viscous forces dominate over the inertia forces. The laminar sub-layer joins a transitional layer in which the velocity fluctuations are so large that they give rise to turbulent shearing stresses, which are comparable with the viscous stresses. The actual turbulent boundary layer occurs at larger distances from the wall, where the turbulent stresses eventually completely outweigh the viscous stresses (Schlichting, 1979). The data necessary for analysis of the fluid flow

problem must include sufficient information concerning all of the boundaries. The analysis consists of the application of the principles of fluid mechanics so as to predict the behaviour of the fluid when subjected to these boundary conditions. The possible conditions specified for a boundary may include its nature whether solid, fluid, or free surface, its geometrical form, the pressure distribution on it or the velocity distribution along or across it (Vallentine, 1969). A full discussion on boundary conditions is given in Chapter Four.

3.4.3.1 Solid Boundary Shear Stress

At solid boundaries the shear stress causing the resistance, may be approximated by steady uniform flow consideration (see Henderson, 1966). This is represented in the form of a quadratic friction law as follows:

$$\tau_{ij_b} = \rho \frac{g}{C^2} u_j V_{si} \tag{3.30}$$

τ_b is the solid boundary shear stress. The notation for the shear stress at the solid boundary is the same provided for the stress tensor; the first subscript indicates the axis to which the face is perpendicular (the solid boundary plane), and the second indicates the direction to which the shearing stress is parallel. In this equation there is no relevance between the shear stresses which have the same subscripts in different order. V_s is the surface fluid speed, and the second subscript indicates the axis to which the plane, that the surface velocity lies in, is perpendicular. To determine the Chézy value, *C*, either a constant value may be specified, or it can be evaluated from the Manning equation, or alternatively the Colebrook-White equation may be used (Henderson, 1966; Falconer and Chen, 1996).

3.4.3.2 Water Surface Elevation

The pressure at the surface is assumed to be atmospheric and the surface elevation η is then calculated with the aid of the kinematic boundary condition at the surface, which assumes that a fluid particle remains on the surface (Vallentine, 1969). Water surface elevation is given by (ASCE, 1988; Falconer and Chen, 1996; Verdier-Bonnet et al., 1999):

$$\frac{\mathrm{d}\eta}{\mathrm{d}t} = \frac{\partial \eta}{\partial t} + u_{(z=\eta)} \frac{\partial \eta}{\partial x} + v_{(z=\eta)} \frac{\partial \eta}{\partial y} = w_{(z=\eta)} \tag{3.31}$$

3.5 TURBULENCE MODELLING

Because the turbulent transport processes cannot be calculated with an exact method, they must be approximated by a turbulence model which, with the aid of empirical information, allows the turbulent transport quantities to be related to the mean flow field. According to Dwoyer et al. (1985) theoretical approaches to model turbulence can be broadly divided into four overlapping categories:

1. Analytical modelling
2. Physical modelling
3. Phenomenological modelling
4. Numerical modelling

A turbulence model is defined as a set of equations which determine the turbulent transport terms in the mean-flow equations and thus close the system of equations. Turbulence models are based on hypotheses about turbulence processes and require empirical input in the form of constants or functions. They do not simulate the details of the turbulent motion but only the effect of turbulence on the mean-flow behaviour (Rodi, 1984).

Geometrical conditions, viscous effects, and buoyancy influence the turbulent transport processes. Turbulence models can only give an approximate description, and a particular set of empirical constants may only be valid for a certain flow or a particular range of flows. Therefore, it is important to find out how well the various models can cope with the manifold complications present in hydraulics problems, such as irregular geometries, buoyancy, and free surface effects. The k-ε model is shown to predict reasonably well a fairly large range of hydraulics problems with the same empirical input (Rodi, 1984).

3.5.1 *Introductory Remarks*

It is mainly the large-scale turbulent motion that transports momentum and concentration and contributes to the turbulence correlations. Therefore it is the large-scale motion that has to be simulated in a turbulence model for the determination of turbulence correlations and the velocity and length scales introduced in turbulence models are parameters which characterise this motion. The rate of energy dissipated is also determined by the large-scale motion although dissipation is a viscous process and takes place at the smallest eddies. Larger Reynolds numbers result in smaller

dissipative eddies relative to the large-scale eddies. When buoyancy forces are present, there is also an exchange between potential energy of the mean flow and turbulent kinetic energy, which can go in both directions but is also affected by the large-scale motion.

Because of its interaction with the mean flow, the large-scale turbulent motion depends strongly on the buoyancy conditions of a problem. The mean flow often has preferred directions which are imposed also on the large-scale turbulent motion. This motion can therefore be strongly anisotropic so that both the intensity of the fluctuations and their length scales are direction dependent. During the cascade process the direction sensitivity is diminished and when the Reynolds number is high enough, the direction sensitivity is entirely lost resulting in isotropy (Rodi, 1984).

3.5.2 *Basic Concepts*

Eddy-viscosity and eddy-diffusivity are the basis of most turbulence models. These two are introduced in the following part.

3.5.2.1 Eddy-viscosity Concept

The Boussinesq concept of eddy-viscosity assumes that the turbulent stresses are proportional to the mean-velocity gradients. For general flow situations, this concept may be expressed as:

$$-\overline{u_i' u_j'} = \nu_T \left(\frac{\partial u_i}{\partial x_j} + \frac{\partial u_j}{\partial x_i} \right) - \frac{2}{3} k \, \delta_{ij} \text{ where } \begin{cases} \delta_{ij} = 1 \text{ for } i = j \\ \delta_{ij} = 0 \text{ for } i \neq j \end{cases} \tag{3.32}$$

where k is the kinetic energy of the fluctuating motion per unit mass. ν_T, the turbulent or eddy viscosity, is not a fluid property but depends on the state of turbulence and may vary significantly over the flow field and also in different flow regimes. By introducing eddy-viscosity concept a turbulence model may now be constructed if the distribution of ν_T is determined. The sum of normal stresses ($\overline{u_i'^2}$ s) is equal to zero due to the continuity equation. However, all normal stresses are by definition positive quantities, and their sum is twice the kinetic energy k of the fluctuating motion per unit mass:

$$k = \frac{1}{2} \left(\overline{u'^2} + \overline{v'^2} + \overline{w'^2} \right) \tag{3.33}$$

According to this equation, k is a direct measure of the intensity of the turbulence fluctuations in the three directions. Inclusion of the second part of the eddy viscosity expression (3.32) assures that the sum of the normal stresses is equal to $2k$. Because the normal stresses are like pressure, and because the energy k is a scalar quantity, the second part of equation (3.32) constitutes a pressure. Therefore, this second part can be absorbed by the pressure-gradient term so that in effect the static pressure is replaced by the pressure $p + 2/3\,k$. For dimensional reasons, the velocity scale and the length scale of the turbulent motion play an important role (ASCE, 1988). The eddy viscosity is considered proportional to a velocity scale $\hat{V}$ characterising the fluctuating motion and to a typical length scale L characterising the large-scale turbulent motion which is called the Prandtl mixing length.

$$\nu_T \propto \hat{V}\, L \tag{3.34}$$

Despite some conceptual objections*, the eddy viscosity concept has often been found to work well in practice, simply because ν_T can be determined to a good approximation in many flow situations (Rodi, 1984). This is because the distribution of the velocity and length scales can be approximated reasonably well in many flows. Although the assumption of an isotropic eddy viscosity is a simplification which is of limited realism in complex flows, in spite of all shortcomings of the eddy viscosity concept, it is still the basis of most turbulence models.

3.5.2.2 Eddy-diffusivity Concept

In analogy to the turbulent momentum transport, the turbulent mass transport is often assumed to be related to the gradient of the transported quantity;

$$-\overline{u_i' C'} = \Gamma \frac{\partial C}{\partial x_i} \tag{3.35}$$

Like the eddy viscosity, Γ, turbulent diffusivity of mass, is not a fluid property but depends on the state of the turbulence. The Reynolds analogy between mass transport and momentum transport suggests that Γ is closely related to ν_T:

$$\Gamma = \frac{\nu_T}{\sigma_T} \tag{3.36}$$

* The fallacy lies in expecting the eddy viscosity to be a scalar, simply related in general to the mean-flow scales, or even the turbulent scales, near the point considered; it is a hybrid quantity, depending on both the turbulence and the mean flow (Bradshaw, 1978).

σ_T is called the turbulent Schmidt number. Experiments have shown that, unlike the turbulent diffusivities for momentum and mass, their ratio σ_T varies only little over the flow field and also little in different flow regimes. Therefore many models make use of equation (3.36) with the turbulent Schmidt number as a constant. It should be mentioned, however, that buoyancy and streamline curvature affect the value of σ_T. Knowledge of σ_T is always used as a means of finding Γ from an already computed value of ν_T (Launder, 1978).

Generally the equations discussed here for the species concentration are equally valid for temperature. Heat transport can be expressed in the same way as mass transport, noting that σ_T is known as Prandtl number for heat in most of the literature. This also implies that the equations used and implemented in the numerical model can be used for stratification due to thermal changes by introducing the appropriate function relating density to temperature.

3.5.3 *Turbulence Model Classification*

Reynolds (1976) classified the turbulence models on the level of partial differential equations used in the models:

1. Zero-equation models use only the partial differential equations for the mean velocity field, and no turbulence partial differential equations are introduced.
2. One-equation models involve one partial differential equation relating to a turbulence velocity scale, in addition to the mean-flow partial differential equations.
3. Two-equation models use an additional partial differential equation related to a turbulence length scale.
4. Stress-equation models involve partial differential equations for all components of the Reynolds stress tensor and in general for a length scale as well.
5. Large-eddy simulations involve the three-dimensional time-dependent large eddy structure and a low-level model for the small-scale turbulence.

Class 1 is also called the class of mean-field closures, classes 2 to 4 being transport-equation closures. An alternative, open-ended classification is based on the highest order of velocity product for which a transport equation is used. Zero-equation models use partial differential equations for u_i only and are therefore first-

order models, classes 2 to 4 use partial differential equations for $\overline{u_i' u_j'}$ and are second-order closures, while some class 4 models approach the stage of using transport equations for third-order products $\overline{u_i' u_j' u_l'}$. In this chapter only some of the models, which belong to the classes 1 to 3, have been reviewed and the buoyant *k*-ε model has been discussed.

3.5.3.1 Zero-equation Models

In this part without going through the details of zero-equation models, only a general overview has been presented.

3.5.3.1.1 Constant Eddy Viscosity/Diffusivity

For the calculation of hydrodynamic properties, the constant-eddy-viscosity model has little significance, as in many calculations, especially for flows in large water bodies, the turbulence terms in the momentum equations are unimportant and consequently the turbulence model does not play a major role, and when the turbulence terms are important for the flow behaviour, the model is mostly too coarse to describe this behaviour correctly. In stratified flows the vertical turbulent transport of both momentum and scalar quantities is strongly influenced by buoyancy effects, and in particular the eddy viscosity and diffusivity are reduced by stable stratification.

3.5.3.1.2 Mixing-length Models

The mixing-length model is not suitable when processes of advective or diffusive transport of turbulence are important. More generally, the model is of little use in complex flows because of the great difficulties in specifying the mixing length. The mixing-length model is suitable only for flows where the turbulence is in local equilibrium.

3.5.3.1.3 Prandtl's Free-shear-layer Model

Because of its simplicity, Prandtl's free-shear-layer model is quite popular for the prediction of mixing layers, jets and wakes. With an appropriate constant it works well when these flows are in a developed state, but transitions from one type of free

flow to another are not well predicted because of the non-universality of the empirical constant.

3.5.3.2 One-equation Models

In order to overcome the limitations of the mixing length hypothesis, turbulence models were developed which account for the transport of turbulence quantities by solving differential transport equations for them. In the models using eddy-viscosity concept, the velocity fluctuations are characterised by $\sqrt{k}$. As the energy *k* is contained mainly in the large-scale fluctuations, $\sqrt{k}$ is a velocity scale for the large-scale turbulent motion. When this scale is used in the eddy viscosity relation (Eq. 3.34), there results:

$$\nu_T = c'_\mu \sqrt{k}\, L \tag{3.37}$$

where c'_μ is an empirical constant. This formula is known as the Kolmogorov-Prandtl expression. They suggested determining the distribution of *k* by solving a transport equation for this quantity. Such an equation can be derived in exact form from the Navier-Stokes equations (See Rodi, 1984). For high Reynolds numbers, this equation in tensor notation reads:

$$\underbrace{\frac{\partial k}{\partial t}}_{\substack{\text{rate of}\\ \text{change}}} + \underbrace{u_i \frac{\partial k}{\partial x_i}}_{\substack{\text{advective}\\ \text{transport}}} = \underbrace{-\frac{\partial}{\partial x_i}\left[\overline{u'_i\left(\frac{u'_j u'_j}{2} + \frac{p}{\rho}\right)}\right]}_{\text{diffusive transport}} \underbrace{-\overline{u'_i u'_j}\frac{\partial u_i}{\partial x_j}}_{\substack{P=\text{production}\\ \text{by shear}}} \underbrace{-\beta\, g_i \overline{u'_i C'}}_{\substack{G=\text{buoyant}\\ \text{production/destruction}}} \underbrace{-\nu \overline{\frac{\partial u'_i}{\partial x_j}\frac{\partial u'_i}{\partial x_j}}}_{\substack{\varepsilon=\text{viscous}\\ \text{dissipation}}} \tag{3.38}$$

The rate of change of *k* is balanced by:

- The advective transport due to the mean motion;
- The diffusive transport due to velocity and pressure fluctuations;
- The production of *k* by interaction of Reynolds stresses and mean-velocity gradients;
- The dissipation of *k* by viscous action into heat;
- The production or destruction of *k* due to buoyancy forces.

The production term *P* represents the transfer of kinetic energy from the mean to the turbulent motion; it appears with opposite sign as a sink term in the equation for the kinetic energy of the mean motion. The buoyancy term *G* represents an exchange between the turbulent kinetic energy *k* and potential energy. In stable stratification, this term is negative so that *k* is reduced and the turbulence is damped while the

potential energy of the system increases. In unstable stratification, turbulent energy is produced at the expense of potential energy. The viscous dissipation ε transfers kinetic energy into internal energy of the fluid and is always a sink term.

The exact *k*-equation cannot be used in a turbulence model because new unknown correlations appear in the diffusion and dissipation terms. To obtain a closed set of equations, model assumptions need to be introduced for these terms. In analogy to the diffusion expression (3.35) for the scalar quantity *C*, the diffusion flux of *k* is often assumed proportional to the gradient of *k*:

$$-\overline{u_i'\left(\frac{u_j'\,u_j'}{2}+\frac{p}{\rho}\right)}=\frac{\nu_T}{\sigma_k}\frac{\partial k}{\partial x_i} \tag{3.39}$$

where σ_k is an empirical diffusion constant. The dissipation ε is usually modelled by the expression (3.40).

$$\varepsilon = c_D\,\frac{k^{3/2}}{L} \tag{3.40}$$

where c_D is an empirical constant.

With the above model assumptions and the eddy-viscosity and diffusivity expressions the *k*-equation reads:

$$\frac{\partial k}{\partial t}+u_i\frac{\partial k}{\partial x_i}=\frac{\partial}{\partial x_i}\left(\frac{\nu_T}{\sigma_k}\frac{\partial k}{\partial x_i}\right)+\nu_T\left(\frac{\partial u_i}{\partial x_j}+\frac{\partial u_j}{\partial x_i}\right)\frac{\partial u_i}{\partial x_j}+\beta\,g_i\frac{\nu_T}{\sigma_T}\frac{\partial C}{\partial x_i}-c_D\frac{k^{3/2}}{L} \tag{3.41}$$

This is the high Reynolds number form of the transport equation used in most one-equation models. $c_\mu' c_D \approx 0.08$ and $\sigma_k \approx 1$ appear to be reasonable values of the empirical constants (Rodi, 1984). The model introduced is restricted to high Reynolds number flows and is not applicable to the viscous sub-layer near walls. For other one-equation models see Rodi (1984).

In conclusion, one-equation models account for advective and diffusive transport, and the history in unsteady flows of the turbulent velocity scale and are therefore superior to the mixing-length hypothesis when this transport is important. The application of one-equation models is restricted mainly to shear layers since it is difficult to specify empirically the length-scale distribution in more complex flows and yet for most shear layers the simpler mixing-length model works equally well. Two-equation models determine the length scale from a transport equation.

3.5.3.3 Two-equation Models

The length scale characterising the size of the large, energy-containing eddies is subject to transport processes in a similar manner to the energy *k*. Other processes influencing the length scale are dissipation, which destroys the small eddies and thus effectively increases the eddy size, and vortex stretching connected with the energy cascade, which reduces the eddy size. The balance of all these processes can be expressed in a model transport equation for *L*, which can then be used to calculate the distribution of *L*. The difficulties in finding widely valid formulae for prescribing or calculating *L*, have stimulated the use of such a length scale equation.

3.5.3.3.1 *ε*-equation

At high Reynolds numbers where local isotropy prevails, the rate of dissipation, *ε*, is equal to the molecular kinematic viscosity times the fluctuating vorticity $\overline{\left(\partial u_i'/\partial x_j'\right)^2}$. An exact transport equation can be derived from the Navier-Stokes equations for the fluctuating vorticity, and thus for the rate of dissipation (Tennekes and Lumley, 1972). This equation contains complex correlations whose behaviour is little known and for which fairly drastic model assumptions must be introduced in order to make the equation tractable. When the turbulence is considered to be locally isotropic the equation contains terms representing the rate of change, advection, diffusion, generation of vorticity due to vortex stretching connected with the energy cascade, and viscous destruction of vorticity. The diffusion, generation and destruction terms require model assumptions. Usually, the diffusion is modelled with the gradient assumption. The generation and destruction terms cannot be modelled separately; it is their difference that has to be modelled. The outcome of the modelling is the *ε*-equation presented in the following section. Together with the *k*-equation and the Kolmogorov-Prandtl expression it forms the so-called *k*-*ε* turbulence model.

3.5.3.3.2 The *k*-*ε* Turbulence Model

The *k*-*ε* model has been included into the numerical model presented herein. The equations which comprise the complete model are as follows (Rodi, 1984):

$$\nu_T = c_\mu \frac{k^2}{\varepsilon} \tag{3.42}$$

$$\Gamma = \frac{\nu_T}{\sigma_T} \tag{3.43}$$

$$\frac{\partial k}{\partial t} + u_i \frac{\partial k}{\partial x_i} = \frac{\partial}{\partial x_i}\left(\frac{\nu_T}{\sigma_k}\frac{\partial k}{\partial x_i}\right) + \underbrace{\nu_T\left(\frac{\partial u_i}{\partial x_j} + \frac{\partial u_j}{\partial x_i}\right)\frac{\partial u_i}{\partial x_j}}_{P} + \underbrace{\beta\, g_i \frac{\nu_T}{\sigma_T}\frac{\partial C}{\partial x_i}}_{G} - \varepsilon \tag{3.44}$$

$$\underbrace{\frac{\partial \varepsilon}{\partial t}}_{\text{rate of change}} + \underbrace{u_i \frac{\partial \varepsilon}{\partial x_i}}_{\text{advection}} = \underbrace{\frac{\partial}{\partial x_i}\left(\frac{\nu_T}{\sigma_\varepsilon}\frac{\partial \varepsilon}{\partial x_i}\right)}_{\text{diffusion}} + \underbrace{c_{1\varepsilon}\frac{\varepsilon}{k}(P+G)\left(1+c_{3\varepsilon}R_f\right) - c_{2\varepsilon}\frac{\varepsilon^2}{k}}_{\text{generation–destruction}} \tag{3.45}$$

The ε-equation contains the empirical constants $\sigma_\varepsilon, c_{1\varepsilon}$, and $c_{2\varepsilon}$, and in buoyant situations also $c_{3\varepsilon}$. The empirical constants recommended by Launder and Spalding are given in Table (3.1) as follows:

Table (3.1) - Values of the constants in the *k*-ε model (adapted from Rodi, 1984)

c_μ	$c_{1\varepsilon}$	$c_{2\varepsilon}$	σ_k	σ_ε
0.09	1.44	1.92	1.0	1.3

These values are based on extensive examination of free turbulent flows, but they can also be used for wall flows. A sensitivity study has shown that the calculations are most sensitive to the values of $c_{1\varepsilon}$ and $c_{2\varepsilon}$. Complete universality of the constants given in Table (3.1) should not be expected. Experience has shown that even in certain fairly simple flows some of the constants require different values. The range of applicability of the *k*-ε model can be extended when some of the constants are replaced by functions of suitable flow parameters.

The standard *k*-ε model is based on the assumption that the eddy viscosity is the same for all Reynolds stresses (isotropic eddy viscosity). To allow for the non-isotropic nature of the eddy viscosity in such cases, the *k*-ε model is refined by introducing an algebraic stress model to replace the eddy-viscosity relation (Eq. 3.32) and the Kolmogorov-Prandtl expression (3.37). This model relates the individual stresses $\overline{u_i' u_j'}$ to mean-velocity gradients, *k* and ε by way of algebraic expressions by simplifying the transport equations for $\overline{u_i' u_j'}$.

Mass transfer is calculated in the same way as in zero- and one-equation models via the turbulent Prandtl/Schmidt number. Buoyancy effects can be accounted for in the *k*-ε model at two levels. The first level is to simply include the buoyancy terms in the *k*- and ε-equations as shown in equations (3.44) and (3.45) and

to leave constants unaffected by buoyancy. However, there is an additional buoyancy constant, $c_{3\varepsilon}$, in the ε-equation, and its value is somewhat controversial, and this is due to the definition of the flux Richardson number of R_f to which $c_{3\varepsilon}$ is a multiplier. If a positive R_f becomes large enough, it leads to complete suppression of all turbulence. Observations have shown that turbulence cannot be maintained if $R_f \rangle 0.2$ approximately (Tennekes and Lumley, 1972). Usually R_f is defined as minus the ratio of buoyancy production of k to stress production, $-G/P$. With this definition, various researchers found that $c_{3\varepsilon}$ should be close to zero and unity for vertical and horizontal buoyant shear layers respectively (Rodi, 1984). $c_{3\varepsilon} = 1$ implies that there is no buoyancy term in the ε- equation while $c_{3\varepsilon} = 0$ implies that the buoyancy-production term is multiplied with the same constant as the stress production. In order to resolve this difficulty Rodi suggested to replace in the R_f definition, the buoyancy production G of the total turbulent energy k by the buoyancy production $G_{\overline{v'^2}}$ of only the lateral energy component $\overline{v'^2}$ and to write $R_f = -\frac{1}{2} G_{\overline{v'^2}} / (P+G)$. In horizontal shear layers then $R_f = -G/(P+G)$ and in vertical layers $R_f = 0$. With this definition, a single value can be used for $c_{3\varepsilon}$ in both vertical and horizontal layers, $c_{3\varepsilon} \approx 0.8$.

The second level of accounting for buoyancy in the k-ε model makes use of the algebraic stress model approach. Modelled transport equations for the stress $\overline{u_i' u_j'}$ and the mass flux $\overline{u_i' C'}$ are simplified to yield algebraic relations. The transport equations contain buoyancy terms, which appear also in the algebraic relations, leading effectively to non-isotropic eddy viscosities and diffusivities as functions of some local Richardson number. This modelling automatically yields a buoyancy influence on c_μ and the turbulent Prandtl/Schmidt number σ_T.

Rodi (1987) employed the following ε- equation:

$$\frac{\partial \varepsilon}{\partial t} + u_i \frac{\partial \varepsilon}{\partial x_i} = \frac{\partial}{\partial x_i}\left(\frac{\nu_T}{\sigma_\varepsilon} \frac{\partial \varepsilon}{\partial x_i} \right) + c_{1\varepsilon} \frac{\varepsilon}{k} \left(P + c_{3\varepsilon} G \right) - c_{2\varepsilon} \frac{\varepsilon^2}{k} \tag{3.46}$$

On discussion for determining $c_{3\varepsilon}$, according to test calculations, he stated that in situations where G is a positive term, as in unstably stratified flows, $c_{3\varepsilon}$ should take

a value of 1, while in stably stratified shear layers, where *G* is a negative term, $c_{3\varepsilon}$ should be chosen near zero. Successful calculations for the latter flows have been obtained with $c_{3\varepsilon}$ in the range 0-0.2. Further, the turbulent Prandtl/Schmidt number σ_T as well as c_μ have also been observed to depend on buoyancy effects and are not really a constant under stratification conditions. An extended version of the *k*-*ε* model has been introduced by Rodi (1987), in which the constants c_μ and σ_T are replaced by functions of suitable stratification parameters. These functions have been derived by simplifying a complex stress/flux-equation model. Yu and Li (1998) adapted the modifications suggested by Viollet (1990) on the standard *k*-*ε* model and used $c_{3\varepsilon} = c_{1\varepsilon}$ when $G \le 0$, and $c_{3\varepsilon} = 0$, when $G > 0$. In a study conducted by Verdier-Bonnet et al. (1999), $c_{3\varepsilon}$ was given the value 0, as was suggested by Rodi (1987) for stable flows. Launder and Spalding (1972) stated that it is likely that a two-equation model provides the best starting point, and perhaps the best finishing point as well. In spite of all significant advances in computer technology, their statement still might be valid at least for turbulence modelling of large water bodies.

3.5.4 *Boundary Conditions*

In this part only physical boundaries are discussed. Turbulent water flow may be bounded by a solid wall, a free surface or by non-turbulent flow. The location of wall and free surface boundaries is well defined, that of a free boundary is not because the interface between turbulent and non-turbulent fluid is highly indented and unsteady. For practical purposes, a free boundary is defined as the location where the velocity (or sometimes a scalar quantity) is nearly equal to its free-stream value (Rodi, 1984). The implementation of boundary conditions in the numerical model has been discussed in Chapter Four.

3.5.4.1 Wall Boundaries

At a solid boundary the no-slip condition applies so that both mean and fluctuating velocities are zero, but the dissipation rate *ε* is finite and requires special attention. When the boundary conditions are specified right at the wall, the equations must be integrated through the viscous sub-layer, which is undesirable for two reasons:

Firstly, very steep gradients prevail in the viscous sub-layer and for a proper resolution, many grid points have to be placed in this layer and the computation becomes expensive.

Secondly, viscous effects are important in this layer so that the high-Reynolds number turbulence models introduced above are not applicable. However, integration through the sub-layer is normally not necessary because empirical laws of sufficient generality are available that connect the wall conditions to the dependent variables just outside the viscous sub-layer. Within a turbulent boundary layer, Prandtl demonstrated that the velocity profile normal to the boundary is approximately logarithmic (Schlichting, 1979). This logarithmic law may be expressed as:

$$\frac{u_{res}}{u_\tau} = \frac{1}{\kappa} \ln \frac{u_\tau \, d}{\nu} + C \tag{3.47}$$

in which, u_{res} is the resultant velocity parallel and in distance *d* from the wall, u_τ is the resultant shear velocity, κ is von Kármán's constant*, which is taken equal to 0.4 (Schlichting, 1979), and C is an absolute constant for a Newtonian flow over a smooth surface and is found experimentally to be in the range of 5.0-5.2 (Bradshaw, 1978). If the roughness length scale, k_s, is made dimensionless by ν/u_τ, then for fully developed roughness ($70 \le k_s u_\tau / \nu$), the velocity distribution in the log-law region is now independent of viscosity because the Reynolds number characteristic of the flow over the rough wall is large (Fernholz, 1978). Then the logarithmic rule takes the following form:

$$\frac{u_{res}}{u_\tau} = \frac{1}{\kappa} \ln \frac{d}{d_0} \tag{3.48}$$

in which, d_0 is a constant, which also now absorbs *C* in equation (3.47). Equation (3.48) is known as the Prandtl-von Kármán velocity law (French, 1986). d_0 is a function of whether the boundary is hydraulically smooth or rough**.

* This constant varies over a small range of values as a function of the Reynolds number (French, 1986).

** Schlichting (1979) determined the following criteria for classifying surfaces:

- Hydraulically smooth boundary; $0 \le \frac{k_s u_\tau}{\nu} \le 5$
- Transition boundary $5 \le \frac{k_s u_\tau}{\nu} \le 70$
- Hydraulically rough boundary $70 \le \frac{k_s u_\tau}{\nu}$

If the boundary is hydraulically smooth, then d_0 depends solely on the kinematic viscosity and shear velocity:

$$d_0 = \frac{m\,\nu}{u_\tau} \tag{3.49}$$

where *m* is a coefficient and equal to approximately 1/9 for smooth surfaces (Chow, 1959). This leads to the following:

$$\frac{u_{res}}{u_\tau} = \frac{1}{\kappa} \ln \frac{9\,u_\tau\,d}{\nu} \tag{3.50}$$

Rodi (1984) used the same equation, which is discussed later in this section.

When the boundary surface is hydraulically rough, d_0 depends only on the roughness height:

$$d_0 = m\,k_s$$

where in this case *m* is a coefficient approximately equal to 1/30 (French, 1986) for sand grain roughness and k_s is the roughness height. Equation (3.48) then becomes:

$$\frac{u_{res}}{u_\tau} = \frac{1}{\kappa} \ln \frac{30\,d}{k_s} \tag{3.51}$$

This equation represents the velocity profile for unstratified flow. In density stratified flows, the density stratification causes the velocity profile to be modified. For these modifications see French (1986).

Rodi (1984) gave the boundary values for *k* and *ε*, which were derived from the universal law of the wall expressed as*:

$$\frac{u_{res}}{u_\tau} = \frac{1}{\kappa} \ln \left(y^+\,E\right) \tag{3.52}$$

where u_{res} is the resultant velocity parallel to the wall, u_τ is the resultant friction velocity, $y^+ = \frac{y u_\tau}{\nu}$ is a dimensionless wall distance, κ is the von Kármán constant, and *E* is a roughness parameter (*E* = 9, for hydraulically smooth walls).

---

* The logarithmic law has been challenged by Barenblatt and Chorin (1997). They have proposed that the relation between u_{res} and *d* depends on Reynolds number, whilst according to the logarithmic law, this relation is independent of *Re*. Their suggested law is as follows:

$$\frac{u_{res}}{u_\tau} = \left(\frac{1}{\sqrt{3}} \ln \mathrm{Re} + \frac{5}{2}\right) \eta^{\frac{3}{2} \ln \mathrm{Re}}$$

where $\eta = u_\tau\,d/\nu$

This law should be applied to a point whose y^+ value is in the range of $30 < y^+ < 100$. It is then sufficiently accurate for most situations.

In the y^+ region specified above, the Reynolds stresses are nearly constant. In this region the advection and diffusion of $\overline{u_i' u_j'}$ are negligible so that local equilibrium prevails.

When buoyancy effects are absent, this implies $P = \varepsilon$ which, together with considering the fact that the shear stress is approximately equal to the wall shear stress, leads to:

$$k_w = \frac{u_\tau^2}{\sqrt{c_\mu}} \tag{3.53}$$

This relation is normally used as boundary condition for *k* in one- and two-equation model calculations.

With $\varepsilon = P = u_\tau^2 \frac{\partial u}{\partial y}$ and $\frac{\partial u}{\partial y}$ from (3.52), there results the following boundary condition for ε:

$$\varepsilon_w = \frac{u_\tau^3}{\kappa\, y} \tag{3.54}$$

The conditions for *k* and ε, k_w and ε_w in equations (3.53) and (3.54), are to be applied to a near-wall point in the y^+ range.

Relations (3.52-3.54) are valid for smooth and rough walls. The roughness enters through the friction velocity, u_τ, whose relation to the velocity outside the sub-layer is governed by the roughness parameter *E*.

3.5.4.2 Free Boundaries

By the definition provided for a free boundary, velocities and scalar quantities are equal to their free-stream, or ambient, values at such boundaries. Often, the ambient stream is assumed to be entirely free of turbulence so that all turbulent stresses and fluxes and the dissipation ε are zero at the free boundary.

3.5.4.3 Free Surface

In the absence of wind-induced shear stresses and of heat exchange with the atmosphere, a free surface may be considered to a first approximation as a symmetry

plane*. When a shear layer is created by forces near the surface, then the boundary conditions expressed in equations (3.52-3.54) for wall boundaries seem appropriate, that is, the surface can be considered as a moving wall, which is certainly only an approximation. For further discussions on free surface boundary condition see Rodi (1984).

3.6 SUMMARY

Basic concepts and assumptions have been provided. The governing equations of fluid motion with particular interest of coastal and estuarine flows have been reviewed. Due to the salt intrusion studies in the current research project the species concentration conservation equation has been presented and discussed. Boundary conditions have been discussed in some detail.

The turbulent Navier-Stokes equations are presented, and the fundamental concepts of turbulence modelling have been reviewed. Although no attempt has been made to discuss details of different turbulence models, a brief review of the most commonly used models has been given, following a summary on the classification of the turbulence models. The buoyant k-ε turbulence model has been discussed in some detail as it has been the choice of the turbulence model in the present study.

* At symmetry planes and lines, the normal gradients are zero for all quantities with symmetrical behaviour such as scalar quantities, velocity components parallel to the symmetry plane or line, and normal stresses. On the other hand, velocity components normal to symmetry planes or lines and shear stresses as well as scalar fluxes are themselves zero (Rodi, 1984).

CHAPTER FOUR

NUMERICAL MODELLING

SCHEME, STRUCTURE AND THE SOLUTION METHOD

"The perfection of this art consists in knowledge of the scientific method by which one determines numerical and geometric unknowns"
Omar Khayyam, Treatise on Demonstration of Problems of Algebra, 1070
(O'Connor and Robertson, 1999)

4.1 INTRODUCTION

An arbitrary Lagrangian-Eulerian (ALE) hydrodynamic free-surface numerical model has been developed, based on the time-dependent Reynolds-averaged Navier-Stokes equations. The model with non-hydrostatic pressure distribution is capable of handling problems involving three-dimensionality and complex bathymetry. It also may be switched to a laterally-averaged model for the problems in which the cross-flow is very weak and therefore negligible. In addition to the free-surface problems, where the water elevation variations are negligible and in conjunction with concerns over the computational time, especially in three-dimensional problems, the model may be deployed with a rigid-lid condition.

A structured non-orthogonal curvilinear staggered mesh for computational domain, based on an arbitrary Lagrangian-Eulerian description, has been deployed. The discretisation of the flow and transport equations has been based on the finite

volume method, providing flexibility to define control volumes in a staggered grid system in three-dimensional environments, especially near the bed and water surface, where rapid changes of bathymetry and free surface have significant effect on the prediction of the flow field. The finite volume method also provides, if correctly implemented, the assurance of global conservation.

For modelling turbulence, and to optimise accuracy and economy, the two-equation k-ε turbulence model with buoyancy terms has been deployed and included in the numerical model.

Salt intrusion is almost always present in estuaries and coastal zones. This may be caused by gravity currents or may be due to the stratification attributable to a non-uniform salinity concentration profile and hence a variable density in harbours or estuarine barrages. The model is also capable of simulating non-homogeneous (i.e. with variable density) stratified flow fields.

The provision of this chapter is aimed to outline the concepts, describe the scheme and discuss the structure of the numerical model. Following a brief explanation of the necessity for a three-dimensional numerical model for simulating stratified turbulent flows for large water bodies, estuaries and harbours, the importance of using the conservative form of the conservation equations of mass, momentum and species concentration in simulating the flow and transport of species is illustrated. The description of the referential domain follows a brief review of the arbitrary Lagrangian-Eulerian (ALE) system.

The solution method was based on a fractional-step scheme whereby the problem was solved by time-splitting the set of the governing conservation equations, which resembles a projection method. The overall accuracy of the set of the equations is first order in time and second order in space. However, as advection plays a major role in the flow characteristics (Falconer, 1980a), as far as the type of water bodies in the present study is concerned, for this part of the transport a new fifth-order-accurate upstream scheme has been deployed. The structure of the numerical model and discretisation of the equations is described and provided in detail. The solution method is thoroughly discussed and a brief flowchart of the program is provided. Initial and boundary conditions for flow and transport, as well as the turbulence model, are discussed. Stability, consistency, convergence and accuracy of the numerical model are briefly discussed.

4.2 STRATIFIED ESTUARIES, HARBOURS AND BARRAGES

In the present study, the numerical model was basically developed to predict the flow field and salinity distribution and profile in large water bodies, estuaries and harbours.

In estuaries with the existence of a barrage or in the harbours with a barrier in the entrance, the vertical eddies may be strong and therefore the need for an accurate simulation of vertical acceleration prescribes the implementation of non-hydrostatic pressure distribution. With the limitations of the 2DH models, simulating the stratification requires a 2DV model, where the currents across the domain are negligible. However, considering the need for simulating vertical eddies for large water bodies with considerable vertical accelerations and variation of currents across the domain, a fully 3D model is required. A fully 3D non-hydrostatic model overcomes the limitations and fulfils the objectives of the numerical modelling of this project.

4.3 CONSERVATIVE FORM OF THE EQUATIONS OF FLOW

The governing equations of flow and transport are presented in Chapter Three. In this section the importance of the conservative form of the equations is illustrated. From the mathematical point of view both conservative and non-conservative forms of the equations are identical. However from the numerical point of view and the discretisation method, the non-conservative form of the equations may give rise to internal sources and reduce the accuracy of the scheme.

4.3.1 *General Form of a Conservation Law*

As the conservative and non-conservative form of the conservation equations are mathematically identical, in Chapter Three attention is given to the physical sense of the problem especially the stress and the rate-of-strain tensors and their relation. The equations, however, are presented in the conservative form and the numerical issues due to non-conservative form of the equations are addressed in this chapter. Here, only the general form of scalar and vectorial conservation laws, required for discretising the governing equations, is presented.

4.3.1.1 Scalar Conservation Law

A scalar quantity per unit volume, Φ, acting in an arbitrary volume, Ω, fixed in space and bounded by a closed surface, S, is considered (Fig. 4.1). The local intensity of Φ varies upon the effect of fluxes through the surrounding points and upon sources, Q. The flux vector $\boldsymbol{F}$ consists of two components, an advective contribution $\boldsymbol{F}_A$, and a diffusive part $\boldsymbol{F}_D$.

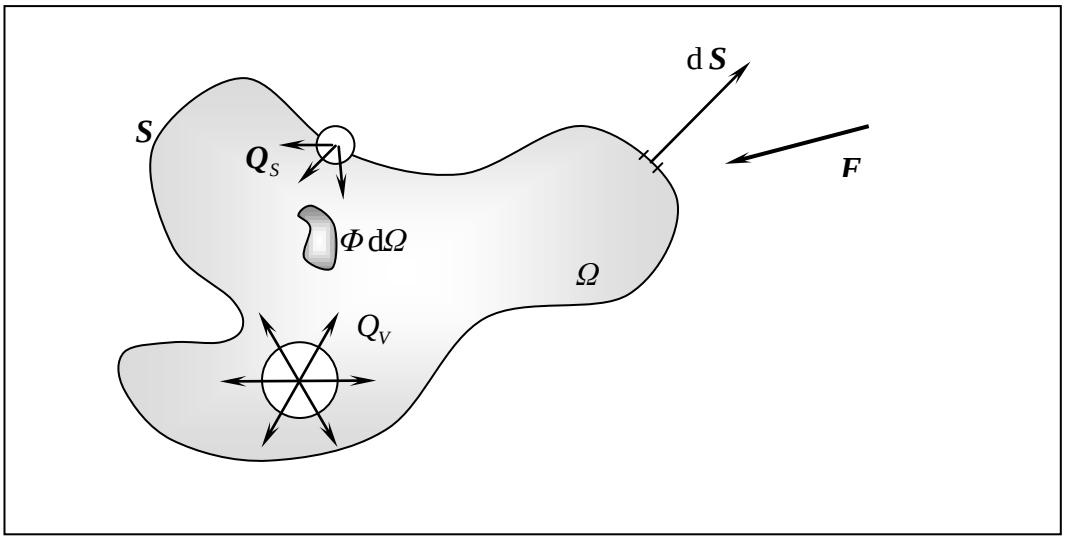

Figure (4.1) - General form of a conservation law for a scalar quantity

The general form of a conservation law expresses the fact that the variation of Φ per unit time within the volume Ω is equal to the net contribution from the incoming fluxes through the surface S, with the surface element vector $\mathrm{d}\boldsymbol{S}$ pointing outward, plus contribution from the sources of the quantity Φ. These sources are divided into volume and surface sources, Q_V and $\boldsymbol{Q}_S$ respectively. The general form of the conservation equation for the quantity Φ is expressed by (Hirsch, 1988):

$$\frac{\partial}{\partial t}\int_{\Omega} \Phi \,\mathrm{d}\Omega + \oint_S \boldsymbol{F}\cdot\mathrm{d}\boldsymbol{S} = \int_{\Omega} Q_V \,\mathrm{d}\Omega + \oint_S \boldsymbol{Q}_S\cdot\mathrm{d}\boldsymbol{S} \tag{4.1}$$

By applying Gauss's theorem, and the assumption of a continuous flow for fluxes and surface sources, equation (4.1) can be written as follows:

$$\int_{\Omega} \frac{\partial \Phi}{\partial t}\,\mathrm{d}\Omega + \int_{\Omega} \nabla\cdot\boldsymbol{F}\,\mathrm{d}\Omega = \int_{\Omega} Q_V\,\mathrm{d}\Omega + \int_{\Omega} \nabla\cdot\boldsymbol{Q}_S\,\mathrm{d}\Omega \tag{4.2}$$

Since equation (4.2) is written for an arbitrary volume Ω, and all terms appear in the form of volume integral, it leads to the differential form of the conservation law as follows:

$$\frac{\partial \Phi}{\partial t} + \nabla \cdot \boldsymbol{F} = Q_V + \nabla \cdot \boldsymbol{Q}_S \quad (4.3) \qquad \text{or} \qquad \frac{\partial \Phi}{\partial t} + \nabla \cdot \left(\boldsymbol{F} - \boldsymbol{Q}_S\right) = Q_V \quad (4.4)$$

It can be seen from the equation (4.1) that, in the absence of volume sources, the internal variation of Φ depends only on the flux contribution through the surface S, and not on the flux values inside the volume Ω. The advective part of the flux vector, $\boldsymbol{F}_A$, is the amount of Φ transported with the flow and is given by the equation (4.5):

$$\boldsymbol{F}_A = \boldsymbol{V}\Phi \quad (4.5)$$

The diffusive flux can be expressed by the generalised gradient law of Fick as follows:

$$\boldsymbol{F}_D = -\lambda\, \rho\ \nabla\phi \quad (4.6)$$

in which ϕ is the quantity Φ per unit mass (i.e. $\Phi = \rho\phi$), ρ is the density of the fluid and λ is a diffusivity. Equation (4.3) can now be rewritten to give the general form of a transport equation for the quantity Φ as follows:

$$\frac{\partial \rho\phi}{\partial t} + \nabla \cdot \left(\rho\ \boldsymbol{V}\,\phi\right) = \nabla \cdot \left(\lambda\, \rho\ \nabla\phi\right) + Q_V + \nabla \cdot \boldsymbol{Q}_S \quad (4.7)$$

4.3.1.2 Vector Conservation Law

If $\boldsymbol{\Phi}$ represents a vector quantity, then the flux and surface source terms become tensors and the volume source term becomes a vector, giving:

$$\frac{\partial}{\partial t}\int_{\Omega} \boldsymbol{\Phi}\, \mathrm{d}\Omega + \oint_S \overline{\boldsymbol{F}} \cdot \mathrm{d}\,\boldsymbol{S} = \int_{\Omega} \boldsymbol{Q}_V\, \mathrm{d}\Omega + \oint_S \overline{\boldsymbol{Q}}_S \cdot \mathrm{d}\,\boldsymbol{S} \quad (4.8)$$

Applying Gauss's theorem, with the assumption of the fluxes and surface sources being continuous, results:

$$\frac{\partial}{\partial t}\int_{\Omega} \boldsymbol{\Phi}\, \mathrm{d}\,\Omega + \int_{\Omega} \nabla \cdot \overline{\boldsymbol{F}}\ d\,\Omega = \int_{\Omega} \boldsymbol{Q}_V\, \mathrm{d}\,\Omega + \int_{\Omega} \nabla \cdot \overline{\boldsymbol{Q}}_S\ d\,\Omega \quad (4.9)$$

The differential form of the equation (4.9) is given by:

$$\frac{\partial \boldsymbol{\Phi}}{\partial t} + \nabla \cdot \left(\overline{\boldsymbol{F}} - \overline{\boldsymbol{Q}}_S\right) = \boldsymbol{Q}_V \quad (4.10)$$

and the advection component of the flux tensor is given by:

$$\overline{\boldsymbol{F}}_A = \boldsymbol{V} \otimes \boldsymbol{\Phi} \quad (4.11)$$

The general forms of conservation laws (Eq. 4.1 and Eq. 4.8) are the most generally valid expressions, since they remain valid in the presence of discontinuous

variations of the flow properties such as inviscid shock waves or constant discontinuities (Hirsch, 1988).

In equation (4.1) if Φ is considered to be the density, ρ, and with noting that no diffusive flux exists for the mass transport and in the absence of source terms, the mass conservation equation can be obtained. The equation of the conservation of momentum can be obtained from equation (4.8). The results for the equations of conservation of mass, momentum and species concentration for an incompressible flow are presented in Chapter Three (Eqs. 3.23-3.25). These are the conservative form of the equations and from a numerical point of view are different from the non-conservative equations. Although both sets of the equations are fully equivalent from a mathematical point of view, they may not necessarily remain so when a numerical discretisation is performed. Equations (3.23-3.25) correspond to the general form of a conservation law and are said to be formally written in conservative or in divergence form (Hirsch, 1988). The importance of the conservative form in a numerical scheme lies in the fact that a discretisation of the set of the non-conservative equations may lead to a numerical scheme in which all the mass fluxes through the cell boundaries may not cancel, and hence the numerical scheme will not maintain global conservation. This is discussed further in the following section.

4.3.1.3 Conservative Discretisation

The presence of sharp slopes in the bed topography, sharp roughnesses of solid boundaries or dramatic changes in the planform geometry may lead to numerical errors. The efficiency of the proposed new high-order scheme to increase the accuracy of the advection part of the transport term, in order to improve on the prediction of the flow characteristics, especially for problems of interest in this study which are advection dominated, may not be fulfilled if the importance of the correct discretisation at such boundaries and situations is not recognised.

To demonstrate the numerical internal volume sources, which may appear in a non-conservative discretisation, a one-dimensional form of the conservation law is written as:

$$\frac{\partial \phi_x}{\partial t} + \frac{\partial f_x}{\partial x} = q_x \tag{4.12}$$

where f_x is the *x*-component of the flux vector. Dropping the *x*-subscript for convenience leads to:

$$\frac{\partial \phi}{\partial t} + \frac{\partial f}{\partial x} = q \tag{4.13}$$

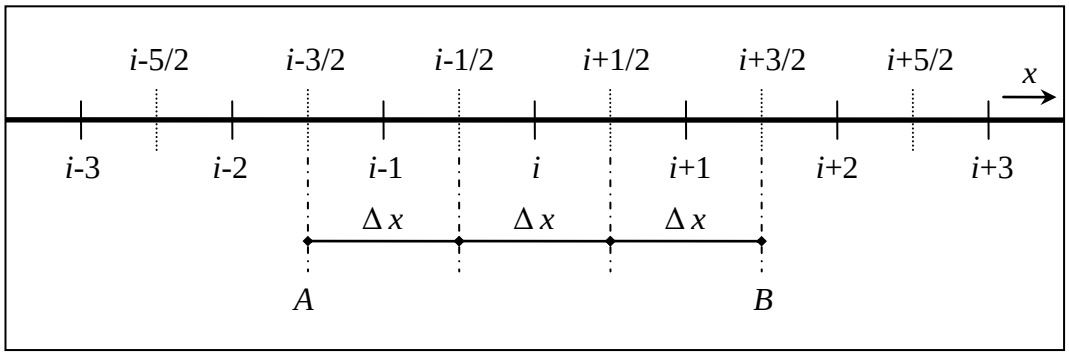

Figure (4.2) - Discretisation of the one-dimensional form of a conservation law

Applying a central difference formulation at point *i* to the mesh of figure (4.2), then the following discretised equation is obtained:

$$\frac{\partial \phi_i}{\partial t} + \frac{f_{i+1/2} - f_{i-1/2}}{\Delta x} = q_i \tag{4.14}$$

Applying the same discretisation to the points (*i*-1) and (*i* +1) and summing the three equations results in a consistent discretisation of the same conservation law for cell *AB* $(i-3/2,\ i+3/2)$ as follows:

$$\frac{\partial}{\partial t}\frac{\left(\phi_{i-1} + \phi_i + \phi_{i+1}\right)}{3} + \frac{f_{i+3/2} - f_{i-3/2}}{3\,\Delta x} = \frac{1}{3}\left(q_{i-1} + q_i + q_{i+1}\right) \tag{4.15}$$

It can be seen from the equation (4.15) that the fluxes at internal points have cancelled out. This conservative scheme has produced a good approximation of equation (4.13). García-Navarro et al. (2002) state that this good approximation lies in cancelling the contributions of the flux at the grid interfaces and therefore global variation of the conserved variable being due to only the source terms and to the flux at the boundaries. This is called the telescoping property for the flux terms (Roache, 1972).

The non-conservative form of the equation can be written as:

$$\frac{\partial \phi}{\partial t} + \frac{\partial f}{\partial \phi}\frac{\partial \phi}{\partial x} = q \tag{4.16}$$

Both equations (4.13) and (4.16) are mathematically equivalent for arbitrary, non-linear fluxes, but their numerical implementation is different. In equation (4.16) if $f = u\phi$, for instance, applying a second-order central difference at mesh point *i* gives:

$$\frac{\partial \phi_i}{\partial t} + \left(\frac{\partial f}{\partial \phi}\right)_i \frac{\phi_{i+½} - \phi_{i-½}}{\Delta x} = q_i \tag{4.17}$$

where term $\left(\frac{\partial f}{\partial \phi}\right)_i$ can be estimated as:

$$\left(\frac{\partial f}{\partial \phi}\right)_i = \frac{1}{2}\left[\left(\frac{\partial f}{\partial \phi}\right)_{i-½} + \left(\frac{\partial f}{\partial \phi}\right)_{i+½}\right] \tag{4.18}$$

Applying the same discretisation for the mesh points (*i*-1) and (*i* +1) and summing the equations and rearranging the resultant equation, a discretised equation for the cell *AB* results in:

$$\frac{\partial}{\partial t}\frac{(\phi_{i-1} + \phi_i + \phi_{i+1})}{3} + \frac{1}{2}\left[\left(\frac{\partial f}{\partial \phi}\right)_{i-3/2} + \left(\frac{\partial f}{\partial \phi}\right)_{i+3/2}\right]\frac{\phi_{i+3/2} - \phi_{i-3/2}}{3\Delta x} - \frac{1}{3}(q_{i-1} + q_i + q_{i+1})$$

$$= \frac{1}{2}\left[\left(\frac{\partial f}{\partial \phi}\right)_{i-3/2} - \left(\frac{\partial f}{\partial \phi}\right)_{i+1/2}\right]\frac{\phi_{i+3/2} - \phi_{i-1/2}}{3\Delta x} - \frac{1}{2}\left[\left(\frac{\partial f}{\partial \phi}\right)_{i-1/2} - \left(\frac{\partial f}{\partial \phi}\right)_{i+3/2}\right]\frac{\phi_{i+1/2} - \phi_{i-3/2}}{3\Delta x} \tag{4.19}$$

From equation (4.19) it can be seen that the discretisation of the non-conservative form of the equation gives rise to internal sources, which in this example are equal to the right-hand side of the equation (4.19). These numerical source terms are of the same order as the truncation error in continuous fluids and can be neglected. However, numerical experiments, especially in the presence of sharp gradients, show that non-conservative forms are generally less accurate than the conservative form of the equations and for discontinuous flows these numerical source terms can become important across the discontinuity and cause sizeable errors (Hirsch, 1988). For rough, shallow estuaries the tidal currents are strongly dependent upon the instantaneous water surface slope and hence the rate of rise and fall of the tide (Burt and Rees, 2001).

The conservativity requirement for equation (4.12) is satisfied if the scheme can be written as:

$$\frac{\partial \phi_{x_i}}{\partial t} + \frac{\left(\hat{f}_{x_{i+1}} - \hat{f}_{x_{i-1}}\right)}{\Delta x} = q_{x_i} \tag{4.20}$$

in which $\hat{f}$ is called the numerical flux and is a function of the values of ϕ_x at (2*k*-1) neighbouring points. In order to generalise to multi-dimensions, this must be

satisfied separately for all the components of the flux vector (Hirsch, 1988). This is demonstrated where the fractional-step method is introduced for solving the flow equations and therefore the transport terms are solved in a locally one-dimensional approach.

4.4 ARBITRARY LAGRANGIAN-EULERIAN DESCRIPTION

For the numerical solution of multi-dimensional problems in fluid dynamics, an important consideration is the relationship between the fluid motion and the computational domain. Nomura and Hughes (1992) stated that the fundamental kinematical relations in the general kinematical theory supporting the ALE description was derived by defining three domains in space, namely the spatial domain, the material domain and the referential domain. Mapping between these domains converts the kinematical and dynamical relations in fluid; in space, in fluid, and in computational domain.

The spatial domain is the domain on which the problem is posed. The material domain is considered the domain occupied at time $t = 0$ by the material particles which occupy the spatial domain at t (the time of interest). The image of the referential domain at time t under a prescribed mapping is the spatial domain. With this description, in the numerical analysis of the problem, the spatial domain becomes a moving mesh and the referential domain a reference state of the moving mesh.

The Eulerian description is regarded as a special case of this description, in which the spatial domain is fixed throughout. This means that the spatial domain always coincides with the referential domain. Another special case where the material domain coincides with the spatial domain is the Lagrangian description, where grids move with material particles. Advantages and disadvantages of each of these descriptions are studied and discussed in the literature (e.g. Hirt and Nichols, 1981).

Zhou and Stansby (1999) further clarified this by stating that the Lagrangian method and the Eulerian method can be seen as two special cases of mesh motion. The ALE becomes the Lagrangian description when the mesh moves with the local fluid velocity and becomes the Eulerian description when the mesh is fixed, which is very desirable for simulating interface and free surface flows.

4.4.1 *Arbitrary Lagrangian-Eulerian (ALE) Concept*

The numerical methods used for calculating the flow with free surface can be classified into three categories, the Eulerian, the Lagrangian and the arbitrary Lagrangian-Eulerian (ALE) methods (Sung et al., 1999). In the Lagrangian framework the mesh moves with the local fluid velocity, while in the Eulerian framework the fluid flows through a fixed grid. Each approach has its own advantages and difficulties. The ALE description combines the advantages of the pure Lagrangian method and the pure Eulerian method but without their disadvantages. The essence of the ALE methodology is that the mesh motion can be chosen arbitrarily, giving flexibility to combine the individual strengths of the two approaches. The Eulerian method gives a rather rough estimate of the free surface especially in the presence of a complex water surface geometry. In the Lagrangian method, the free surface is computed by a coordinate system which moves with the fluid particle and gives an accurate free surface shape with the ease of free surface boundary condition implementation. However, at large deformations of fluid elements, fluid particle trajectories may cross each other. In the ALE method, the newly updated free surface is determined purely by the Lagrangian method, by the velocities of the fluid particles at the free surface, while the nodes in the interior of the domain are displaced in an arbitrary prescribed way to be redistributed to avoid mesh crossing. Because of this feature the ALE provides additional flexibility and potential accuracy for describing a flow, which is very desirable in a numerical analogue for interface and free surface flows or general problems involving moving boundaries. In the oceanic tidal flow problems and for the interests of the numerical model developed herein, the grid movement is considered only in the vertical direction. The grid generation and redistribution was accomplished by a subroutine which updated the mesh geometry after the completion of each and every half-time-step (Figure 4.9). The inclusion of the vertical grid velocity had negligible effect on computational efficiency.

4.4.2 *Flow and Transport Equations in ALE*

For the flows with moving boundaries the locus of the moving boundary is unknown a priori and is fully coupled with the velocity through the kinematic condition. Sung et al. (2000) stated that for flow problems with moving boundaries

and deformable meshes, the geometric conservation law (GCL) has to be satisfied which states that the change in volume must be equal to the volume swept by the cell boundary during one time step. In an approach to the solution of unsteady free surface flows, taken by Thé et al. (1994), the control volume corners were moved by applying a natural closure of the mass and momentum equations along the surface. Lesoinne and Farhat (1996) presented a unified theory for deriving geometric conservation laws (GCLs) and considered the arbitrary Lagrangian-Eulerian (ALE) finite volume method.

Here, the universal flow and transport equations in the ALE form are derived by a simple approach presented by Zhou and Stansby (1999). The observation point, *P* (*x*, *y*, *z*), of the moving coordinate at time *t* in Cartesian coordinates (Fig. 4.3) is considered. The gird velocity at point *P* is $\boldsymbol{V}_g = u_g \boldsymbol{i} + v_g \boldsymbol{j} + w_g \boldsymbol{k}$ and $\phi(x, y, z, t)$ denotes a scalar or vector quantity (e.g. $\boldsymbol{V}$) at this point. In a small time Δt, the fluid particle moves to point $P'(x + u\Delta t, y + v\Delta t, z + w\Delta t)$, where ϕ' at point P' can be expressed by use of a Taylor series expansion, after ignoring terms of second order or higher, as:

$$\phi'(x+u\Delta t, y+v\Delta t, z+w\Delta t, t+\Delta t) = \phi(x, y, z, t) + \Delta t \frac{\partial \phi}{\partial t} + u\Delta t \frac{\partial \phi}{\partial x} + v\Delta t \frac{\partial \phi}{\partial y} + w\Delta t \frac{\partial \phi}{\partial z} \tag{4.21}$$

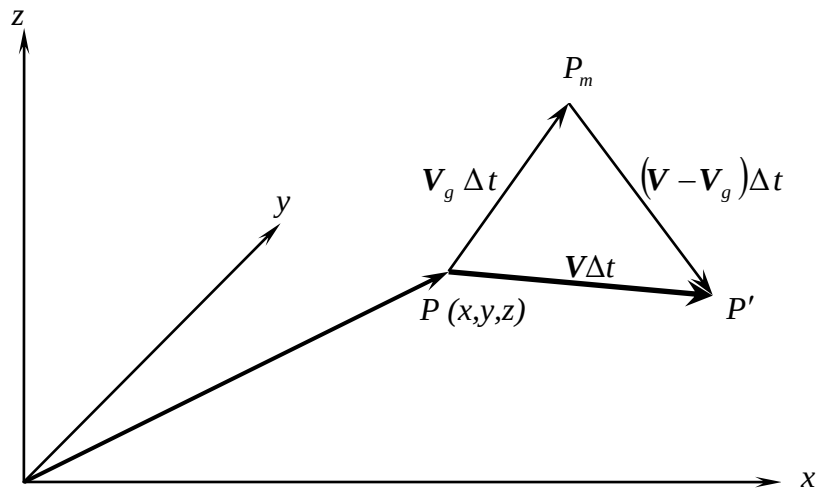

Figure (4.3) - Definition for moving grid in Cartesian coordinates

Because the coordinate moves at the same time, the observation point therefore has moved to the point $P_m(x + u_g \Delta t, y + v_g \Delta t, z + w_g \Delta t)$ at time $t + \Delta t$. So ϕ_m at point P_m and time *t* can also be expressed by use of the Taylor series:

$$\phi_m\left(x+u_g\Delta t, y+v_g\Delta t, z+w_g\Delta t, t\right)=\phi(x,y,z,t)+u_g\Delta t\frac{\partial\phi}{\partial x}+v_g\Delta t\frac{\partial\phi}{\partial y}+w_g\Delta t\frac{\partial\phi}{\partial z} \quad (4.22)$$

The change in quantity ϕ with reference to the point P_m in the time interval Δt can be obtained by subtracting equation (4.22) from equation (4.21). The following equation is then obtained:

$$\Delta\phi=\phi'-\phi_m=\Delta t\frac{\partial\phi}{\partial t}+\left(u-u_g\right)\Delta t\frac{\partial\phi}{\partial x}+\left(v-v_g\right)\Delta t\frac{\partial\phi}{\partial y}+\left(w-w_g\right)\Delta t\frac{\partial\phi}{\partial z} \quad (4.23)$$

The time derivative in the ALE description is then expressed as:

$$\frac{\mathrm{D}\phi}{\mathrm{D}t}=\frac{\partial\phi}{\partial t}+\left(u-u_g\right)\frac{\partial\phi}{\partial x}+\left(v-v_g\right)\frac{\partial\phi}{\partial y}+\left(w-w_g\right)\frac{\partial\phi}{\partial z} \quad (4.24)$$

which in vectorial form can be written as follows:

$$\frac{\mathrm{D}\phi}{\mathrm{D}t}=\frac{\partial\phi}{\partial t}+\left(\boldsymbol{V}-\boldsymbol{V}_g\right)\cdot\mathrm{grad}\,\phi \quad (4.25)$$

If the observation point does not move, (i.e. mesh velocity is zero, $\boldsymbol{V}_g=0$), equation (4.25) becomes the time derivative in an Eulerian frame as follows:

$$\frac{\mathrm{D}\phi}{\mathrm{D}t}=\frac{\partial\phi}{\partial t}+\boldsymbol{V}\cdot\mathrm{grad}\,\phi \quad (4.26)$$

On the other hand if the observation point moves with local fluid particle (i.e., if the mesh velocity is the same as particle velocity, $\boldsymbol{V}_g=\boldsymbol{V}$), the advection term disappears in the governing equations and the fluid particles are always located at the same mesh points. In this case equation (4.25) becomes the time derivative in a Lagrangian frame as follows:

$$\frac{\mathrm{D}\phi}{\mathrm{D}t}=\frac{\partial\phi}{\partial t} \quad (4.27)$$

By substitution of the expression (4.25) into equations (3.24) and (3.25), the Navier-Stokes and species concentration conservation equations in the ALE form are obtained. Usually, the grid does not move in the horizontal direction, in which case the horizontal components of $\boldsymbol{V}_g$ (i.e. u_g and v_g) are equal to zero, however if a movable boundary is considered, they can readily be re-included in the equations and the general form of the equation (Eq. 4.24) is then solved. With this consideration for the Navier-Stokes and species concentration conservation equations, the set of the equations for flow and transport (Eqs. 3.23-3.25) can be rewritten in the conservative ALE form as follows:

$$\frac{\partial u_i}{\partial x_i} = 0 \tag{4.28}$$

$$\frac{\partial u_i}{\partial t} + \frac{\partial u_j u_i}{\partial x_j} - w_g \frac{\partial u_i}{\partial z} = \frac{1}{\rho_r} X_i - \frac{1}{\rho_r} \frac{\partial p}{\partial x_i} + \frac{\partial}{\partial x_j} \left(\nu_T \frac{\partial u_i}{\partial x_j} \right) + g_i \frac{\rho - \rho_r}{\rho_r} \tag{4.29}$$

$$\frac{\partial C}{\partial t} + \frac{\partial C u_i}{\partial x_i} - w_g \frac{\partial C}{\partial z} = \frac{\partial}{\partial x_i} \left(\nu_T \frac{\partial C}{\partial x_i} \right) \tag{4.30}$$

The transport equation for the species concentration is used together with an equation of state for the density of water which is presented in Chapter Seven.

4.4.3 *Turbulence Closure in ALE*

The approaches based on mixing length or one-equation (turbulence energy) modelling are not predictive because the empirical coefficients applied are not shown to be universally applicable (Alfrink and van Rijn, 1983). Falconer and Li (1994) concluded that the *k-ε* turbulence model solutions for the tidal eddies in the rectangular harbours gave markedly different eddy viscosity distributions from those predicted using a simple mixing-length model. To optimise accuracy and economy the two-equation *k-ε* turbulence model with buoyancy terms has been deployed and included in the numerical model. The model and its terms are discussed in Chapter Three. The empirical constants are taken equal to those proposed by Rodi (1987). The conservative form of the *k-ε* equations in ALE form in tensor notation is as follows:

$$\nu_T = c_\mu \frac{k^2}{\varepsilon} \tag{4.31}$$

$$\frac{\partial k}{\partial t} + \frac{\partial u_i k}{\partial x_i} - w_g \frac{\partial k}{\partial z} = \frac{\partial}{\partial x_i} \left(\frac{\nu_T}{\sigma_k} \frac{\partial k}{\partial x_i} \right) + P + G - \varepsilon \tag{4.32}$$

$$\frac{\partial \varepsilon}{\partial t} + \frac{\partial u_i \varepsilon}{\partial x_i} - w_g \frac{\partial \varepsilon}{\partial z} = \frac{\partial}{\partial x_i} \left(\frac{\nu_T}{\sigma_\varepsilon} \frac{\partial \varepsilon}{\partial x_i} \right) + c_{1\varepsilon} \frac{\varepsilon}{k} \left(P + c_{3\varepsilon} G \right) - c_{2\varepsilon} \frac{\varepsilon^2}{k} \tag{4.33}$$

P and *G* are shear and buoyancy productions respectively and are given by:

$$P = \nu_T \left(\frac{\partial u_i}{\partial x_j} + \frac{\partial u_j}{\partial x_i} \right) \frac{\partial u_i}{\partial x_j} \tag{4.34}$$

$$G = \beta \, g_i \frac{\nu_T}{\sigma_T} \frac{\partial C}{\partial x_i} \tag{4.35}$$

4.5 REFERENTIAL DOMAIN DESCRIPTION

A non-orthogonal curvilinear grid system in the ALE description has been deployed. A backward staggered grid has been used which eliminates the need for interpolation to calculate velocities at the scalar cell faces, as they are generated at exactly the locations where they are required for the scalar transport computations. The problems associated with decoupling of velocity and pressure on even and odd points are also cured by a staggered grid. Advantages of using a staggered grid is discussed and demonstrated in Patankar (1980), Fletcher (1991) and Versteeg and Malalasekera (1995). The accuracy and convergence of a finite volume calculation depends on the quality of grids, which can be characterised as:

- Non-orthogonality: deviation of grid line intersections from 90 degrees;
- Aspect ratio: the ratio of length of the cell to its width in a quadrilateral shaped grid cell;
- Expansion ratio: the ratio of grid size to its neighbouring cells (the ratio of the longer grid to shorter grid) in the same grid direction.

Olsen (1997) gave guidelines for the acceptable range of these characteristics, which are summarised below and taken into account in the present study.

If the line intersection is more than 45 degrees different from orthogonal, the grid is considered as very non-orthogonal, a situation which should be avoided. However low non-orthogonality of the grid leads to more rapid convergence, and in some cases better accuracy. Aspect ratios of 2-3 should not be a problem if the flow direction is parallel to the longest side of the cell. Experience shows that aspect ratios of 10-50 give extremely slow convergence for water flow calculations. Expansion ratios under 1.2 do not pose problems for the solution. Experience shows that expansion ratios of around 10 can give very unphysical results for the water flow calculation.

In the present study, due to direct solution of the equations, no concern over the speed of convergence was encountered. The non-orthogonality for simulating the physical model was almost negligible, and for the test cases provided in Chapter Five the recommended range for maintaining accuracy has been observed. The aspect ratio varies over a small range depending on the water elevation, but remains in the range of 1-3, provided that the flow direction is parallel to the longest side of the cell. As the grid size is constant in each direction, the expansion ratio is equal to one.

4.5.1 *Grid Configuration and Control Volume Definitions*

The bathymetry is considered to be known and water elevations are to be calculated at the same local *z*-axis as the pressure nodes are located. Therefore a control volume containing, for example, the scalar quantities, consists of twelve faces which from, four are the lateral vertical planes, and eight are the curvilinear top and bottom surfaces. Four of the latter form the top and the other four the bottom of the control volume. Due to the complexity of such a configuration and difficulties associated with the graphical presentation of the referential domain, the projection of the grid configuration and geometry on the *xoy*, *yoz* and *xoz* reference planes is demonstrated herein.

Figure (4.4) shows the projection of the geometry and configuration of the grids, the locations of the scalar and vector quantities and their control volumes on *xoy* reference plane. It can be seen that the scalar variables including pressure, species concentration, density, k, ε and viscosity are calculated at the nodal points, and the velocity components are calculated for points or locations on the faces of a control volume that is drawn around the pressure points. The velocity components are located midway between pressure points, which are centred on the cell faces of the staggered grids.

The scalar variables are stored at the nodes marked (●). The velocities are defined at the cell faces in between the nodes and are indicated by arrows. The arrows in *x*-, *y*- and *z*-directions indicate the location for *u*-, *v*- and *w*-velocity components respectively.

For computer storage $u_{i,j,k}$ physically considered to be located at $u_{i-1/2,j,k}$, $v_{i,j,k}$ at $v_{i,j-1/2,k}$, and $w_{i,j,k}$ at $w_{i,j,k-1/2}$. The projection of the geometry and grid configuration, and the locations of the scalar and vector quantities and their control volumes on *xoz* reference plane is illustrated in figure (4.5). The projection on *yoz* plane is schematically exactly the same if *x*, *i*, *u* and Δx are replaced by *y*, *j*, *v* and Δy respectively.

The arrangement illustrated in figure (4.5) shows that the control volumes for the scalar quantities and the *w*-velocity component consist of twelve faces and the *u*- and *v*-velocity component control volumes consist of six faces. For demonstration of a possible distortion, a control volume with pressure (or any scalar quantity) on all its corners is shown in figure (4.6).

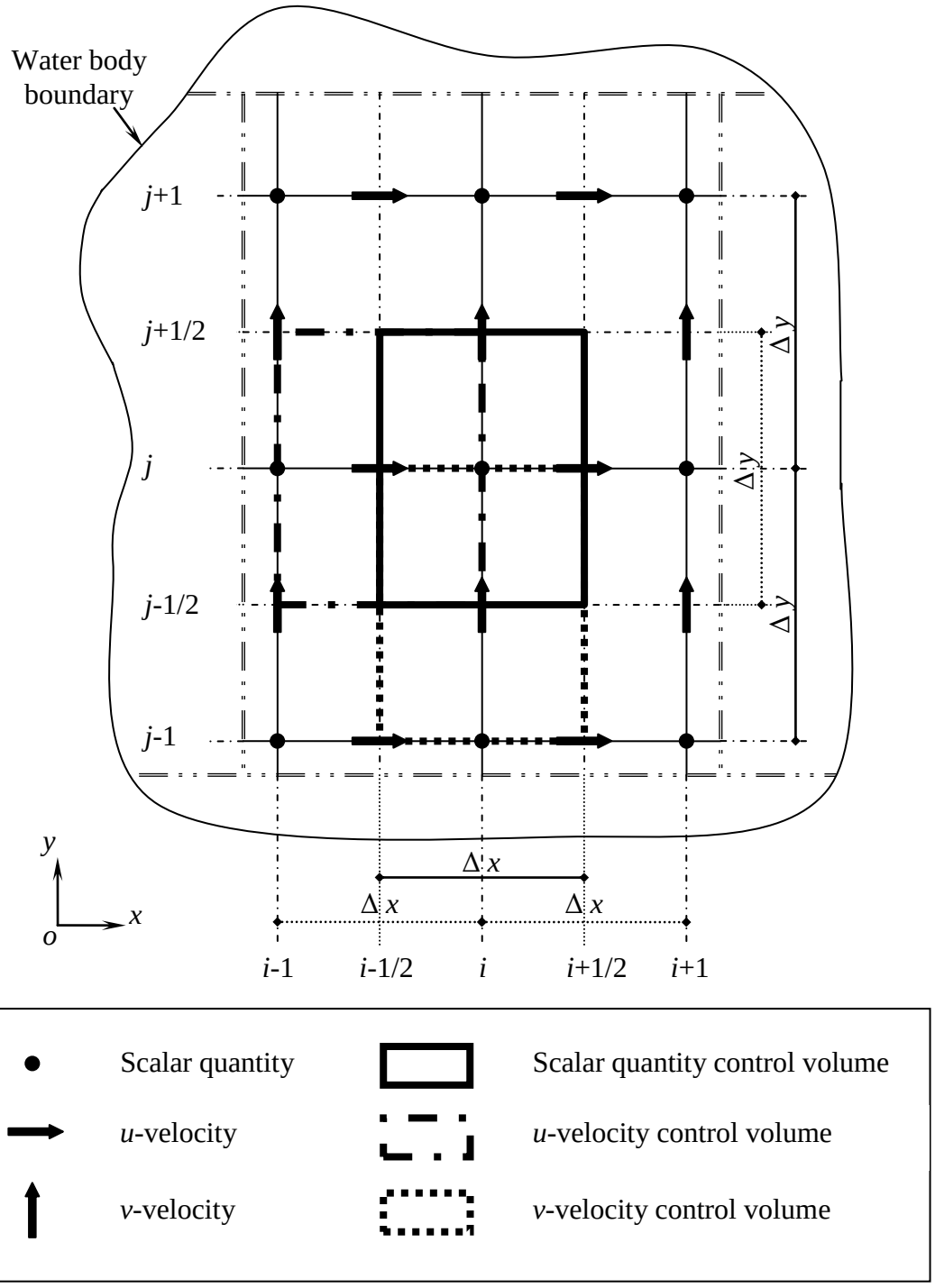

Figure (4.4) - Projection of the geometry of grids, location of the scalar and vector quantities and their control volumes on *xoy* reference plane

In the numerical scheme, the eight surfaces on the top and bottom of the scalar and *z*-velocity-component control volumes were approximated by two surfaces, one for the top and the other for the bottom. However the water elevation, bed level, and the *z*-coordinate of the nodal points where the scalar quantities are located, were

calculated according to the general configuration presented in figure (4.5). Regarding the cell-centred finite volume geometry, the boundaries of the computational domain are located on scalar-quantity cell faces.

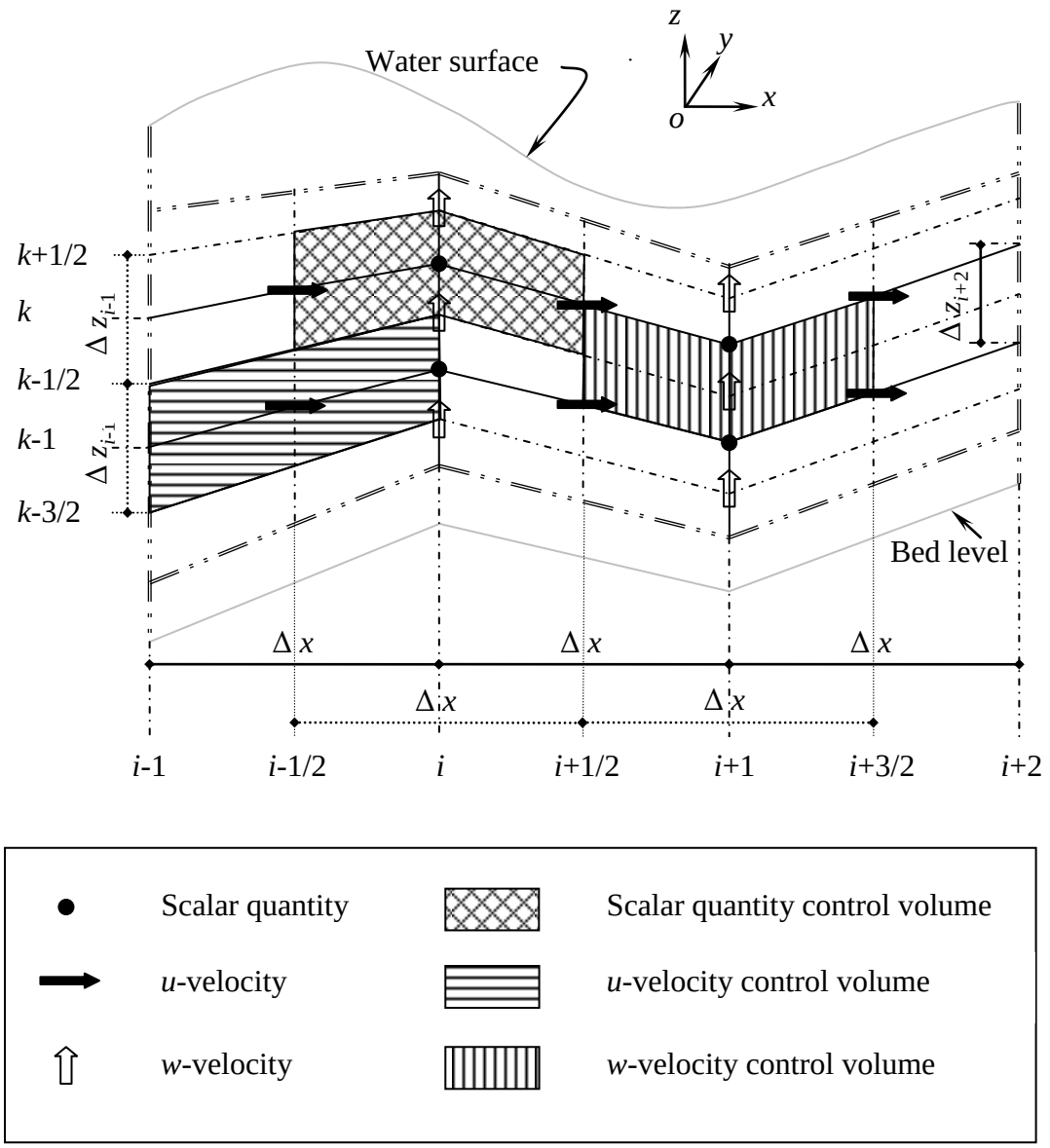

Figure (4.5) - Projection of the geometry of grids, location of the scalar and vector quantities and their control volumes on *xoz* reference plane

4.5.2 *General Characteristics of Discretisation of the Quantities by Finite Volume Method*

The method takes full advantage of an arbitrary mesh. The integral conservation laws are written for a discrete volume as follows:

$$\frac{\partial}{\partial t}\int_{\Omega} \Phi \, \mathrm{d}\Omega + \oint_{S} \boldsymbol{F} \cdot \mathrm{d}\boldsymbol{S} = \int_{\Omega} Q \, \mathrm{d}\Omega \tag{4.36}$$

This law can be applied to the control volume $\Omega_{i,j,k}$, illustrated in figure (4.7). In this figure the approximation mentioned in the proceeding section has been implemented and the four surfaces on the top and on the bottom of the control volume have been approximated by one surface, for each end. The discretised equation associated with $\Phi_{i,j,k}$, the quantity that the control volume of which is drawn in figure (4.7), is to be defined. It can be seen from figure (4.7) that the geometrical domain consists of hexahedral control volumes, where the four points forming the top as well as the four points forming the bottom of the control volume are not necessarily coplanar.

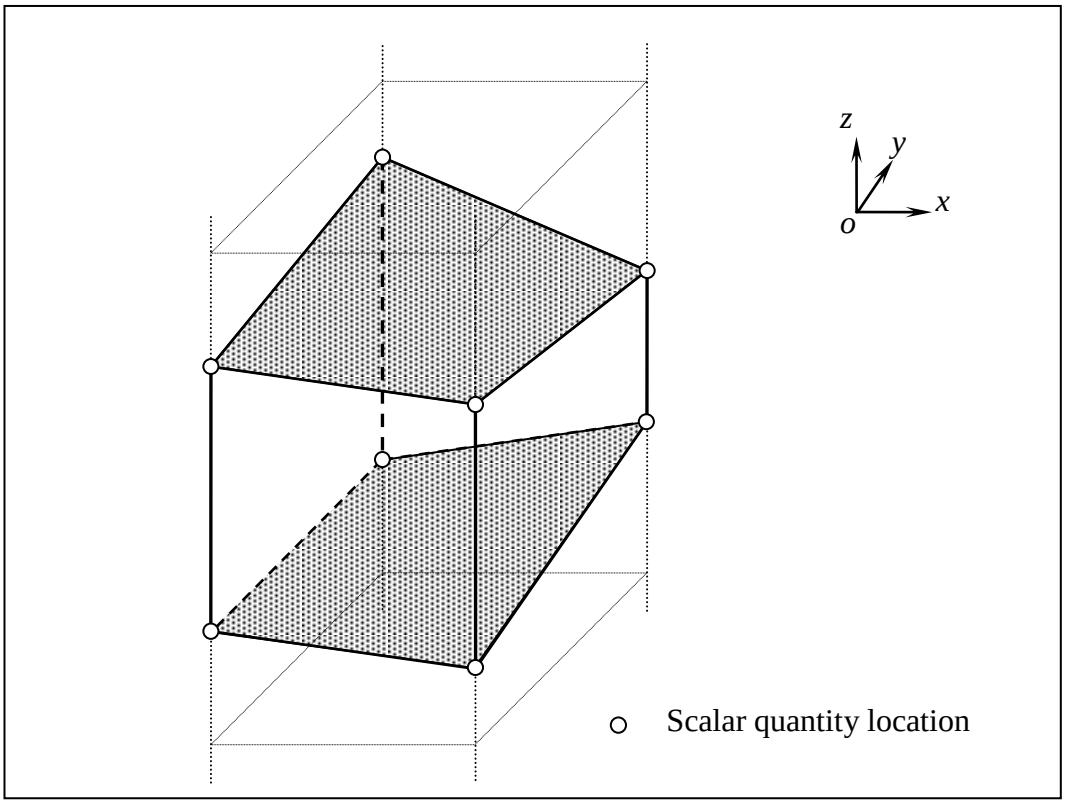

Figure (4.6) - Typical volumetric shape of a control volume with scalar quantities at its corners

Equation (4.36) assumes the discrete form as follows:

$$\frac{\partial}{\partial t}\left(\Phi_{i,j,k}\ \Omega_{i,j,k}\right)+\sum_{\text{sides}}\left(\boldsymbol{F}\cdot\boldsymbol{S}\right)=Q_{i,j,k}\ \Omega_{i,j,k} \tag{4.37}$$

where the sum of the flux terms refers to all the external sides of the control cell $\Omega_{i,j,k}$, which referring to figure (4.7) and to cell (*i*, *j*, *k*) the flux terms of the control volume $\Omega_{i,j,k}$ are summed over the six sides.

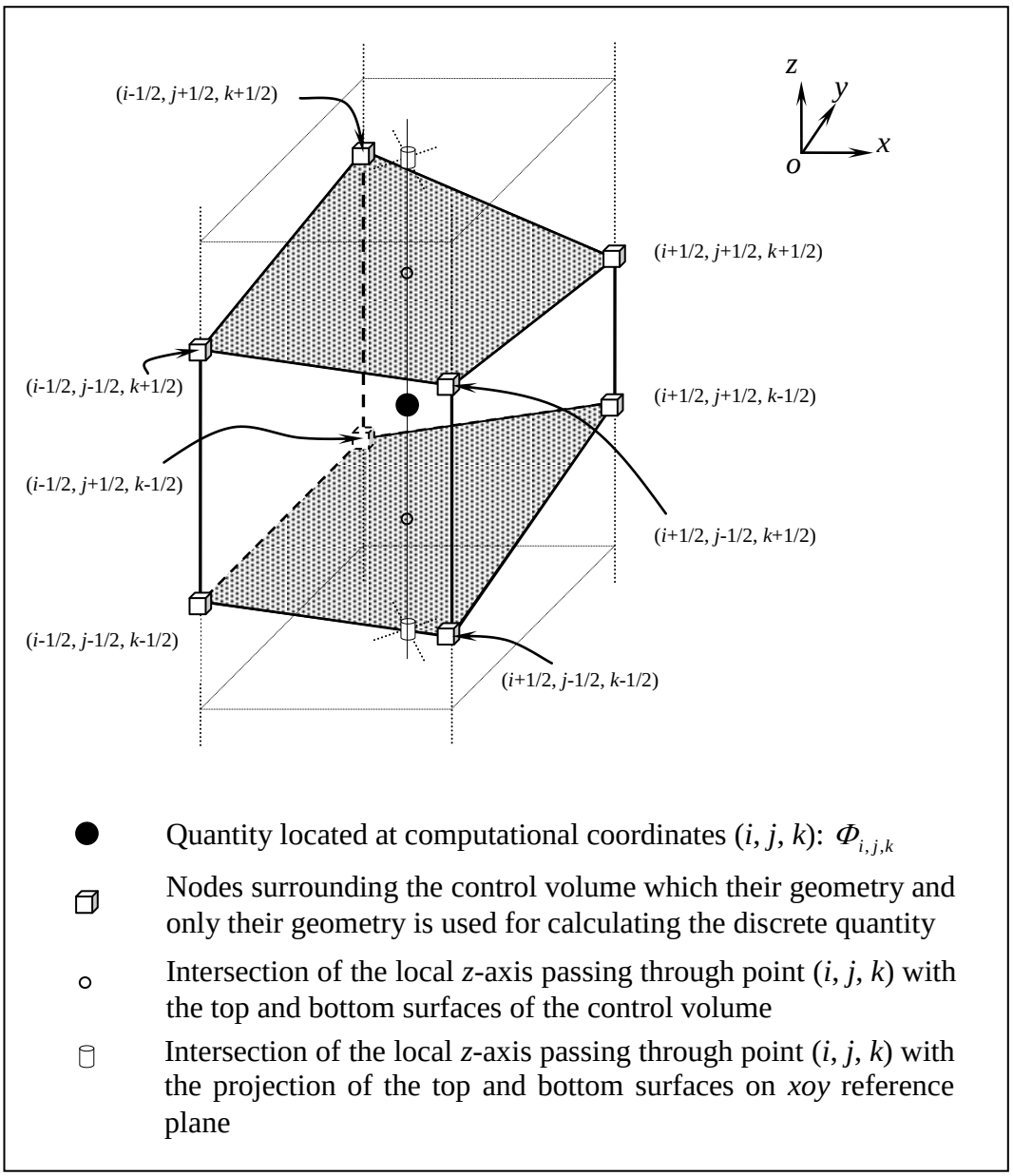

Figure (4.7) - Typical control volume ($\Omega_{i,j,k}$) for discretisation of quantities

This is the general formulation of the finite volume method. For each of the quantities contributed in flow and species concentration equations, as well as the turbulence model equations, the control volumes were specified and the fluxes passing through the cell faces were calculated.

The features which distinguish the interpretation of finite volume methods from the finite difference and finite element approaches can be demonstrated by equation (4.37) and figure (4.7). The finite volume method has a clear advantage over a finite difference method if the physical domain is highly irregular and complicated, since arbitrary volumes can be utilised to subdivide the physical

domain. Also since the integral equations are solved directly in the physical domain, no coordinate transformation is required (Tannehill et al., 1997).

The distinctive characteristic of the finite volume method is that a balance of some physical quantity is made on the region of the control volume drawn around a grid point. For example the coordinate of point (*i*, *j*, *k*), which is the precise location of the variable Φ inside the control volume $\Omega_{i,j,k}$, do not appear explicitly. Only the coordinates of the corner nodal points are needed to determine the cell volume and side areas. Consequently, $\Phi_{i,j,k}$ is not necessarily attached to a fixed point inside the control volume and can be considered as an average value of the flow variable Φ over the control cell and can be considered as representative of some point inside the cell, for instance, the central point of the cell. The first term of equation (4.37) therefore represents the time rate of change of the averaged flow variable over the selected finite volume. The resulting solution also implies that the integral conservation of quantities such as mass and momentum is exactly satisfied over any group of control volumes and over the whole calculation domain. This characteristic exists for any number of grid points and even the coarse-grid solution exhibits integral balance (Patankar, 1980). In the absence of source terms, the finite volume formulation expresses that the variation of the average value Φ over a time interval Δt is equal to the sum of the fluxes exchanged between neighbouring cells. The algorithm used for the transport terms, advection and diffusion, has taken full advantage of this feature and has been programmed by sweeping through the cell faces and, when calculating the flux through sides, to add the contribution to the flux balance of one cell and subtract it from the flux balance of the adjacent cell. This automatically guarantees global conservation.

4.6 THE SOLUTION METHOD

In this section the numerical approximation for the solution of the continuity and Navier-Stokes equations is presented. These equations are a mixed set of elliptic-parabolic equations that contain the unknowns $\boldsymbol{V}$, p and ρ. v and ρ, which appear in the Navier-Stokes equations, are calculated by turbulence and species concentration transport equations respectively. These equations can be uncoupled from the continuity and momentum equations as they maintain a set of parabolic partial differential equations, so long as velocity is considered to be previously calculated. It

must be noted that the variation of density is independent of pressure (Vreugdenhil, 1994) and is due to variations of salinity. So the main task of the numerical approximation to the solution of the set of the equations remains in determining the appropriate method by which the continuity and momentum equations are solved.

The approaches based on derived variables such as the vorticity-stream function and dual-potential methods lose some of their attractiveness when applied to three-dimensional problems (Hirsch, 1990; Tannehill et al., 1997). Consequently, the incompressible Navier-Stokes equations are most often solved in their primitive-variable form (u, v, w and p). The method of artificial compressibility is a coupled approach of this type, while the pressure correction methods are the uncoupled approach. The distinguishing feature of the latter approach is the use of a derived equation to determine the pressure.

In pressure-correction methods, typically, the momentum equations are solved for the velocity components in an uncoupled manner and the equations are linearised by using values lagged in iteration level for the other unknowns, including pressure. The velocity components are thus computed without using the continuity equation as a constraint. Usually, a Poisson equation is developed for the pressure, or changes in the pressure, that alters the velocity field in a direction such as to satisfy the continuity equation. Such an equation for pressure can be derived from the conservation equations in a rigorous manner.

Due to the points made about the vorticity-stream function approach and the limitations associated with the original method of the artificial pressure (Tannehill et al., 1997), the uncoupled method and then the fractional-step method, which basically belongs to the pressure-correction family methods, has been chosen for solving the set of the equations in this study.

4.6.1 *Pressure-correction Methods*

The general pressure-correction method is characterised by a formulation in which the momentum equations are solved sequentially for the velocity components using the best available estimate for the pressure distribution. Such a procedure does not yield a velocity field that satisfies the continuity equation unless the correct pressure distribution is employed. The variety of the methods differ primarily in the algorithms used to solve the component equations and the strategies employed to develop an equation to be solved for an improved pressure, which most often is a

Poisson equation. Some of the most commonly used variations of the pressure-correction methods are the SIMPLE family methods and the fractional-step methods.

In the SIMPLE family of methods the procedure is based on a cyclic series of guess-and-correct operations to solve the governing equations. The velocity components are first calculated from the momentum equations using an initiail pressure field. The pressure and velocities are then corrected, so as to satisfy the continuity equation. This procedure continues until the solution converges. The main distinction between this method and the projection methods is in the way in which the pressure and velocity corrections are achieved.

The SIMPLE algorithm is a semi-implicit scheme based on the general pressure correction idea to satisfy the momentum and continuity conservation equations as well as the equations containing the quantities which influence the flow field (e.g. turbulence quantities and species concentration) at the end of each time step when a converged solution is obtained. A comprehensive discussion on the pressure-correction equation has been presented in Patankar (1980). One major point of this discussion is that the omission of the term representing an implicit influence of the pressure correction on velocity from the equation leading to the velocity-correction equation does not ultimately affect the results. The omission of this term is in favour of avoiding the involvement of the pressure correction at all grid points in the calculation domain in the velocity-correction equation. This involvement would lead to direct solution of the set of the momentum and continuity equations, which does not follow the original idea of the SIMPLE algorithm. The omission of the implicit influence term of the pressure correction on velocity explains the name which has been given to the SIMPLE algorithm. A great many number of studies for two- and three-dimensional problems have been based on SIMPLE family methods. For instance, Zhou (1995) used a modified SIMPLE-like algorithm to treat the velocity-depth coupling in a depth-averaged model and Sung et al. (1999) used a Chorin-type SIMPLE algorithm. Ouillon and Dartus (1997) and Stansby and Zhou (1998) also used SIMPLE family algorithms.

A revised algorithm to improve the rate of convergence for a faster solution has been proposed by Patankar (1981). The motive behind the revised algorithm lies in overcoming the problems associated with the approximation made in the derivation of the pressure-correction equation, which were introduced by the omission of the term representing the implicit influence of the pressure correction on velocity. This

omission leads to exaggerated pressure corrections, which the latter in turn lead to obtaining an early and correct velocity field, but also result in many iterations before a converged pressure field is established. The revised algorithm, SIMPLER, consists of solving the pressure equation to obtain the pressure field and solving the pressure-correction equation only to correct the velocities. One iteration of the SIMPLER algorithm involves about 30% more computational effort (Patankar, 1981), but it requires fewer iterations for convergence. On the whole the computational time required for convergence by the SIMPLER algorithm is noticeably less than SIMPLE algorithm. Other pressure-correction methods (e.g. SIMPLEC) can be found in Versteeg and Malalasekera (1995).

4.6.1.1 Projection (Fractional-step) Methods

Many variations to this type of splitting the solution procedure have been suggested, among them are the time-splitting approach used for solving the compressible Navier-Stokes equations (Batten et al., 1996), split operator approach (Komatsu et al. ,1997; Yu and Li, 1998; Lin and Li, 2002), semi-implicit time-splitting (Zhou and Stansby, 1999), and the method proposed by Chorin (1968) and Temam (1969) which is known as the projection method, or the method of fractional steps. The method may generally be accomplished in two steps. The pressure gradient terms are omitted from the momentum equations in the first step, and the unsteady equations are advanced in time to obtain a provisional velocity $\boldsymbol{V}^*$. In the second step, the provisional velocity is corrected by accounting for the pressure gradient and the continuity equation as follows:

$$\frac{\boldsymbol{V}^{n+1} - \boldsymbol{V}^*}{\Delta t} + \nabla p^{n+1} = 0 \tag{4.38}$$

subject to the continuity constraint:

$$\mathrm{div}\,\boldsymbol{V}^{n+1} = 0 \tag{4.39}$$

By taking the divergence of equation (4.38), subject to the continuity constraint (Eq. 4.39), a Poisson equation is obtained:

$$\nabla^2 p^{n+1} = \frac{\mathrm{div}\,\boldsymbol{V}^*}{\Delta t} \tag{4.40}$$

The solution procedure consists of first computing $\boldsymbol{V}^*$ from the momentum equations while neglecting the pressure gradient terms. The pressure Poisson

equation is then solved for the pressure field, after which the velocities are computed from equation (4.38). E and Liu (1995) provided a comprehensive discussion on projection methods.

Fractional-step (projection) methods have been widely studied for solving the incompressible Navier-Stokes equations. Casulli and Stelling (1998) considered the hydrostatic and the dynamic components of the pressure separately in a two-step method. Daubert et al. (1982) and Daubert and Cahouet (1984) used a three-step fractional method. Four-step fractional methods were used in the studies of Choi et al. (1997) and Sung et al. (2000). Blasco et al. (1998) studied a first-order-accurate method in time and Brown et al. (2001) studied accurate projection methods. A variety of projection methods were studied by Vincent and Caltagirone (1999), Minev (2001) and Chang et al. (2002). Armfield and Street (2003) studied the pressure accuracy of fractional-step methods. The method of algebraic splitting was used by Henriksen and Holmen (2002), which can be seen as the matrix equivalent of the fractional-step or projection method.

A fractional-step method has been used in the present study. However the scheme that has been deployed for three-dimensional problems and in conjunction with the provisional velocity fields, obtained from the computation of the advection and the diffusion terms, together with the variable density and eddy viscosity, is a novel approach for solving the three-dimensional stratified flow problems in ALE by the projection (fractional-step) method.

4.6.2 *Numerical Approximation*

The solution method is described. For discretising the equations a temporal discretisation is presented first, followed by a spatial discretisation in the favour of generality and conciseness.

The computational procedure of the solution of continuity and Navier-Stokes equations consists of a total number of twenty four fractional-steps for the three-dimensional problem. The fractional-step method combined with alternating direction implicit (ADI) method resulted in a locally one-dimensional (LOD) or fractional splitting approximation for the transport terms and two-dimensional solution to the Poisson equation. The validity and accuracy of the split formulae is demonstrated in Lapidus and Pinder (1982).

4.6.2.1 In the Domain

Firstly the entire procedure is split into two main fractional-steps, which constitute an alternating direction implicit (ADI) form algorithm. This idea has been used in a number of numerical models (e.g. DIVAST, originally developed by Falconer, 1980b, 1984). In the following parts each of these two main fractional-steps is referred as one half-time-step. The ADI algorithm provides a three-dimensional implicit scheme, but considering one vertical plane implicitly for each half-time-step which requires the solution of a two-dimensional block tri-diagonal matrix for each direction for each half-time-step. The planes in alternate directions, which are swept in one complete time-step, form the columns and rows of the projection of the whole domain on the *xoy* reference plane as has been demonstrated in figure (4.4). In other words the three-dimensional procedure is accomplished by sweeping all the vertical planes in, for instance, *x*-direction for the first half-time-step and sweeping all the vertical planes in, therefore, *y*-direction for the second half-time-step. The numerical procedure for each of the two half-time-steps has been described in the following paragraphs.

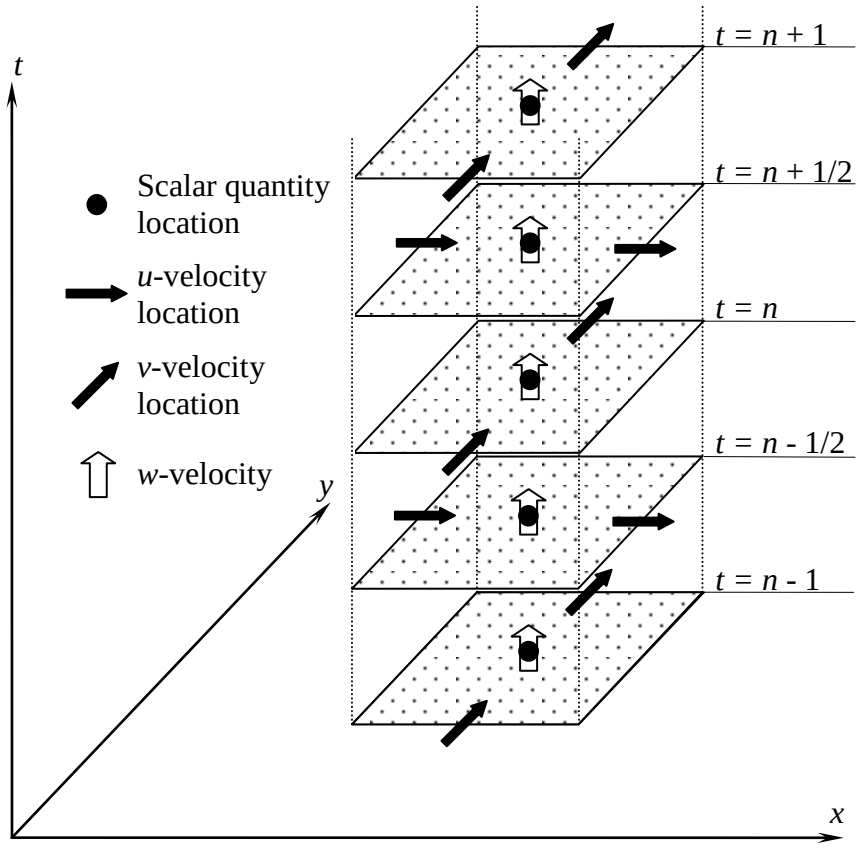

Figure (4.8) - Temporal levels of calculation of the unknowns

In the first half-time-step, for instance, the *u*- and *w*-momentum equations are solved together with continuity equation. In the second half-time-step, therefore, the *v*-momentum equation and again *w*-momentum and continuity equations are solved. In each half-time-step the alternate horizontal velocity component has an explicit contribution to the solution. *w* and pressure are calculated in both half-time-steps. This has been illustrated in figure (4.8) in which the *z*-direction spatial coordinate has been replaced by time to demonstrate the temporal procedure of the solution and therefore the *z*-component of the velocity (*w*), originally located at points half-way between the pressure points (or in general; scalar quantity locations) in the *z*-direction, has been demonstrated at the same location as the pressure. Recalling figures (4.4) and (4.5), the vertical planes do not necessarily have same dimensions in either direction. In general the vertical planes can be characterised by:

- The *xoz* planes with an arbitrary length and an independent longitudinal location with respect to the neighbouring planes in *x*-direction.
- The *yoz* planes with an arbitrary width and an independent transverse location with respect to the neighbouring planes in *y*-direction.

This provides better and more accurate boundary-fitting in the horizontal plane, especially in irregular geometries, and facilitates consideration of islands, or permanently dry zones in the domain without any discontinuity. Therefore any vertical plane in either direction contains only wet cells.

Secondly the time advancement of each half-time-step is decomposed into two fractional-time-steps and instead of simultaneously satisfying two of the momentum equations and the continuity equation, the method proceeds, for example for the first half-time-step, as follows:

- The first fractional-step, which includes advective and diffusive terms, consists of finding , providing that $\boldsymbol{V}^{n}$ is known, an intermediate or provisional velocity, $\boldsymbol{V}^{*}$:

$$\frac{\boldsymbol{V}^{*}-\boldsymbol{V}^{n-1/2,n}}{\delta t}+\operatorname{div}\left(\boldsymbol{V}\otimes\boldsymbol{V}\right)^{n-1/2,n} = \operatorname{div}\left[\nu_{T}^{n}\cdot\operatorname{grad}\left(\left(1-\theta_{D}\right)\boldsymbol{V}^{n-1/2,n}+\theta_{D}\,\boldsymbol{V}^{*}\right)\right]-w_{g}^{n}\left(\frac{\partial\boldsymbol{V}}{\partial z}\right)^{n-1/2,n} \tag{4.41}$$

in which δt is the time increment and the superscript *n* denotes the time level; $t_n = n\cdot\Delta t$. Double superscripts of *n* (i.e. *n*-1/2, *n*) denote that the components of velocity which were last updated at (*n*-1/2) and *n* time levels, have contributed to

the $\boldsymbol{V}$ velocity. So for the solution of the first half-time-step in the *x*-direction, for example, *u* which was last updated at time level (*n*-1/2) and *v* and *w* which were last updated at time level *n* are used. θ_D is the implicit weighting factor for the diffusion, where $\theta = 1$ implies a fully implicit diffusion solution and $\theta = 0$, denotes a fully explicit diffusion solution. The first step of the method can be thought of as a Burgers' equation.

- The second fractional-step makes use of the Hodge decomposition theorem, which states that any vector function can be decomposed into a divergence-free part plus the gradient of a scalar potential (Brown, 2001). So the second step proceeds by solving the Poisson equation as follows:

$$\nabla^2 p^{n+1/2} = \frac{\operatorname{div} \boldsymbol{V}^*}{\delta t} \tag{4.42}$$

and then computing $\boldsymbol{V}^{n+1/2}$ as:

$$\frac{\boldsymbol{V}^{n+1/2} - \boldsymbol{V}^*}{\delta t} + \nabla p^{n+1/2} = 0 \tag{4.43}$$

Thirdly, the first fractional-step of each half-time-step is further split into two sub-fractional-steps, so that allowing for separately computing of advective and diffusive terms. This approach allows the use of suitable approximation for each term. Therefore equation (4.41) is split into two equations which are computed sequentially as follows:

$$\left.\begin{aligned} &\frac{\boldsymbol{V}^{n \xrightarrow{A} n+1/2} - \boldsymbol{V}^{n-1/2,n}}{\delta t} + \operatorname{div}\left(\boldsymbol{V} \otimes \boldsymbol{V}\right)^{n-1/2,n} - w_g^n \left(\frac{\partial \boldsymbol{V}}{\partial z}\right)^{n-1/2,n} = 0 \\ &\frac{\boldsymbol{V}^* - \boldsymbol{V}^{n \xrightarrow{A} n+1/2}}{\delta t} = \operatorname{div}\left[\nu_T^n \cdot \operatorname{grad}\left(\left(1-\theta_D\right)\boldsymbol{V}^{n \xrightarrow{A} n+1/2} + \theta_D \boldsymbol{V}^*\right)\right] \end{aligned}\right\} \tag{4.44}$$

In the first equation symbol $(n \longrightarrow n+1/2)$ denotes that the computation is taking place to update the $\boldsymbol{V}$ value in the time interval $(t, t+1/2\delta t)$. "*A*" stands for advection and its appearance denotes that the value corresponds to the time level after the advection process is completed in the time interval $n \longrightarrow n+1/2$. In the second equation, the same definition applies.

Fourthly the advective contribution of the transport term in equation (4.44) is further split into three sub-sub-fractional-steps. For the first half-time-step (i.e.

considering *u*- and *w*-momentum equations to be solved) and for the *x*-component of velocity (*u*) this sub-fractional-time-step comprises of:

$$\left.\begin{aligned}
&\frac{u^{n\xrightarrow{\mathbf{A}_x}n+1/2}-u^{n-1/2}}{\Delta t}+\frac{\partial}{\partial x}\left(u^2\right)^n+\frac{1}{2}\frac{\partial}{\partial y}\left(v^n\,u^{n-1/2}\right)=0\\
&\frac{u^{n\xrightarrow{\mathbf{A}_{x,z}}n+1/2}-u^{n\xrightarrow{A_x}n+1/2}}{\Delta t}+\frac{1}{2}\frac{\partial}{\partial y}\left(v^n\,u^{n-1/2}\right)+\frac{\partial}{\partial z}\left(w^n\,u^{n\xrightarrow{A_x}n+1/2}\right)=0\\
&\frac{u^{n\xrightarrow{\mathbf{A}}n+1/2}-u^{n\xrightarrow{A_{x,z}}n+1/2}}{\Delta t}-w_g^n\left(\frac{\partial u}{\partial z}\right)^{n\xrightarrow{A_{x,z}}n+1/2}=0
\end{aligned}\right\} \qquad (4.45)$$

A_x denotes the time level after the advection process in *x*-direction is completed, $A_{x,z}$ denotes the time level of completion of the advection in both *x* and *z* directions, and *A* denotes the time level of completion of the whole advection process including the grid velocity. The treatment for the *z*-velocity component (*w*), however, is somehow different. *w* is computed in both half-time-steps, therefore its time advancement should be halved. This also applies for the advection of all scalar quantities. There exist two strategies:

- The advection of *w* in all directions is only advanced one half-time-step. This scheme involves the newly updated *u*-velocity for the first half-time-step but employs the *v*-velocity from the previous half-time-step and vice versa for the second half-time-step.
- The advection of *w* in the *x*- and *y*-directions, terms $\partial wu/\partial x$ and $\partial wv/\partial y$ respectively, is advanced for a full-time-step at their own share of each half-time-step and only its advection in the *z*-direction, term $\partial w^2/\partial z$, is advanced a half-time-step. This scheme involves the newly updated *u* and *v* velocities and therefore uses the more implicit values than the previous scheme.

The diffusive contribution is split into two sub-sub-fractional steps. For the first half-time-step, considering *u*- and *w*-momentum equations to be solved, and for the *x*-component of velocity (*u*) the diffusion sub-fractional-step comprises of equation (4.46) in which "*D*" stands for diffusion. D_x denotes the time level of completion of diffusion process in *x*-direction and *D* denotes the time level of the completion of the whole diffusion process (i.e. D_x and D_z). For the treatment of *z*-velocity component same discussion which was provided for the advection of *w* applies.

$$\left.\begin{aligned}
&\frac{u^{n\xrightarrow{D_x}n+1/2}-u^{n\xrightarrow{A}n+1/2}}{\Delta t}\\
&=\frac{\partial}{\partial x}\left[\nu_T^n\left((1-\theta_D)\frac{\partial}{\partial x}\left(u^{n\xrightarrow{A}n+1/2}\right)+\theta_D\frac{\partial}{\partial x}\left(u^{n\xrightarrow{D_x}n+1/2}\right)\right)\right]\\
&+\frac{1}{2}\frac{\partial}{\partial y}\left[\nu_T^n\frac{\partial}{\partial y}\left(u^{n-1/2}\right)\right]\\
&\frac{u^{n\xrightarrow{D}n+1/2}-u^{n\xrightarrow{D_x}n+1/2}}{\Delta t}=\frac{1}{2}\frac{\partial}{\partial y}\left[\nu_T^n\frac{\partial}{\partial y}\left(u^{n-1/2}\right)\right]\\
&+\frac{\partial}{\partial z}\left[\nu_T^n\left((1-\theta_D)\frac{\partial}{\partial z}\left(u^{n\xrightarrow{D_x}n+1/2}\right)+\theta_D\frac{\partial}{\partial z}\left(u^{n\xrightarrow{D}n+1/2}\right)\right)\right]
\end{aligned}\right\} \tag{4.46}$$

4.6.2.2 On the Free Surface

On the free surface a special treatment is applied. The pressure within the top layer has been defined with a hydrostatic pressure assumption as follows:

$$p_{\left(z=\eta-\frac{\delta z}{2}\right)}=\rho_r\, g\,\eta+P_a+(\rho-\rho_r)\,g\,\frac{\delta z}{2} \tag{4.47}$$

where P_a is the atmospheric pressure acting on the free surface. By defining (Namin et al., 2001):

$$P=\frac{p}{\rho_r} \tag{4.48}$$

then the pressure within the top layer becomes:

$$P_{\left(z=\eta-\frac{\delta z}{2}\right)}=g\,\eta+\frac{P_a}{\rho_r}+\left(\frac{\rho}{\rho_r}-1\right)g\,\frac{\delta z}{2} \tag{4.49}$$

The free surface equation is obtained by integrating the continuity equation over the depth with the kinematic conditions at the bed and free surface as follows:

$$\frac{\partial\eta}{\partial t}-\frac{\partial z_b}{\partial t}+\frac{\partial}{\partial x}\int_{z_b}^{\eta}u\,\mathrm{d}z+\frac{\partial}{\partial y}\int_{z_b}^{\eta}v\,\mathrm{d}z=0 \tag{4.50}$$

in which z_b is bed elevation above datum. For a fixed bed, the second term in equation (4.50) is equal to zero.

Equations (4.51) and (4.52) show the integrated temporal procedure of the solution in the domain and on the free surface for the first half-time-step respectively. θ scheme is used for the pressure in the domain (θ_P) and for the

velocity on the free surface (θ_η), which are the implicit weighting factors, where θ = 1 implies a fully implicit solution and θ = 0, denotes a fully explicit solution. Casulli and Cattani (1994) used a θ scheme without the dynamic contribution of the pressure term and demonstrated that the semi-implicit form (θ = 1/2) was non-dissipative for a linearised one-dimensional problem without viscosity or diffusion, while the implicit form (θ = 1) showed undesirable dissipation. In these equations two time levels at the left-hand side of arrows denote that the values from the corresponding time levels have contributed in the computation. For the second half-time-step similar equations apply. A brief flowchart which is presented in figure (4.9) summarises the main parts and the structure of the model.

$$\left.\begin{aligned}
&\text{Momentum:}\\
&\frac{\boldsymbol{V}^{n+1/2}-\boldsymbol{V}^{n-1/2,\,n\xrightarrow{D}n+1/2}}{\delta t}+\operatorname{div}\left(\boldsymbol{V}\otimes\boldsymbol{V}\right)^{n-1/2,\,n\xrightarrow{A}n+1/2}-w_g^n\left(\frac{\partial \boldsymbol{V}}{\partial z}\right)^{n-1/2,\,n\xrightarrow{A}n+1/2}\\
&=\frac{1}{\rho^n}\boldsymbol{F}^{\,n-1/2,\,n\xrightarrow{D}n+1/2}-\operatorname{grad}\left[\theta_P\,P^{n+1/2}+\left(1-\theta_P\right)P^n\right]+\boldsymbol{g}\left(\frac{\rho^n}{\rho_r}-1\right)\\
&+\operatorname{div}\left[\nu_T^n\cdot\operatorname{grad}\left(\left(1-\theta_D\right)\boldsymbol{V}^{\,n-1/2,\,n\xrightarrow{A}n+1/2}+\theta_D\,\boldsymbol{V}^{\,n-1/2,\,n\xrightarrow{D}n+1/2}\right)\right]\\
&\text{Continuity:}\\
&\operatorname{div}\boldsymbol{V}^{\,n,n+1/2}=0
\end{aligned}\right\}\quad(4.51)$$

$$\left.\begin{aligned}
&\frac{\eta^{n+1/2}-\eta^n}{0.5\delta t}+\frac{\partial}{\partial x}\int_{z_b}^{\eta}\left[\theta_\eta\,u^{n+1/2}+\left(1-\theta_\eta\right)u^{\,n-1/2\xrightarrow{D}n+1/2}\right]\mathrm{d}z+\frac{\partial}{\partial x}\int_{z_b}^{\eta}v^n\,\mathrm{d}z=0\\
&\eta^{n+1/2}=\frac{1}{g}P^{n+1/2}_{\left(z=\eta-\frac{\delta z}{2}\right)}-\left(\frac{\rho^n}{\rho_r}-1\right)\frac{\delta z}{2}\\
&w^{n+1/2}_{(z=\eta)}=\frac{\eta^{n+1/2}-\eta^n}{0.5\delta t}+u^{n+1/2}_{\left(z=\eta-\delta z/2\right)}\cdot\left(\frac{\partial\eta}{\partial x}\right)^{n+1/2}+v^n_{\left(z=\eta-\delta z/2\right)}\cdot\left(\frac{\partial\eta}{\partial y}\right)^n
\end{aligned}\right\}\quad(4.52)$$

4.6.2.3 Temporal Discretisation

Temporal discretisation of the complete set of the equations is provided in equations (4.53-4.62) for the first half-time-step. For the second half-time-step similar equations apply. The equations consist of continuity and momentum equations, free surface water elevation, species concentration conservation and turbulence model transport equations.

Figure (4.9) - Flowchart of the program

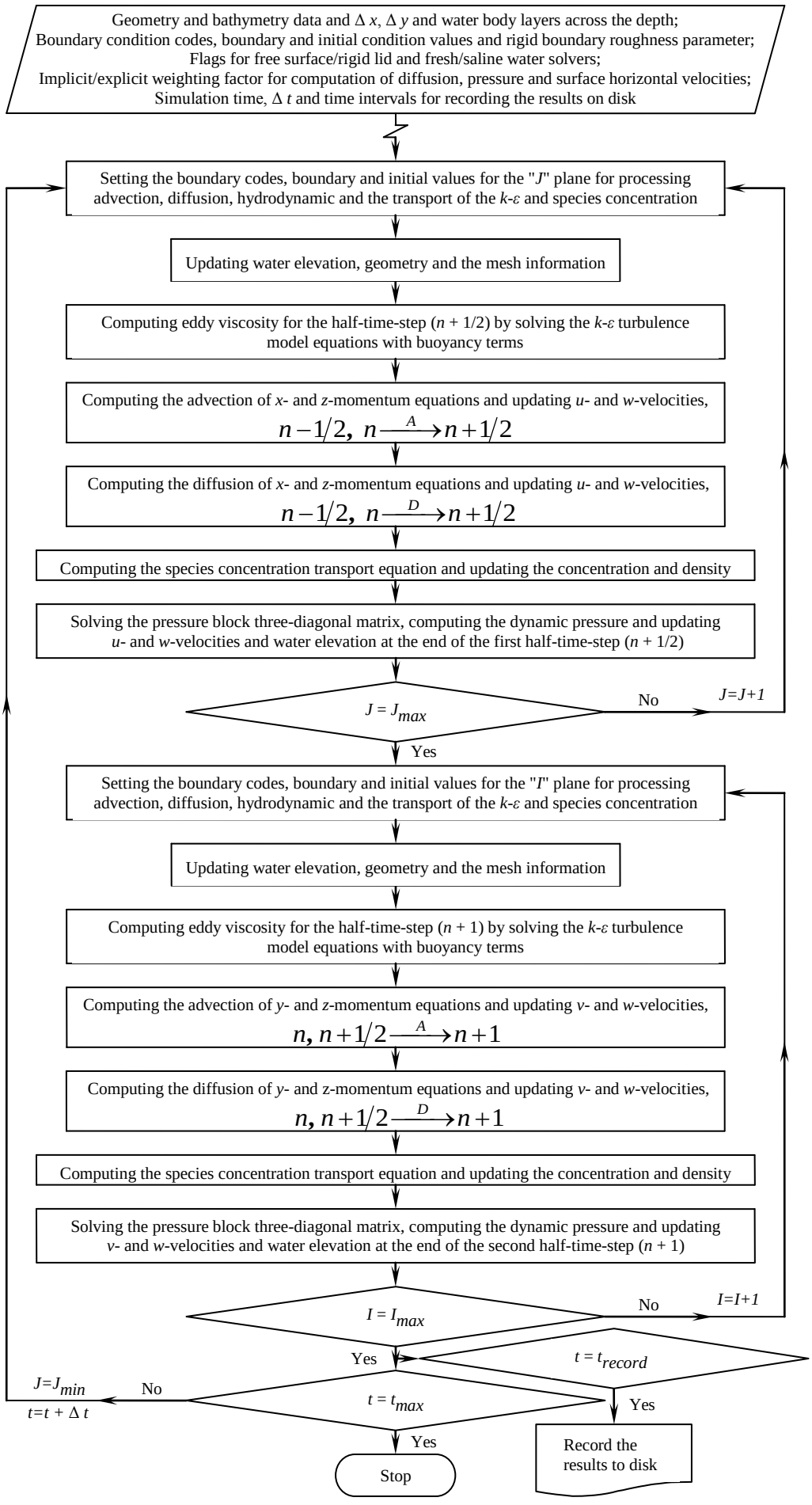

x-momentum equation at half-time-step (*n* + 1/2):

$$
\begin{aligned}
&\frac{u^{n+1/2} - u^{n-1/2 \xrightarrow{D} n+1/2}}{\Delta t} + \\
&\frac{\partial}{\partial x}\left(u^2\right)^{n-1/2} + \frac{\partial}{\partial y}\left(v^n\, u^{n-1/2}\right) + \frac{\partial}{\partial z}\left(w^n\, u^{n-1/2 \xrightarrow{A_x} n+1/2}\right) - w_g^n\, \frac{\partial}{\partial z}(u)^{n-1/2 \xrightarrow{A} n+1/2} \\
&= -\frac{1}{\rho^n}\, f\, u^{n-1/2 \xrightarrow{D} n+1/2} - \frac{\partial}{\partial x}\left[\theta_P\, P^{n+1/2} + (1-\theta_P) P^n\right] + \\
&\left(\frac{\partial}{\partial x}\right)\left[\nu_T^n \cdot \frac{\partial}{\partial x}\left((1-\theta_D)\, u^{n-1/2 \xrightarrow{A} n+1/2} + \theta_D\, u^{n-1/2 \xrightarrow{D_x} n+1/2}\right)\right] + \\
&\left(\frac{\partial}{\partial y}\right)\left[\nu_T^n \cdot \frac{\partial}{\partial y}\left(u^{n-1/2}\right)\right] + \\
&\left(\frac{\partial}{\partial z}\right)\left[\nu_T^n \cdot \frac{\partial}{\partial z}\left((1-\theta_D)\, u^{n-1/2 \xrightarrow{D_x} n+1/2} + \theta_D\, u^{n-1/2 \xrightarrow{D} n+1/2}\right)\right]
\end{aligned}
\tag{4.53}
$$

z-momentum equation at half-time-step (*n* + 1/2):

$$
\begin{aligned}
&\frac{w^{n+1/2} - w^{n \xrightarrow{D} n+1/2}}{0.5\Delta t} + \\
&\frac{\partial}{\partial x}\left(u^{n-1/2}\, w^n\right) + \frac{\partial}{\partial y}(v\, w)^n + \frac{\partial}{\partial z}\left(w^2\right)^n - w_g^n\, \frac{\partial}{\partial z}(w)^{n \xrightarrow{A} n+1/2} \\
&= -\frac{\partial}{\partial z}\left[\theta_P\, P^{n+1/2} + (1-\theta_P) P^n\right] - g\left(\frac{\rho^n}{\rho_r} - 1\right) + \\
&\left(\frac{\partial}{\partial x}\right)\left[\nu_T^n \cdot \frac{\partial}{\partial x}\left((1-\theta_D)\, w^{n \xrightarrow{A} n+1/2} + \theta_D\, w^{n \xrightarrow{D_x} n+1/2}\right)\right] + \\
&\left(\frac{\partial}{\partial y}\right)\left[\nu_T^n \cdot \frac{\partial}{\partial y}\left(w^n\right)\right] + \\
&\left(\frac{\partial}{\partial z}\right)\left[\nu_T^n \cdot \frac{\partial}{\partial z}\left((1-\theta_D)\, w^{n \xrightarrow{D_x} n+1/2} + \theta_D\, w^{n \xrightarrow{D} n+1/2}\right)\right]
\end{aligned}
\tag{4.54}
$$

Continuity equation at half-time-step (*n* + 1/2):

$$
\left(\frac{\partial u}{\partial x}\right)^{n+1/2} + \left(\frac{\partial v}{\partial y}\right)^n + \left(\frac{\partial w}{\partial z}\right)^{n+1/2} = 0 \tag{4.55}
$$

Water elevation and *z*-velocity at water surface at half-time-step (n + 1/2):

$$\left.\begin{aligned} \frac{\eta^{n+1/2}-\eta^{n}}{0.5\delta t}+\sum_{k=1}^{k_{max}}\frac{\partial}{\partial x}\left[\theta_\eta\, u_k^{n+1/2}+\left(1-\theta_\eta\right)u_k^{n-1/2}\right]\mathrm{d}z+\sum_{k=1}^{k_{max}}\frac{\partial}{\partial y}v_k^{n}\,\mathrm{d}z=0 \\ \eta^{n+1/2}=\frac{1}{g}P^{n+1/2}_{\left(z=\eta-\frac{\delta z}{2}\right)}-\left(\frac{\rho^{n}}{\rho_r}-1\right)\frac{\delta z}{2} \\ w^{n+1/2}_{(z=\eta)}=\frac{\eta^{n+1/2}-\eta^{n}}{0.5\delta t}+u^{n+1/2}_{\left(z=\eta-\delta z/2\right)}\cdot\left(\frac{\partial\eta}{\partial x}\right)^{n+1/2}+v^{n}_{\left(z=\eta-\delta z/2\right)}\cdot\left(\frac{\partial\eta}{\partial y}\right)^{n} \end{aligned}\right\} \tag{4.56}$$

Species concentration equation at half-time-step (n + 1/2):

$$\begin{aligned} &\frac{C^{n+1/2}-C^{n}}{\Delta t}+\frac{\partial}{\partial x}\left(u^{n-1/2\xrightarrow{D}n+1/2}\,C^{n}\right)+\frac{1}{2}\frac{\partial}{\partial z}\left(w^{n\xrightarrow{D}n+1/2}\,C^{n\xrightarrow{A_x}n+1/2}\right) \\ &-\frac{1}{2}w_g^{n}\,\frac{\partial}{\partial z}\left(C^{n\xrightarrow{A}n+1/2}\right) \\ &=+\quad\frac{\partial}{\partial x}\left[\nu_T^{n}\,\frac{\partial}{\partial x}\left(\left(1-\theta\right)C^{n\xrightarrow{A}n+1/2}+\theta\,C^{n\xrightarrow{D_x}n+1/2}\right)\right] \\ &+\frac{1}{2}\frac{\partial}{\partial z}\left[\nu_T^{n}\,\frac{\partial}{\partial z}\left(\left(1-\theta\right)C^{n\xrightarrow{D_x}n+1/2}+\theta\,C^{n\xrightarrow{D}n+1/2}\right)\right] \end{aligned} \tag{4.57}$$

The equation of state gives the density at half-time-step (n + 1/2):

$$\rho^{n+1/2}=f\left(C^{n+1/2}\right) \tag{4.58}$$

The temporal discretisation of the transport equations of turbulence model for half-time-step (n + 1/2) is same as the species concentration equation for which the temporal discretisation of the variables P, G and β are as follows:

$$P^{n}=\nu_T^{n}\left[2\left(\frac{\partial u^{n-1/2}}{\partial x}\right)^2+\left(\frac{\partial w^{n}}{\partial z}\right)^2+\left(\frac{\partial u^{n-1/2}}{\partial z}+\frac{\partial w^{n}}{\partial x}\right)^2+\frac{1}{2}\left(\frac{\partial u^{n-1/2}}{\partial y}+\frac{\partial v^{n}}{\partial x}\right)^2\right] \tag{4.59}$$

$$G^{n}=-\frac{1}{2}\,\beta\,g\,\frac{\nu_T^{n}}{\sigma_T}\,\frac{\partial C^{n}}{\partial z} \tag{4.60}$$

$$\beta=\frac{1}{\rho_r}\,\frac{\partial\rho}{\partial C} \tag{4.61}$$

where β is the rate of change of density due to concentration at time level (n), and therefore the viscosity at half-time-step (n + 1/2) is obtained:

$$\nu_T^{n+1/2}=c_\mu\left(\frac{k^2}{\varepsilon}\right)^{n+1/2} \tag{4.62}$$

These equations involve the velocities from previously updated half-time-step.

4.6.2.4 Spatial Discretisation

The complete presentation of the spatially discretised three-dimensional set of the equations would be very tedious and lengthy. Therefore the strategy involves presenting one example of each term and also demonstrating the mechanism that has been used in the numerical model to optimise the programming and minimise the computational time for processing each term, hence resulting in a more efficient algorithm. Moreover the spatial discretisation is presented for the first half-time-step, therefore following the same pattern used in the previous section, the *x*- and *z*-momentum and continuity equations were involved. For the second half-time-step the relevant equations were accordingly discretised in the exactly same manner.

Recalling equation (4.10), $\boldsymbol{\Phi}$ is now the velocity, $\boldsymbol{V}$, and $\overline{\boldsymbol{F}}$ is the flux tensor, which comprises of advection and diffusion components, $\overline{\boldsymbol{F}}_A$ and $\overline{\boldsymbol{F}}_D$ respectively. Pressure in the equation (4.10) is included in the source term, without restriction to its exact implication. This equation can be written for its three Cartesian components, which then results in all the equations discussed for the flow in Chapter Three and this chapter. Considering the conservative form, the momentum equation in three dimensions that should be discretised, in the absence of source terms, is as follows:

$$\frac{\partial \boldsymbol{V}}{\partial t} + \frac{\partial \boldsymbol{F}_x}{\partial x} + \frac{\partial \boldsymbol{F}_y}{\partial y} + \frac{\partial \boldsymbol{F}_z}{\partial z} = \boldsymbol{Q} \tag{4.63}$$

where $\boldsymbol{V}$, $\boldsymbol{F}_x$, $\boldsymbol{F}_y$, $\boldsymbol{F}_z$ and $\boldsymbol{Q}$ are vectors as follows:

$$\boldsymbol{V} = \begin{bmatrix} u \\ v \\ w \end{bmatrix} \tag{4.64}$$

$$\boldsymbol{F}_x = \begin{bmatrix} u^2 - \nu_T \dfrac{\partial u}{\partial x} + P \\ uv - \nu_T \dfrac{\partial v}{\partial x} \\ uw - \nu_T \dfrac{\partial w}{\partial x} \end{bmatrix}; \quad \boldsymbol{F}_y = \begin{bmatrix} vu - \nu_T \dfrac{\partial u}{\partial y} \\ v^2 - \nu_T \dfrac{\partial v}{\partial y} + P \\ vw - \nu_T \dfrac{\partial w}{\partial y} \end{bmatrix}; \quad \boldsymbol{F}_z = \begin{bmatrix} wu - w_g u - \nu_T \dfrac{\partial u}{\partial z} \\ wv - w_g v - \nu_T \dfrac{\partial v}{\partial z} \\ w^2 - w_g w - \nu_T \dfrac{\partial w}{\partial z} + P \end{bmatrix}$$

(4.65a) (4.65b) (4.65c)

$$\boldsymbol{Q} = \begin{bmatrix} f\,v \\ -f\,u \\ -g\dfrac{\rho - \rho_r}{\rho_r} \end{bmatrix} \tag{4.66}$$

where pressures are now included in $\boldsymbol{F}_x$, $\boldsymbol{F}_y$ and $\boldsymbol{F}_z$. The discretisation for the first line of the equations (4.64-4.66) of the vectorial equation (4.63) is presented here together with the continuity equation. It can be seen from these equations that in all terms either the derivative of a quantity or derivative of a flux is required to be computed and hence needs to be discretised.

Equation (4.63) and its components (Eqs. 4.64-4.66) assume the form of equation (4.36) if they are expressed in integral form and if Φ is replaced by $\boldsymbol{V}$, $\boldsymbol{F}$ by $\overline{\boldsymbol{F}}$ and Q by $\boldsymbol{Q}$ as follows:

$$\frac{\partial}{\partial t}\int_{\Omega} \boldsymbol{V}\, \mathrm{d}\Omega + \oint_{S} \overline{\boldsymbol{F}} \cdot \mathrm{d}\,\boldsymbol{S} = \int_{\Omega} \boldsymbol{Q}\, \mathrm{d}\Omega \tag{4.67}$$

Equation (4.67) can be written in discrete form for a finite volume $\Re$ as follows:

$$\frac{\partial}{\partial t}\left(\boldsymbol{V}_{\Re}\ \Omega_{\Re}\right) + \sum_{\text{sides}}\left(\overline{\boldsymbol{F}} \cdot \boldsymbol{S}\right) = \boldsymbol{Q}_{\Re}\ \Omega_{\Re} \tag{4.68}$$

where $\boldsymbol{V}_{\Re}$ and $\boldsymbol{Q}_{\Re}$ are the values of $\boldsymbol{V}$ and $\boldsymbol{Q}$ associated with the finite volume $\Re$, and the summation is applied to all exterior sides of the finite volume. $\Omega_{\Re}$ is the value of the volume of the finite volume $\Re$. Recalling figure (4.5) and the approximation which was made for the top and the bottom faces of a control volume, it is further assumed that the cell-face surface-area vectors, $\mathrm{d}\,\boldsymbol{S}$, at the top and bottom faces lie in a vertical plane. This assumption simplifies the calculation of the volume of control volume $\Re$. It further eliminates the need for computation of the lateral component of cell-face surface-area vectors for the top and bottom faces. This assumption was thought to have very little influence on the accuracy of the scheme. It may be considered as a finite laterally-averaged geometry. Therefore for the discretisation in *x*- and *y*- directions, the control volumes lying in the reference planes *xoz* and *yoz* were considered. For *z*-direction, depending on which alternating direction was considered, control volumes lay in the corresponding vertical referential planes. Due to the approximation which was made, the control volume for *z*-velocity component (*w*), which in figure (4.5) is located at (*i* +1, *k*-1/2) grid point, is bound by the straight lines connecting the points (*i* +3/2, *k*-1) and (*i* +3/2, *k*), (*i* +3/2, *k*) and (*i* +1/2, *k*), (*i* +1/2, *k*) and (*i* +1/2, *k*-1) and (*i* +1/2, *k*-1) and (*i* +3/2, *k*-1). The control volume for scalar quantities including pressure, which in figure (4.5) is located at (*i*, *k*) grid point, is bound by straight lines connecting points (*i* +1/2, *k*-1/2) and (*i* +1/2, *k* +1/2), (*i* +1/2, *k* +1/2) and (*i*-1/2, *k* +1/2), (*i*-1/2, *k* +1/2) and (*i*-1/2, *k*-

1/2) and (*i*-1/2, *k*-1/2) and (*i* +1/2, *k*-1/2) and leaving the control volume for *x*-velocity component (*u*) unchanged. It is noted, however, that this approximation leaves the *z*-coordinate of the nodal points unchanged. A typical control volume is illustrated in figure (4.10).

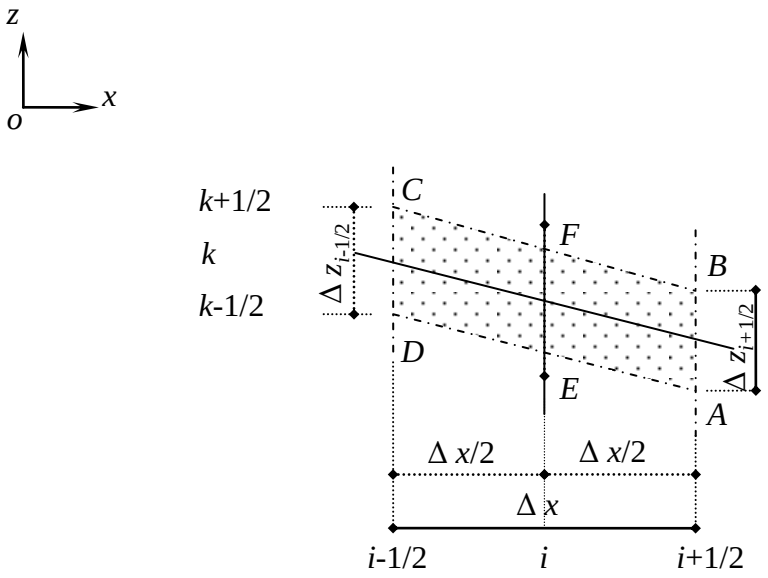

Figure (4.10) - A typical control volume in *xoz* reference plane

With this approximation the discretisation of the equations for each alternating direction only involves the finite volumes lying in the corresponding vertical reference planes, and hence reduces to a geometrically two-dimensional discretisation for each term. This also only requires the computation of the area of a control cell, the area *ABCD* of figure (4.10) for example, instead of the volume of the finite volume $\Re$. Therefore for a quantity of value Φ, equation (4.63), in the absence of source terms, takes the form as follows:

$$\frac{\partial \Phi}{\partial t} + \frac{\partial f_x}{\partial x} + \frac{\partial f_z}{\partial z} = Q \tag{4.69}$$

where f_x and f_z are the Cartesian components of the flux vector $\boldsymbol{F}$.

Applying the same procedure carried out for the three-dimensional problem and considering the control cell *ABCD* of figure (4.10), gives:

$$\frac{\partial}{\partial t}\int_{\Omega_{ik}} \Phi \, \mathrm{d}\Omega + \oint_{ABCD} \left(f_x \, \mathrm{d}z - f_z \, \mathrm{d}x \right) = \int_{\Omega_{ik}} Q \, \mathrm{d}\Omega \tag{4.70}$$

The surface vector has been considered for an integration path around the boundary in a counter-clockwise direction. For side *AB* it is defined as:

$$\boldsymbol{S}_{AB} = \Delta z_{AB}\ \boldsymbol{i} - \Delta x_{AB}\ \boldsymbol{k} = \left(z_B - z_A\right)\boldsymbol{i} - \left(x_B - x_A\right)\boldsymbol{k} \tag{4.71}$$

and then the finite volume equation for cell Ω_{ik} is obtained:

$$\frac{\partial}{\partial t}\left(\Phi\Omega\right)_{ik} + \sum_{ABCD}\left[f_{x\,AB}\left(z_B - z_A\right) - f_{z\,AB}\left(x_B - x_A\right)\right] = \left(Q\Omega\right)_{ik} \tag{4.72}$$

The sum $\sum_{ABCD}$ extends over the four sides of the quadrilateral *ABCD*. The term on the left containing the time derivative was evaluated by assuming that the quantity Φ at point (*i*, *k*) is the mean value for the volume and then using a forward time difference, the expression (4.72) was further approximated as:

$$\begin{aligned}&\left(\frac{\Phi_{i,k}^{n+1} - \Phi_{i,k}^{n}}{\Delta t}\right) S_{ABCD}\\ &+\left[f_{xAB}\left(z_B - z_A\right) + f_{xBC}\left(z_C - z_B\right) + f_{xCD}\left(z_D - z_C\right) + f_{xDA}\left(z_A - z_D\right)\right]\\ &-\left[f_{zBC}\left(x_C - x_B\right) + f_{zDA}\left(x_A - x_D\right)\right] = Q_{i,k}\ S_{ABCD}\end{aligned} \tag{4.73}$$

and

$$S_{ABCD} = \Delta x\left[\left(z_C + z_B + 2z_F\right) - \left(z_D + z_A + 2z_E\right)\right]/\,4 \tag{4.74}$$

is the area of the quadrilateral *ABCD*, which is assumed to be constant, but has been calculated according to figure (4.5) to account for the area of the hexagonal control cells, and $\Phi_{i,k}$ is the average value of Φ in the cell.

The time level at which the fluxes were evaluated, which determines whether the scheme is explicit or implicit, is completely presented for all terms of all equations in temporal discretisation of the equations in previous section.

The evaluation of the flux components along the sides of the control cell depends on the scheme as well as on the location of the flow variables with respect to the mesh. Essentially central and upwind discretisation schemes are distinguished. Central schemes are based on local flux estimations, while upwind schemes determine the cell face fluxes according to the propagation.

As was mentioned, in the discretisation of the equations the numerical cell averages of derivatives of mesh variables are required. A general procedure, valid for an arbitrary control volume, can be derived by application of the divergence theorem. This theorem can be considered as defining the average of the gradient of a scalar Φ as a function of its values at the boundaries of the volume under consideration. For an arbitrary volume Ω there exists:

$$\int_{\Omega} \nabla\Phi\ \mathrm{d}\,\Omega = \oint_{S} \Phi\ \mathrm{d}\,\boldsymbol{S} \tag{4.75}$$

where $\boldsymbol{S}$ is the closed boundary surface. The averaged gradients are defined as:

$$\overline{\left(\frac{\partial \Phi}{\partial x}\right)}_{\Omega} \approx \frac{1}{\Omega}\int_{\Omega}\frac{\partial \Phi}{\partial x}\,\mathrm{d}\Omega = \frac{1}{\Omega}\oint_{S}\Phi\ \boldsymbol{i}\cdot\mathrm{d}\boldsymbol{S} \tag{4.76}$$

and

$$\overline{\left(\frac{\partial \Phi}{\partial z}\right)}_{\Omega} \approx \frac{1}{\Omega}\int_{\Omega}\frac{\partial \Phi}{\partial z}\,\mathrm{d}\Omega = \frac{1}{\Omega}\oint_{S}\Phi\ \boldsymbol{k}\cdot\mathrm{d}\boldsymbol{S} \tag{4.77}$$

For two-dimensional control cells after partial integration this leads to the averaged *x*- and *z*-direction gradients as follows:

$$\overline{\left(\frac{\partial \Phi}{\partial x}\right)}_{\Omega} \approx \frac{1}{\Omega}\oint_{S}\Phi\,\mathrm{d}z \tag{4.78}$$

$$\overline{\left(\frac{\partial \Phi}{\partial z}\right)}_{\Omega} \approx -\frac{1}{\Omega}\oint_{S}\Phi\,\mathrm{d}x \tag{4.79}$$

Therefore for the control cell *ABCD* (Fig. 4.10) the approximation for the gradients of Φ in the *x*- and *z*-directions are obtained:

$$\overline{\left(\frac{\partial \Phi}{\partial x}\right)}_{ABCD} \approx \frac{1}{S_{ABCD}}\left[\begin{array}{l}\Phi_{i+\frac{1}{2},k}\left(z_{i+\frac{1}{2},k+\frac{1}{2}}-z_{i+\frac{1}{2},k-\frac{1}{2}}\right)+\Phi_{i,k+\frac{1}{2}}\left(z_{i-\frac{1}{2},k+\frac{1}{2}}-z_{i+\frac{1}{2},k+\frac{1}{2}}\right)\\ +\Phi_{i-\frac{1}{2},k}\left(z_{i-\frac{1}{2},k-\frac{1}{2}}-z_{i-\frac{1}{2},k+\frac{1}{2}}\right)+\Phi_{i,k-\frac{1}{2}}\left(z_{i+\frac{1}{2},k-\frac{1}{2}}-z_{i-\frac{1}{2},k-\frac{1}{2}}\right)\end{array}\right] \tag{4.80}$$

$$\overline{\left(\frac{\partial \Phi}{\partial z}\right)}_{ABCD} \approx \frac{\Delta x}{S_{ABCD}}\left(\Phi_{i,k+\frac{1}{2}}-\Phi_{i,k-\frac{1}{2}}\right) \tag{4.81}$$

With the equations (4.73), (4.74), (4.80) and (4.81) all terms can now be approximated. For the problem under consideration, the main fractional-steps for each half-time-step comprise the advection, the diffusion and the propagation procedure. The fractional-step method made it possible to deploy suitable spatial approximation for each part.

4.6.2.4.1 Advection

The derivative approximation needed to represent the advection was obtained by assuming that the solution to the problem was locally approximated by a polynomial as the shape function of the quantity to be advected. The polynomial was then fitted to the points surrounding the point (*i*, *k*), utilising values of the function at the grid points. In the large Reynolds numbers the flow is effectively advection

dominated (E and Liu, 1995). Hence, to achieve more realistic prediction of the flow characteristics a new fifth-order-accurate scheme has been deployed. It was assumed that both *x*- and *z*-dependency of quantity Φ were expressed by a quadric polynomial. Therefore holding *z* fixed, for example, it was assumed that the quantity Φ varied over five adjacent cells in the *x*-direction. Therefore the quantity Φ at various *x* locations was determined by:

$$\Phi(x, z_0) = a\,x^4 + b\,x^3 + c\,x^2 + d\,x + e \tag{4.82}$$

Five points were used to determine the coefficients of the polynomial. For convenience it was considered that at point (*i*, *k*), *x* = 0. The coefficients *a*, *b*, *c*, *d* and *e* were then evaluated by using five neighbouring points, (*i*-2, *k*), (*i*-1, *k*), (*i*, *k*), (*i* +1, *k*) and (*i* +2, *k*). Concentrating the attention to the one-dimensional solution as each direction is solved in one sub-sub-fractional-step, the coefficients were obtained using the integration of equation (4.83) for the points involved in the scheme, and solving the resulting set of the linear equations.

$$\int_{x_l - \frac{\Delta x}{2}}^{x_l + \frac{\Delta x}{2}} \Phi(x)\,\mathrm{d}x = \Phi_l \cdot \Delta x \qquad \text{for} \quad l = i - 2,\ i - 1,\ i,\ i + 1,\ i + 2 \tag{4.83}$$

The flux passing through face *AB* in figure (4.10) was then evaluated by:

$$f_{x_{i+1/2}} = \frac{1}{\Delta t} \int_{\frac{\Delta x}{2} - u_{i+1/2}\cdot\Delta t}^{\frac{\Delta x}{2}} \Phi(x)\cdot \mathrm{d}x \tag{4.84}$$

If $u > 0$ then $\Phi(x)$ was defined on cells (*i* - 2) - (*i* + 2) and if $u < 0$ then $\Phi(x)$ was defined on cells (*i* - 1) - (*i* + 3), constituting a fifth-order-accurate upstream centred scheme. Since the scheme accounts for the direction of the flow, the transportiveness property (Versteeg and Malalasekera, 1995) required for a numerical scheme is built into the formulation. The comparisons made for this scheme and some most commonly used schemes for advection and few more new schemes are demonstrated in Chapter Five.

The flux for the case $u > 0$ was calculated as follows:

$$f_{x_{i+1/2}} = \frac{\Delta x}{\Delta t} \sum_{l=i-2}^{l=i+2} c_l\,\Phi_l = \frac{\Delta x}{\Delta t}\left(c_{i-2}\Phi_{i-2} + c_{i-1}\Phi_{i-1} + c_i\Phi_i + c_{i+1}\Phi_{i+1} + c_{i+2}\Phi_{i+2}\right) \tag{4.85}$$

in which

$$c_l = m_{1l}\,\beta^5 + m_{2l}\,\beta^4 + m_{3l}\,\beta^3 + m_{4l}\,\beta^2 + m_{5l}\,\beta \tag{4.86}$$

where

$$\beta = u_{i+1/2}\,\frac{\Delta t}{\Delta x} \tag{4.87}$$

and m's are constant coefficients. The influence of a limiter for avoiding the oscillations is demonstrated in Chapter Five. A linear stability analysis for the new scheme is also carried out in Chapter Five. Discretisation of the advection terms of the first line of the equations (4.63-4.66), for example, for the control cell of figure (4.10) to be considered the *x*-velocity (*u*) control cell, proceeded by using equation (4.73) as follows:

$$\begin{aligned}&\left(\frac{u_{i,k}^{n+1/2} - u_{i,k}^{n-1/2}}{\Delta t}\right) S_{ABCD} \\ &+\left[f_{xAB}\left(z_B - z_A\right) + f_{xBC}\left(z_C - z_B\right) + f_{xCD}\left(z_D - z_C\right) + f_{xDA}\left(z_A - z_D\right)\right] \\ &-\left[f_{zBC}\left(x_C - x_B\right) + f_{zDA}\left(x_A - x_D\right)\right] = 0\end{aligned} \tag{4.88}$$

$$S_{ABCD} = \Delta x\left[\left(z_{i-1/2,k+1/2} + z_{i+1/2,k+1/2} + 2z_{i,k+1/2}\right) - \left(z_{i-1/2,k-1/2} + z_{i+1/2,k-1/2} + 2z_{i,k-1/2}\right)\right] / 4 \tag{4.89}$$

in which the second and third terms constitute the *x*- and *z*-component of the fluxes respectively, passing through the sides of the control volume. Discretisation of f_{xAB} is demonstrated by the equations (4.85-4.87) for $u > 0$. For $u < 0$ same discretisation was used with the appropriate shape function definition for $\Phi(x)$. As the strategy involved sweeping each line and computing the fluxes at each face of the control volumes in the corresponding direction, computation of f_{xCD} automatically took place when the computation of the flux passing through the right-hand-side of the cell (*i*-1, *k*) was performed. This was achieved by adding $f_{x_{i-1/2}}$ to the control volume (*i*, *k*) and deducing it from control volume (*i*-1, *k*) for $u > 0$, which assures the global conservation and therefore the conservativeness property essential for a discretisation scheme (Versteeg and Malalasekera, 1995) is fulfilled. f_{xBC} and f_{xDA} were advected in the *z*-direction together with *z*-direction flux components. f_{zBC} and f_{zDA} comprise the term $\frac{\partial}{\partial x}(w\,u)$ whose discretised equations were obtained in the exactly same manner which was explained for f_{xAB}. It must be emphasised that the discretisation presented herein is for a typical control volume (Fig. 4.10) and for each case the

appropriate control volume for *u*, *v*, *w* and the scalar quantity was used. The values of *u* used for the computation of the fluxes in the *x*- and *z*-directions (the values which advect the *u*-velocity value of the control volume *ABCD* and are located at the cell faces) were computed by averaging the *u*-velocity-component values of adjacent cells in *x*- and *z*-directions respectively. The value of *w* for computing the flux in *z*-direction was taken the average of its adjacent *w*-velocity-cells in *x*-direction.

Term $\frac{\partial}{\partial y}(v\,u)$ was advected as source term and was handled together with the diffusion process giving more implicit solution to the *v* velocity contribution of the advective flux of the previous half-time-step. This term was approximated as:

$$\left[\frac{\partial}{\partial y}(vu)\right]_{i,j,k} \approx \frac{1}{S_{i,j,k}}\left[\begin{array}{l} v_{i,j+\frac{1}{2},k}\cdot\left(\frac{u_{i,j,k}+u_{i,j+1,k}}{2}\right)\left(z_{i,j+\frac{1}{2},k+\frac{1}{2}}-z_{i,j+\frac{1}{2},k-\frac{1}{2}}\right) \\ +v_{i,j,k+\frac{1}{2}}\cdot\left(\frac{u_{i,j,k}+u_{i,j,k+1}}{2}\right)\left(z_{i,j-\frac{1}{2},k+\frac{1}{2}}-z_{i,j+\frac{1}{2},k+\frac{1}{2}}\right) \\ +v_{i,j-\frac{1}{2},k}\cdot\left(\frac{u_{i,j,k}+u_{i,j-1,k}}{2}\right)\left(z_{i,j-\frac{1}{2},k-\frac{1}{2}}-z_{i,j-\frac{1}{2},k+\frac{1}{2}}\right) \\ +v_{i,j,k-\frac{1}{2}}\cdot\left(\frac{u_{i,j,k}+u_{i,j,k-1}}{2}\right)\left(z_{i,j+\frac{1}{2},k-\frac{1}{2}}-z_{i,j-\frac{1}{2},k-\frac{1}{2}}\right) \end{array}\right] \tag{4.90}$$

The *v* velocities at corresponding faces were approximated as follows:

$$v_{i,j+\frac{1}{2},k} \approx \frac{v_{i+\frac{1}{2},j+\frac{1}{2},k}+v_{i-\frac{1}{2},j+\frac{1}{2},k}}{2} \quad \text{(4.91a)} \qquad v_{i,j-\frac{1}{2},k} \approx \frac{v_{i+\frac{1}{2},j-\frac{1}{2},k}+v_{i-\frac{1}{2},j-\frac{1}{2},k}}{2} \quad \text{(4.91b)}$$

$$v_{i,j,k+\frac{1}{2}} \approx \frac{\left(\begin{array}{llll} v_{i+\frac{1}{2},j+\frac{1}{2},k} & +v_{i-\frac{1}{2},j+\frac{1}{2},k} & +v_{i+\frac{1}{2},j-\frac{1}{2},k} & +v_{i-\frac{1}{2},j-\frac{1}{2},k} \\ +v_{i+\frac{1}{2},j+\frac{1}{2},k+1} & +v_{i-\frac{1}{2},j+\frac{1}{2},k+1} & +v_{i+\frac{1}{2},j-\frac{1}{2},k+1} & +v_{i-\frac{1}{2},j-\frac{1}{2},k+1} \end{array}\right)}{8} \tag{4.91c}$$

$$v_{i,j,k-\frac{1}{2}} \approx \frac{\left(\begin{array}{llll} v_{i+\frac{1}{2},j+\frac{1}{2},k} & +v_{i-\frac{1}{2},j+\frac{1}{2},k} & +v_{i+\frac{1}{2},j-\frac{1}{2},k} & +v_{i-\frac{1}{2},j-\frac{1}{2},k} \\ +v_{i+\frac{1}{2},j+\frac{1}{2},k-1} & +v_{i-\frac{1}{2},j+\frac{1}{2},k-1} & +v_{i+\frac{1}{2},j-\frac{1}{2},k-1} & +v_{i-\frac{1}{2},j-\frac{1}{2},k-1} \end{array}\right)}{8} \tag{4.91d}$$

and *S* was approximated as follows:

$$S_{i,j,k} = \Delta y\left[\frac{\left(z_{i,j+\frac{1}{2},k+\frac{1}{2}}+z_{i,j-\frac{1}{2},k+\frac{1}{2}}+2z_{i,j,k+\frac{1}{2}}\right)-\left(z_{i,j+\frac{1}{2},k-\frac{1}{2}}+z_{i,j-\frac{1}{2},k-\frac{1}{2}}+2z_{i,j,k-\frac{1}{2}}\right)}{4}\right] \tag{4.92}$$

The term $w_g \dfrac{\partial u}{\partial z}$ was advected in the same manner as the *z*-direction component of advective flux and after the completion of *x*- and *z*-direction advection procedures. w_g for the first half-time-step was discretised as follows:

$$w_{g_{i,k}} = \frac{z_{i,k}^{n} - z_{i,k}^{n-1/2}}{0.5\Delta t} \tag{4.93}$$

4.6.2.4.2 Diffusion

Due to the dissipative nature of the viscous terms, they are almost always discretised using central differences (Tannehill et al., 1997). For the diffusive contribution of transport, the Crank-Nicolson method was employed. However, a variable-weighted implicit approximation has been implemented in the program. Equation (4.73) was used for the evaluation of the diffusion contribution of the transport. The time discretisation of the diffusive term follows the rules set for the diffusion fractional-step as is demonstrated under the temporal discretisation in the previous section. Here the attention is given to the spatial discretisation, and the temporal discretisation of the equation (4.73) has symbolically performed to imply the time advancement. The diffusive fluxes were approximated as follows:

$$\left.\begin{aligned} f_{xAB} &\approx -\nu_{i+1/2,k}\left(\frac{\partial \Phi}{\partial x}\right)_{i+1/2,k} \\ f_{xCD} &\approx -\nu_{i-1/2,k}\left(\frac{\partial \Phi}{\partial x}\right)_{i-1/2,k} \end{aligned}\right\} \tag{4.94}$$

$$\left.\begin{aligned} f_{xBC} &\approx -\nu_{i,k+1/2}\left(\frac{\partial \Phi}{\partial x}\right)_{i,k+1/2} \\ f_{xDA} &\approx -\nu_{i,k-1/2}\left(\frac{\partial \Phi}{\partial x}\right)_{i,k-1/2} \end{aligned}\right\} \tag{4.95}$$

$$\left.\begin{aligned} f_{zBC} &\approx -\nu_{i,k+1/2}\left(\frac{\partial \Phi}{\partial z}\right)_{i,k+1/2} \\ f_{zDA} &\approx -\nu_{i,k-1/2}\left(\frac{\partial \Phi}{\partial z}\right)_{i,k-1/2} \end{aligned}\right\} \tag{4.96}$$

The expression for the net flow of the quantity Φ out of the volume is exact if the derivatives represent suitable average values for the boundaries concerned. The derivative of the quantity Φ, for face (i +1/2, k) for example, is approximated as:

$$\left(\frac{\partial \Phi}{\partial x}\right)_{i+1/2,k} \approx \frac{1}{S_{i+1/2,k}}\left[\begin{aligned} &\Phi_{i+1,k}\left(z_{i+1,k+1/2} - z_{i+1,k-1/2}\right) + \Phi_{i+1/2,k+1/2}\left(z_{i,k+1/2} - z_{i+1,k+1/2}\right) \\ &+\Phi_{i,k}\left(z_{i,k-1/2} - z_{i,k+1/2}\right) + \Phi_{i+1/2,k-1/2}\left(z_{i+1,k-1/2} - z_{i,k-1/2}\right) \end{aligned}\right] \tag{4.97}$$

in which the average quantities for top and bottom faces were used as follows:

$$\left.\begin{aligned} \Phi_{i+1/2,k+1/2} &\approx \frac{1}{4}\left(\Phi_{i,k} + \Phi_{i+1,k} + \Phi_{i,k+1} + \Phi_{i+1,k+1}\right) \\ \Phi_{i+1/2,k-1/2} &\approx \frac{1}{4}\left(\Phi_{i,k} + \Phi_{i+1,k} + \Phi_{i,k-1} + \Phi_{i+1,k-1}\right) \end{aligned}\right\} \tag{4.98}$$

and S was calculated in the same manner as demonstrated before. $\left(\frac{\partial \Phi}{\partial x}\right)$ was discretised for the other faces of the control cell in the same manner. The derivative in the z-direction was approximated, for example for face $(i, k + 1/2)$ as:

$$\left(\frac{\partial \Phi}{\partial z}\right)_{i,k+1/2} \approx \frac{\Delta x}{S_{i,k+1/2}}\left(\Phi_{i,k+1} - \Phi_{i,k}\right) \tag{4.99}$$

The other z-derivative was computed similarly. Like advection, diffusion was also computed locally one-dimensional in sub-sub-fractional-steps as was discussed. Diffusion was computed by the Crank-Nicolson method, therefore the quantities were computed implicitly and more precisely for the Crank-Nicolson method with a diffusion weighting-factor set to 0.5. This needed the solution of a set of equations for each row and column of a vertical plane. As it can be seen from the example given for computing the x-derivatives of the scalar quantity, the resultant equation contains values of the quantity ($\Phi_{i-1,k}$, $\Phi_{i,k}$ and $\Phi_{i+1,k}$) from the k^{th} row, and values of the quantity from the upper and lower rows. In the z-direction, however, the derivatives only contain the values of the i^{th} column ($\Phi_{i,k-1}$, $\Phi_{i,k}$ and $\Phi_{i,k+1}$). Therefore in the solution to the diffusion term in the x-direction the values of upper and lower rows were regarded as source terms and had an explicit contribution of the fluxes from time step n. For the values of the same row as the control cell, a weighting-factor equal to 0.5 was used resulting in the Crank-Nicolson method. For the k^{th} row the matrix of coefficients of unknowns form a tri-diagonal matrix and the set of the equations take the form as equation (4.100). The set of the equations for each row or column were solved by forward elimination and back substitution (double sweep) algorithm (Greenspan and Casulli, 1988) which has excellent round-off characteristics (Lapidus and Pinder, 1982) and requires only $\left[5\left(i_{\max} - i_{\min} + 1\right) - 4\right]$ multiplications or divisions and $\left[3\left(i_{\max} - i_{\min} + 1\right) - 3\right]$ additions or subtractions and has a considerable advantage in CPU time over other methods (Twizell ,1984; Stoer and Bulirsch, 1993).

$$\begin{bmatrix} d_{i_{\min}} & e_{i_{\min}} & & & & \cdots & 0 \\ c_{i_{\min+1}} & d_{i_{\min+1}} & e_{i_{\min+1}} & & & & \vdots \\ & \ddots & \ddots & \ddots & & & \\ & & c_i & d_i & e_i & & \\ & & & \ddots & \ddots & \ddots & \\ \vdots & & & & c_{i_{\max-1}} & d_{i_{\max-1}} & e_{i_{\max-1}} \\ 0 & \cdots & & & & c_{i_{\max}} & d_{i_{\max}} \end{bmatrix} \cdot \begin{bmatrix} \Phi_{i_{\min}} \\ \Phi_{i_{\min+1}} \\ \vdots \\ \Phi_i \\ \vdots \\ \Phi_{i_{\max-1}} \\ \Phi_{i_{\max}} \end{bmatrix} = \begin{bmatrix} b_{i_{\min}} \\ b_{i_{\min+1}} \\ \vdots \\ b_i \\ \vdots \\ b_{i_{\max-1}} \\ b_{i_{\max}} \end{bmatrix} \tag{4.100}$$

Therefore the term $\frac{\partial}{\partial x}\left(\nu_T \frac{\partial u}{\partial x}\right)$, corresponding to the *x*-direction derivative of the diffusion term (Eqs. 4.94 and 4.95) and the term $\frac{\partial}{\partial z}\left(\nu_T \frac{\partial u}{\partial z}\right)$, corresponding to the *z*-direction derivative of the diffusion term (Eq. 4.96) were discretised in the same way by replacing the Φ quantity by *u*. Term $\frac{\partial}{\partial y}\left(\nu_T \frac{\partial u}{\partial y}\right)$ was approximated in the same manner which was discussed for the lateral contribution of the advective term of the transport. This term was halved and each half was considered as a source term while computing the diffusion in the alternate directions. For the *v* values which were required at the cell faces where the *v* values were not originally stored, appropriate approximation was made. A numerical test is presented in Chapter Five for the assessment of the diffusion contribution of the transport equation.

4.6.2.4.3 Solution to the Poisson Equation

For propagation the approach consists in solving the momentum equations in connection with a Poisson equation for the pressure obtained by taking the divergence of the momentum equations and expressing the condition of the divergence-free velocity field. A central discretising of the propagation part of the momentum equation in the same manner which was described for the diffusion, leads to a set of the equations in the form:

$$\overline{\overline{C}}\ \overline{P}_{i-1} + \overline{\overline{D}}\ \overline{P}_i + \overline{\overline{E}}\ \overline{P}_{i+1} = \overline{Q}_i \tag{4.101}$$

This comprises a block tri-diagonal matrix in the form of equation (4.102), which is an $(i_{\max} - i_{\min} + 1) \times (i_{\max} - i_{\min} + 1)$ matrix, where $i_{\min}$ is the reference number of the first column and $i_{\max}$ is the reference number of the last column of the corresponding

vertical plane which the pressures are under computation in the positive direction of *x*-axis. Each block of the block tri-diagonal matrix takes the form as equation (4.103).

$$\begin{bmatrix} D_{i_{\min}} & E_{i_{\min}} & & & & \cdots & 0 \\ C_{i_{\min+1}} & D_{i_{\min+1}} & E_{i_{\min+1}} & & & & \vdots \\ & \ddots & \ddots & \ddots & & & \\ & & C_i & D_i & E_i & & \\ & & & \ddots & \ddots & \ddots & \\ \vdots & & & & C_{i_{\max-1}} & D_{i_{moax\text{-}1}} & E_{i_{\max-1}} \\ 0 & \cdots & & & & C_{i_{\max}} & D_{i_{\max}} \end{bmatrix} \cdot \begin{bmatrix} P_{i_{\min}} \\ P_{i_{\min+1}} \\ \vdots \\ P_i \\ \vdots \\ P_{i_{\max-1}} \\ P_{i_{\max}} \end{bmatrix} = \begin{bmatrix} Q_{i_{\min}} \\ Q_{i_{\min+1}} \\ \vdots \\ Q_i \\ \vdots \\ Q_{i_{\max-1}} \\ Q_{i_{\max}} \end{bmatrix}$$

(4.102)

$$\begin{bmatrix} d_{k\min_{k\min}} & f_{k\min_{k\min+1}} & f_{k\min_{k\min+2}} & & & \cdots & 0 \\ f_{k\min+1_{k\min}} & d_{k\min+1_{k\min+1}} & f_{k\min+1_{k\min+2}} & f_{k\min+1_{ki\min+3}} & & & \vdots \\ f_{k\min+2_{k\min}} & f_{k\min+2_{k\min+1}} & d_{k\min+2_{k\min+2}} & f_{k\min+2_{k\min+3}} & f_{k\min+2_{k\min+4}} & & \\ 0 & & & & & & \\ & f_{k_{k-2}} & f_{k_{k-1}} & d_{k_k} & f_{k_{k+1}} & f_{k_{k+2}} & \\ & & & & & & 0 \\ \vdots & & f_{k\max-2_{k\max-4}} & f_{k\max-2_{k\max-3}} & d_{k\max-2_{k\max-2}} & f_{k\max-2_{k\max-1}} & f_{k\max-2_{k\max}} \\ 0 & \cdots & & f_{k\max-1_{k\max-3}} & f_{k\max-1_{k\max-2}} & d_{k\max-1_{k\max-1}} & f_{k\max-1_{k\max}} \\ f_{k\max_{k\min}} & f_{k\max_{k\min+1}} & \cdots & f_{k\max_k} & \cdots & f_{k\max_{k\max-1}} & d_{k\max_{k\max}} \end{bmatrix}$$

(4.103)

which is a $(k_{\max} - k_{\min} + 1) \times (k_{\max} - k_{\min} + 1)$ matrix where $k_{\min}$ is the reference number of the bottom layer and $k_{\max}$ is the reference number of the top layer. The subscript of each element refers to the layer which the element belongs and the sub-subscript refers to the layer which has a contribution to the value of the pressure coefficient of the layer which the value belongs. As it can be seen each of the elements of the block tri-diagonal matrix constitutes a penta-diagonal matrix except at the last row which is the solution to the free surface and has been integrated over all the layers and hence containing all the pressure unknowns of the corresponding column. The penta-diagonal matrix shows that the pressure coefficient for each cell is a function of the two upper layers and two lower layers of the cell together with the layer that the cell belongs. For the first and second layers next to the top and bottom boundaries (i.e. free surface and bed) this general rule of the contribution of the neighbouring cells to the coefficient of the unknown pressures in the block tri-

diagonal matrix has the restriction of being stretched only as far as the cell next to the boundary. A typical P_i and a typical Q_i are in the form of vectors (4.104) and (4.105) respectively as follows:

$$\begin{bmatrix} p_{k_{\min}} \\ p_{k_{\min+1}} \\ \vdots \\ p_k \\ \vdots \\ p_{k_{\max-1}} \\ p_{k_{\max}} \end{bmatrix} \qquad (4.104) \qquad \begin{bmatrix} q_{k_{\min}} \\ q_{k_{\min+1}} \\ \\ q_k \\ \\ q_{k_{\max-1}} \\ q_{k_{\max}} \end{bmatrix} \qquad (4.105)$$

The block tri-diagonal matrix was solved by block forward and back substitution (Twizell, 1984; Golub and Van Loan, 1989). The matrices were diagonally dominant and hence no pivoting was required (Kincaid and Cheney, 1991). The diagonal dominance property also satisfies the boundedness requirement (Versteeg and Malalasekera, 1995) of the numerical scheme. The scheme is non-iterative and the momentum and Poisson equations were only solved once at each half-time-step. The elements of $\overline{Q}$ are the components of the vector $\boldsymbol{Q}$ in the equation (4.63) which were considered as source terms. These include the elements attributable to Coriolis force and buoyancy terms. Appropriate approximation was used for each term and the resultant value was included in the right-hand side of the equations. The approximation followed exactly the general rules which were described and was demonstrated for other terms. For the evaluation of capability of the numerical model in simulating wave propagation, the simulations of a small amplitude standing wave sloshing in a confined container, a small amplitude progressive wave in deep water, and propagation of solitary wave in constant water depth have been presented in Chapter Five.

4.6.2.4.4 Species Concentration Equation

The species concentration equation was discretised in the same manner which was demonstrated for quantity Φ by replacing Φ with the concentration of species. The numerical simulation of internal seiche waves and lock-release turbulent gravity currents are demonstrated in Chapter Five, which show the capability of the

numerical model in simulating internal waves and variable density stratified flows where an accurate scheme for computation of species concentration distribution is highly important.

4.6.2.4.5 *k-ε* Turbulence Model Equations

The transport equations for the turbulence model were discretised as it was demonstrated for the transport of a scalar quantity. For the contribution of the production term (*P*) of the equations the following mechanism was used. Equation (4.34) can be fully rewritten as follows:

$$P = \nu_T \left[\underbrace{2\left(\frac{\partial u}{\partial x}\right)^2}_{1} + \underbrace{2\left(\frac{\partial w}{\partial x}\right)^2}_{2} + \underbrace{2\left(\frac{\partial v}{\partial y}\right)^2}_{3} + \underbrace{\left(\frac{\partial u}{\partial z} + \frac{\partial w}{\partial x}\right)^2}_{4} + \underbrace{\left(\frac{\partial v}{\partial z} + \frac{\partial w}{\partial y}\right)^2}_{5} + \underbrace{\left(\frac{\partial u}{\partial y} + \frac{\partial v}{\partial x}\right)^2}_{6} \right] \tag{4.106}$$

Term (1), half of term (2), term (4) and half of term (6) contributed to the first half-time-step. Half of term (2), term (3), term (5) and half of term (6) contributed to the second half-time-step. The discretisation of each term followed the general rules demonstrated, and appropriate approximations were made. The development of turbulent flow over a steep-sided trench has been simulated and compared against the laboratory measurements in Chapter Five.

4.6.2.4.6 Mechanism of the Algorithms for Computing the Derivatives and Coefficients of Unknown Pressures by Using Geometry Matrices

For computing the pressure coefficients for forming the block tri-diagonal matrix and to solve the Poisson equation, it is necessary to compute the pressure derivatives on *u* velocity locations. For ease of handling this on all grid points with different geometries, an algorithm which is described herein has been used. Recalling equation (4.80) for the control volume of a scalar quantity, its derivative, for instance for the first half-time-step and therefore in the *x*-direction at point (*i*, *k*), is required (Figure 4.11). This derivative at point (*i*, *k*) can be rewritten as follows:

$$\overline{\left(\frac{\partial \Phi}{\partial x}\right)}_{i,k} \equiv \frac{1}{S_{i,k}} \left[\begin{array}{c} \Phi_{i+1/2,k}\left(z_{i+1/2,k+1/2} - z_{i+1/2,k-1/2}\right) + \Phi_{i,k+1/2}\left(z_{i-1/2,k+1/2} - z_{i+1/2,k+1/2}\right) \\ + \Phi_{i-1/2,k}\left(z_{i-1/2,k-1/2} - z_{i-1/2,k+1/2}\right) + \Phi_{i,k-1/2}\left(z_{i+1/2,k-1/2} - z_{i-1/2,k-1/2}\right) \end{array} \right] \tag{4.107}$$

If this equation is written out fully with the approximations made for Φs, the following equation results:

$$\overline{\left(\frac{\partial \Phi}{\partial x}\right)}_{i,k} \approx \frac{1}{S_{i,k}} \left[\begin{array}{l} \Phi_{i+\frac{1}{2},k}\left(z_{i+\frac{1}{2},k+\frac{1}{2}} - z_{i+\frac{1}{2},k-\frac{1}{2}}\right) \\ + \left(\frac{\Phi_{i-\frac{1}{2},k} + \Phi_{i+\frac{1}{2},k} + \Phi_{i-\frac{1}{2},k+1} + \Phi_{i+\frac{1}{2},k+1}}{4}\right)\left(z_{i-\frac{1}{2},k+\frac{1}{2}} - z_{i+\frac{1}{2},k+\frac{1}{2}}\right) \\ + \Phi_{i-\frac{1}{2},k}\left(z_{i-\frac{1}{2},k-\frac{1}{2}} - z_{i-\frac{1}{2},k+\frac{1}{2}}\right) \\ + \left(\frac{\Phi_{i-\frac{1}{2},k} + \Phi_{i+\frac{1}{2},k} + \Phi_{i-\frac{1}{2},k-1} + \Phi_{i+\frac{1}{2},k-1}}{4}\right)\left(z_{i+\frac{1}{2},k-\frac{1}{2}} - z_{i-\frac{1}{2},k-\frac{1}{2}}\right) \end{array} \right] \tag{4.108}$$

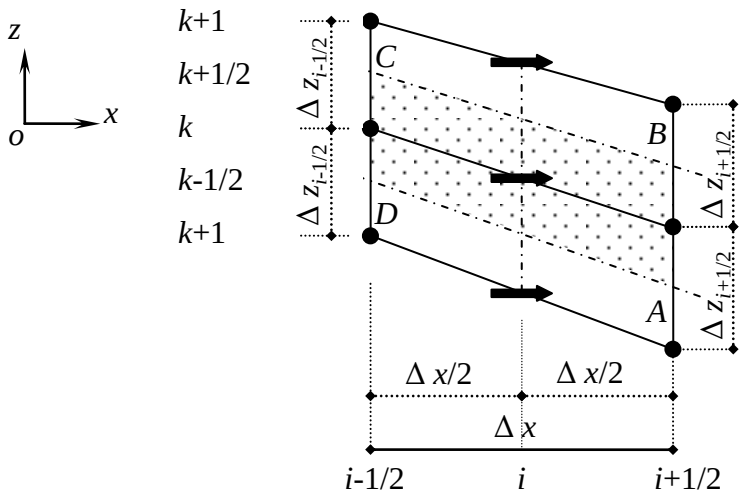

Figure (4.11) - Control volume for computing the derivative of a scalar quantity at the location of *x*-velocity component in *xoz* reference plane

A quantity matrix was defined as follows:

$$\begin{bmatrix} \Phi_{i-\frac{1}{2},k+1} & \Phi_{i+\frac{1}{2},k+1} \\ \Phi_{i-\frac{1}{2},k} & \Phi_{i+\frac{1}{2},k} \\ \Phi_{i-\frac{1}{2},k-1} & \Phi_{i+\frac{1}{2},k-1} \end{bmatrix} \tag{4.109}$$

and a geometry matrix was defined as follows:

$$\begin{bmatrix} 0.25(\mathrm{d}z)_{HP} & 0.25(\mathrm{d}z)_{HP} \\ 0.25(\mathrm{d}z)_{HP} + (\mathrm{d}z)_{VM} + 0.25(\mathrm{d}z)_{HM} & 0.25(\mathrm{d}z)_{HP} + (\mathrm{d}z)_{VP} + 0.25(\mathrm{d}z)_{HM} \\ 0.25(\mathrm{d}z)_{HM} & 0.25(\mathrm{d}z)_{HM} \end{bmatrix} \tag{4.110}$$

in which $(\mathrm{d}z)_{HP}$ refers to the *z*-coordinate difference of the ending nodes of the upper face, $(\mathrm{d}z)_{HM}$ refers to the *z*-coordinate difference of the ending nodes of the lower face, $(\mathrm{d}z)_{VM}$ refers to the *z*-coordinate difference of the ending nodes of the vertical face on the left-hand, and $(\mathrm{d}z)_{VP}$ refers to the *z*-coordinate difference of the ending nodes of the vertical face on the right-hand. For all cells these values for each half-time-step were computed and then used to compute the elements of the matrix (4.110). Equation (4.108) was then computed simply by an equation as follows:

$$\overline{\left(\frac{\partial \Phi}{\partial x}\right)}_{i,k} \approx \frac{1}{S_{i,k}} \sum_{m=1}^{3} \sum_{n=1}^{2} \Phi_{mn}\, G_{mn} \tag{4.111}$$

in which Φ_{mn} denotes the value of the quantity located at row *m* and column *n* of the quantity matrix and G_{mn} denotes the corresponding geometry values of the geometry matrix. Other possible forms of the matrices for other variables and at other locations take the form of (2×3) and (3×3) matrices.

4.7 BOUNDARY CONDITIONS

In general the boundary conditions at closed boundaries, or solid walls, are assumed to reflect the physical condition that there can be no mass flow, momentum, or solute transport through such a wall. At an open boundary (i.e. not at a solid boundary) the time varying water elevation, velocity and solute concentrations are prescribed (Nece and Falconer, 1989a). The spatial and temporal boundary conditions of the problems of interest of this study are discussed. Spatial boundary conditions have been determined for free surface, rigid lid, rigid surfaces including bed and walls, inlet and outlet boundaries for flow, transport of species and turbulence parameters. Temporal boundary conditions, which are termed initial conditions, are also discussed for flow, transport of species and turbulence parameters.

The boundary layer structure is strongly influenced by the boundary condition for pressure at the projection step. The numerical approximation of velocity has the maximum accuracy. The Dirichlet numerical boundary condition for the pressure leads to first-order numerical boundary layers in the pressure, and deteriorates the accuracy in the interior (E and Liu, 1995). The analysis of E and Liu (1995) favours strongly the choice of Neumann boundary conditions.

4.7.1 *Kinematic Boundary Conditions*

At any boundary which is free to deform under the influence of forces, kinematic boundary conditions must be satisfied. These boundaries include the fixed boundaries (e.g. bed and wall boundaries) and free surface. If the surface is expressed by $f_{\Re}(x,y,z,t)=0$, equating the total derivative of the surface with respect to time to zero, results as follows (Chiang, 1989; Dingemans, 1997):

$$\frac{D f_{\Re}(x,y,z,t)}{Dt}=0=\frac{\partial f_{\Re}}{\partial t}+u\frac{\partial f_{\Re}}{\partial x}+v\frac{\partial f_{\Re}}{\partial y}+w\frac{\partial f_{\Re}}{\partial z} \text{ on } f_{\Re}(x,y,z,t)=0 \qquad (4.112)$$

The unit vector normal to the surface reads as follows:

$$\boldsymbol{n}=\frac{\text{grad } f_{\Re}}{|\text{grad } f_{\Re}|} \qquad (4.113)$$

where

$$|\text{grad } f_{\Re}|=\sqrt{\left(\frac{\partial f_{\Re}}{\partial x}\right)^2+\left(\frac{\partial f_{\Re}}{\partial y}\right)^2+\left(\frac{\partial f_{\Re}}{\partial z}\right)^2} \qquad (4.114)$$

Rearranging equation (4.112) gives (Dean and Dalrymple, 1991):

$$\boldsymbol{V}\cdot\boldsymbol{n}=-\frac{1}{|\text{grad } f_{\Re}|}\frac{\partial f_{\Re}}{\partial t} \qquad (4.115)$$

4.7.2 *Flow Boundary Condition on Free Surface*

The free surface can be expressed as $f_{\Re}(x,y,z,t)=z-\eta(x,y,t)=0$. Applying equation (4.116) gives the kinematic boundary condition at the free surface as follows:

$$w=\frac{\partial\eta}{\partial t}+u\frac{\partial\eta}{\partial x}+v\frac{\partial\eta}{\partial y} \quad \text{on} \quad z=\eta(x,y,t) \qquad (4.116)$$

In the absence of wind, the free surface is considered to be a free slip boundary. Neglecting the cross influence in a vertical plane, *xoz* reference plane for example, this condition leads to (Daubert and Cahouet, 1984):

$$\boldsymbol{\tau}\cdot\overline{\boldsymbol{T}}\,(\boldsymbol{n})=\boldsymbol{\tau}\cdot(\overline{\boldsymbol{\sigma}}\cdot\boldsymbol{n}) \qquad (4.117)$$

in which $\boldsymbol{n}$ and $\boldsymbol{\tau}$ are the normal and tangential unit vectors of the free surface (in *xoz* plane). $\overline{\boldsymbol{\sigma}}$ is a two-dimensional stress tensor in *xoz* reference plane and $\overline{\boldsymbol{T}}$ is a two-dimensional stress tensor with only shear stress terms. Calculating the normal unit

vector by equation (4.114) for surface equation $z = \eta(x,t)$ and tangential unit vector and carrying out the dot product the tangential constraint is obtained as follows:

$$\left[1-\left(\frac{\mathrm{d}\eta}{\mathrm{d}x}\right)^2\right]\left(\frac{\partial u}{\partial z}+\frac{\partial w}{\partial x}\right)-2\left(\frac{\mathrm{d}\eta}{\mathrm{d}x}\right)\left(\frac{\partial u}{\partial x}-\frac{\partial w}{\partial z}\right)=0 \tag{4.118}$$

4.7.3 *Flow Boundary Condition on Bed*

If the bed is assumed to be impermeable and fixed, applying the no-flow boundary condition for the normal direction to bed prescribes:

$$\boldsymbol{V}\cdot\boldsymbol{n}=0 \tag{4.119}$$

where $\boldsymbol{n}$ is the unit vector normal to the bed surface.

The surface equation for the bottom is $f_{\Re}(x,y,z,t)=z-z_b(x,y)=0$. Applying the same procedure as was applied to the free surface gives:

$$w=u\frac{\mathrm{d}z_b}{\mathrm{d}x}+v\frac{\mathrm{d}z_b}{\mathrm{d}y} \text{ on } z=z_b(x,y) \tag{4.120}$$

For a non-slip horizontal bottom, $w = 0$ on $z=z_b(x,y)$. It is clear that the kinematic condition states that the flow at bottom is tangent to the bottom. In fact, bottom can be considered as a streamline that the flow is everywhere tangential to it.

Theoretically the tangential flow component holds the value zero on bed and this satisfies the no-slip boundary on bed. However to express conditions in the range of no-slip to free-slip , and with neglecting the cross flow influence, the tangential component of velocity in a vertical two-dimensional plane, *xoz* reference plane for instance, is written as follows:

$$\hbar\left(\frac{\partial V_\tau}{\partial n}+\frac{\partial V_n}{\partial \tau}\right)=V_\tau \tag{4.121}$$

in which V_n and V_τ are the normal and tangential components of the velocity respectively and $\hbar$ is a parameter which describes the boundary condition; $\hbar = 0$ corresponds to a no-slip boundary and $\hbar=\infty$ describes a free-slip boundary. Equation (4.121) by the same treatment applied for the free surface leads to:

$$\hbar\left[1-\left(\frac{\mathrm{d}z_b}{\mathrm{d}x}\right)^2\right]\left(\frac{\partial u}{\partial z}+\frac{\partial w}{\partial x}\right)-2\left(\frac{\mathrm{d}z_b}{\mathrm{d}x}\right)\left(\frac{\partial u}{\partial x}-\frac{\partial w}{\partial z}\right)=\left(u+w\frac{\mathrm{d}z_b}{\mathrm{d}x}\right)\left[1+\left(\frac{\mathrm{d}z_b}{\mathrm{d}x}\right)^{1/2}\right] \tag{4.122}$$

In the present study $\hbar$ has been calculated by the logarithmic law of the velocity (Eq. 3.51). This law is valid for the near bottom region which is approximately 0.1 - 0.2 times the water depth (Alfrink and van Rijn, 1983). The equation reads:

$$\hbar = d \ln \frac{30\,d}{k_s} \tag{4.123}$$

with the same definition of the variables as equation (3.51). Discretisation problems will arise when the no-slip boundary condition is applied, due to the large velocity gradients that occur close to the bottom. Therefore, the computations have been made at some distance from the bottom where the velocity gradients are relatively smaller. Then the velocity component normal to the bottom was set zero, while the tangential shear was computed from the logarithmic profile.

4.7.4 *Flow Boundary Conditions at Inlet and Outlet*

At inlet and outlet boundaries the horizontal components of velocity (*u* and *v*) or pressure or water elevation may be known. In the case of the known velocity or pressure, the corresponding distribution is applied at the boundary. If the water elevation is known, $f_\eta(y,t)$ for a boundary for the *x*-direction computations or $f_\eta(x,t)$ for a boundary for the *y*-direction computations, then a pressure at the free surface, which corresponds to the relevant water elevation (Eq. 4.49) is imposed at the boundary. For the vertical velocity (*w*) the following is applied for inlet and outlet boundaries:

$$\left.\frac{\partial w}{\partial x} = 0 \quad \text{for } y-\text{direction}; \quad \frac{\partial w}{\partial y} = 0 \quad \text{for } x-\text{direction}\right\} \tag{4.124}$$

For the outlet boundary if the exact details of the flow distributions were not known but the boundary values of pressure were known a constant pressure distribution at the boundary was used. It was further assumed that the flow was fully developed at the outlet (Armfield and Street, 2002) and the normal derivative of the velocity components was set to zero.

4.7.5 *Flow Boundary Condition on Walls*

On walls equation (4.122) with the assumption of flat surface and considering the equation (4.124) reduces to equation (4.125) in which u_d and v_d are the normal velocity components at distance *d* from the corresponding boundary.

$$\left.\frac{\partial u}{\partial z}=\frac{u_d}{\hbar} \quad \text{for } y-\text{direction}; \quad \frac{\partial v}{\partial z}=\frac{v_d}{\hbar} \quad \text{for } x-\text{direction}\right\} \tag{4.125}$$

4.7.6 *k and ε Boundary Conditions*

Turbulence model boundary conditions on bed and walls were considered as discussed in Chapter Three. On the free surface, Neumann boundary for *k* and Dirichlet boundary for *ε* were used and set to zero. At the outlet, Neumann boundary for *k* and *ε* was set to zero. At the inlet boundary it was assumed that the flow is low-turbulent and *k* and *ε* were set to a small value different from zero.

4.7.7 *Species Concentration Boundary Conditions*

On the free surface, bed and outlet, Neumann condition was set to zero. At the inlet boundary, the corresponding inlet values of species for the Dirichlet boundary condition were imposed.

4.7.8 *Initial Conditions*

In addition to the open and closed boundary conditions, initial values are required for the water elevations, velocity components and solute concentration within the computational domain (Nece and Falconer, 1989a). Velocity and pressure were set equal to zero. Species concentration and density were set to their specific values for each case. *k* and *ε* were set to appropriate values that a kinematic value for viscosity was obtained.

4.8 CONSISTENCY, STABILITY, CONVERGENCE AND ACCURACY OF THE SCHEME

Versteeg and Malalasekera (1995) state that conservativeness, boundedness and transportiveness are commonly accepted as alternatives for the more mathematically rigorous concepts of convergence, consistency and stability. These properties were addressed and satisfied in the discretisation procedure. They also state that because making the mesh spacing very close to zero is not feasible due to finite representation of numbers on computers, the conclusive approval of convergence for a numerical scheme may be relaxed. Consequently the convergence study is bound to the equivalent theorem of Lax which states that for linear problems

a necessary and sufficient condition for convergence is that the method is both consistent and stable.

Falconer (1976) demonstrated a comprehensive analysis of stability of the shallow water wave equations and studied the influence of a number of factors on the stability of the numerical scheme. The stability of the numerical scheme may be seen in three major fractional-steps namely, advection, diffusion and propagation. For the advection part a von Neumann stability analysis was carried out and the results are demonstrated in Chapter Five.

Another stability restriction is related to the diffusion process. The amplification factor for the Crank-Nicolson method has modulus unity, and so the method is unconditionally stable (Mitchell, 1969). The Crank-Nicolson scheme is usually described as unconditionally stable but this does not mean, however, that a physically realistic solution will result no matter how large the time step is. The stability in a mathematical sense simply ensures that the oscillations caused by large time steps will eventually die out, but it does not guarantee physically plausible solutions. Some examples of unrealistic solutions given by the Crank-Nicolson scheme can be found in Patankar and Baliga (1978). They concluded that the fully implicit method produces a physically realistic as well as a stable solution even for arbitrary large time steps. For small time steps, however, the accuracy of the fully implicit method is not as good as that of the Crank-Nicolson method. The truncation error for the Crank-Nicolson scheme is $O\left[(\Delta t)^2\right]+O\left[(\Delta x)^2\right]$ when evaluated about either point (n, i) or point (n + 1/2, i) (Smith, 1985; Tannehill et al., 1997).

Gresho (1990) carried out a detailed analysis of projection methods in a finite element context, labelling the method in which the pressure gradient is dropped from the momentum equations, P1, and the pressure correction method, P2. It was demonstrated analytically that P1 was first-order accurate in time whereas P2 was second-order accurate in time for the pressure term. Both the P1 and P2 methods provide second-order in time accuracy for the velocity field provided the momentum equation is integrated using a second-order-accurate scheme. The present scheme therefore may be considered second-order-accurate in time and space, however a number of investigations have shown the pressure to be only first-order-accurate in time, irrespective of the accuracy of the velocity (Gresho, 1990; Armfield and Street, 2002, 2003).

The species concentration equation was solved at each half-time-step prior to the solution of the Poisson equation. This allowed the species concentration in the buoyancy term to be located at the centred time location for each half-time-step. As the species concentration depends only on the n and (n + 1/2) level velocities, for the second half-time-step for example, their solution was uncoupled from the solution of the momentum Poisson equation for the (n + 1) level velocities and the pressure.

4.9 SUMMARY

Details are given of a novel arbitrary Lagrangian-Eulerian (ALE) three-dimensional numerical model for simulating time-dependent free-surface flows, using a non-hydrostatic pressure distribution with the capability of simulating stratified flows. The finite volume method (FVM) was deployed for discretisation of the set of the equations which combines the advantages of finite element method, for geometric flexibility, and finite difference method, for ease of calculation of fluxes through faces.

A fractional-step (projection) method has been deployed for solving the set of the equations by which the pressure gradient term was decoupled from the advection and diffusion. This introduced an intermediate velocity which did not necessarily satisfy the continuity equation. At the next fractional-time-step, the pressure was obtained from the continuity constraint by solving the Poisson equation and the velocity was corrected by the pressure.

The equations were discretised using a fifth-order-accurate upstream scheme to obtain the face values for use in the advection terms. For the diffusion term the Crank-Nicolson method was deployed and for the propagation, the Poisson equation was solved using a central difference scheme.

The solution of the species concentration equation was uncoupled from the solution of the momentum Poisson equation. It was discretised using the same approach as was used for the momentum equations, and was solved at each half-time-step prior to the solution of the Poisson equation.

The k-ε turbulence model with buoyancy terms was deployed and included in the numerical model. The solution of the turbulence transport equations advanced at the beginning of each half-time-step and the computed eddy viscosities were used in the flow equations of the same half-time-step.

CHAPTER FIVE

NUMERICAL MODELLING

TEST CASES, ACCURACY ASSESSMENT AND PERFORMANCE OF THE SCHEME

"All things are numbers"
Pythagoras (Langhaar, 1951)

5.1 INTRODUCTION

This chapter is dedicated to the presentation of the performance of the model and to the accuracy assessment of different aspects of the numerical scheme. The simulated results of the two-dimensional laterally-averaged module are compared with the corresponding analytical and experimental values. Three-dimensional validations are presented in Chapter Nine. The tests which have been carried out are outlined in the following paragraphs.

For advection six new schemes are presented. Three of these handle advection by the locally-one-dimensional (LOD) method which is discussed in Chapter Four and is deployed in the numerical model. The other three process advection by a two-dimensional approach. The performance of the new schemes has been demonstrated and compared with the conventional methods. A von Neumann stability analysis has been carried out for the proposed scheme and the amplitude and the phase portrait of the new scheme are presented. The influence of a limiter on the scheme is

demonstrated. For diffusion the performance of the Crank-Nicolson scheme by the LOD method is illustrated.

For the free surface, three tests are simulated: a small amplitude standing wave sloshing in a confined container, a small amplitude progressive wave simulating a flap-type wave-maker, and a solitary wave propagating in a constant water depth. The simulation of a nonlinear regime of soliton formation in a rectangular closed basin filled with two water layers with different densities is presented to evaluate the performance of the model for internal waves. A mesh convergence study has been carried out and the results are compared with a reference grid, whereby the influences of different characteristics for the grid generation are demonstrated.

Flow over a trapezoidal trench has been simulated to examine the performance of the model over a steep bed. The flow characteristics are illustrated and compared with experimental results. Computed turbulence parameters of the buoyant k-ε model are presented and compared with experimental results.

Three tests have been carried out to show the performance of the model in non-homogenous flows. In this part the gravity currents due to the salinity distribution variation have been studied.

5.2 ADVECTION

As the flows of estuarine water bodies and tidal circulation in harbours are mostly advection dominated (Falconer, 1980a), more attention has been given to the advective contribution of the transport term in the Navier-Stokes equations and the transport of the species concentration and turbulence parameters. For the advection of a quantity such as salinity or any species concentration, the following properties are required to properly reproduce dynamics of such quantities and particles:

- Local mass conservation;
- Positivity;
- Low numerical diffusion;
- Low numerical dispersion.

Six new schemes have been studied, three of which handle advection in a locally-one-dimensional fashion as described in Chapter Four. The other three process the advection by a two-dimensional approach. The accuracy of the new schemes has been studied and compared with the conventional schemes by a one-

dimensional approach. In two dimensions comparisons have been made for the locally-one-dimensional and two-dimensional approaches for the new schemes. All the schemes studied and discussed herein are explicit. Further test cases have been applied to the new proposed scheme to demonstrate its performance in the domains with steep bed and variable water surface and extremely irregular geometry. The effect of a limiter, which has been implemented in the numerical model, is shown.

5.2.1 *Accuracy of the New Locally-one-dimensional (LOD) Schemes and Comparison with the Conventional Methods*

Three new schemes, which process advection by an LOD approach, are presented. The approximations were obtained by assuming that the solution to the problem was approximated by considering a polynomial as the shape function of the quantity to be advected. The polynomial was then fitted to the points surrounding point (*i*), utilising values of the function at the grid points. Two shape functions were considered, a cubic and a quadric polynomial. The three schemes are summarised as:

i. A fourth-order-accurate scheme approximated by a cubic polynomial as a shape function whereby the quantity Φ_i varies over the four adjacent cells (*i*-2), (*i*-1), (*i*) and (*i* +1) for $u > 0$.
ii. A fourth-order-accurate scheme approximated by a cubic polynomial as a shape function whereby the quantity Φ_i varies over the four adjacent cells (*i*-1), (*i*), (*i* +1) and (*i* +2) for $u > 0$.
iii. A fifth-order-accurate scheme approximated by a quadric polynomial as a shape function whereby the quantity Φ_i varies over the five adjacent cells (*i*-2), (*i*-1), (*i*), (*i* +1) and (*i* +2) for $u > 0$.

The third scheme is discussed in Chapter Four. For the first and second schemes the quantity Φ at various *x* locations was determined by the equation as follows:

$$\Phi(x) = a\,x^3 + b\,x^2 + c\,x + d \tag{5.1}$$

Four points were used to determine the coefficients for each polynomial. The coefficients *a*, *b*, *c* and *d* were evaluated by using four neighbouring points (*i*-2), (*i*-1), (*i*) and (*i* +1) for the first scheme, and four neighbouring points (*i*-1), (*i*), (*i* +1) and (*i* +2) for the second scheme. The coefficients were obtained using the integration of equation (5.2) for the points involved in the scheme, and solving the resulting set of the linear equations.

$$\int_{x_l-\frac{\Delta x}{2}}^{x_l+\frac{\Delta x}{2}} \Phi(x)\,\mathrm{d}x = \Phi_l \cdot \Delta x \begin{cases} \text{for } l = i-2, i-1, i, i+1 & \text{for the first scheme} \\ \text{for } l = i-1, i, i+1, i+2 & \text{for the second scheme} \end{cases} \tag{5.2}$$

The flux passing through the right-hand face of cell *i* for $u > 0$ was evaluated by:

$$f_{x_{i+1/2}} = \frac{1}{\Delta t}\int_{\frac{\Delta x}{2}-u_{i+1/2}\cdot\Delta t}^{\frac{\Delta x}{2}} \Phi(x)\,\mathrm{d}x \tag{5.3}$$

For comparing the accuracy of these schemes with the conventional schemes a Gaussian initial condition was considered as follows:

$$\Phi = \exp\left[-\frac{(x-x_0)^2}{2\sigma^2}\right] \tag{5.4}$$

A base width of fourteen cells was considered. The mean value, x_0, was set zero and the standard deviation σ was chosen so that the Gaussian function was equal to 0.01 at x = half of the base width, and to one at x = 0. The computational domain was considered of 500 cells where $\Delta x = 0.03$ m. A constant velocity was applied and the simulation was completed after one minute, advancing 600 time steps, with a Courant number of 0.7. Four conventional schemes were chosen for comparisons:

- First-order backward;
- Second-order central Lax (Lax, 1954);
- Second-order upwind Fromm (Fromm, 1968);
- Third-order QUICKEST: quadratic upstream interpolation for convective kinematics with estimated streaming terms (Leonard, 1979).

The results of the tests are shown in figure (5.1). In comparison with conventional schemes, the schemes (i) and (ii) have a considerably closer peak to the analytical solution, but they suffer from larger negative errors and oscillations. The proposed scheme peaks at 0.922 while the QUICKEST stands at 0.722. The negative error for the proposed scheme is -0.024 compared with -0.041 of the QUICKEST. It is seen that the solution by the proposed scheme, except for the difference in the peak and negative error, very nearly lies on the exact solution.

5.2.2 *Accuracy Assessment of the New Two-dimensional Schemes*

Three new schemes, which process the advection in a two-dimensional fashion, have been developed. The performance of these schemes is compared with the Fromm, QUICKEST and new proposed scheme, which process the two-dimensional advection in a locally-one-dimensional (LOD) fashion.

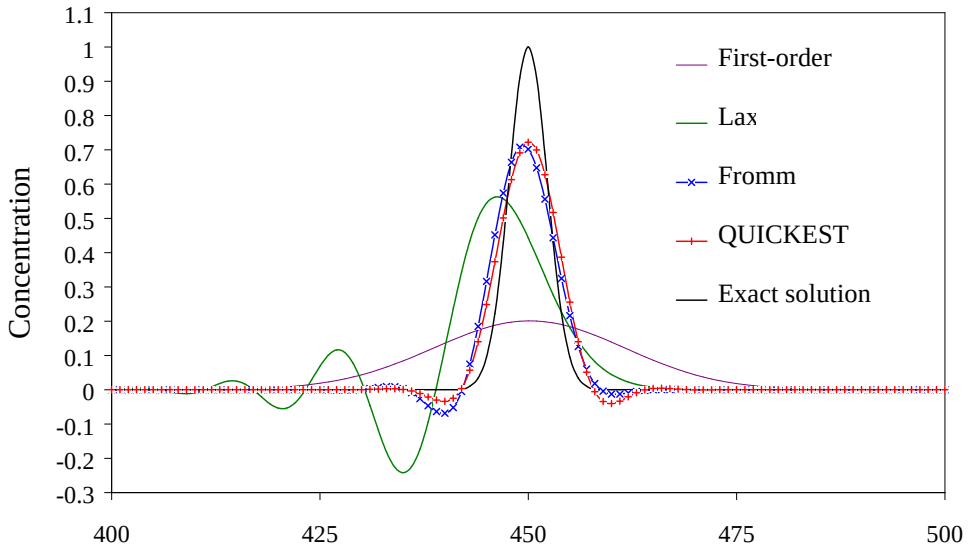

(a) - Comparison of the conventional schemes

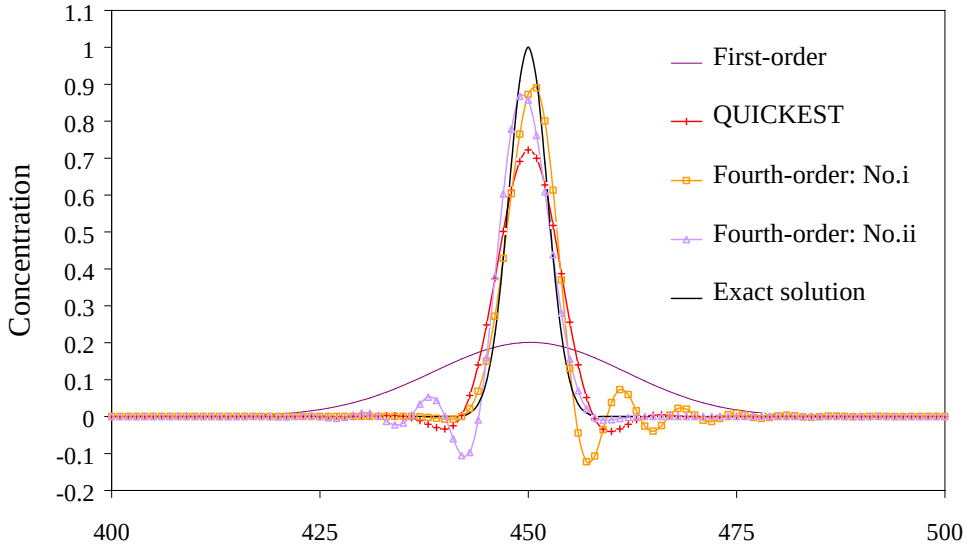

(b) - Comparison of the fourth-order schemes and conventional schemes

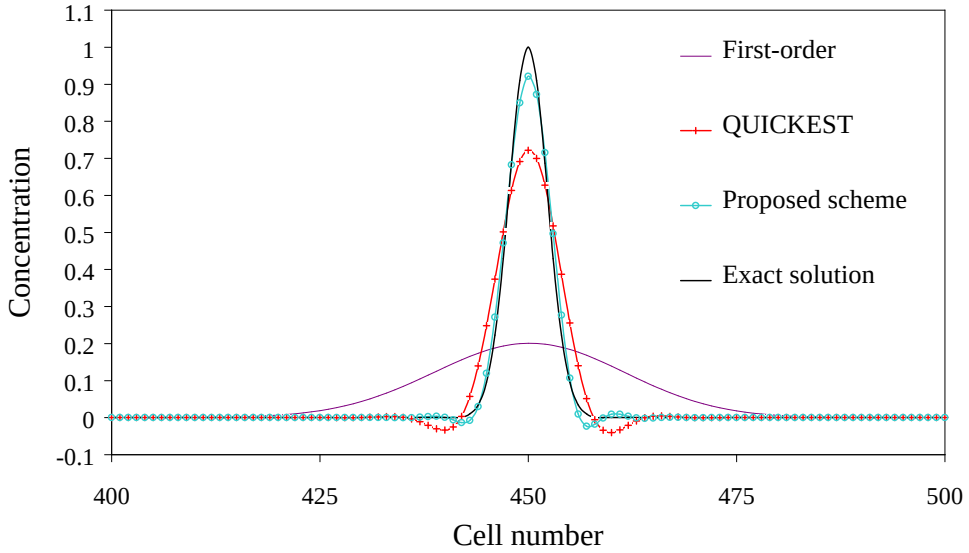

(c) - Performance of the proposed fifth-order scheme

Figure (5.1) - Conventional and new schemes for one-dimensional advection

The main difference in these schemes is the shape function over which the variation of the concentration of each cell is defined. For the first scheme a plane, and for the other two, membranes of 2nd and 4th degree are utilised to define the shape function. This was inspired by the linear, 2nd and 4th degree polynomials defined for one-dimensional schemes of Fromm, QUICKEST and the new proposed scheme respectively. It is assumed that the advection of quantities can only stretch as far as the neighbouring grids surrounding the grid (*i, j*) in one time-step. For comparisons a Gaussian cone was considered as the initial condition and a constant rotational velocity was applied in the domain.

5.2.2.1 Two-dimensional Scheme No. 1

For this scheme it is assumed that the concentration of grid point (*i, j*) varies according to a shape function defined by a plane. The plane is then defined such that it passes through point $\Phi_{i,j}$ and is parallel with two lines which connect the pairs of points ($\Phi_{i-1,j}$ and $\Phi_{i+1,j}$) and ($\Phi_{i,j-1}$ and $\Phi_{i,j+1}$). Therefore five grid points including the point (*i, j*) are involved in the definition of the concentration of grid point (*i, j*). The concentration of each control volume in a pure advection process can move in an arbitrary direction as is shown in figure (5.2). It is assumed that this movement can only stretch as far as the neighbouring grids surrounding the grid (*i, j*) in one time step. The concentration of each grid is representative of the average concentration of its control volume. After one time step the cell containing the concentration at point (*i, j*) has slid to its new position, which in an arbitrary displacement consists of four parts as shown in figure (5.2).

The slopes of the lines connecting the two pairs of the neighbouring points are calculated as:

$$\left.\begin{aligned} m_x &= \frac{\Phi_{i+1,j} - \Phi_{i-1,j}}{2\Delta x}, \qquad m_y = \frac{\Phi_{i,j+1} - \Phi_{i,j-1}}{2\Delta y} \end{aligned}\right\} \tag{5.5}$$

Therefore the two straight lines passing the two pairs of points are described as:

$$\left.\begin{aligned} \begin{vmatrix} \boldsymbol{i} & \boldsymbol{j} & \boldsymbol{k} \\ m_x & 0 & -1 \\ 0 & 1 & 0 \end{vmatrix} &= \boldsymbol{i} + m_x\,\boldsymbol{k} \qquad \begin{vmatrix} \boldsymbol{i} & \boldsymbol{j} & \boldsymbol{k} \\ 0 & m_y & -1 \\ 1 & 0 & 0 \end{vmatrix} = -\boldsymbol{j} - m_y\,\boldsymbol{k} \end{aligned}\right\} \tag{5.6}$$

The equation of the plane passing through point (0, 0, $\Phi_{i,j}$) and parallel with the lines of equation (5.6) is then obtained as:

$$\begin{vmatrix} x & y & \Phi-\Phi_{i,j} \\ 1 & 0 & m_x \\ 0 & -1 & -m_y \end{vmatrix} = 0 \quad \Rightarrow \quad \Phi = m_x\ x + m_y\ y + \Phi_{i,j} \tag{5.7}$$

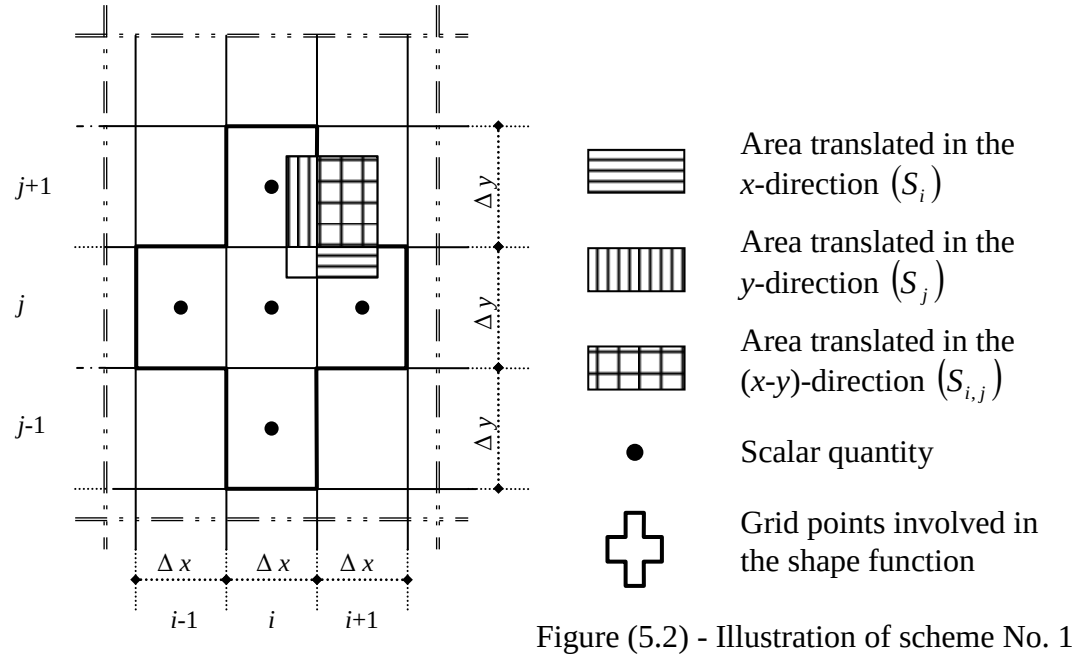

Figure (5.2) - Illustration of scheme No. 1

The total value of the quantity Φ for each of the four parts, shown in figure (5.2), is then expressed by:

$$\int_{y_c}^{y_d}\int_{x_a}^{x_b}\left(m_x\ x + m_y\ y + \Phi_{i,j}\right)\mathrm{d}\,x\,\mathrm{d}\,y \tag{5.8}$$

x_a, x_b, y_c and y_d are then the boundaries of the corresponding areas shown in figure (5.2). The upwind scheme is also deployed and therefore for $u > 0$ and $v > 0$ and for area S_i, for example, these values read:

$$x_a = \frac{\Delta x}{2} - u\,\Delta t; \qquad x_{.b} = \frac{\Delta x}{2}; \qquad y_{.c} = -\frac{\Delta y}{2} \qquad y_{.d} = \frac{\Delta y}{2} - v\,\Delta t \tag{5.9}$$

$\Phi^{n\to n+1}$, the change of Φ during the time interval ($n \to n+1$), for all grids involved in the translation of the quantity $\Phi_{i,j}$ is then computed as follows:

$$\left.\begin{aligned} \Phi_{i,j}^{n\to n+1}\,\Delta x\,\Delta y &= \Phi_{i,j}^{n} \quad \Delta x\,\Delta y - S_i - S_j - S_{i,j} \\ \Phi_{i+1,j}^{n\to n+1}\,\Delta x\,\Delta y &= \Phi_{i+1,j}^{n} \quad \Delta x\,\Delta y + S_i \\ \Phi_{i,j+1}^{n\to n+1}\,\Delta x\,\Delta y &= \Phi_{i,j+1}^{n} \quad \Delta x\,\Delta y + S_j \\ \Phi_{i+1,j+1}^{n\to n+1}\,\Delta x\,\Delta y &= \Phi_{i+1,j+1}^{n} \quad \Delta x\,\Delta y + S_{i,j} \end{aligned}\right\} \tag{5.10}$$

The same procedure is repeated for each cell and conservation is satisfied at the end of each time step. A Gaussian initial condition was considered as follows:

$$\Phi = \exp\left[-\frac{(x-x_0)^2+(y-y_0)^2}{2\sigma^2}\right] \tag{5.11}$$

The computational domain was considered of 101×101 cells where Δx and Δy were set 0.03 m. A base-diameter of fourteen cells for the Gaussian initial condition was considered and the centre of the cone was placed at x_0 and y_0 corresponding to the coordinates of the point (50, 25). The standard deviation σ was chosen so that the Gaussian cone was equal to 0.01 for d = half of the base width, and to one for d = 0, where d is the distance from the centre of the cone. A constant rotational velocity was applied in the domain where the axis of rotation was at the central point (51, 51) of the computational domain. The simulation was completed after one full rotation in 300 seconds, advancing 600 time steps. The simulated result after one full rotation is demonstrated in figure (5.3b).

5.2.2.2 Two-dimensional Scheme No. 2

For scheme No. 2 it was assumed that the concentration of grid point (*i*, *j*) varied according to a shape function defined by a second degree surface passing over five adjacent cells forming a cross. Therefore five grid points, including point (*i*, *j*), were involved in the definition of the shape function of the concentration of the grid point (*i*, *j*), similar to that, which was considered for scheme No. 1 as is shown in figure (5.2). The translation of the cell containing the concentration $\Phi_{i,j}$ follows the same assumptions and considerations made for scheme No. 1. The surface equation was defined as:

$$\Phi(x,y) = A\,x^2 + B\,y^2 + C\,x + D\,y + E \tag{5.12}$$

The coefficients were obtained using the integration of equation (5.13) for the five points involved and solving the resulting set of linear equations.

$$\int_{y_n-\frac{\Delta y}{2}}^{y_n+\frac{\Delta y}{2}}\int_{x_m-\frac{\Delta x}{2}}^{x_m+\frac{\Delta x}{2}}\Phi(x,y)\,\mathrm{d}x\,\mathrm{d}y = \Phi_{m,n}\cdot\Delta x\cdot\Delta y \quad \text{for} \quad \begin{Bmatrix} m = i-1,\ i,\ i+1 \\ n = j-1,\ j,\ j+1 \end{Bmatrix} \tag{5.13}$$

The total value of Φ for each part, shown in figure (5.2), was calculated by:

$$\int_{y_c}^{y_d}\int_{x_a}^{x_b}\left(\Phi_{x,y}\right)\mathrm{d}x\,\mathrm{d}y \tag{5.14}$$

The computation of fluxes and updating values of Φ follows the same definitions and procedure as scheme No. 1. The result of application of the same initial and flow field conditions considered for scheme No. 1 is shown in figure (5.3c).

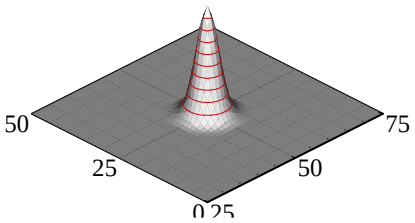

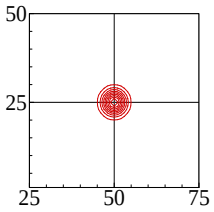

(5.3a) - Exact solution

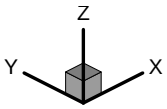

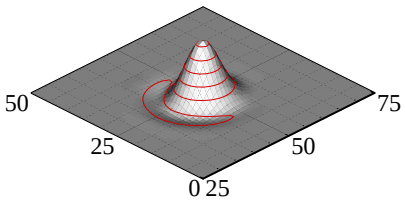

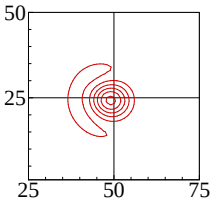

(5.3b) - Scheme No. 1

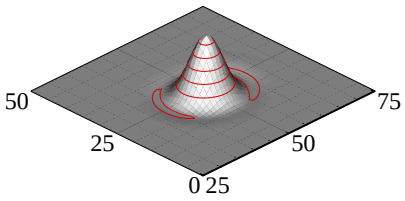

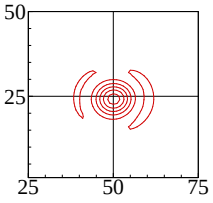

(5.3c) - Scheme No. 2

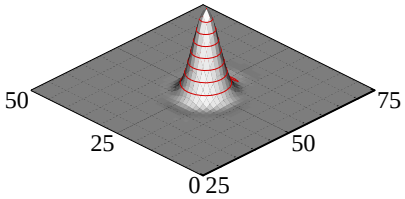

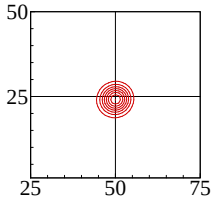

(5.3d) - Scheme No. 3

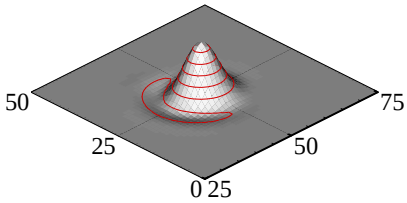

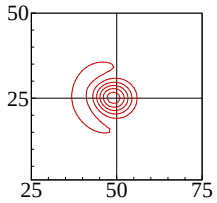

(5.3e) - 2D solution of Fromm scheme

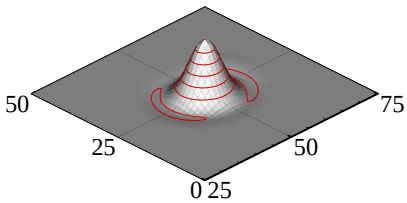

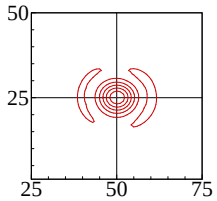

(5.3f) - 2D solution of QUICKEST scheme

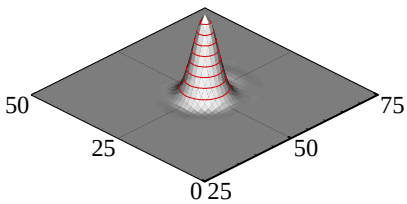

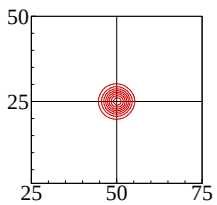

(5.3g) - 2D solution of proposed scheme

Figure (5.3) - Comparison of the two-dimensional schemes. *x* and *y* values refer to the cell numbers in the corresponding direction

5.2.2.3 Two-dimensional Scheme No. 3

The shape function for scheme No. 3 was assumed such that the concentration of grid point (*i, j*) varied upon a fourth degree surface over the grid point (*i, j*) and its neighbouring cells forming a cross involving nine grid points for definition of the concentration function of point (*i, j*). The translation of the cell containing the concentration $\Phi_{i,j}$ follows the same assumptions and considerations as was made for scheme No. 1. The shape function equation was defined as follows:

$$\Phi(x,y) = A\,x^4 + B\,y^4 + C\,x^3 + D\,y^3 + E\,x^2 + F\,y^2 + G\,x + H\,y + Q \qquad (5.15)$$

The coefficients were obtained using the integration of equation (5.16) for the nine points involved and solving the resulting set of linear equations.

$$\int_{y_n-\frac{\Delta y}{2}}^{y_n+\frac{\Delta y}{2}} \int_{x_m-\frac{\Delta x}{2}}^{x_m+\frac{\Delta x}{2}} \Phi(x,y)\,\mathrm{d}x\,\mathrm{d}y = \Phi_{m,n}\cdot\Delta x\cdot\Delta y \quad \text{for} \quad \begin{Bmatrix} m = i-2\cdots i+2 \\ n = j-2\cdots j+2 \end{Bmatrix} \qquad (5.16)$$

The total value of the quantity Φ for each of the four parts, shown in figure (5.2), was then expressed by:

$$\int_{y_c}^{y_d}\int_{x_a}^{x_b}\left(\Phi_{x,y}\right)\mathrm{d}\,x\,\mathrm{d}\,y \qquad (5.17)$$

The computation of the fluxes and updating the values of Φ for each control cell took place with the same definitions and procedure as was made for the scheme No. 1. The result of the application of the same initial and flow field conditions as was considered for scheme No. 1 is illustrated in figure (5.3d).

The two-dimensional schemes No. 1, No. 2, and No. 3 were compared with the two-dimensional solution of the Fromm, QUICKEST and the new proposed schemes respectively, where the latter schemes were performed by a locally-one-dimensional procedure. In the LOD approach to the two-dimensional solution of these schemes, it was assumed that both *x* and *y* dependencies of quantity Φ were expressed by the one-dimensional expression of each scheme in the corresponding direction. Therefore holding *y* fixed, for example, it was assumed that the quantity Φ varied over the adjacent relevant cells of each scheme in the *x*-direction.

The same initial and flow field conditions described for scheme No. 1 are applied to the Fromm, QUICKEST and the new proposed schemes, the results of which and the comparisons with the new two-dimensional schemes are illustrated in figure (5.3). The peak and negative error of each scheme is tabulated in Table (5.1). From this table it can be seen that the scheme No.3 and the proposed scheme have

considerably higher accuracy. It also shows that the two-dimensional solution of the proposed scheme drops the peak by only 4.01% compared to the one-dimensional solution, whereas the negative error is halved.

Table (5.1) - Peak values and negative errors of the two-dimensional schemes

Scheme	No. 1	No. 2	No.3	Fromm	QUICKEST	Proposed
Peak	0.532	0.557	0.799	0.568	0.596	0.885
Negative error	0.032	0.018	0.012	0.035	0.018	0.012

The similar performance of the schemes No. 1 and 2D solution of the Fromm scheme, lies in the fact that the surface shape function of the scheme No.1 is a plane, parallel to two lines connecting the concentration of the neighbouring cells adjacent to the cell under consideration in each direction, and passing through the concentration of the cell which for, the shape function is defined. In the Fromm scheme the shape function is a straight line, parallel to the line connecting the concentration of the two neighbouring cells adjacent to the cell under consideration, and passing through the concentration of the cell which for, the shape function is defined.

Rather similar argument applies to the similarity of the performance of the scheme No. 2 and 2D solution of the QUICKEST scheme. The discussion can be made in the same way, which was made for the schemes No.1 and Fromm, and with considering the shape function defined in the previous section for the scheme No. 2 and that of QUICKEST (Leonard, 1979).

The high performance of the scheme No. 3 and the proposed scheme, however, does not only follow the geometrical considerations made for definition of their shape functions. Their rather similar performance also lies in the fact of their high accuracy. However it can be seen from Table (5.1) that the peak of the concentration for the proposed scheme is favourably closer to the exact solution compared to the two-dimensional scheme No.3.

The closest results to the analytical solution obtained for the fifth-order-accurate scheme in both one- and two-dimensional advection processes, led to the inclusion of this scheme in the numerical model for computing the advection terms in Navier-Stokes equations, the transport equation of species concentration and the turbulence model transport equations.

5.2.3 *Performance of the Proposed Scheme*

Zalesak's problem (1979) is applied to the QUICK and the proposed schemes. The performance of the proposed scheme is also shown in the domains with steep bed and variable water surface and irregular geometry.

Zalesak's problem, in which a slotted disk is rotated through one revolution, is widely used as a test for scalar advection methods. The accuracy of the advection algorithm is assessed by comparing the initial and final conditions of the disk. This problem is used to measure the diffusive error of the advection scheme. The diffusive errors can be evaluated by checking the degree of distortion of the disk boundary. This test is considered a difficult simulation for a scalar advection method, as near the sharp corners there are not enough cells to resolve the advection equation correctly. In fact advecting the discontinuities present at the corners poses the greatest difficulty for the scheme.

For the Zalesak's test, the geometry of the domain and the velocity field were considered the same as that used for the two-dimensional test cases in the previous section. The diameter of the slotted cylinder was set to 28, and the slot width to 7 mesh cells. The performance of the scheme in comparison with the QUICK scheme is shown in figure (5.4). The figure shows that the QUICK scheme is diffusive because the slot is smeared out. The sections of the interface which are located in areas around the corners of the slot have deformed and curved, to smooth out the discontinuities that are present at these points. Although the QUICK is a third-order upwind scheme, the slot boundary deviates from its original position, whilst the proposed scheme has maintained its original shape to a good degree.

For examining the performance of the scheme in the domains with steep bed and high gradients of water elevation, three tests have been considered. The geometries of the domains for these three, in a *xoz* reference plane, are illustrated in figure (5.5). For the first two cases the same initial and flow field conditions described for the scheme No. 1 in previous section, were considered. The centre of the Gaussian cone was placed at the grid point (50, 25) while the computational domain consisted of 99×99 cells. The results after one full rotation are demonstrated in figure (5.6). In figure (5.6b), which corresponds to the case of steep bed and variable water surface, the peak drops to 0.875, from 0.885 for a regular mesh, and the negative error increases by 0.004 to 0.016. In figure (5.6d), corresponding to extremely irregular geometry, the peak drops to 0.785 and the

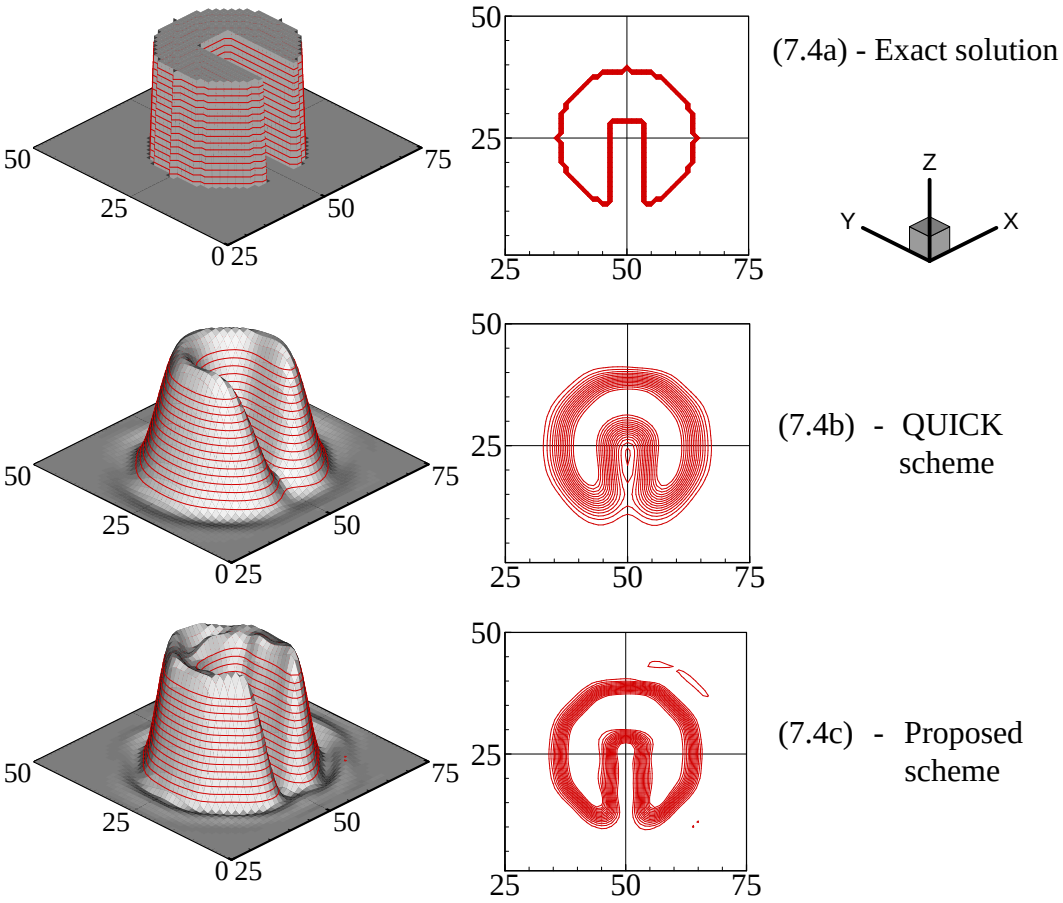

Figure (5.4) - Comparison of the results of the QUICK and new proposed schemes for Zalesak's problem. *x* and *y* values refer to the cell numbers in the corresponding direction

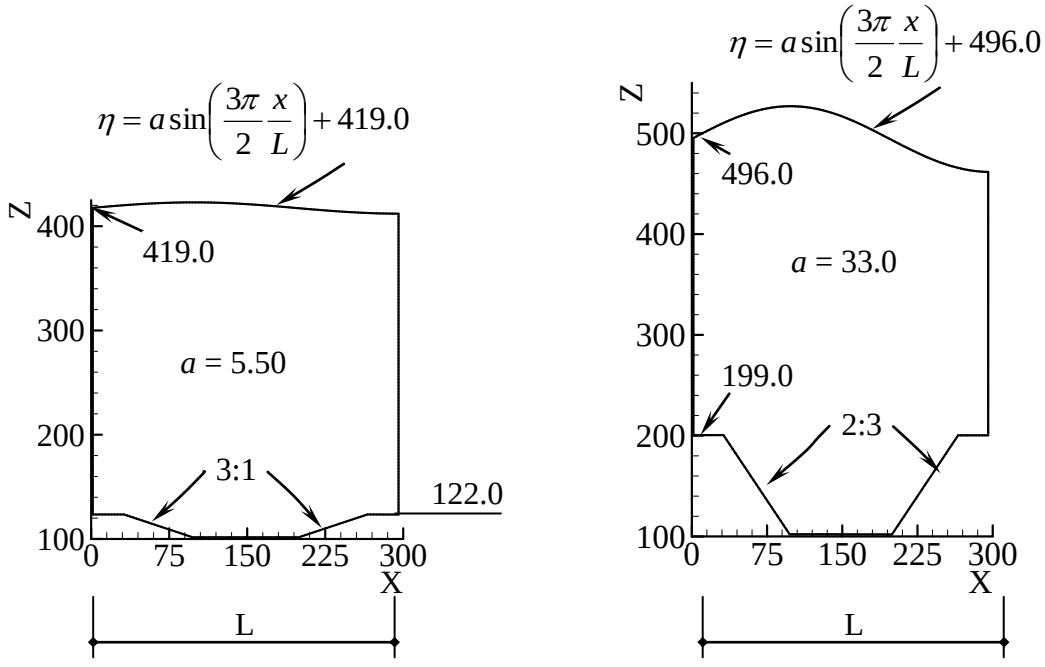

(a) - Steep bed and variable water surface

(b) - Extremely irregular geometry

Figure (5.5) - Geometry of the domains with steep bed and variable water surface. *x* and *z* values refer to the same direction length scales

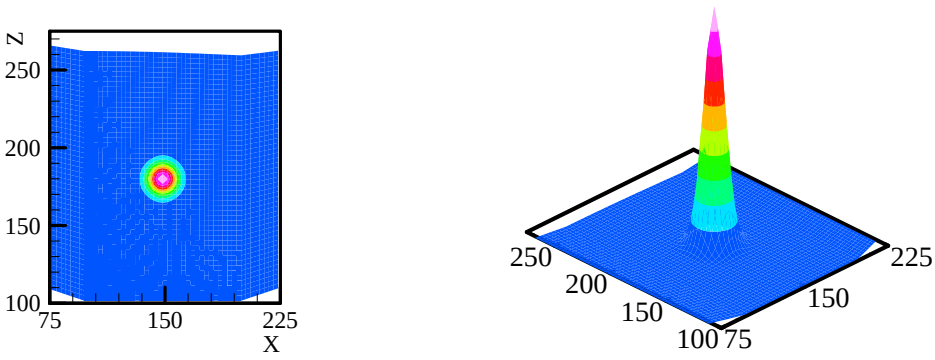

(5.6a) - Initial condition and exact solution for steep bed and variable water surface

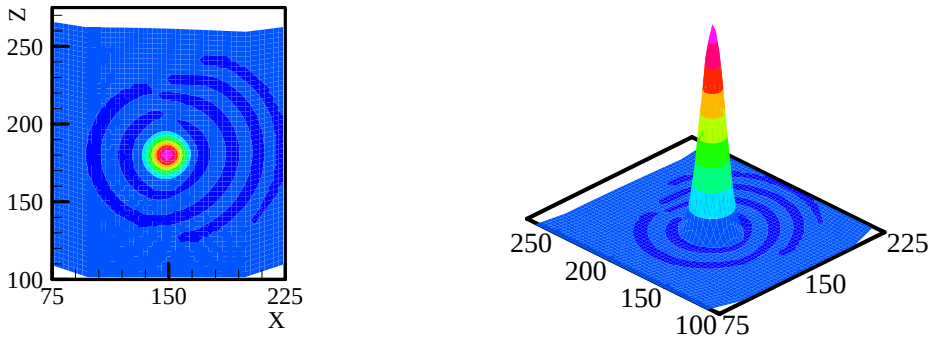

(5.6b) - Concentration after one full rotation in the domain for steep bed and variable water surface

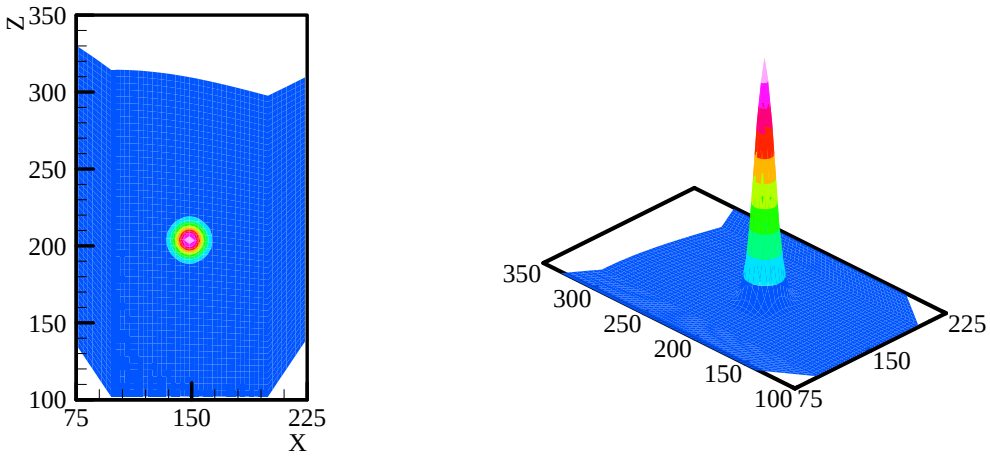

(5.6c) - Initial condition and exact solution for extremely irregular geometry

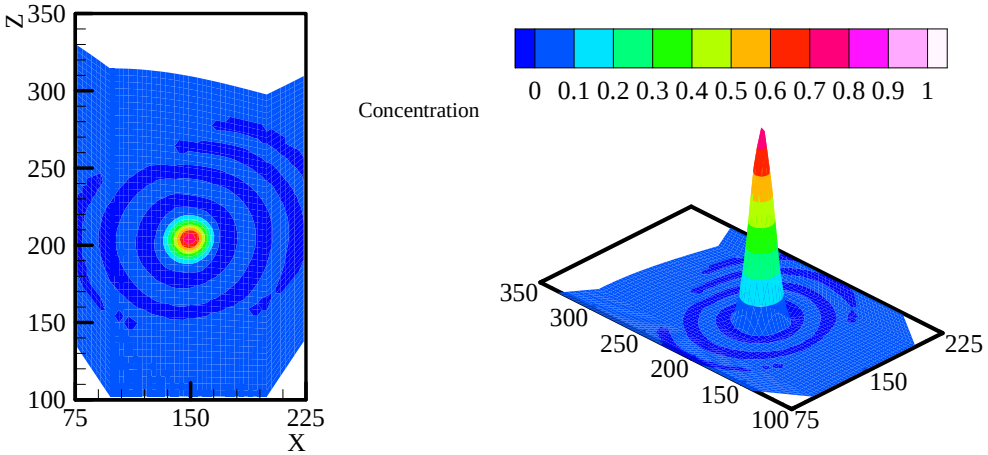

(5.6d) - Concentration after one full rotation in the domain for extremely irregular geometry

Figure (5.6) - Concentration after one full rotation in mild and extremely irregular geometries. *x* and *z* values refer to the same direction length scales

negative error rises to 0.035. The very narrow difference in the peak and negative error, for the case of steep bed and variable water surface, compared with the results for a regular mesh, is encouraging and the concerns over the accuracy of the scheme due to non-orthogonality and curvilinear grids can be relaxed. For the case of extremely irregular geometry the peak falls by 0.10 compared with the regular mesh, but is still higher than the results of other schemes for regular geometry, bearing in mind that this test case is not practically representing the usual geometries for the problems of interest of the present study and tidal currents, and basically is demonstrated to examine the performance of the scheme in very sharp gradients.

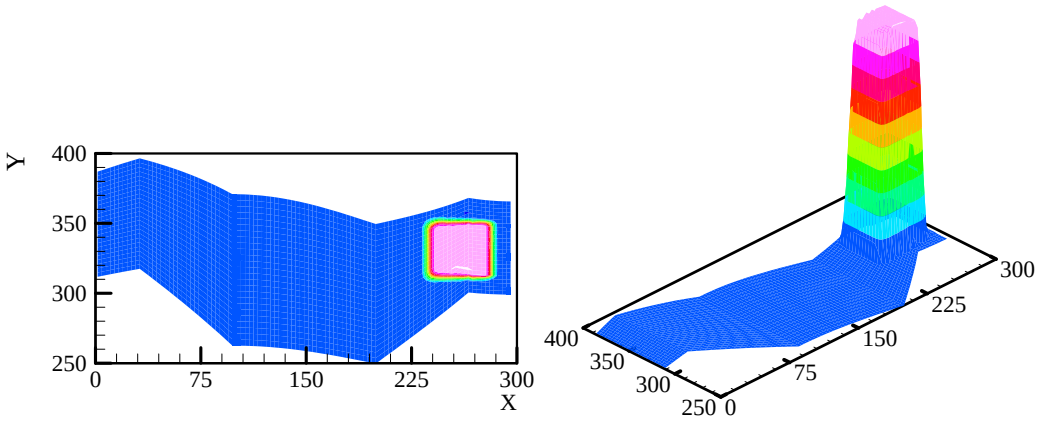

(a) - A prism after advancing 15 time steps entering the domain from the right-hand side border

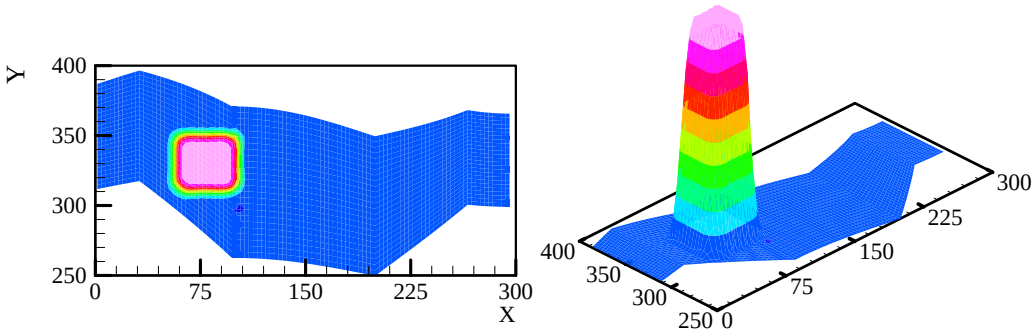

(b) - The prism after advancing 195 time steps entering the domain from the right-hand side border

Figure (5.7) - Translation of a prism of concentration in a horizontal line in an extremely irregular geometry. *x* and *z* values refer to the same direction length scales

In a highly non-orthogonal mesh structure, the approximation for the derivatives of the quantities, which contribute to the advection for instance, may not satisfy global conservation. Therefore in an extremely irregular geometry where the curvilinear mesh exceeds the acceptable limits set for non-orthogonal grids and the mesh structure is highly distorted, it is crucial to ensure that global conservation is

maintained. To demonstrate the performance of the numerical model in highly irregular geometries and to examine the performance of the proposed scheme for advection, the domain with the geometry illustrated in figure (5.5b) has been used. A prism of uniform concentration enters the domain form the right-hand boundary travelling in a straight horizontal line. Remaining in the same *y*-coordinates, same as the initial position of the prism when entering the domain, and after the translation, shows that the numerical scheme has ensured global conservation after solving the advection in an irregular and non-orthogonal mesh structure. The performance of the Dirichlet boundary type is also tested. The computational domain consisted of 99×99 cells. A uniform horizontal velocity field in the *x*-direction was applied and the initial uniform concentration was set equal to one. The results are shown in figure (5.7). In the *y*-direction, the strip of the grids in the region of cell numbers 38-63 is illustrated. After entering the domain and the advancement of 195 time steps, the horizontal alignment of the concentration prism and its location in the *y*-direction was in complete agreement with the analytical solution. The peak of the concentration was 0.998 and the negative error 10^{-5}.

5.2.4 *Influence of a Limiter*

Godunov (1959) showed that monotone behaviour of a solution cannot be assured for finite difference methods with more than first-order accuracy. This monotone property is very desirable when discontinuities are computed as part of the solution. The desirability of monotone behaviour must be reconciled with the highly dissipative character of the results (Tannehill et al., 1997). In regions where discontinuities develop, measures must be taken in order to avoid oscillations. One major approach to achieve this is to use a limiter to avoid the shape function exceeding the local extreme values. In the present study using the general idea of the ULTIMATE scheme (Leonard, 1991) an algorithm which is described in the following paragraphs has been used. The following parameters have been defined:

$$\left.\begin{aligned} \Delta\Phi = \Phi_{i+1} - \Phi_{i-1} \qquad & \hat{f} = \frac{f_i}{C_{r_i}} \cdot \frac{\Delta t}{\Delta x} \\ \hat{\Phi} = \frac{\Phi_i - \Phi_{i-1}}{\Delta\Phi} \qquad & \breve{\Phi} = \frac{\hat{f} - \Phi_{i-1}}{\Delta\Phi} \end{aligned}\right\} \tag{5.18}$$

where f_i and C_{r_i} are the flux and Courant number of cell (*i*) respectively.

The algorithm was then established as follows:

$$\left\{\begin{array}{l} \text{If } \left(\bar{\Phi} > 1.0 \text{ .Or. } \bar{\Phi} < 0.0\right) \text{ then } \hat{f} = \Phi_i \\ \text{Else if } \left(\breve{\Phi} < \bar{\Phi}\right) \text{ then } \hat{f} = \Phi_i \\ \text{Else if } \left(\breve{\Phi} > {}^{1}\!/\!_{C_{r_i}}\ \bar{\Phi}\right) \text{ then } \hat{f} = \Phi_{i-1} + \dfrac{\Phi_i - \Phi_{i-1}}{C_{r_i}} \\ \text{Else if } \left(\breve{\Phi} > 1\right) \text{ then } \hat{f} = \Phi_{i+1} \end{array}\right\} \tag{5.19}$$

For examining the influence of the limiter, same initial and flow field conditions as two-dimensional schemes were set. The computational domain was considered of 199×199 cells where Δx and Δy were set 0.015 m and the centre of the Gaussian cone was placed at the grid point (100, 50). A constant rotational velocity was applied in the domain with the axis of rotation at the centre of the computational domain (100, 100). The simulation was completed after one full rotation in 300 seconds, advancing 600 time steps. The results are demonstrated in figure (5.8). The peak dropped to 0.710 from 0.888 without the limiter, and the negative error vanished as was expected.

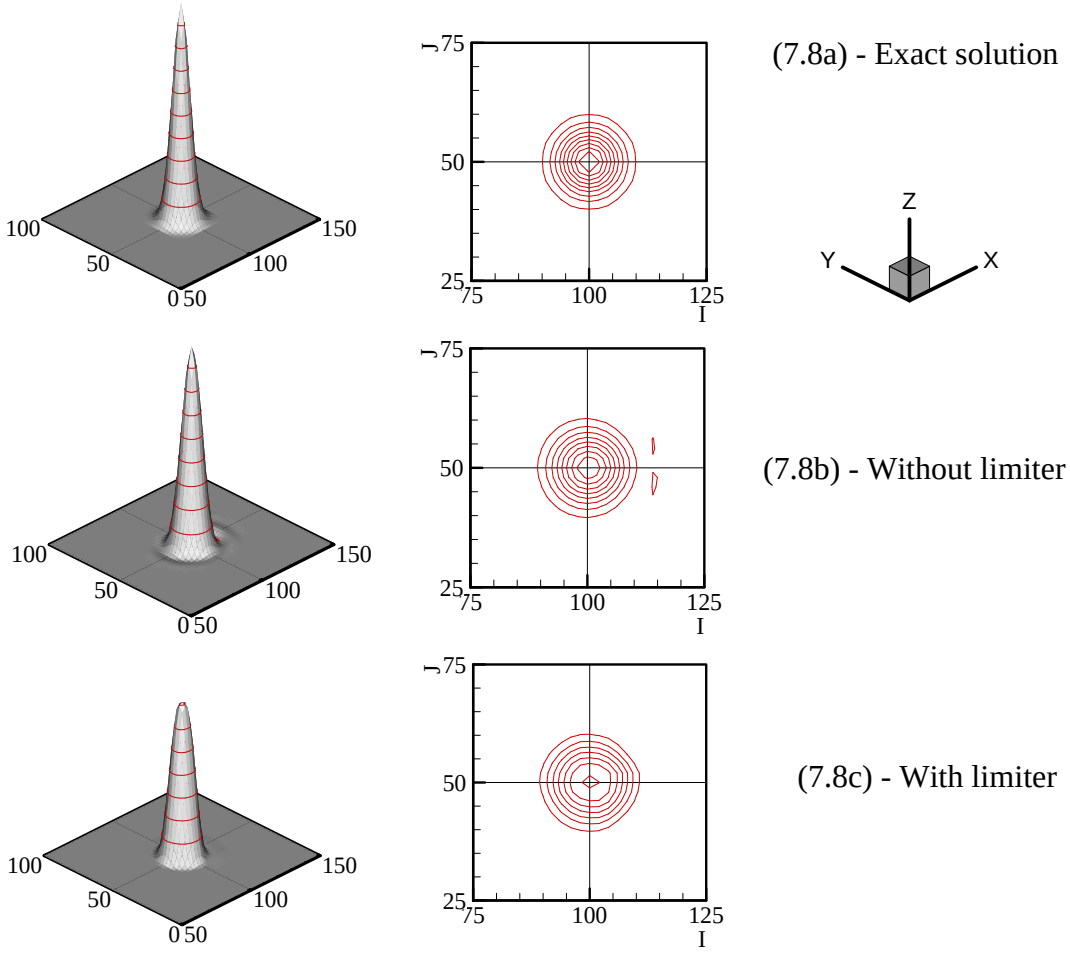

Figure (5.8) - Effect of the limiter on the solution for the proposed scheme. I and J values correspond to cell numbers in *x* and *y* directions respectively

5.2.5 *Linear Stability Analysis*

The stability of a linear problem with constant coefficients can be analysed when the influence of boundaries is neglected or removed. In periodic conditions on a finite domain, it is considered that the computational domain is repeated periodically and therefore all quantities, the solution and the errors, can be developed in a finite Fourier series over the domain. This development in the frequency domain forms the basis of the von Neumann (Fourier) method for stability analysis. Despite its lack of rigour, the von Neumann method is more commonly used and generally gives valid answers and is less cumbersome mathematically and much easier to apply than more careful methods (Press et al., 1986; Hoffmann and Chiang, 1993). It is supposed that the solution of any discretised scheme can be written as a Fourier series in complex, exponential form for any time level, *n*, as follows (Mitchell, 1969; Abbott and Basco, 1989):

$$\Phi_j^n = \sum_{k=1}^{k=k_{\max}} \xi_k^n \; e^{i\,k\,\alpha\,j} \tag{5.20}$$

where $k = 1, 2, 3, \ldots, k_{\max}$, is a finite length index and ξ_k^n is the Fourier coefficient for wave number k at time level n. $\alpha = 2\pi/N$ is the dimensionless wave number where N is the number of grid intervals over one wavelength. For linear stability analysis the resulting equation is arranged into the form of:

$$\xi^{n+1} = A\,\xi^n \tag{5.21}$$

At each time step for any wave number the right-hand side Fourier coefficient of equation (5.21) is multiplied by the factor *A*, the amplification factor. For stable schemes, the Fourier coefficients cannot grow without bound. Therefore to maintain stability it is required $|A| \le 1$, which means the magnitude of the Fourier coefficient of each and every wave number component should not increase in time. This is the Courant-Friedrichs-Lewy criterion, often called Courant condition. The celerity ratio, *Q*, is defined as (Abbott and Basco, 1989):

$$Q = \frac{-\tan^{-1}\left(\dfrac{\text{Imag } A}{\text{Real } A}\right)}{\text{C}_\text{r}\;\alpha} = \frac{-\tan^{-1}\left[\dfrac{-C_r\,\sin\alpha}{1-C_r\,(1-\cos\alpha)}\right]}{\text{C}_\text{r}\;\alpha} \tag{5.22}$$

The numerical phase is too fast if $Q > 1$, too slow if $Q < 1$ and exact if $Q = 1$.

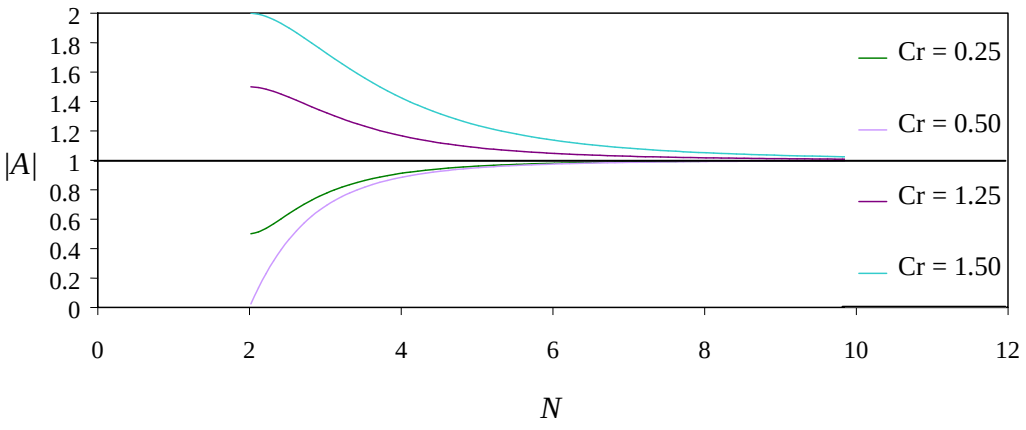

(a) - Amplitude portrait for QUICKEST scheme

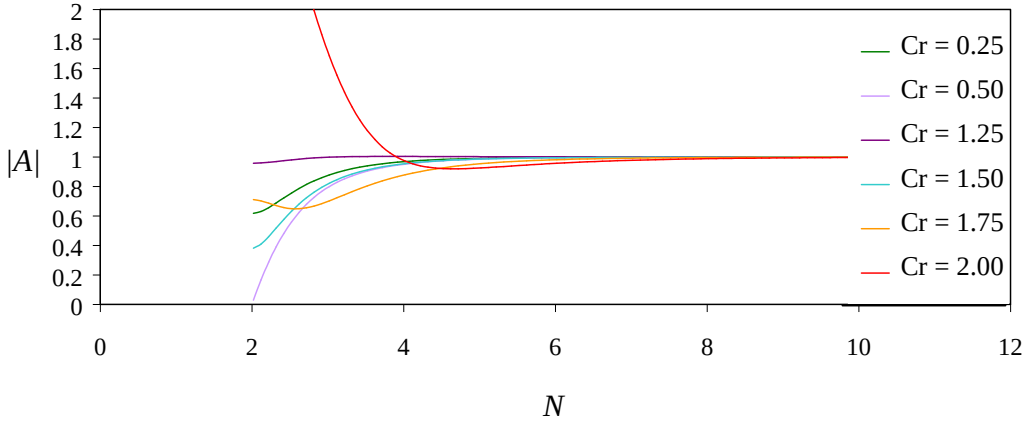

(b) - Amplitude portrait for the proposed scheme

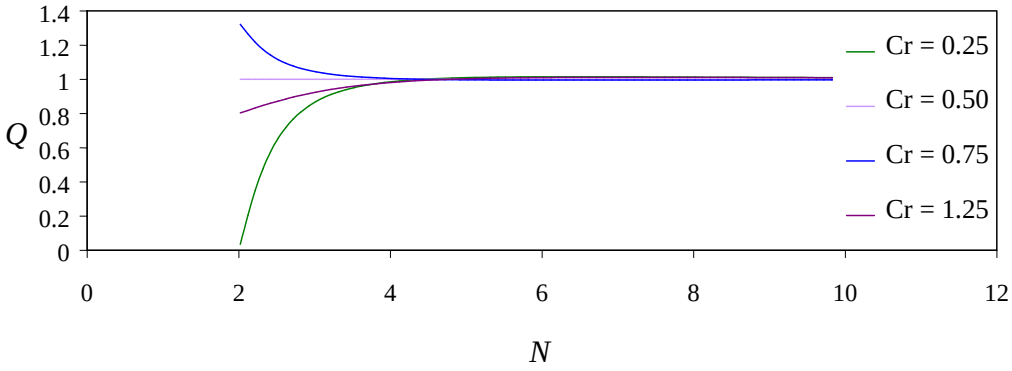

(c) - Phase portrait for QUICKEST scheme

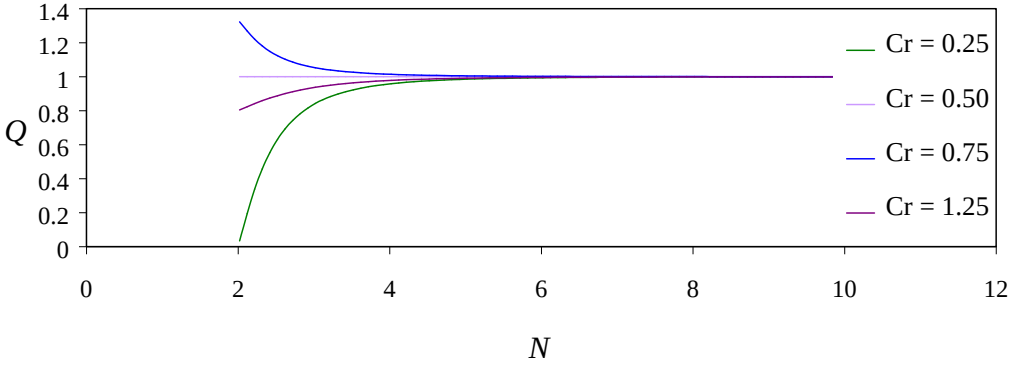

(d) - Phase portrait for the proposed scheme

Figure (5.9) - Amplitude and phase portraits for QUICKEST and the proposed schemes

A von Neumann (Fourier) stability analysis for the proposed scheme has been carried out and the amplitude and phase portraits of this scheme are compared with the QUICKEST scheme. Figure (5.9) shows the amplitude and phase portraits for different Courant numbers over a range of number of grids per wave length for the QUICKEST and proposed schemes.

At first glance it may appear that the proposed scheme has a Courant number bound about two, as the amplification factor is far below the unstable zone for Courant numbers equal to 1.5 and 1.75, but through closer inspection of values of the amplification factor it was seen that at Courant number equal to 1.25, the amplification factor actually rises to 1.003. Therefore the Courant number limit for the proposed scheme is equal to one, as for explicit schemes. It is assumed that the proof of weak stability by Fourier analysis or von Neumann method implies strong stability (Tannehill et al., 1997).

5.3 DIFFUSION

For testing the performance of the diffusion contribution of the Navier-Stokes equations and the transport of species concentration and turbulence parameters, the domain with the geometry described in figure (5.5a) has been utilised. The numerical discretisation for diffusion, which is based on the Crank-Nicolson scheme, is presented in Chapter Four.

The concentration, by the use of a Gaussian cone, was defined as follows:

$$\Phi = f(x, z, t) = \frac{250}{\lambda T} e^{-\frac{\left[(x-x_0)^2 + (z-z_0)^2\right]}{4\lambda T}} \tag{5.23}$$

in which λ is the diffusion coefficient and T reads as follows:

$$T = T_0 + t \tag{5.24}$$

where T_0 is the time when the concentration is assumed to be the initial value for the commencement of the diffusion process, and t is the simulation time. In this test T_0 was set to 500 seconds, resulting in a peak for initial concentration equal to five units. The simulation was carried out for 1000 time steps corresponding to 1000 s. The computational domain was considered of 99×99 cells where Δx and Δz were set 0.03 m and the centre of the cone was placed at the centre of the domain where x_0 and z_0 were corresponding to the coordinates of the grid point (50, 50). The

results are demonstrated in figure (5.10), which shows very good agreement with the analytical solution. The analytical solution indicates the peak of the Gaussian cone to be 1.667, whereas in the numerical simulation this value decreases to 1.648.

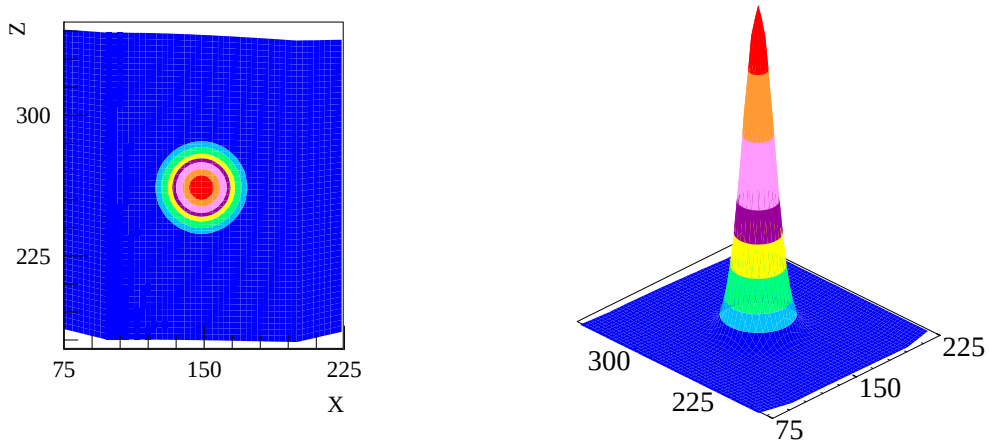

(a) - Initial condition of the concentration

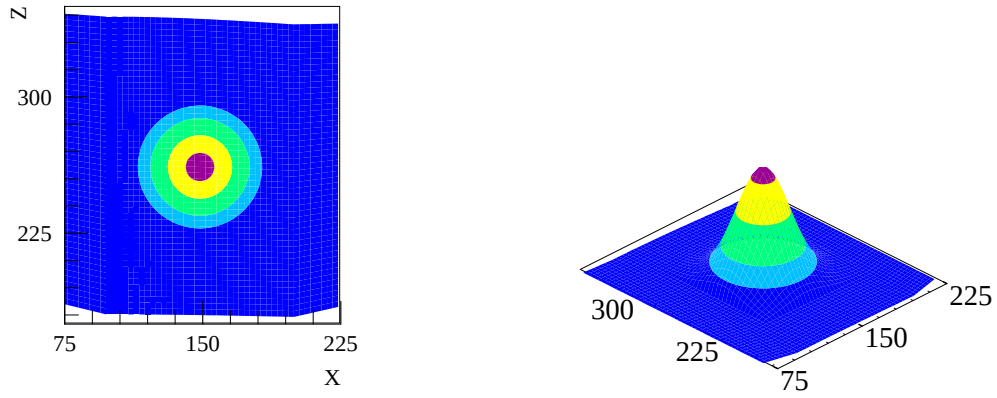

(b) - Analytical solution after 1000 seconds

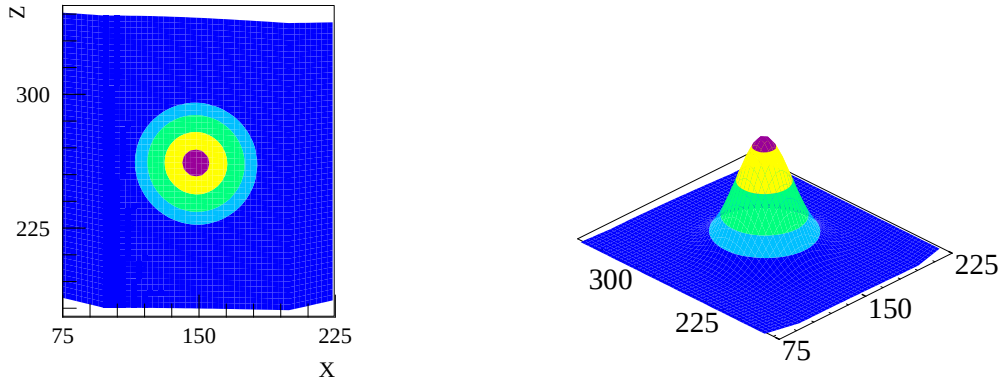

(c) - Predicted concentration distribution after 1000 seconds equal to 1000 time steps

Figure (5.10) - Diffusion process in a two-dimensional domain with steep bed and variable water surface. *x* and *z* values correspond to the length scales in the same directions

5.4 WAVE PROPAGATION

Numerical simulation of wave propagation has been compared with the analytical solutions for the following tests:

- A small amplitude standing wave sloshing in a confined container;
- A small amplitude progressive wave in deep water;
- Solitary wave propagation in a constant water depth.

5.4.1 *Water Sloshing in a Confined Container*

This test involved studying the oscillations of a uni-nodal standing wave in a confined container with infinite length in the *y*-direction. The width of the container in the *x*-direction (*W*) and the still water depth (*H*) are both equal to one metre. If the viscous and nonlinear effects are neglected, the motion of the fluid can be approximated by the linear wave theory. Gravity waves are defined as short waves when $H/L > 1/20$ (Yalin, 1971). For a sufficiently deep tank, the shape of the free surface of a periodic standing wave is given analytically by (Eagleson and Dean, 1966; Dean and Dalrymple, 1991):

$$\eta(x,t) = a\cos(k\,x)\cos(\varpi\,t) \tag{5.25}$$

where k is the wave number, ϖ the angular frequency and a the amplitude of the standing wave. k and ϖ are expressed as follows:

$$k = \frac{2\,\pi}{L} \tag{5.26}$$

$$\varpi = \left[g\,k\tanh(k\,H)\right]^{1/2} \tag{5.27}$$

where *g* is the acceleration of the gravity. For a uni-nodal standing wave, $L = 2\,W$.

The initial shape of the free surface was considered the solution of equation (5.25) at $t = 0$ with an amplitude of 0.01 m. With the lapse of time, the potential energy of the fluid is changed into the kinetic energy, and vice versa. The sloshing amplitude is very small, so that it will decay rapidly if a numerical code is not conservative. In the numerical solution, the domain is discretised by 100 grid cells in the *x*-direction and 25 layers in the *z*-direction. The time step was set to 0.001 s and the simulation advanced for three periods. The viscosity was set to zero and the boundary condition without wall function was used such that the Dirichlet boundary condition for *u* and *w* was set zero at side walls and bottom, and the Neumann boundary condition for *u* and *w* was set zero in the *z*- and *x*-directions as follows:

$$u_{x=0} = u_{x=W} = 0 \quad \text{and} \quad w_{z=0} = 0 \qquad (5.28) \qquad \left.\frac{\partial u}{\partial z} = 0 \quad \text{and} \quad \frac{\partial w}{\partial x} = 0\right\} \qquad (5.29)$$

For a uni-nodal standing wave where $L = 2W = 2$ m, the wave number is equal to $k = \pi$ m^{-1} and the period of wave for a basin with the depth of 1.0 m, is calculated $T \cong 1.1341\,\text{s}$. For a standing wave the analytical solution for the velocity components (u and w), dynamic pressure ($P = p/\rho$), speed of wave propagation (wave celerity, C) and wave length (L), are given as follows (Dean and Dalrymple, 1991):

$$u = a\,\varpi\,\frac{\cosh k(H+z)}{\sinh k\,H}\sin k\,x \sin \varpi\,t \qquad (5.30)$$

$$w = -\,a\,\varpi\,\frac{\sinh k(H+z)}{\sinh k\,H}\cos k\,x \sin \varpi\,t \qquad (5.31)$$

$$P = \frac{p}{\rho} = g\,a\,\frac{\cosh k(H+z)}{\cosh k\,H}\cos k\,x \cos \varpi\,t = g\,K_p(z)\,\eta(x,t) \qquad (5.32)$$

$$C = \frac{L}{T} = \left[\frac{g}{k}\tanh(k\,H)\right]^{1/2} \qquad (5.33)$$

$$L = \frac{g}{2\pi}T^2 \tanh\frac{2\pi H}{L} \qquad (5.34)$$

$K_p(z)$ is the pressure response function. Under the nodes, the pressure is solely hydrostatic. The dynamic pressure is in phase with the water surface elevation, and is a combined result of the local water surface displacement and the vertical accelerations of the overlying water particles.

Figure (5.11) shows the numerical results for velocity field and dynamic pressure in the basin at six time phases of the simulation. In figure (5.12), comparisons between the numerical results and analytical solution are presented at times very nearly, equal to $t/T \cong 0.0, 1/8, 1/4, 1/2, 1.0$ for water elevation.

These comparisons show that the numerical results agree satisfactorily well with the analytical solution during the first period. Figure (5.13) shows the time histories of the oscillating wave heights at left and right walls and the middle of the basin for three wave periods. Small discrepancy appears in the comparisons, but the overall comparisons with the notion of the neglect of nonlinear effect in analytical solution indicate that the model can predict the free surface location accurately. Numerical simulation results for velocity and dynamic pressure distribution compared against analytical solution in figure (5.14) are encouraging.

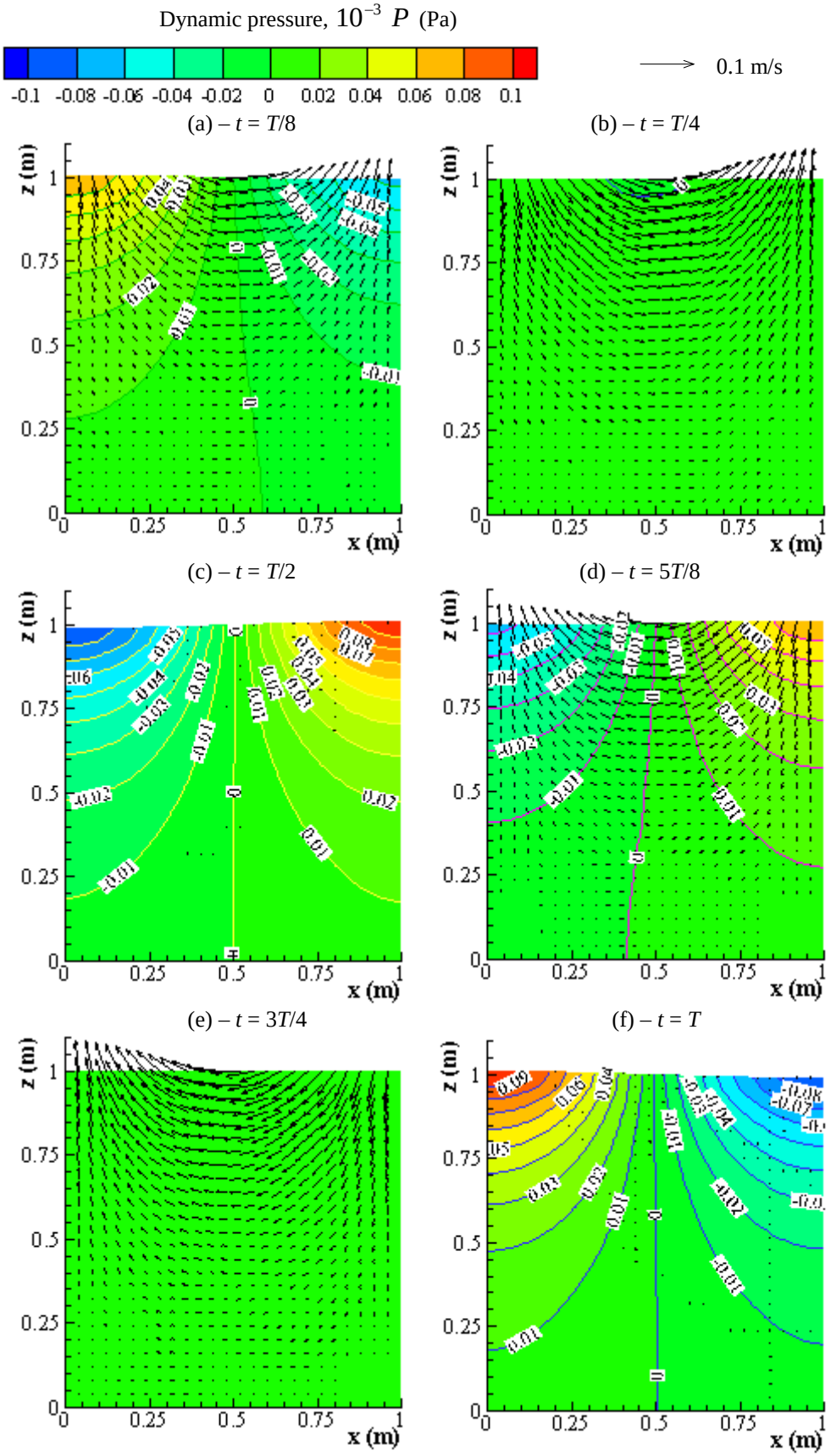

Figure (5.11) - Circulation in oscillating basin with dynamic pressure

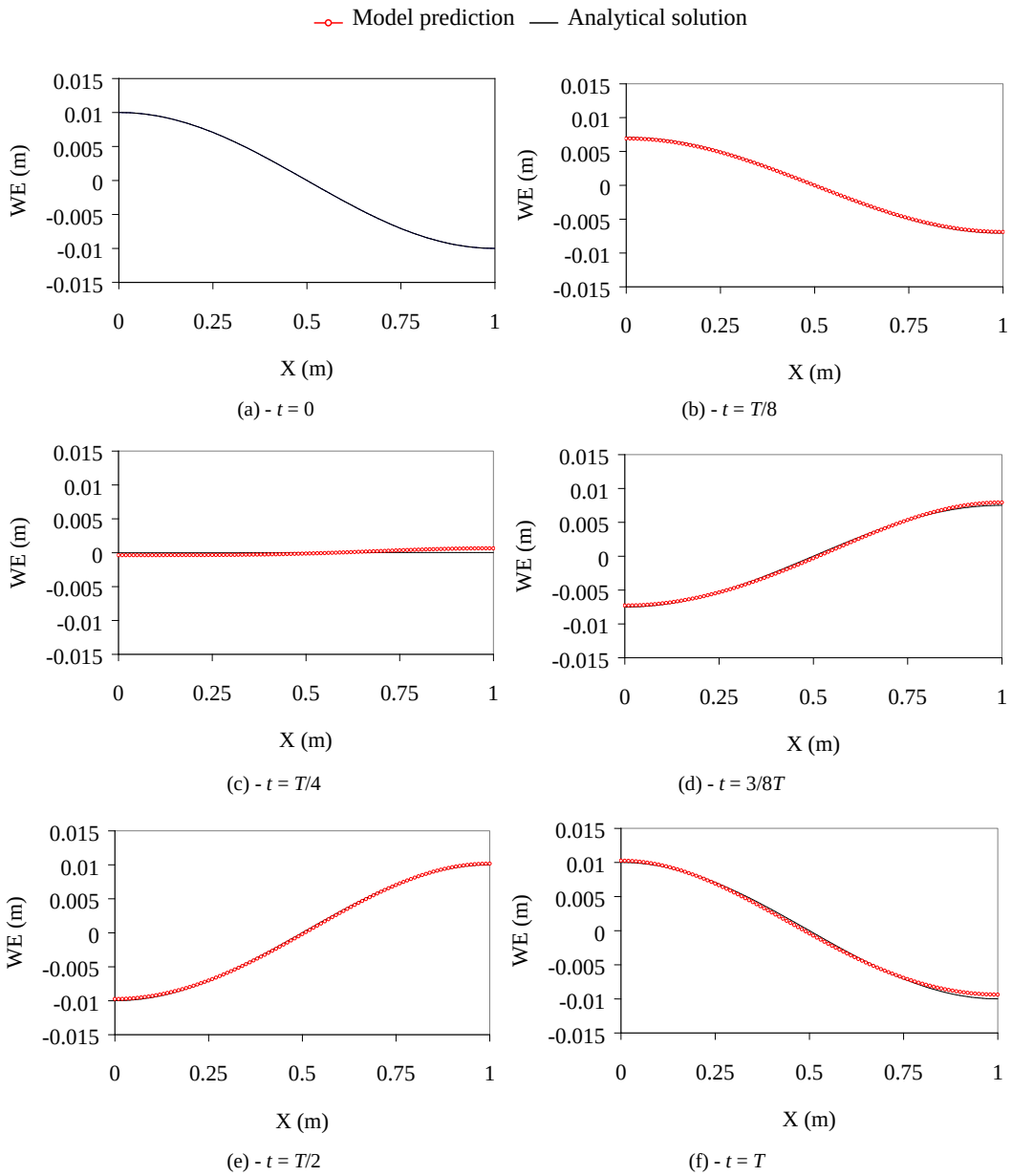

Figure (5.12) - Comparisons of numerical prediction and analytical solution of water surface for a small amplitude wave sloshing in a confined container

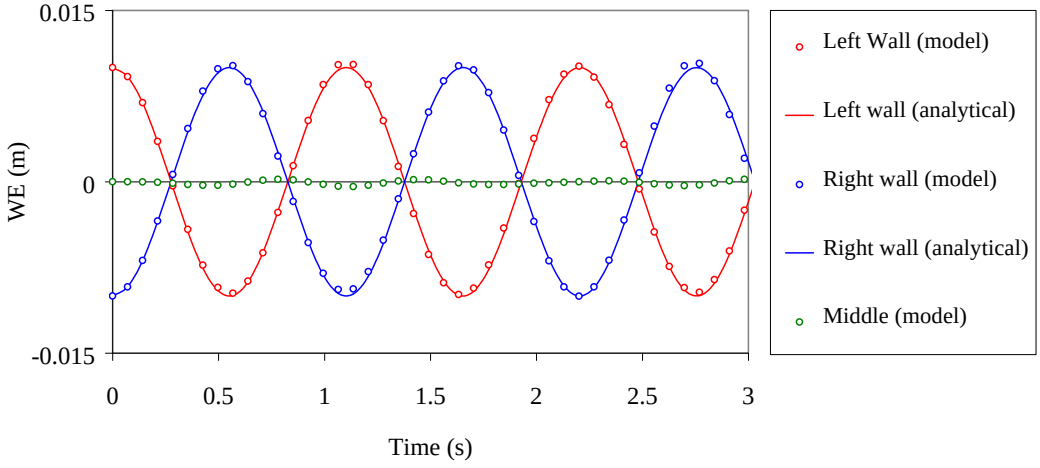

Figure (5.13) - Time histories of the oscillating wave heights

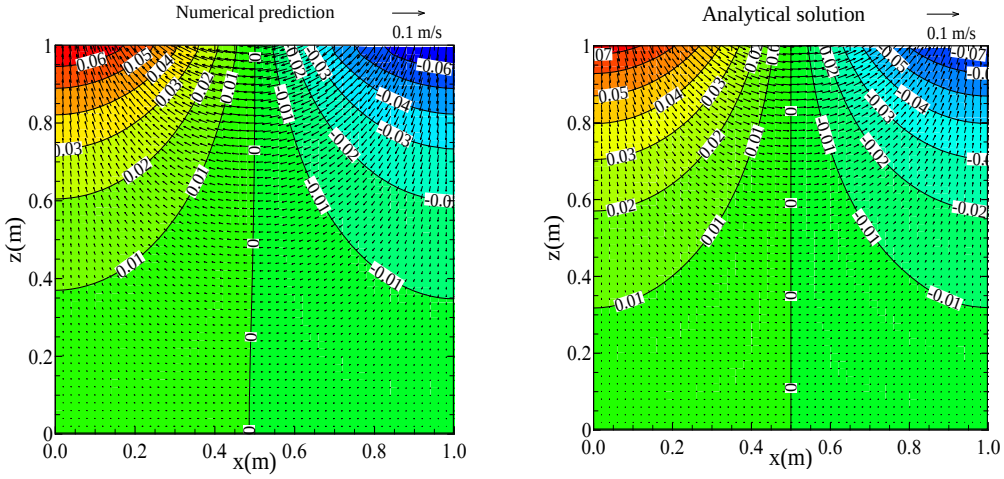

Figure (5.14) - Dynamic pressure distribution and velocity field at $t = 5T/6$. Left: Numerical prediction, Right: Analytical solution. The dynamic pressure values are in kPa

5.4.2 *Small Amplitude Progressive Wave Train*

For this test a wave train produced by a flap-type wave-maker is simulated. The boundary value problem for the wave-maker in a wave tank follows directly from the boundary value problem for two-dimensional waves propagating in an incompressible, irrotational fluid. For a progressive wave the water elevation, velocity components and dynamic pressure are as (Dean and Dalrymple, 1991):

$$\eta(x,t) = a\cos(k\,x - \varpi\,t) \tag{5.35}$$

$$u = a\,\varpi\,\frac{\cosh k(H+z)}{\sinh k\,H}\cos(k\,x - \varpi\,t) \tag{5.36}$$

$$w = a\,\varpi\,\frac{\sinh k(H+z)}{\sinh k\,H}\sin(k\,x - \varpi\,t) \tag{5.37}$$

$$P = \frac{p}{\rho} = g\,a\,\frac{\cosh k(H+z)}{\cosh k\,H}\cos(k\,x - \varpi\,t) = g\,K_p(z)\,\eta(x,t) \tag{5.38}$$

The pressure response factor $K_p(z)$ is always less than unity below the mean water surface. By assuming that the wave board is driven in a sinusoidal motion, if S_0 is the stroke of the wave-maker at still water surface (i.e. mean water level), its horizontal displacement is described as follows:

$$X_{0(z=\eta)} = \frac{S_0}{2}\sin(\varpi\,t) \tag{5.39}$$

where $S_0/2$ is the stroke amplitude and ϖ is the wave-maker frequency. The motion of the wave-maker can then be expressed as follows:

$$\mathrm{d}X_{0(z=\eta)}/\mathrm{d}t = \varpi\, S_0/2\, \cos(\varpi\, t) \tag{5.40}$$

To first order, the water surface will be represented as the progressive wave solution and the first order flap-type wave-maker solution, giving the ratio of wave height (H_W) to stroke (S_0) at water surface as follows (Dean and Dalrymple, 1991; Hughes, 1993):

$$\frac{H_W}{S_0} = \frac{4\sinh(k\,H)}{\sinh(2k\,H)+2k\,H}\left[\sinh(k\,H)+\frac{1-\cosh(k\,H)}{k\,H}\right] \tag{5.41}$$

The wave period has been taken equal to 5 seconds and the wave height 0.50 m. The water depth is 15 m giving a wave number equal to $k \cong 0.16344$ according to the equation (5.27). The stroke at water surface was then calculated by the equation of ratio of wave height to stroke (Eq. 5.41) to obtain the velocity of the wave-maker at water surface (Eq. 5.40) which was set 0.2604 m/s. The velocity for different layers of water simply followed the flap-type wave-maker performance which was a linear function being zero at bed and equal to the maximum velocity at the still water surface. This constituted the left hand-side boundary condition of the domain with the Neumann boundary condition set to zero for *w* in the *x*-direction. For the right hand-side a free-exit for water was maintained by setting a zero dynamic pressure at the far end of the domain. The Dirichlet boundary condition was set zero for *w* velocities at bed (flatbed) and a Neumann boundary condition equal to zero was prescribed for *u* in the *z*-direction. The length of domain was considered 1000 m which was discretised by grids equal to one metre in the *x*-direction. The depth of the domain was divided into 15 layers. The time step was set 0.025 s and the simulation was performed for 120 seconds where the celerity of wave was calculated 7.689 m/s.

The comparisons of the numerical simulation and the analytical solution after 24 periods, corresponding to time t = 120 s, for the dynamic pressure and velocity field, shown in figures (5.15) and (5.16) respectively, confirm the capability of the numerical model in prediction of the progressive waves. The difference present in figure (5.15) for the first few waves is expected until the wave train is established.

The plot of the water elevation predicted by the numerical simulation is compared against the analytical solution in more detail in figure (5.17). A small discrepancy, which partly may be due to linear assumption for the analytical solution, can be seen but wave does not dissipate or decay over the time and the difference does not grow.

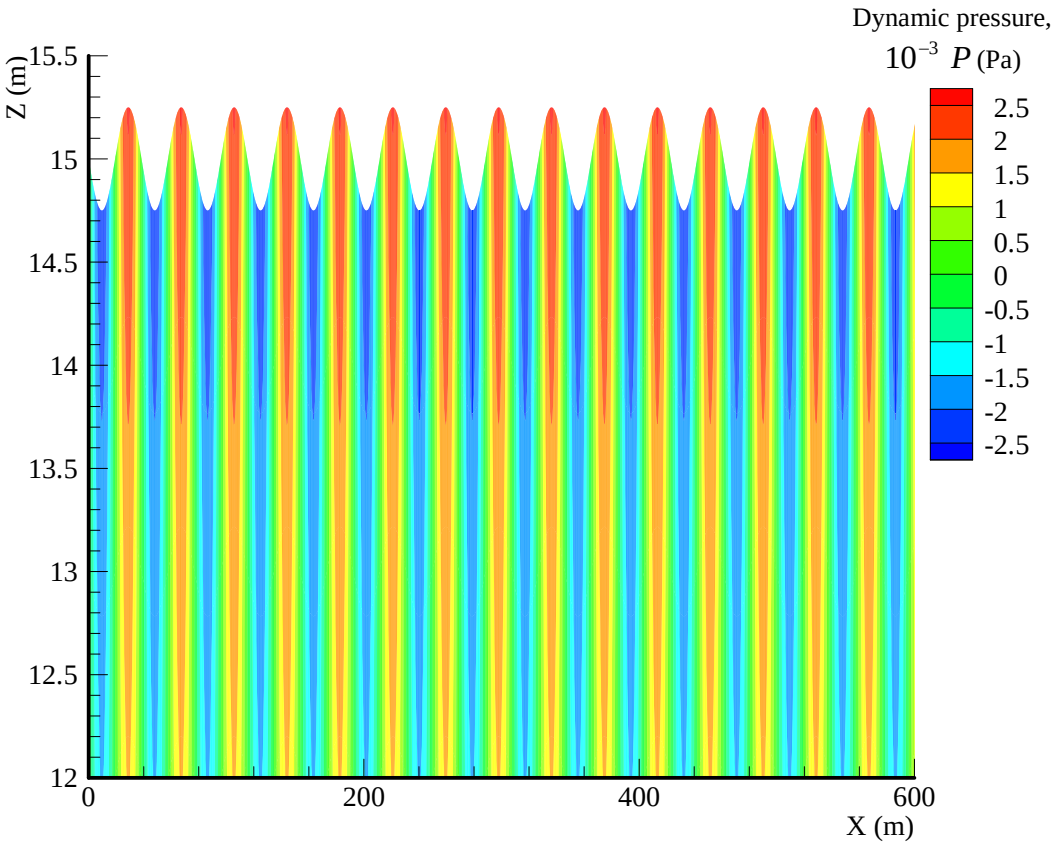

(a) – Dynamic pressure distribution under the wave train and in domain (analytical solution)

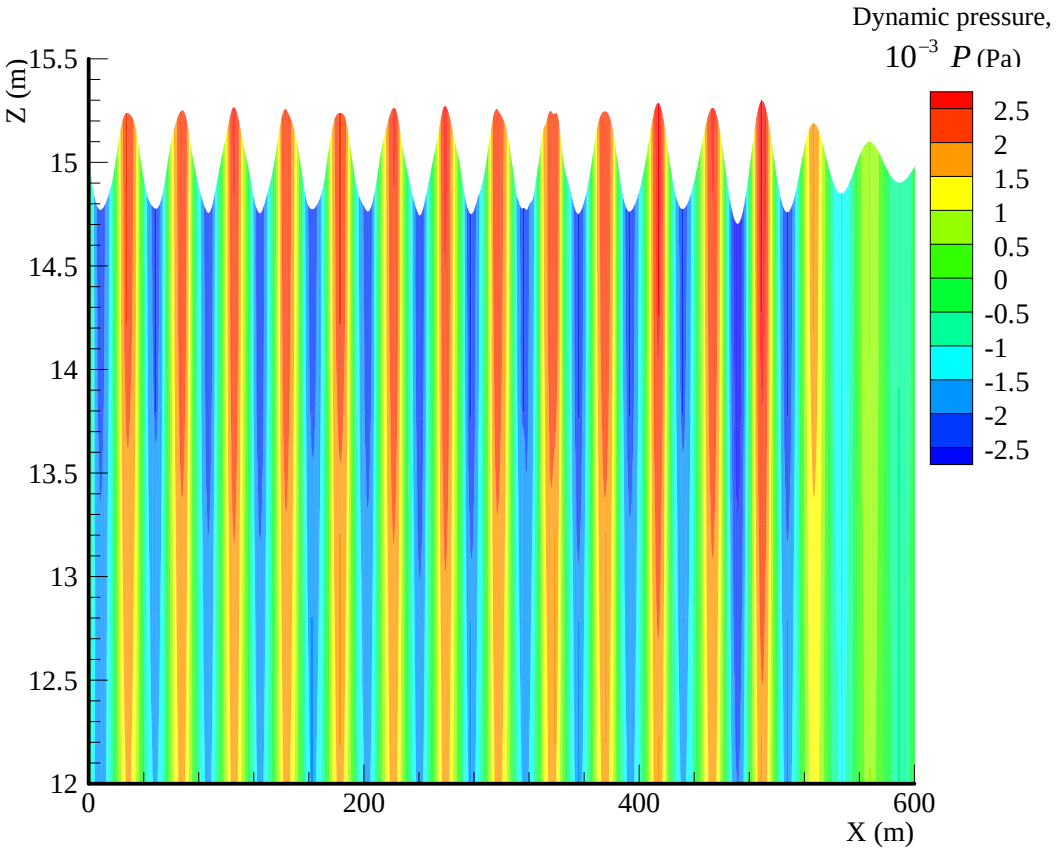

(b) – Dynamic pressure distribution under the wave train and in domain (model prediction)

Figure (5.15) – Dynamic pressure distribution under the Stokes wave train

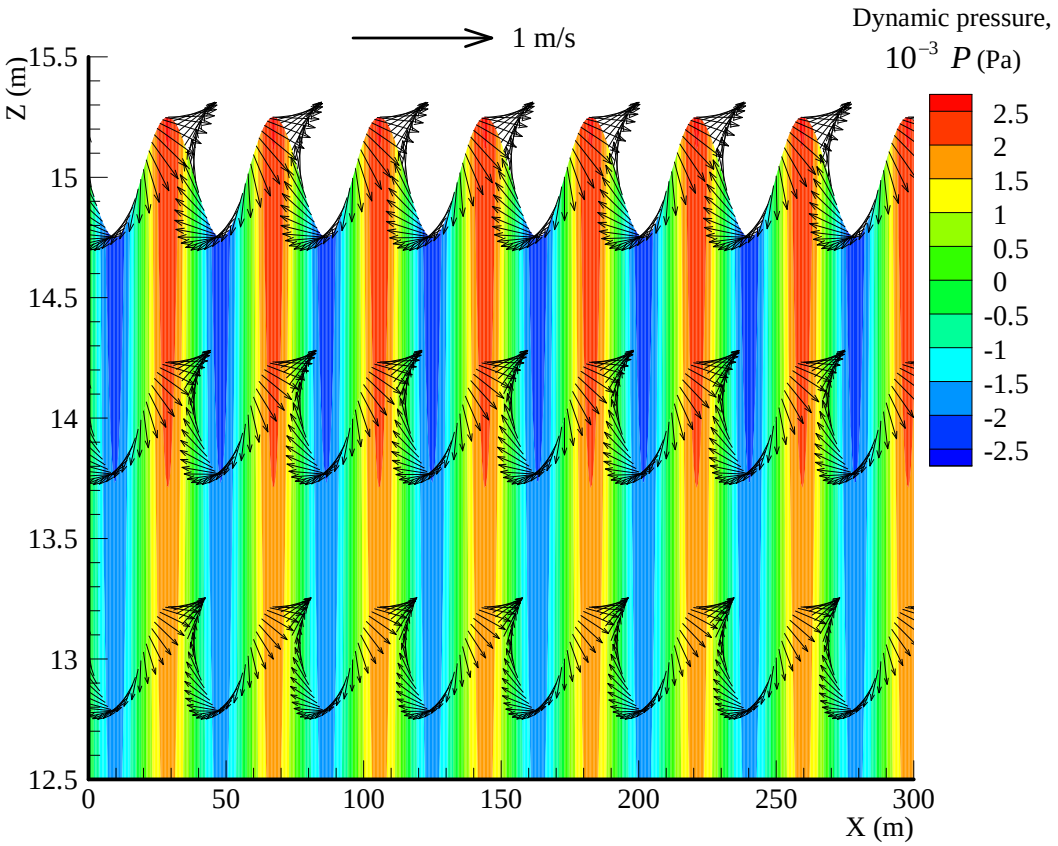

(a) – Velocity field under the wave crest and in the domain (analytical solution)

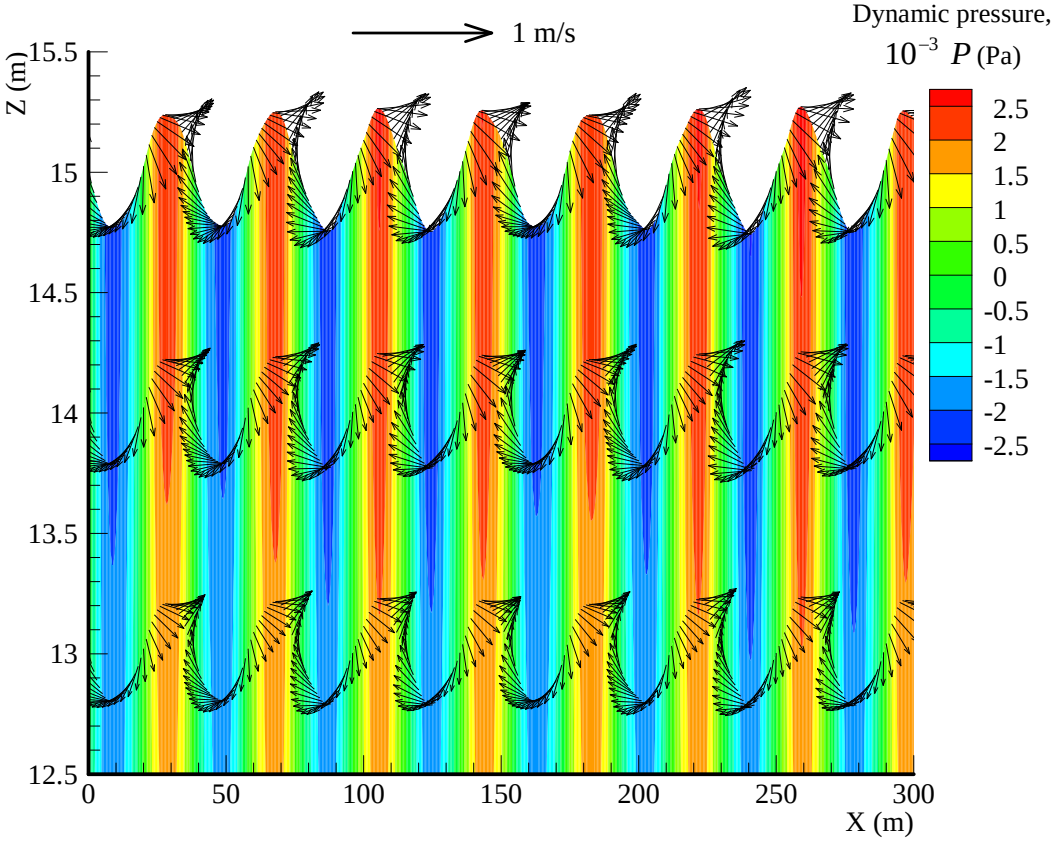

(b) – Velocity field under the wave crest and in the domain (model prediction)

Figure (5.16) – Hydrodynamic velocity field under the Stokes wave train

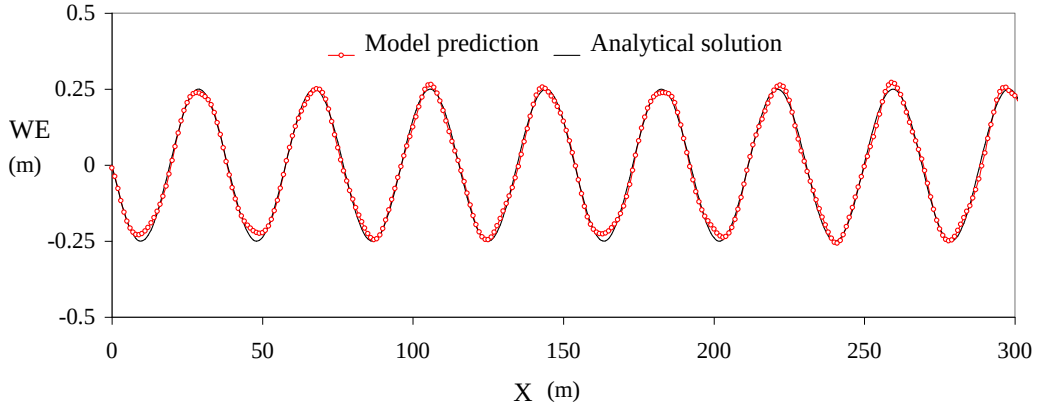

Figure (5.17) - Model prediction of the water surface compared with the analytical solution simulating the flap-type wave-maker for small amplitude Stokes wave at time 120 s

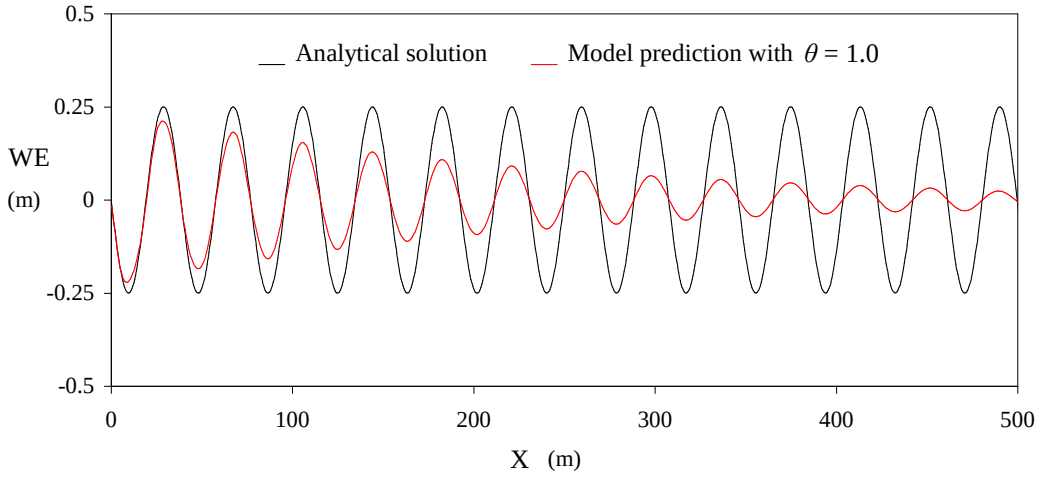

Figure (5.18) - Water surface computation compared with the analytical solution for small amplitude wave train with $\theta = 1.0$

In all tests for the free surface simulation presented herein the value of θ was set equal to 0.5 (Eqs. 4.53-4.56). To show the influence of the value θ in the numerical scheme, the same test was carried out with θ =1. The result is plotted against the analytical solution in figure (5.18). From this figure and figure (5.17) it is clear that the numerical scheme is almost non-dissipative when $\theta = 0.5$, while it is highly dissipative when $\theta = 1$. The numerical results thus indicate that the numerical scheme is stable and accurate when $\theta = 0.5$ and stable but dissipative when $\theta = 1$. It should be noted, however, that the numerical scheme for tidal waves, which are very long waves, is also stable and accurate for $\theta = 1$.

5.4.3 *Solitary Wave Propagation in a Constant Water Depth*

Propagation of solitary wave in constant water depth is simulated to evaluate the capability of the model in tackling nonlinear terms. According to the potential flow theory, a small-amplitude solitary wave propagates at a constant speed without changes in the form, amplitude, and velocities in a constant depth (Mei, 1983).

A solitary wave with amplitude of 1 m in a constant water depth of 10 m has been considered. At the inlet, the time series of horizontal velocities based on the analytical solution of Sorensen (1997) was applied, where the initial position of the wave crest was specified at $x = -150$ m. For the outlet, a free-exit for water was maintained by setting the dynamic pressure equal to zero at the end of the domain. The Dirichlet boundary condition was set zero for w velocities at the flat bed and a Neumann boundary condition equal to zero was prescribed for u in the z-direction. The domain was considered to be 2,000 m in length, which was discretised by grids equal to $\Delta x = 2$ m. The depth of the domain was divided into ten layers. The time step was set to $\Delta t = 0.1$ s and the wave celerity and Courant number were calculated $c = 10.388$ m/s and Cr = 0.519, respectively. Comparisons of the numerical prediction and analytical solution for free surface elevation at $t = 45$, 90, 135, and 180 s are shown in figure (5.19). Dynamic pressure and velocity fields at $t = 180$ s are shown in figure (5.20). Horizontal and vertical velocities at the free surface are also shown and compared with analytical results in figure (5.21). Overall, numerical predictions are almost identical with the analytical solutions, suggesting the capability of the model in simulating non-linear terms in Navier-Stokes equations.

5.5 INTERNAL SEICHE WAVES

Internal waves play an important role in driving mixing in stratified basins. The simulation of the dynamics of a nonlinear regime of soliton formation for basin-scale waves in a rectangular closed basin filled with two water layers with different densities is presented. The results are compared with the experiments of Horn et al. (2001). The motion in the experimental basin is caused by an initial tilt of the interface between two fluids with amplitude η_0. The depth of the lower layer is h_1 and of the upper layer is h_2. The seiche problem is studied by Horn et al. (2001) in a fully enclosed clear acrylic tank, $L = 600$ cm long, $H = 29$ cm deep and $W = 30$ cm wide. The tank could rotate about a horizontal axis approximately through its centre

so that the interface could be initially tilted. A schematic diagram of the tank is shown in figure (5.22). To establish the stratification, the tank was tilted through its maximum angle and partly filled with the volume of fresh water necessary for the upper layer. Salt water at the correct density was then allowed to slowly flow into the bottom of the tilted tank, underneath the previous lighter layer. When the tank was completely filled, it was slowly rotated to a horizontal position. The tank was then very slowly rotated to the required initial angle of tilt. To commence the experiment, the tank was quickly returned to a horizontal position so that the interface was then inclined at the original angle of tilt of the tank. The overall density difference between the upper and lower layers was kept approximately constant at 20 kgm^{-3} $\pm 2kgm^{-3}$ making a buoyancy difference of $g' = 0.2$ m/s^2. When the initially tilted tank was returned to the horizontal, the fluid immediately responded to the baroclinic pressure gradient, the lower layer flowing towards the downwelled end and the upper layer flowing in the opposite direction towards the upwelled end.

The experiments are distinguished by dimensionless amplitude $\gamma = \eta_0/h_1$, and the ratio of depths, $\delta = h_1/H$. The regime is characterised by propagating soliton waves where nonlinear steepening is balanced by dispersive effects for small initial disturbance with parameters $\delta = 0.3$ and $\gamma = 0.3$ (Experiment No. 1) or large amplitude with parameters $\delta = 0.3$ and $\gamma = 0.9$ (Experiment No. 2). For Experiment No. 1 the flow develops solitons after only 5 periods for the interface displacement at the centre of the basin, which is shown in figure (5.23a) for both experimental results and numerical predictions. For larger amplitude of initial tilt (Experiment No. 2), the fluid in the thinner layer is piled up in the left corner of the basin and then reflects from the vertical wall and propagates away from the wall as an internal bore (Fig. 5.23b). This bore develops a tail of solitons after reflection. The degeneration of an initially large-scale wave into solitons is shown in Fig. (5.24) for both numerical simulations and experiments, which shows good agreements.

5.6 MESH CONVERGENCE STUDY

A numerical study has been carried out to assess the mesh convergence of the model, which can provide useful information about the optimal mesh generation for a general 2D problem. Water sloshing in a confined container presented in Section (5.4.1) has been simulated. Ten additional computations have been performed using the numerical domain discretisation as follows:

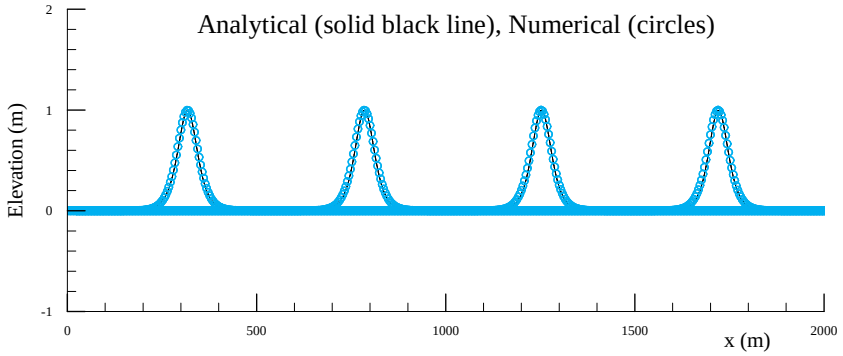

Fig. (5.19) - Comparison of analytical solution and numerical simulations for surface elevation of solitary wave propagation in a constant water depth at t = 45, 90, 135, and 180 s

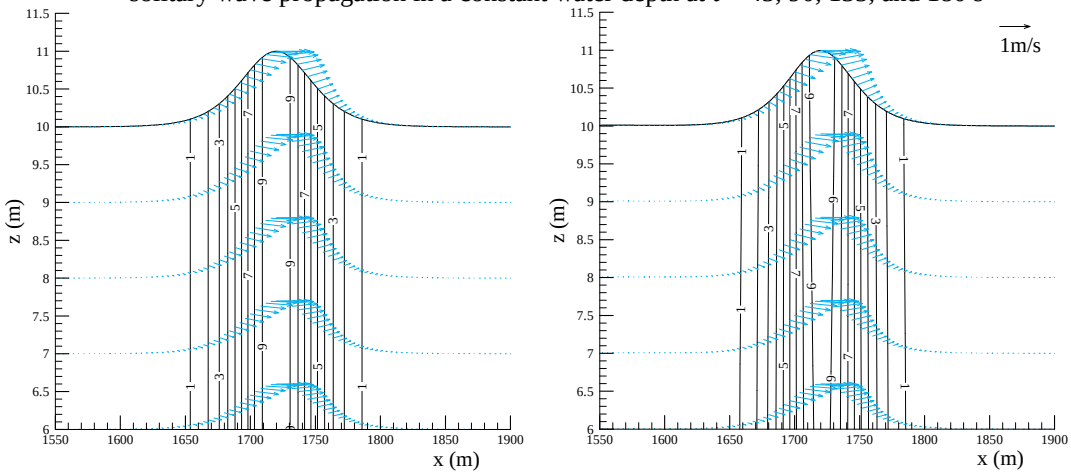

Fig. (5.20) - Comparison of dynamic pressure and velocity field for solitary wave propagation in a constant water depth at t = 180 s. (a) Model prediction, (b) Analytical solution, the dynamic pressure contour values are in Pa.

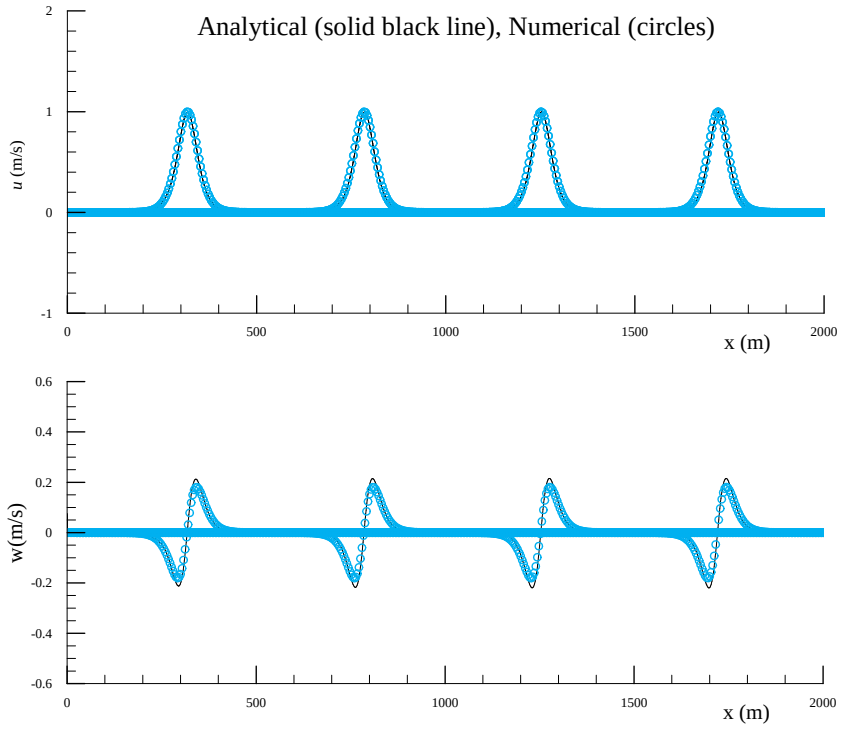

Fig. (5.21) - Predicted horizontal and vertical velocity components compared with analytical solution for solitary wave propagation in a constant water depth at t = 45, 90, 135, and 180 s. (a) Horizontal velocity components, (b) Vertical velocity components

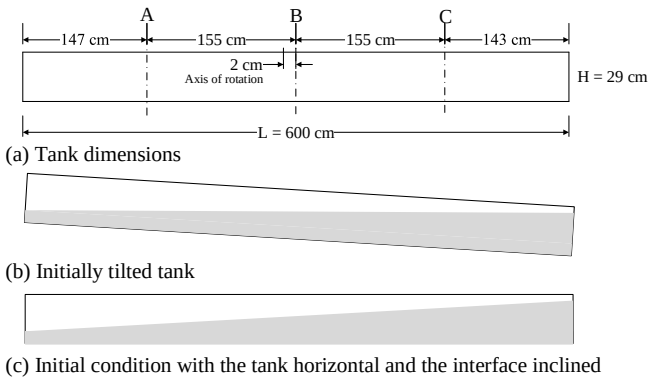

Figure (5.22) - Schematic diagram of the experimental set-up. (a) Geometry detail of the flume, (b, c) The tank and the density structure immediately before and after the commencement of the experiment

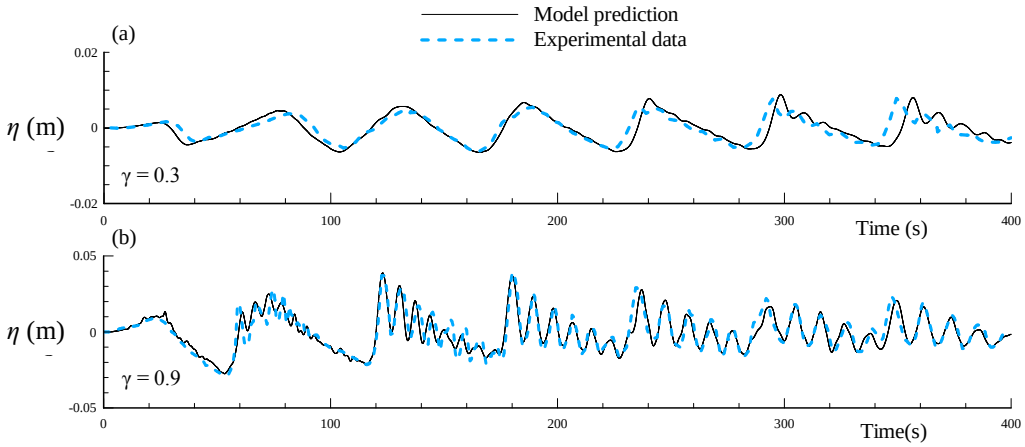

Fig. (5.23) - Interface displacement in the centre of the tank in (a) Exp. No.1, (b) Exp. No. 2

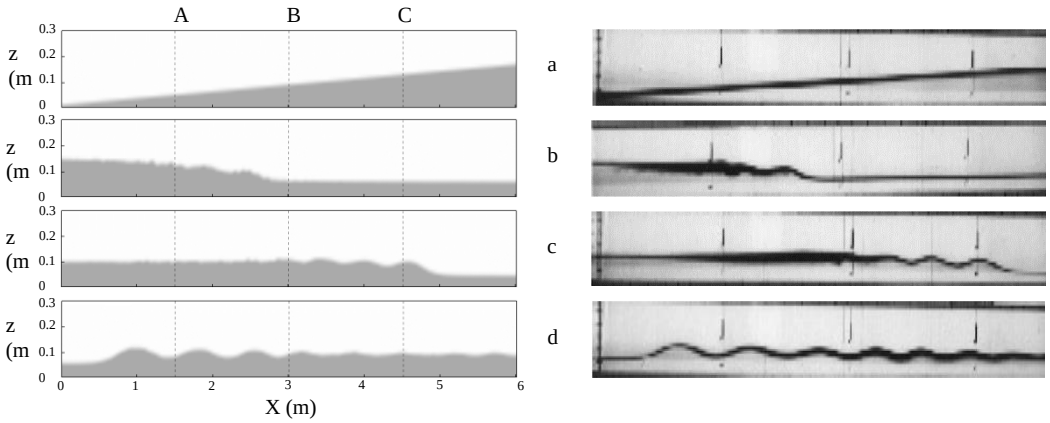

Fig. (5.24) - Density evolution in Experiment No. 2 at successive times: (left) computational and (right) experimental (Horn et al., 2001). (a) t = 0, (b) t = 50, (c) t = 75, (d) t = 140 s

I. Keeping the number of the grids in the *x*-direction fixed and equal to the standard test (100 grid cells: $\Delta x = 0.01\,\text{m}$) and the number of layers as:
   a. 50 layers in *z*-direction
   b. 20 layers in *z*-direction
   c. 15 layers in *z*-direction
   d. 10 layers in *z*-direction
   e. 5 layers in *z*-direction

II. Keeping the number of layers in the *z*-direction constant and equal to the standard test (25 layers) and the *x*-direction grid size according to:
   f. 200 grid cells with $\Delta x = 0.005\,\text{m}$
   g. 50 grid cells with $\Delta x = 0.02\,\text{m}$
   h. 25 grid cells with $\Delta x = 0.04\,\text{m}$
   i. 20 grid cells with $\Delta x = 0.05\,\text{m}$
   j. 10 grid cells with $\Delta x = 0.10\,\text{m}$

The free surface displacement at $t = T$ for the cases (I) including the standard case are plotted in figure (5.25). Figure (5.26) shows the results for the cases (II) and the standard case for the same time.

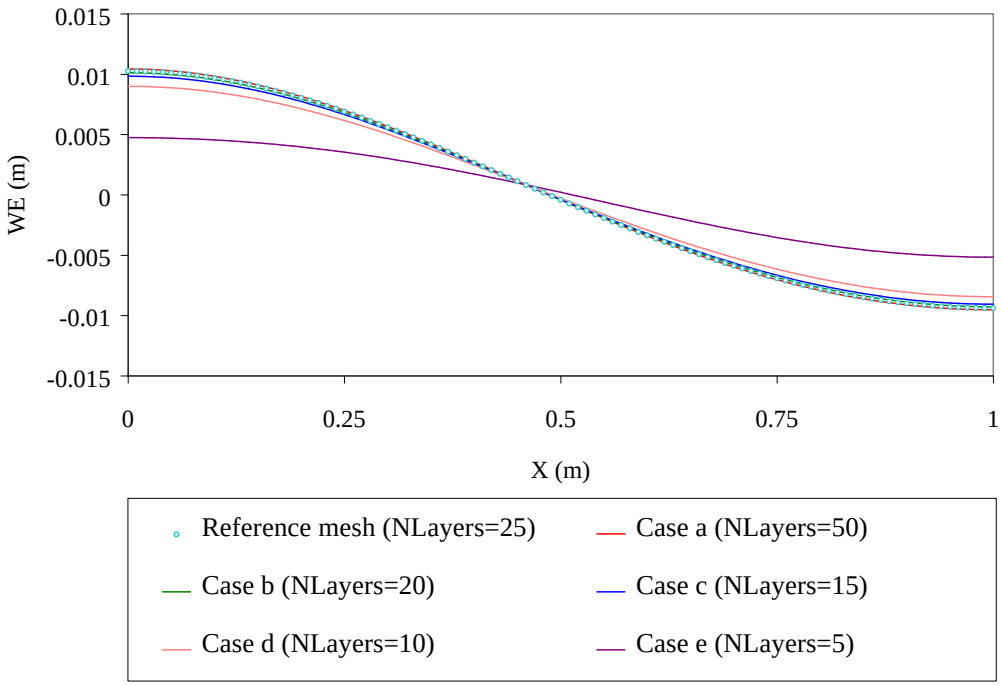

Figure (5.25) - Mesh convergence test in terms of free surface elevation at $t = T$ (grid numbers in the *x*-direction are fixed)

For case (I) the difference for four numerical results are very small, especially between the reference and the finest mesh, implying that the solution is already

convergent in terms of free surface computation when the reference mesh system is used. The other two tests (i.e. n = 20 and n = 15) also show very little difference compared with the reference test results implying that the number of the layers can be chosen as few as 15. For the case with 10 layers the results show noticeable differences and for the case with 5 layers the results are not acceptable. For the simulation of tidal currents, however, the results are much less sensitive to the number of layers in the z-direction and consideration of 10 layers gives satisfactory accurate results. For case (II) the differences for the variation of grid numbers in the range of 10 and 200 in the x-direction are not detectable, implying that the solution in the specified range is independent of the number of grid cells in the x-direction.

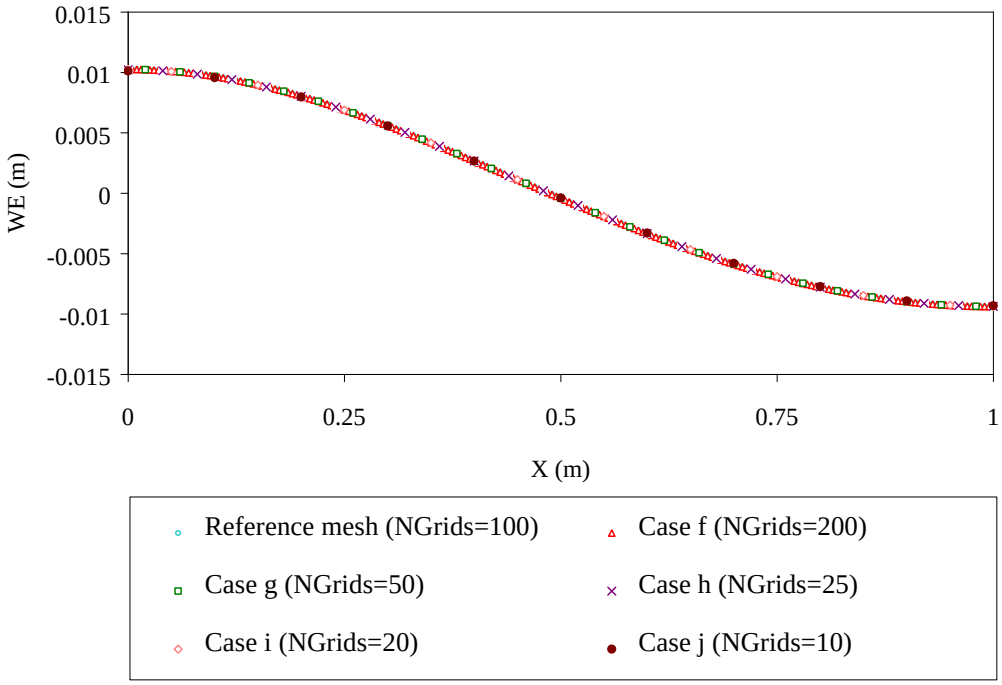

Figure (5.26) - Mesh convergence test in terms of free surface elevation at $t = T$ (number of layers are fixed)

5.7 STEEP-SIDED TRAPEZOIDAL TRENCH

Turbulent flows may develop over steep-sided trapezoidal trenches, for instance in a trench dug along the approach channel to a harbour to facilitate the movement of large carriers. In this test the flow is considered to be steady and the model is applied to a steep-sided trapezoidal trench, which is placed perpendicular to the main flow direction. The numerical predictions have been compared against experimental data, reported by Alfrink and von Rijn (1983). The measurements were carried out in the centre line of a flume in Delft Hydraulics Laboratory. The

geometrical description of the trench and the location of the measurement stations are given in figure (5.27). The bottom of the flume was lined with gravel and the corresponding roughness height, k_s, was taken equal to 0.02 m (Alfrink and von Rijn, 1983).

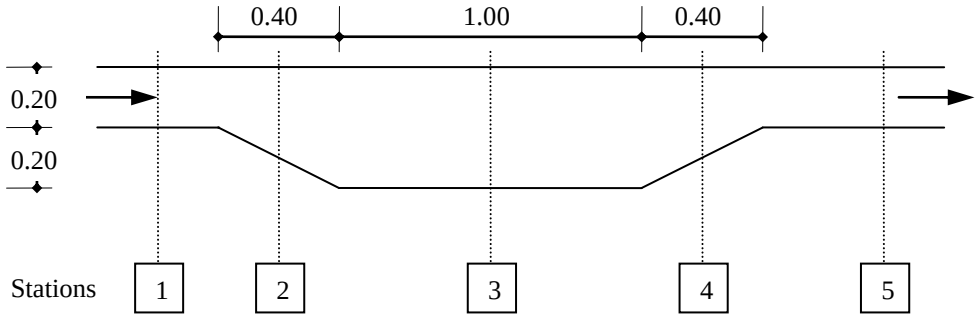

Figure (5.27) - Trapezoidal trench dimensions and location of measuring stations

5.7.1 *Flow Characteristics*

At the inlet, velocity components were prescribed using the standard formulas for open channel flow (Prandtl-von Kármán universal velocity law, equation 3.48) giving:

$$\left.\begin{aligned} \frac{\bar{u}_n}{u_\tau} &= \frac{1}{\kappa}\ln\left(\frac{z}{z_0}\right) \\ \bar{v}_s &= 0 \end{aligned}\right\} \tag{5.42}$$

in which $\bar{u}_n$ is the flow velocity normal and $\bar{v}_s$ the flow velocity parallel to the inlet boundary. The flow velocity profile at the inlet boundary was described by equation (5.42), using the values given by Alfrink and von Rijn (1983) for bed-shear velocity, the constant of von Kármán and the equivalent roughness of Nikuradse as follows:

$$\left.\begin{aligned} u_\tau &= 0.038 \text{ m/s} \\ \kappa &= 0.35 \\ z_0 &= 0.0022 \text{ m} \end{aligned}\right\} \tag{5.43}$$

The computational domain was considered of 10 layers in *z*-direction and grids of 0.05 m in *x*-direction. The time step was set 0.05 s, which maintained the bound limit for Courant number, and the simulation time was 120 s, but the steady state was reached after about 30 s. Figure (5.28) shows the velocity field and the separation and re-attachment points in the trench for the free-surface simulation.

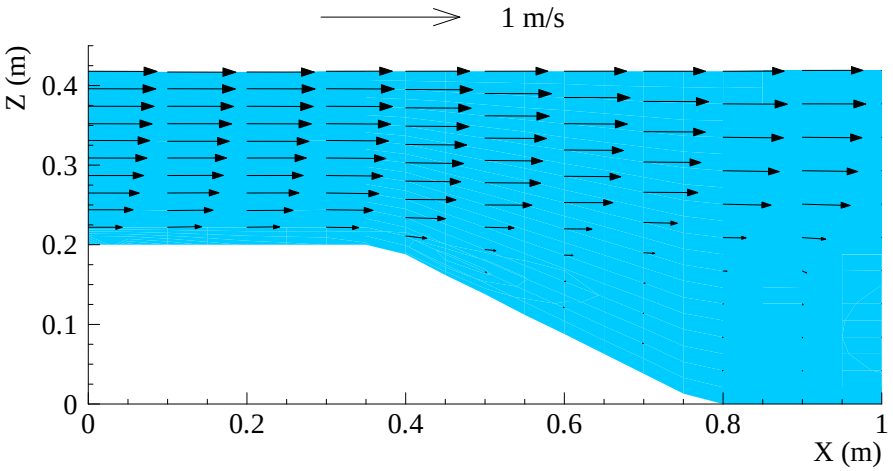

(a) - Velocity field in the first part of the trench showing the separation point happening near the leading edge of the trapezoidal section

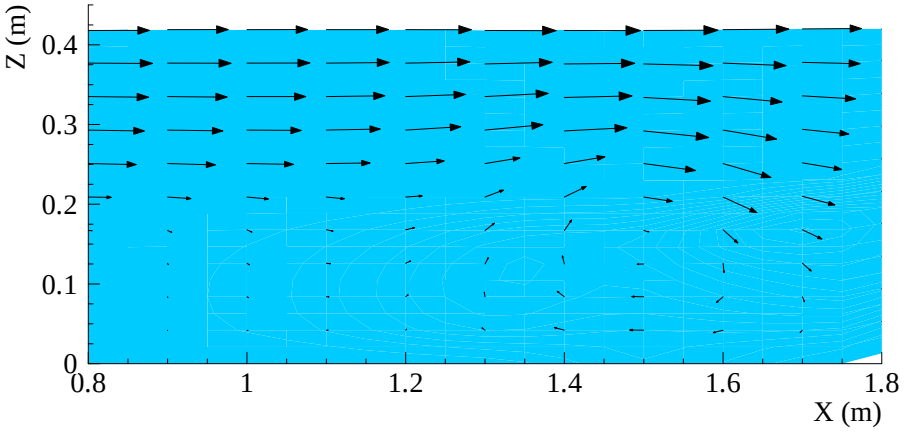

(b) - Velocity field in the middle part of the trench

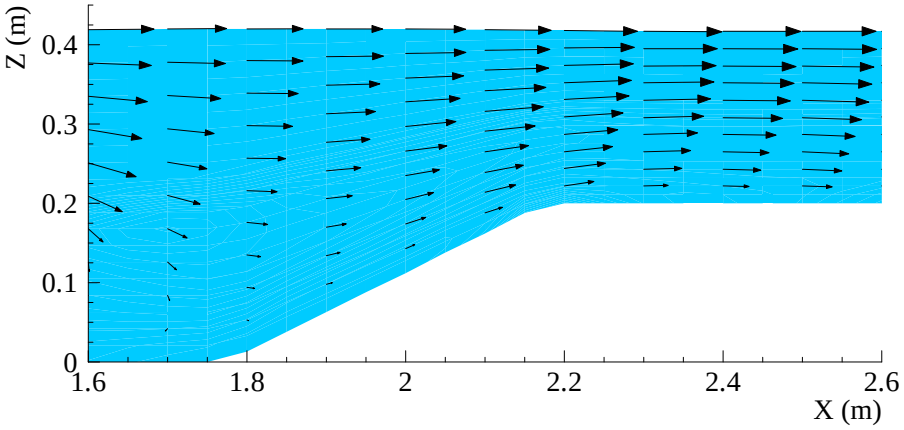

(c) - Velocity field in the last part of the trench showing the re-attachment point happening near the far end of the flat part of the trapezoidal section

Figure (5.28) - Velocity field in the trapezoidal trench

Rigid-lid assumption had generally little effect on the results, which can be added to the attractiveness of this solution and for this case if concerns over

computational time are present. Figure (5.29) shows the general flow field predictions for free-surface and rigid-lid solutions.

Figure (5.30) shows the comparison of the *u* velocity values between the numerical model predictions for the free-surface solution and the experimental measurements (Alfrink and von Rijn, 1983). Flow deceleration with passage over the trench in the numerical simulation results, reported by Basara and Younis (1995), using the same experimental data, is not present in the numerical predictions demonstrated herein. Numerical predictions show a good agreement with the experimental data, but the discrepancy near the bed is apparent, which was thought to be due to the coarse grid size near the bed. The predictions may improve by the use of a coordinate stretching system towards the bed.

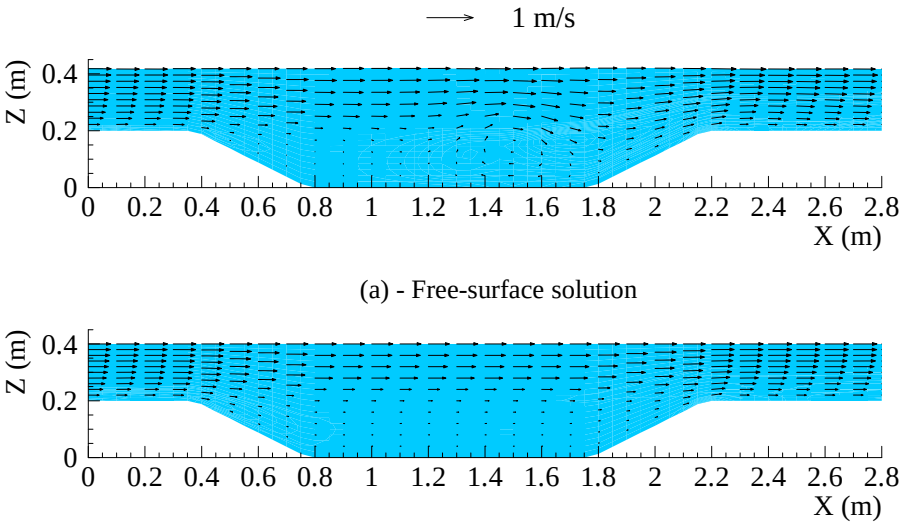

(a) - Free-surface solution

(b) - Rigid-lid solution

Figure (5.29) - Predicted flow field patterns in the steep-sided trapezoidal trench for free-surface and rigid-lid solutions

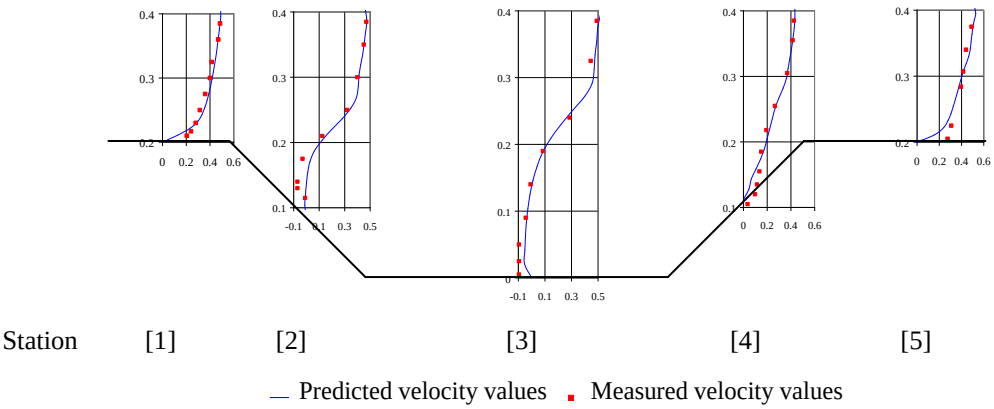

Figure (5.30) - Predicted and measured flow velocity (*u*) values (m/s)

5.7.2 *Turbulence Parameters*

For the numerical simulation the values of the constants in the *k*-*ε* model, were taken as the values presented in Table (3.1), except for $c_{1\varepsilon}$ which was taken equal to 1.60. The plots of turbulent kinetic energy (Fig. 5.31) show this quantity to be finite at the free surface, which is expected with the use of the zero Neumann boundary condition at that boundary. One reason for the large discrepancies between predictions and the experimental data, for upper part of the profiles and at upstream of the trench, was thought to be due to the absence of fully-developed turbulent flow, which suggests that the flume may not have been long enough for fully-developed profiles to be attained. Downstream of the trench, predictions and measured values show much better agreement where the turbulent flow is thought to be developed.

To further investigate the reason for the unsatisfactory predicted results of turbulent kinetic energy, a mesh refinement study was carried out and the inlet boundary conditions for the *k* and *ε* were set to the recommended values of Alfrink and von Rijn (1983). The inlet boundary conditions for *k* and *ε* were prescribed using the standard formulae for open channel flow as follows:

$$\left.\begin{aligned} k &= \frac{u_\tau^{\,2}}{c_\mu^{\,0.5}}\left(1-\frac{z}{H}\right) \\ \varepsilon &= \frac{|u_\tau|^3}{\kappa z}\left(1-\frac{z}{H}\right) \end{aligned}\right\} \qquad (5.44)$$

in which *H* is the local flow depth. The implementation of the inlet boundary conditions according to the equations (5.44) had a substantial effect on the results and the general trend of the simulated graphs was similar to the measured values reported by Alfrink and von Rijn (1983). To attain better agreements a mesh refinement study was carried out where three tests with the new inlet boundary conditions were conducted; (a): 10 layers in *z*-direction and dx = 0.04 m, (b): 20 layers in *z*-direction and dx = 0.02 m, and (c): 40 layers in *z*-direction and dx = 0.01 m. Figure (5.32) shows the comparison of the simulated turbulent kinetic energy values for different mesh configurations against the measured values and the predicted results of Alfrink and von Rijn (1983). It is concluded that the grid configuration (b) with 20 layers in *z*-direction and dx = 0.02 m, exhibits the closest agreement of the predictions with the measured values and is very close to the numerical predictions of Alfrink and von Rijn (1983).

Figure (5.33) confirms the logic presented for better agreement of the turbulence parameters in the downstream; due to fully-developed turbulent flow. The turbulence eddy viscosity attains a profile which is very similar to the profile expected theoretically, in a fully-developed turbulent flow.

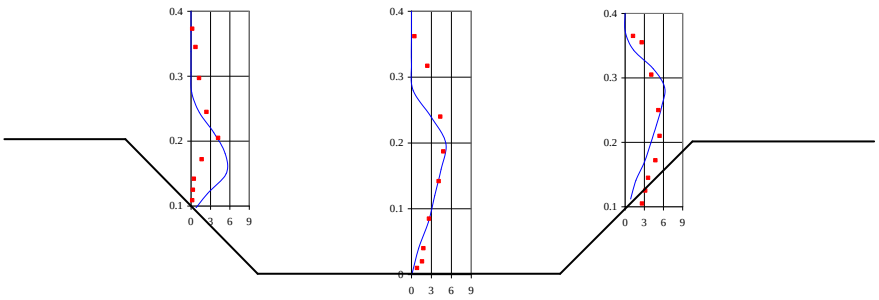

Station [2] [3] [4]

Predicted turbulence energy values Measured turbulence energy values

Figure (5.31) – Predicted and measured turbulence energy values ($10^3 k\,\mathrm{m}^2/\mathrm{s}^2$)

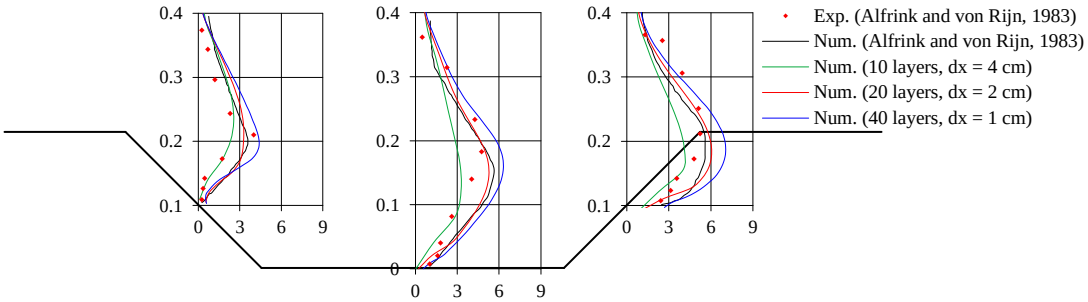

Figure (5.32) – Predicted and measured turbulence energy values ($10^3 k\,\mathrm{m}^2/\mathrm{s}^2$), using the inlet boundary conditions for k and ε by standard formulae for open channel flow, and for different mesh configurations

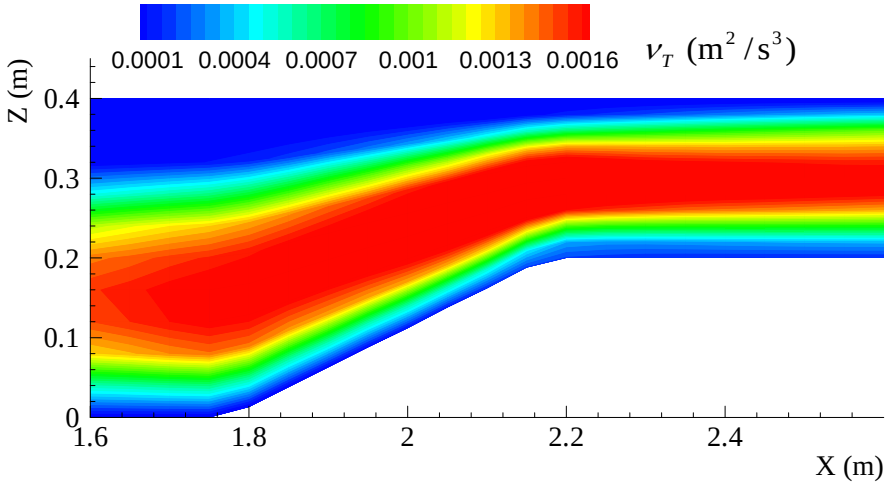

Figure (5.33) – Developed turbulence eddy viscosity in the trench

5.8 NUMERICAL SIMULATION OF TURBULENT GRAVITY CURRENTS OF LOCK-RELEASE TYPE

The time evolution of turbulent gravity current of lock-release type, formed by a finite volume of saline water released instantaneously into water of density ρ_r is studied numerically and compared with the data reported in literature. The *k*-ε turbulence model with buoyancy terms has been used to predict the turbulent eddy viscosity. Many experimental observations based on shadowgraph were consistently successful in determining the general picture and the front location as a function of time after release for the lock-release gravity currents (Simpson, 1997). The observations show that the gravity current passes through two distinct phases, an initial slumping adjustment phase during which the current head advances steadily, and a second phase during which the front velocity decreases with the negative third power of the time after release (Chen and Lee, 1998).

In this study the numerical predictions have been compared against the experimental results reported by Huppert and Simpson (1980). The experiments were carried out in a Plexiglas channel 9.6 m long, 0.27 m wide and 0.50 m high. From their set of the experiments, tests No. 1 and 7 have been chosen to be simulated by the numerical model. The experiment No. 1 is a typical lock-release gravity current case, for which the initial depth h_0 of the saline water is the same as H_0, that of fresh water. In this experiment the channel was filled with tap water to a depth of h_0 = 0.149 m and then a wooden gate was placed in the channel at a distance l_0 = 0.390 m from the left end. Household salt was added to the water behind the gate until density corresponding to $g' = 0.091\ \mathrm{m/s^2}$, was obtained. The gate was then quickly removed and the position of the front of the gravity current was recorded at pre-set time intervals. In experiment No. 7, h_0, l_0 and g' were 0.15m, 0.391 m and $0.094\ \mathrm{m/s^2}$ respectively. Further tap water was then added to both sides of the gate, until the total depth of both sides was H_0 = 0.44 m. The numerical domain was considered of 10 and 15 layers in *z*-direction for experiments No. 1 and 7 respectively, and was discretised by 0.065 m grids in *x*-direction. The time step was set to 0.05s and 0.025 s for experiments No.1 and 7 respectively and in both cases the numerical simulation was carried out for 180 s where the experimental observations were reported for 160 s with time intervals of 10 s. The free-surface model with wall

boundaries at two ends was used and the appropriate boundary conditions for wall and bed were subscribed. The *k*-ε turbulence model with buoyancy terms was used and the values of constants were set according to Table (3.1).

Figure (5.34) shows the numerical prediction of the location of the gravity current for the lock-release type, experiment No. 1. In figure (5.35) the numerical prediction of the location of the gravity current for the experiment No. 7 is illustrated. Both cases show very good agreements with experimental results, which is thought is partly due to using the high-accurate scheme for advection.

In figure (5.36) the numerical solution of mixing in a pool due to gravity currents of lock-release type is presented. A pool of the length of 8.00 m is considered, where half of the pool is assumed to be filled with saline water of salt concentration of 100 g/l and the other half with the water of density $1000\,\mathrm{kg/m^3}$. Both sides are assumed to be 2.5 m deep and to be separated by an impermeable divider at $t = 0$. The divider was then assumed to be suddenly pulled out and the simulation was carried out for 16 minutes with 0.025 s time steps. The numerical domain was considered of 10 layers in *z*-direction and 0.20 m grids in *x*-direction.

5.9 SUMMARY

Six new explicit schemes are introduced for advection. All schemes make use of the upwind quantities, which ensures the fulfilment of the transportiveness requirement. Two high accurate schemes, one in a LOD fashion and the other by the two-dimensional approach, showed considerably higher performance and accuracy. The fifth-order-accurate (on a uniform mesh) upstream LOD scheme is then deployed in the numerical model, which involves six neighbouring points and reduces the discretisation errors by bringing in a wider influence, hence minimising the numerical diffusion errors. The proposed scheme also showed satisfactory results in steep bed, variable water surface and irregular geometries. For diffusion, the performance of the Crank-Nicolson scheme in a domain with non-orthogonal curvilinear mesh shows encouraging results.

A von Neumann stability analysis for the proposed scheme of advection, showed stable solutions for a Courant number below or equal to one for the scheme. For monotone behaviour of the solution, a limiter was used and its influence on the scheme was demonstrated.

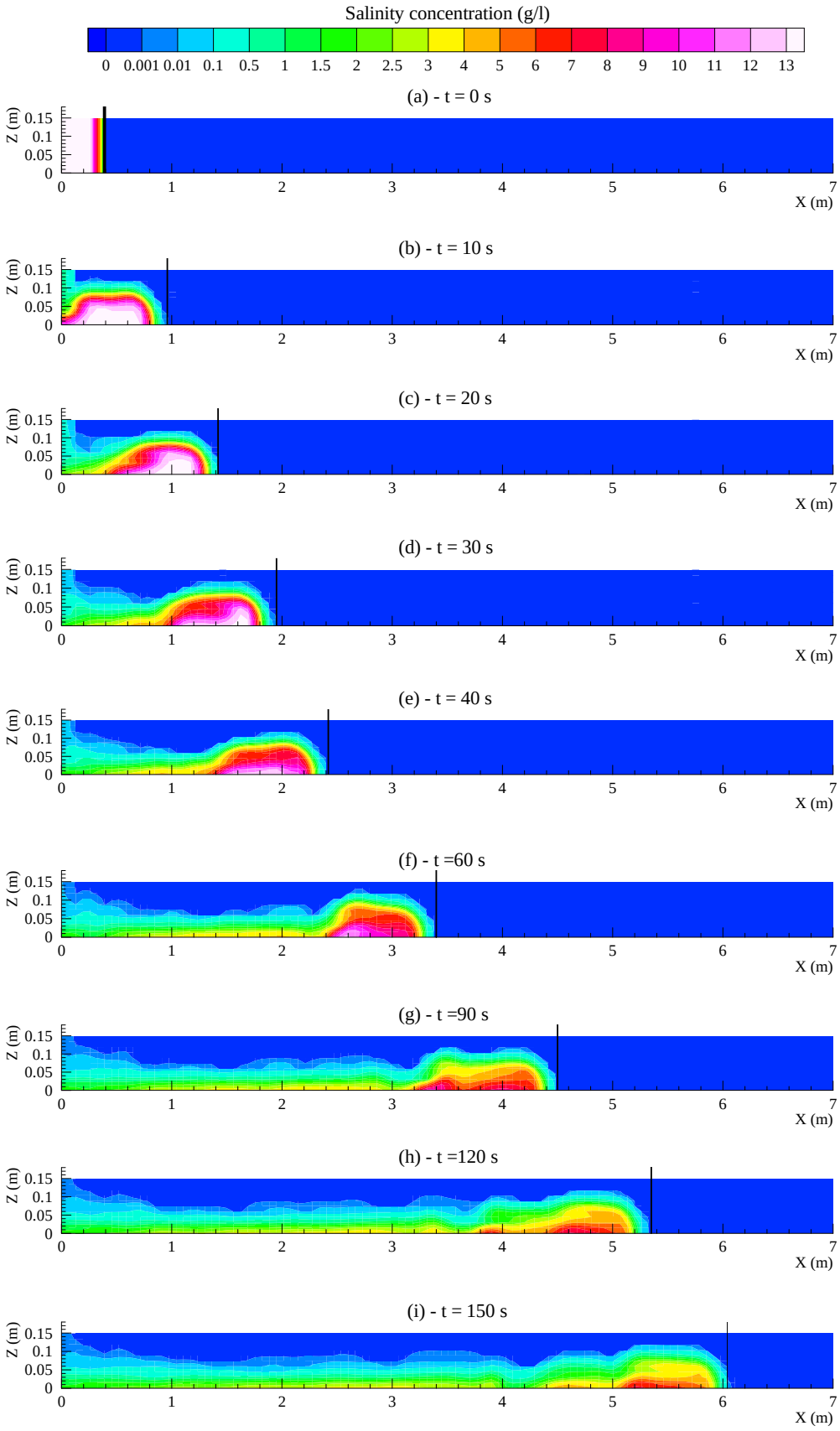

Figure (5.34) – Numerical prediction of time evolution of the gravity current for experiment No.1. The solid line in figure (a) is the location of the wooden gate and in the other frames is the experimentally reported location of the nose of the gravity current

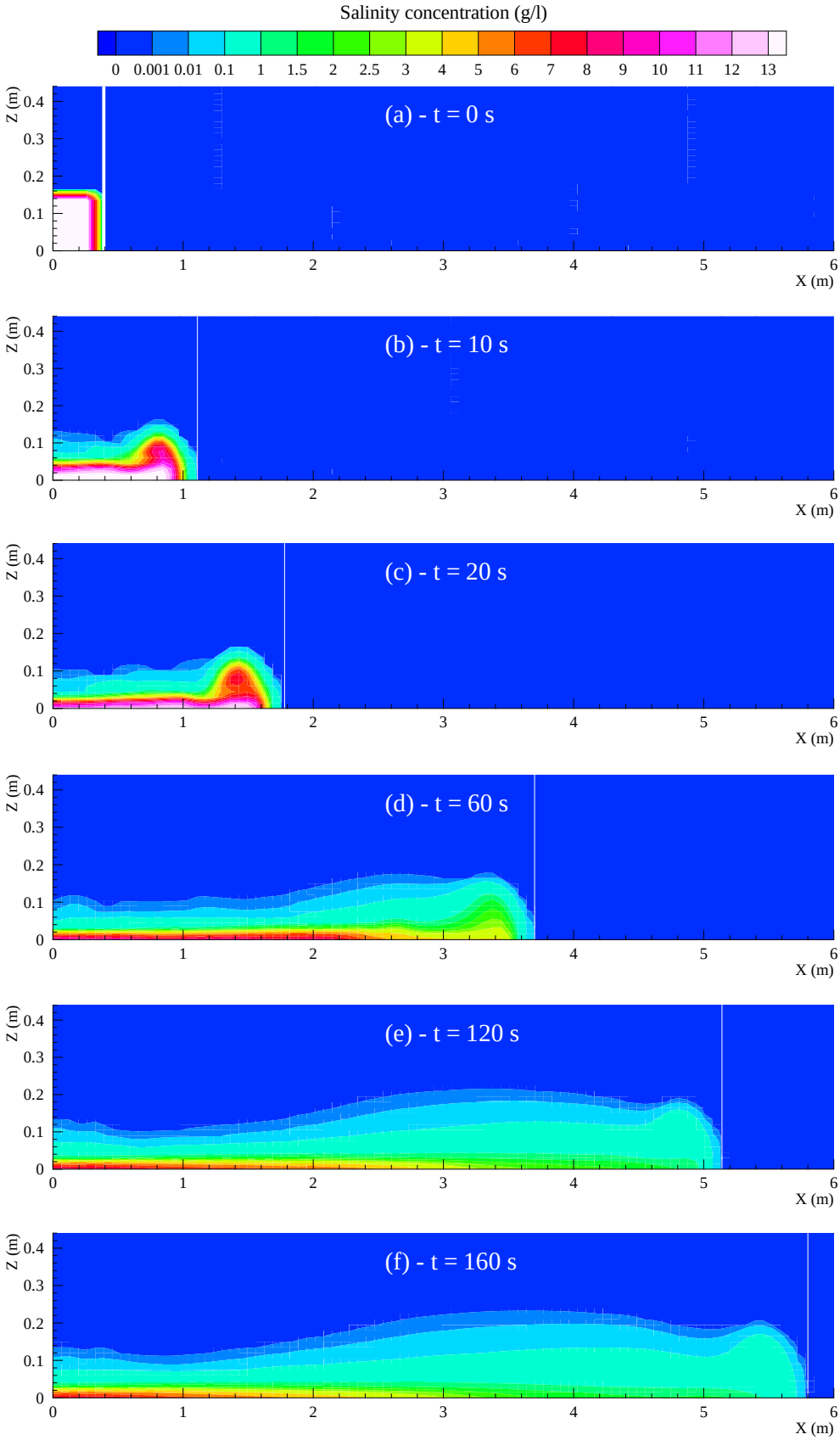

Figure (5.35) – Numerical prediction of time evolution of the gravity current for experiment No.7. The solid white line in figure (a) is the location of the wooden gate and in the other frames is the experimentally reported location of the nose of the gravity current

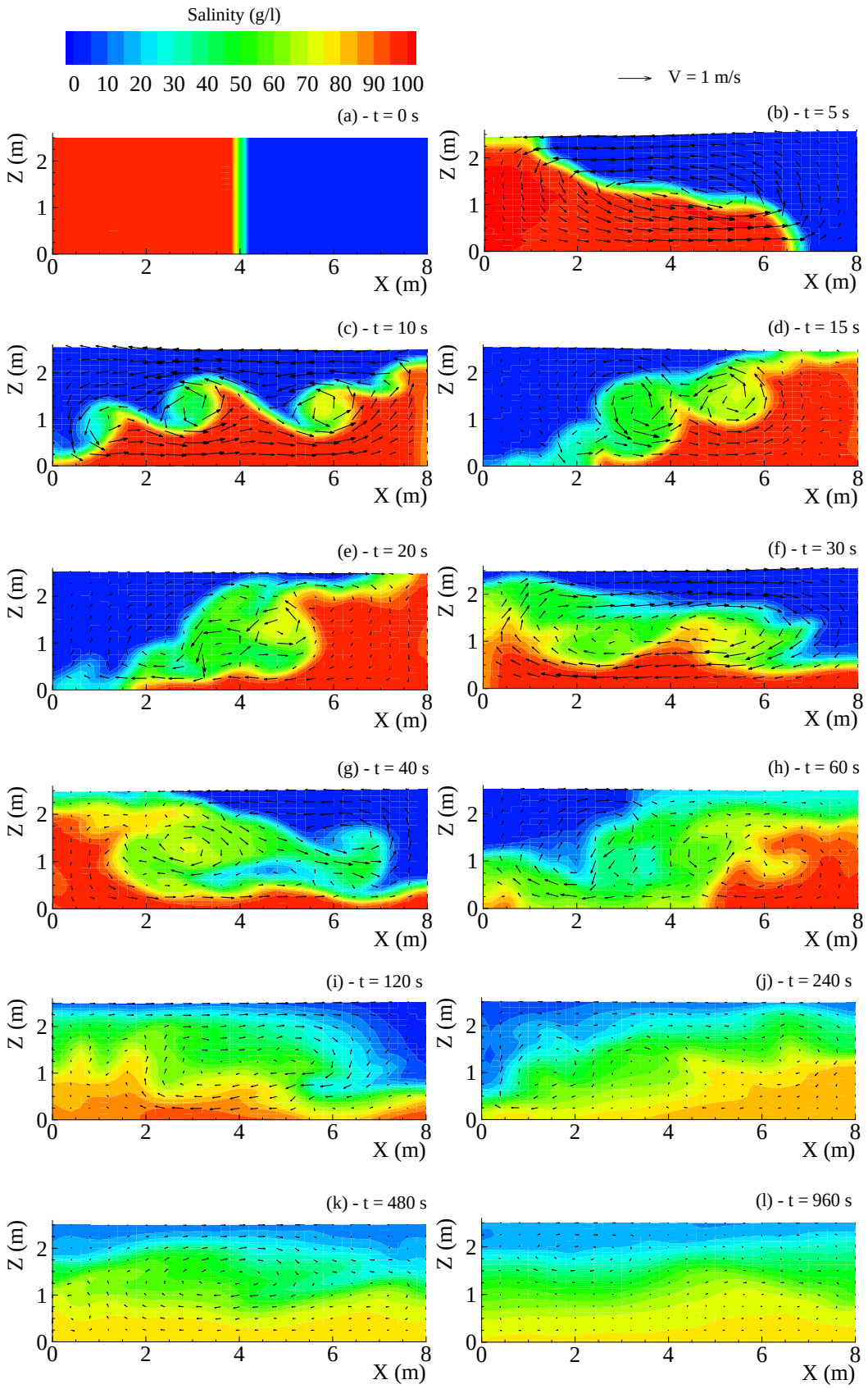

Figure (5.36) – Numerical prediction of salinity distribution and flow field in a pool at different time levels. Left-half is filled with saline water (100 g/l) and right-half with water of zero salinity at time $t = 0$

The prediction of the free surface was demonstrated by the application of a small amplitude standing wave oscillating in a confined basin. The results of the water elevation, velocity field and dynamic pressure distribution compared with the analytical solution were encouraging and confirmed the conservativeness of the numerical scheme. The results of the simulation of a flap-type wave-maker for prediction of water elevation of a small amplitude progressive wave compared with the analytical solution also confirmed the capability of the numerical scheme for satisfactory prediction of free surface. The simulated results of a solitary wave propagating in a constant water depth suggest the capability of the model in simulating non-linear terms in Navier-Stokes equations. The degeneration of an initially large-scale wave into solitons shows the capability of the model in simulating internal waves. To optimise the accuracy and computational time a grid sensitivity study has been carried out.

Turbulent flow characteristics over a steep-sided trapezoidal trench have been compared with the experimental results reported in literature. The flow and turbulent parameters were predicted reasonably well by the numerical model.

The propagation of gravity currents has been studied by prediction of the rate of advance of the front. The numerical results compared against experimental data reported in literature confirmed the capability of the model, using the k-ε turbulence model with buoyancy terms, for predicting gravity currents.

CHAPTER SIX

PHYSICAL MODEL STUDIES

DESIGN AND OPERATION OF THE LABORATORY TIDAL BASIN AND MODEL HARBOUR

"When dealing with water, first experiment then use judgement"

Leonardo da Vinci (Price 1978)

6.1 INTRODUCTION

The hydraulic model was used to verify the mathematical model. The method of numerical modelling the physical model enables distinctions to be made between inadequacies and limitations of the mathematical model and inadequacies and deficiencies of knowledge about the phenomena in real life. The synergistic combination of numerical and hydraulic modelling is especially valuable in complex hydrodynamic situations. It has been particularly used for estuaries, which are inherently complex systems. In addition to the main purpose of using the physical model, which was obtaining appropriate data to develop and verify the numerical model, similitude criteria were deployed to make the physical model, as closely as possible, similar to an idealised prototype in order to achieve a better understanding of the phenomena in the real world.

An idealised, vertically-distorted hydraulic model harbour was utilised to conduct experimental tests for varying distortion ratios, mean water depths, tidal ranges and periods, as well as entrance barrier heights, for both homogeneous and

density stratified flows. Design of the laboratory tidal basin and model harbour has been explained, following a concise review of similitude and scaling criteria, and preceding the demonstration of operation and set-up procedure of the tidal basin and model harbour. The main topics, which are covered in this chapter, will be addressed in the next paragraphs.

Geometric, kinematic (time and velocity), and dynamic (force) similarity should be maintained between model and prototype. Strict satisfaction of the three criteria dictates use of a model scale of 1:1, however, practical considerations often make this ideal difficult to achieve. As a consequence, it is a matter of necessity to identify the processes of primary importance and determine the dominant forces. Subsequently, it is essential to scale the model and model-material properties so as to maintain, as closely as practicable, the same ratios between the primary forces in the model as in the prototype. The forces associated with coastal and estuarine flows are ascribable to fluid inertia, gravity, the physical properties of the fluid, and boundary drag or friction. In almost all situations involving fluid movement, fluid inertia is an important force as well as gravity, which is of prime importance for free surface flows. For many estuaries, bays, and marinas, it is necessary to employ a vertically distorted model; otherwise flows would be laminar and dominated by viscous and surface-tension effects. To counteract this, vertical scales are typically 5 to 20 times larger than the horizontal scales (ASCE, 2000).

Estuaries and harbours located in coastal zones typically are density-stratified, which requires implementation of additional similitude criteria. Density differences can cause buoyancy forces that may have profound effects on flow dynamics. Because the flows in coastal engineering are usually turbulent, they are difficult to model mathematically and physical models can play a significant role in understanding them. Laboratory experimental investigations will always remain one of the most useful tools in coastal engineering because of the inherent limits of deterministic fluid mechanics attributed to turbulence (Le Méhauté, 1990).

6.2 GOALS IN CONDUCTING THE PHYSICAL MODEL

The combination of classifications provided by Dalrymple (1989) and Kamphuis (1991) categorises the physical model used in this study as a validation model and, to some degree, a process model.

Validation models, as their name suggests, are those physical models used to verify numerical models. Because these models are often idealised and simplified to minimise scale effects and originally have been designed to provide a test case that more closely fits the assumptions inherent in the numerical model, they may not resemble anything in the real world. Hughes (1993) has considered an idealised, rectangular harbour constructed with reflecting vertical sidewalls as an example of a validation model. A process model is a physical model designed to study a physical process in order to achieve a better understanding about the phenomena. To complete this classification, the third type of physical model has the goal of attempting to predict prototype behaviour by reproducing to the extent possible all the features and forces of an actual prototype situation and has been termed a design model (Kamphuis, 1991).

As a validation model, the results of the experiments were used for verifying the three-dimensional numerical model, and as a process model, the data obtained from flow-velocity and water elevation measurements in homogeneous tests, and velocity and conductivity measurements in density-stratified tests have been compared, analysed and investigated. Presentation, interpretation, and discussion of the results are demonstrated in Chapter Eight.

6.3 SIMILITUDE AND SCALING CRITERIA

Similitude criteria have been commonly discussed in literature; among them are Langhaar (1951), Yalin (1971), Hughes (1993) and ASCE (2000). Full model-prototype similitude requires satisfaction of the following conditions:

1. Geometric similitude, whereby the ratios of all corresponding linear dimensions are equal and where only similarity in form is involved.
2. Kinematic similitude, whereby at geometrically equivalent points in model and prototype, components of all vectorial motions are in a constant ratio at all times.
3. Dynamic similitude, whereby in addition to kinematic similitude, the force polygons are similar at geometrically equivalent points for model and prototype.

Once the criteria for geometric and dynamic similitude are satisfied, the criteria for kinematic similitude automatically follow.

6.3.1 *Hydrodynamic Similitude*

Tidally induced circulations in estuaries, bays, and harbours are dominated by gravity, and for flows driven by gravity, notably flows with a free surface, a central similitude requirement is equality of Froude number (*Fr*) characterising free surface flow in model and prototype at geometrically similar locations;

$$Fr = \frac{V}{\sqrt{g\,D}} \tag{6.1}$$

where V is the water velocity, g the gravity acceleration, and D is the water depth. This essentially requires that the ratio of inertia to gravity forces be the same in model and prototype. It also may be viewed as a ratio of water velocity (V) to shallow-water wave velocity (i.e. $\sqrt{g\,D}$), in a channel of depth D. The Froude-number similarity criterion, with the notion of $g_r = 1$ where subscript r is the scale ratio, prescribes as follows:

$$Fr_r = \frac{Fr_p}{Fr_m} = \frac{V_r}{\sqrt{D_r}} = 1 \tag{6.2}$$

Modelling difficulties may arise for models of gravity-driven flows, designed primarily on the basis of Froude-number similitude, when the reduced value of the Reynolds number at model scale shifts the flow from the fully rough zone, which prevails at full scale, into a transition-flow or possibly even a laminar-flow zone. The shift in flow region signifies a change in local flow pattern near boundaries, exaggerated emphasis in the model of viscous resistance relative to form resistance, and overall increase in resistance coefficient (ASCE, 2000). As it is not practically possible to select a smaller scale reduction for the estuarine models, an alternate means to remain in the same flow region is to distort flow depths.

Geometrically similar models may prescribe model depths of the order of a few millimetres. Flows that shallow would be laminar and dominated by viscous and surface-tension effects, which do not prevail at full scale. To ensure that the model flow is fully turbulent and gravity dominates, vertical scales may have to be adjusted to typically 5 to 20 times the horizontal scales (ASCE, 2000). Falconer (1980a) used a distorted physical model with vertical distortion of 20:1 in studying the planform influence on circulation in harbours. Falconer and Li (1994) used distortion ratios of 12:1-6.25:1. This vertical exaggeration distorts wide and shallow cross-sections. The distortion increases the model Reynolds number based on depth and makes the flow

turbulent. Table (6.1) demonstrates the relationship between variables of distorted models based on Froude-number similitude. The same notation for variables has been used throughout the thesis.

Table (6.1) - Scale relationships based on Froude-number similitude for vertically distorted models, with $\rho_r = 1$

Variable	Relationship	Scale Distortion Ratio: $G = \frac{X_r}{Z_r}$
Length	L = Length	Horizontal Length: $L_{rx} = X_r$ Vertical Length: $L_{rz} = Z_r$
Slope	$S = \frac{\text{Horizontal Length}}{\text{Vertical Length}}$	$S_r = \frac{Z_r}{X_r} = \frac{1}{G}$
Velocity	$V = \frac{\text{Length}}{\text{Time}}$	$V_r = Z_r^{1/2} = \left(\frac{X_r}{G}\right)^{1/2}$
Time	$t = \frac{\text{Length}}{\text{Velocity}}$	Horizontal Motion: $t_{x_r} = \frac{X_r}{Z_r^{1/2}} = \left(G\,X_r\right)^{1/2}$ Vertical Motion: $t_{z_r} = \frac{Z_r}{Z_r^{1/2}} = Z_r^{1/2}$
Reynolds number	$Re = \frac{V\,L}{\nu}$	$\left(Re\right)_{rz} = Z_r^{1/2}\,Z_r = Z_r^{3/2} = \left(\frac{X_r}{G}\right)^{3/2}$

6.3.2 *Distorted Models*

Attaining adequate dynamic similitude or facilitating sufficiently accurate measurements of flow properties may require violating the criterion for geometric similitude. In that instance a geometrically distorted model is needed, which if employed, might accordingly give rise to scale effects. Practical issues may result in larger distortion of bigger models, encompassing larger areas of shallow flow. For instance, models of estuaries typically have distortion giving G = 5 to 10, and sometimes more. In a study of tidal circulation and flushing in five western Washington marinas, Nece et al. (1980) used distorted hydraulic models with G = 10 and 12.5. The main advantages of vertical distortion are:

1. Reducing expenses incurred in constructing and operating a model;
2. Increasing model values of *Re* by reduction of scale ratio from $X_r^{1.5}$ to $\left(X_r / G\right)^{1.5}$ or *Re* in terms of flow depth (Table 6.1);
3. Providing the possibility of performing flow-velocity and depth measurements with increased accuracy in the model.

Nece (1992) mentioned that the vertical scale must be large enough to permit accurate measurement of water surface elevations, to allow measurements of velocities at various elevations and to produce turbulent flows for most of the tidal cycle.

The main drawbacks of vertical distortion are that three-dimensional and vertically two-dimensional flow patterns and pressure distributions are distorted in response to the altered aspect ratio of the flow. Vertical distortion produces flow cross-sections that have larger flow depths and greater vertical gradients and that should ensure that model flow is turbulent and maintains kinematic similitude, however, this results in reduction of accuracy of geometric and dynamic similitude. In ASCE (2000), the following factors have been addressed to be considered when using vertical distortion:

1. Exaggeration of secondary currents;
2. Distortion of eddies;
3. Occurrence of flow separation on inclined boundaries, whose slope is increased, where separation would not occur at full scale;
4. In consequence to, and interactive with, (1) through (3), lateral distributions of flow in the model may differ from lateral flow distributions at full scale;
5. The ratios between vertical and horizontal forces at full scale will not be preserved at model scale.

When considering the models of large areas, distortion of the models often becomes necessary due to the effect of the viscous boundary layers at the rigid boundaries. This follows from the limitation imposed by viscosity, which establishes an upper bound for the vertical scale, giving (Keulegan, 1966):

$$Z_r^{3/4} = \frac{D_p}{3.5\left(\nu T_p\right)^{1/2}} \tag{6.3}$$

where D_p and T_p are the water depth and tidal period in the prototype respectively.

Complete dynamic and mass-transfer similitude is not possible in distorted models. Introducing dimensionless dispersion Reynolds number as $V_0 L_0 / D_0$ from one-dimensional conservation of mass equation (Harleman, 1966b), where L_0 is a characteristic horizontal length (such as the tidal excursion), V_0 is a characteristic velocity (such as the maximum tidal velocity at the injection point), and D_0 is the longitudinal dispersion coefficient at the injection point, mass-transfer similitude prescribes:

$$\frac{V_r L_r}{D_r} = 1 \tag{6.4}$$

Using the longitudinal dispersion coefficient for homogeneous uniform free surface flow (Harleman, 1966a), and applying the similitude criteria gives:

$$D_r = R_{h_r}^{3/2} S_{e_r}^{1/2} \tag{6.5}$$

In a distorted model, by approximating R_{h_r} with Z_r, and considering $S_{e_r} = Z_r / L_r$, equation (6.5) becomes as follows:

$$D_r = \frac{Z_r^2}{L_r^{1/2}} \tag{6.6}$$

from which it can be seen that the similitude condition given by equation (6.4) is not satisfied;

$$\frac{V_r L_r}{D_r} = \frac{Z_r^{1/2} L_r}{Z_r^2 / L_r^{1/2}} = \left(\frac{L_r}{Z_r}\right)^{3/2} \tag{6.7}$$

Therefore a reduction in the distortion of the model results in a significant improvement in similitude of the diffusion process. Equation (6.7) also shows that diffusive transport in the model is greater than it would be in the prototype. Although physically correct, the equations (6.4-6.7) are based on open channel flow relationships, for instance flows in estuaries and narrow passages. In marinas and small harbours the transport and exchange processes are advection dominated. Flushing behaviour into the harbour can be regarded like jets and the expansion of these jets is similar over a range of scales. It follows that the large scale eddies, which are responsible for much of this mixing, should also scale well. Novak and Cabelka (1981) noted that a correct reproduction of the dispersion coefficients in three-dimensional flow requires an undistorted model. ASCE (2000) also demonstrates the effects of vertical distortion on flow patterns in a figure adapted

from Kobus (1980). It shows that in a distorted model, vertical eddies are larger than in a geometrically similar model and they retain the same shape, instead of the expected stretching in the vertical direction due to distortion. Fischer (1976) concludes that while there is no total agreement on how well physical hydraulic models simulate mixing, such models constitute a useful engineering tool for problems involving three-dimensionality and complex boundaries (in a study conducted by Nece et al., 1979).

6.3.2.1 Flow Resistance

The Froude-number criterion prescribes similitude for forces attributable to fluid inertia and gravity. However, it may be insufficient for prescribing similitude of flow resistance. Flow resistance can be described by relationships such as the Darcy-Weisbach, Manning, Maning-Strickler, and Chézy equations. The Darcy-Weisbach equation states:

$$V = \sqrt{\frac{8\,g\,R_h\,S_e}{f}} \tag{6.8}$$

where S_e is the slope of the energy gradient of the flow, and *f* is the dimensionless resistance coefficient. As demonstrated in Henderson (1966),

$$f \propto \left(\frac{k_s}{R_h}\right)^{1/3} \tag{6.9}$$

where k_s is a length parameter characteristic of the surface roughness (i.e. a characterising surface particle diameter). From equation (6.9), the resistance coefficient scale can be written as follows:

$$f_r = \left(\frac{k_{sr}}{R_{hr}}\right)^{1/3} \tag{6.10}$$

Ideally, when the flow is fully rough, exact geometric similitude is needed to attain $f_r = 1$. The Darcy-Weisbach resistance equation (Eq. 6.8), reduced to the similitude criterion;

$$f_r = \left(S_e\right)_r \left[\frac{R_{h_r}}{V_r^2}\right] = \frac{Z_r}{X_r} = \frac{1}{G} \tag{6.11}$$

and taken together with equation (6.10), indicates that the scale of the roughness elements (i.e. k_{s_r}), varies with the third power of vertical distortion, *G*. The

important conclusion here is that the greater the distortion of vertical and horizontal scales, the greater is the required exaggeration of the model roughness. Because it usually is not practical to select the roughness elements in exact accordance with equation (6.10), considerable trial-and-error adjustment of boundary conditions may be needed to calibrate the model. However in a study of flushing characteristics of small-boat marinas, Nece and Richey (1972) have mentioned that tides are the dominant mechanism for producing water motions in such marinas and bottom frictional effects are not significant in the gross current patterns of the relatively short and deep water bodies; consequently model construction and operation can be simplified.

6.3.3 *Dynamic Similitude for Buoyancy Modified Flows*

Fluid motions in a gravitational field which are originated or influenced by variations in density within the fluid are characterised by the term stratified flow (Harleman, 1961). Density differences lead to dynamic effects through their production of buoyancy forces in a gravitational field. This may be explained by considering the force acting in a stationary fluid. A homogeneous fluid is in a state of neutral equilibrium. The weight of a fluid element is balanced by the pressure exerted on it by the surrounding fluid. This condition holds if elements are displaced to other positions of rest, and no work is required to move them. The commensurate pressure distribution in the fluid is simply the hydrostatic pressure distribution;

$$p = p_0 - g\,\rho\,z \tag{6.12}$$

where p and p_0 are local and a reference pressure respectively, g is the acceleration due to gravity, ρ fluid density, and z is the elevation.

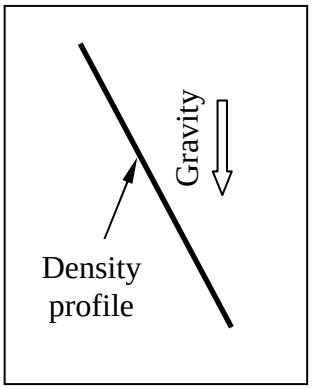

Figure (6.1) - Density profile in a density stratified flow

But in a stratified fluid, the density difference produces a restoring force when a fluid element moves to a less or more dense position in density-stratified surrounding fluid. This can be explained by considering the density profile shown in Figure (6.1). A fluid element moved from a lower to a higher elevation finds itself heavier than its surrounding fluid. Therefore, it is subject to a gravity, or buoyancy force, which tries to restore to its original position. Work is required to move the element of fluid against this force. The same holds for moving the element from a higher to a lower elevation. In this case, the fluid finds itself surrounded by more dense fluid and is again subject to buoyancy restoring force that will try to bring it back to its original position. Again work is required to move the element against this force. A consequence of these forces is that vertical motion, and therefore vertical mixing, is suppressed (ASCE, 2000). The particle, if moved to either lower or higher elevation will return to its original position. It will overshoot and oscillate around its equilibrium position with a frequency of oscillation that is deduced in Section 6.3.3.1. The physical cause of the oscillatory nature of all waves is the restoring force acting on a material particle as the particle is displaced from its mean position. This situation can be clarified by consideration of static stability. Considering a fluid consisting of two layers of different density, as shown in Figure (6.2), the hydrostatic pressure equation (Eq. 6.12) may be presented as follows:

$$p = p_0 - \int_0^z \rho\, g\, dz \tag{6.13}$$

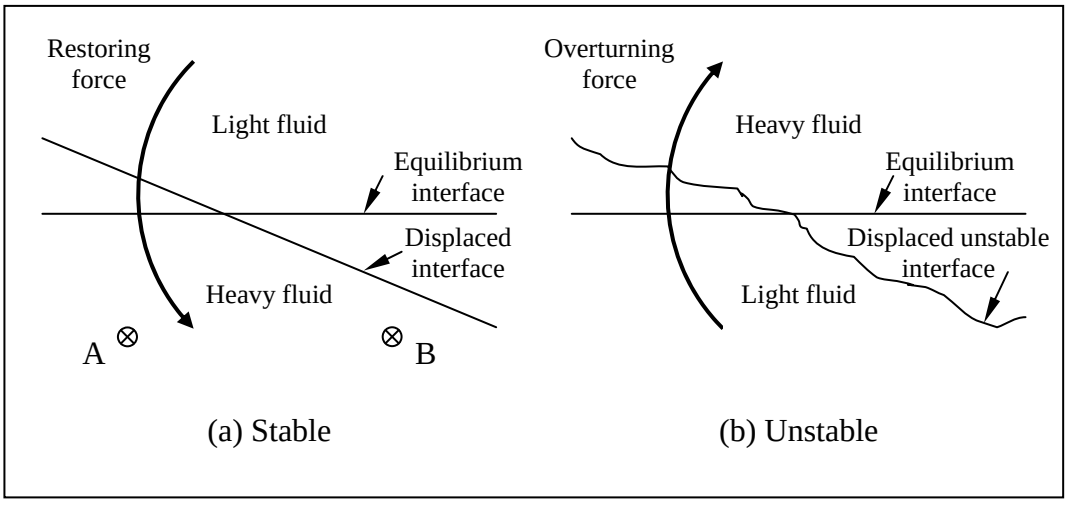

Figure (6.2) - Behaviour of an interface between two stratified fluids of different density (adapted from ASCE, 2000)

so that the pressure at point A is higher than at point B on the same horizontal plane (Fig. 6.2a). A horizontal pressure gradient therefore exists that will cause a restoring force attempting to move the interface back to its horizontal position. The resulting motion can overshoot the equilibrium position and oscillate about it, giving rise to internal waves. The fluid can therefore only be in static equilibrium when density is constant in every horizontal plane. When light fluid is below the heavier fluid (Fig. 6.2b), the equilibrium is unstable and small displacements from the horizontal will grow and lead to advective motions. Oscillation, which characterises wave motion, is therefore possible only if density decreases upward that provides a statically stable state of stratification (Yih, 1980).

6.3.3.1 Similitude Criteria from Equations of Motion

To show the relationship between certain dynamic similitude criteria, the equations of motion for a fluid subject to density differences are considered. Normalisation of the equations for buoyancy modified flows reveals the dominant dimensionless parameters that prescribe dynamic similitude.

The equations of flow can be written for vertically two-dimensional flow (in the *x*-*z* plane) as:

$$\rho\left(\frac{\partial u}{\partial t}+u\frac{\partial u}{\partial x}+w\frac{\partial u}{\partial z}\right)=-\frac{\partial p}{\partial x}+\mu\left(\frac{\partial^2 u}{\partial x^2}+\frac{\partial^2 u}{\partial z^2}\right) \tag{6.14a}$$

$$\rho\left(\frac{\partial w}{\partial t}+u\frac{\partial w}{\partial x}+w\frac{\partial w}{\partial z}\right)=-\frac{\partial p}{\partial z}-\rho g+\mu\left(\frac{\partial^2 w}{\partial x^2}+\frac{\partial^2 w}{\partial z^2}\right) \tag{6.14b}$$

where, *u* and *w* are velocity components in the *x*- and *z*-directions respectively, *t* is time, and μ is the dynamic viscosity of the fluid. Pressure and density, *p* and ρ, can be expanded about the values p_0 and ρ_0, which comprise a reference state of hydrostatic equilibrium for which,

$$\frac{\partial p_0}{\partial z}=-\rho_0\, g \tag{6.15}$$

so that $p = p_0 + \Delta p$ and $\rho = \rho_0 + \Delta\rho$. Then, if viscosity effects are neglected, equation (6.14b) becomes:

$$\left(1+\frac{\Delta\rho}{\rho_0}\right)\left(\frac{\partial w}{\partial t}+u\frac{\partial w}{\partial x}+w\frac{\partial w}{\partial z}\right)=-\frac{1}{\rho_0}\left(\frac{\partial(\Delta p)}{\partial z}\right)-\frac{\Delta\rho}{\rho_0}g \tag{6.16}$$

From equation 6.16, it can be seen that the ratio $(\Delta\rho / \rho_0)$ appears both in the inertial and buoyancy terms. When $(\Delta\rho / \rho_0)$ is much less than one, which is the case in most estuarine situations, it produces only a small correction to the inertia force compared to a fluid of uniform density ρ_0, but it is of great importance in the buoyancy term. For this case, equation (6.16) approximates as follows:

$$\left(\frac{\partial w}{\partial t} + u\frac{\partial w}{\partial x} + w\frac{\partial w}{\partial z}\right) = -\frac{1}{\rho_0}\left(\frac{\partial(\Delta p)}{\partial z}\right) - \frac{\Delta\rho}{\rho_0}g \tag{6.17}$$

which essentially neglects variations in density insofar as they affect inertia, but retains them in the buoyancy terms. This important approximation was first introduced by Boussinesq and is usually true for flows of hydraulic importance. Thus the effects of density variations are embodied only in the combination $(g\,\Delta\rho / \rho_0)$. This combination occurs so frequently that it is given its own symbol, g', which is known as the modified acceleration due to gravity (ASCE, 2000).

A fluid element in a linearly stratified flow, with a density profile as shown in figure (6.1), which is displaced a small distance from its equilibrium position and released, is considered. The linearised form of equation (6.17) gives for this case:

$$\frac{\partial^2 \eta}{\partial t^2} = \frac{g}{\rho}\frac{\partial \rho_0}{\partial z}\eta \tag{6.18}$$

where η is the displacement from the equilibrium position. The element therefore oscillates in simple harmonic motion with a frequency:

$$N = \left(-\frac{g}{\rho}\frac{\partial \rho_0}{\partial z}\right)^{1/2} \tag{6.19}$$

where *N* is known as the buoyancy frequency.

6.3.3.2 Dynamic Similitude Parameters

In a shear flow, the vertical gradient of the horizontal velocity ($\partial u / \partial z$), also has the dimensions of frequency. A useful non-dimensional parameter results when *N* is combined with $\partial u / \partial z$ as follows (ASCE, 2000):

$$Ri = \frac{N^2}{\left(\frac{\partial u}{\partial z}\right)^2} = \frac{-g\frac{\partial \rho}{\partial z}}{\rho\left(\frac{\partial u}{\partial z}\right)^2} \tag{6.20}$$

which is called the gradient Richardson number, *Ri*. It is the ratio of stabilising gradient to disturbing (shear) gradient. An overall Richardson number is a parameter describing the whole flow where the scales of velocity *V* and length *L* are imposed by the boundary conditions as follows:

$$Ri_0 = \frac{g\left(\Delta\rho / \rho_0\right)L}{V^2} \tag{6.21}$$

A stable density gradient decreases the rate of vertical transport of mass and momentum in turbulent flows, and the most important parameter to describe this effect that follows both from theory and experiment, is the Richardson number (Karelse et al, 1974). This effect arises because vertical mixing involves an increase in potential energy which has to be derived from the turbulent kinetic energy in the water, and such energy is usually generated by shearing action in the mean flow (Bowden, 1983). The Richardson number is a measure of the stability of a stratified flow; the higher *Ri* the more stable is the stratification (Novak and Cabelka 1981). In hydraulic engineering, the square root of the inverse of equation (6.21) is more commonly used; namely densimetric or internal Froude number:

$$Fr_D = \frac{V}{\sqrt{g\left(\Delta\rho / \rho_0\right)L}} \tag{6.22}$$

where *L* can be substituted by *D*, for convenience, to retain the same notation as was used for Froude number. The ratio of Richardson number is (Fischer et al, 1979):

$$\left(Ri\right)_r = \frac{g_r^{'} Z_r}{V_r^2} = \left(Fr\right)_r^{-2} \tag{6.23}$$

The equivalence of Richardson numbers ensures that internal stratified flow phenomena such as generation and breaking of interfacial waves are correctly modelled dynamically. Dynamic similitude of flows in which buoyancy effects are important usually requires the densimetric Froude number to be equal in model and prototype (i.e. $\left(Fr_D\right)_r = 1$). It should be noted that equality of Froude number (Eq. 6.22), does not require the density differences to be the same in model and prototype. However, equivalence of the free-surface Froude number (F_r), and the densimetric Froude number (Fr_D), requires that the same density ratios be used in the model and prototype. Viscous effects are described by the Reynolds number,

$$Re = \frac{\rho V L}{\mu} \tag{6.24}$$

In general, if the same fluid is used in model and prototype, it is not possible to satisfy equality of Reynolds number simultaneously with equality of Froude number (Sharp, 1981). The Reynolds number in the model usually is much smaller than in the prototype. In a laboratory study investigating the effectiveness of using a small-scale laboratory model to predict tidal flushing patterns in small-boat marinas, Nece and Richey (1972) reported that despite the presence of jets and wakes formed by the tidal flows past the vertical breakwater at the entrance and past other sharp corners in the boundary planform, much of the model basin flow was in the laminar regime and had Reynolds number ($Re = V\,d\,/\,\nu$, where V is the local depth-averaged velocity and d is the corresponding water depth) considerably below the 1,000 value commonly associated with the lower limit of turbulent free surface flow. The Reynolds number should, however, be in the same range of flow behaviour. So if prototype flows are turbulent, which happens in most situations in coastal engineering problems, then model flows must also be turbulent. Ensuring that the model flow is turbulent will generally suffice (ASCE, 2000).

Vertical distortion, and also low Reynolds numbers in the model, rules out equivalence of local diffusion characteristics in the model and prototype (Nece, 1984). ASCE (2000) has given an example of ratios of the vertical and transverse diffusion coefficients for distorted models and has concluded that the implication of the result is that mixing in the model would be too slow vertically and too fast transversely. Nevertheless, it is apparent that diffusion coefficients in physical models may differ significantly from the correct values. Despite all shortcomings and limitations for physical models, which have been addressed in this chapter, Fischer et al. (1979) mentioned that although hydraulic models may be more expensive than computer models, they have a very great advantage for some situations, especially for three-dimensional density-stratified flows.

6.4 DESIGN OF THE LABORATORY TIDAL BASIN

Although provision of wave protection is the primary objective in the design layout of a harbour, knowledge about nature of internal hydraulics governing the tidal flushing and circulation in the harbour is of major importance (Nece and Falconer, 1989a). In order to study the tidal circulation in small harbours and marinas and in particular the model harbour of this study, a tidal basin was designed and constructed to carry out distorted-scale hydraulic model studies for varying mean

depths, tidal ranges and periods, tidal forms, and commonly used distortion ratios in estuarine and coastal studies. Of prime importance for such a laboratory facility is the tide generator component, which needs to be able to produce irregular tides to simulate complex prototype conditions and spring-neap cycles, as well as the regular sinusoidal tides which were used in the current study.

6.4.1 *Hydraulic Design of the Laboratory Tidal Basin*

The tidal basin was constructed by bolting 1.00 m × 1.00 m pressed fibre glass panels together, with the overall tank dimensions being 7.02 m by 4.01 m and with a maximum depth of 0.76 m. All joints were water proofed with silicone sealant. 10 mm thick fibre board laid on the concrete floor of the laboratory, acting as a cushion, provided a smooth surface for appropriate transfer of the weight of the tidal basin to the floor. Tides were generated by a variable elevation waste weir which was fed by a constant-rate water supply diffuser entering the tank through a 6 inch PVC-U pipe. Water then was discharged to the tank through a multiport manifold, surrounded by a perforated stainless steel cylinder containing two 8 mm thick layers of synthetic fibre matting wrapped around the pipe, which acted as a turbulence damping filter material.

The inlet pipe was full of water throughout the experiments as it was fed by another pipe. The discharge through the latter pipe was controlled by a butterfly valve. This allowed the water to fill the inlet pipe and maintain a constant hydrostatic pressure on the pipe in order to provide a uniform delivery of water through the manifold. The inflow was just sufficient to provide a small overflow over the weir for the largest tidal range and shortest tidal period of this study. The whole system was then fed by a tank, which was situated on the roof and water was pumped by a Sulzer experimental pump with maximum speed of 1450 rev/min, total head of 73 ft, and maximum power of 70 hp, from a reservoir, which was located in the basement, back to the tank. The level of water in this tank, which had a capacity of approximately 5 m^3, was controlled by an overflow weir and the capacity of the reservoir was about 50 m^3. A 50 mm thick honeycomb baffle further separated the main working area of the basin from the manifold system to produce a uniform inflow to the 5.28 m by 4.01 m working plan area of the tank. Another 50 mm thick honeycomb baffle was placed near the other end of the basin and at 0.44 m distance from it. The space between this honeycomb baffle and the end wall, which

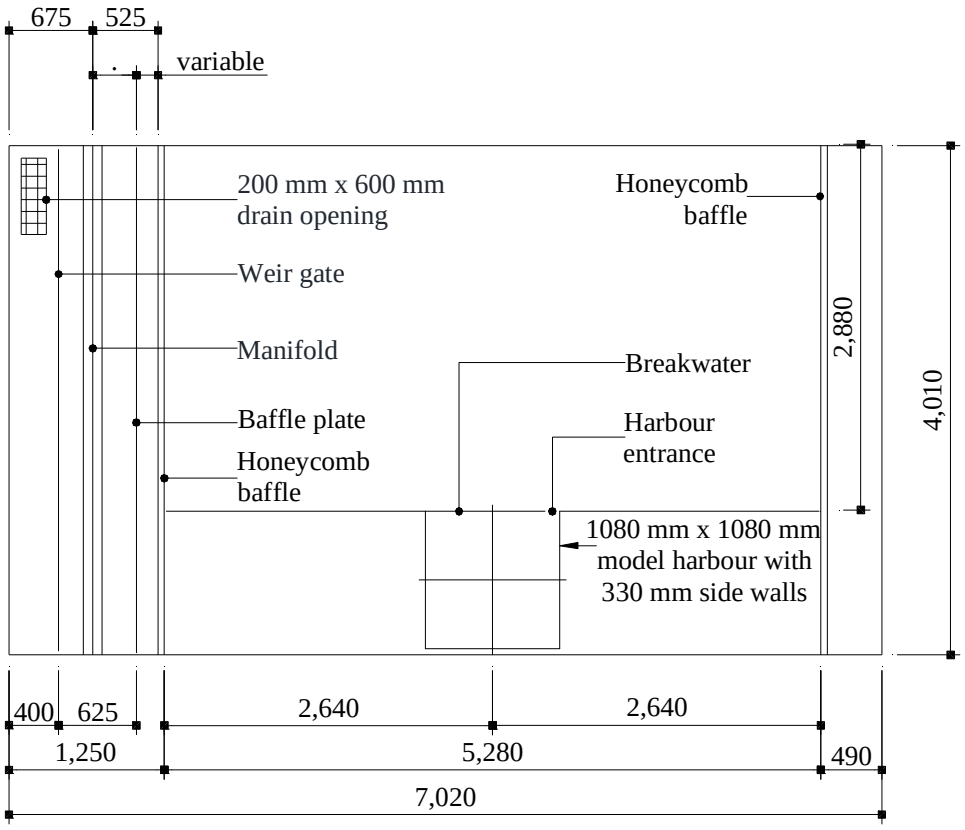

(a) Plan of the laboratory tidal basin and model harbour
Dimensions are in millimetres

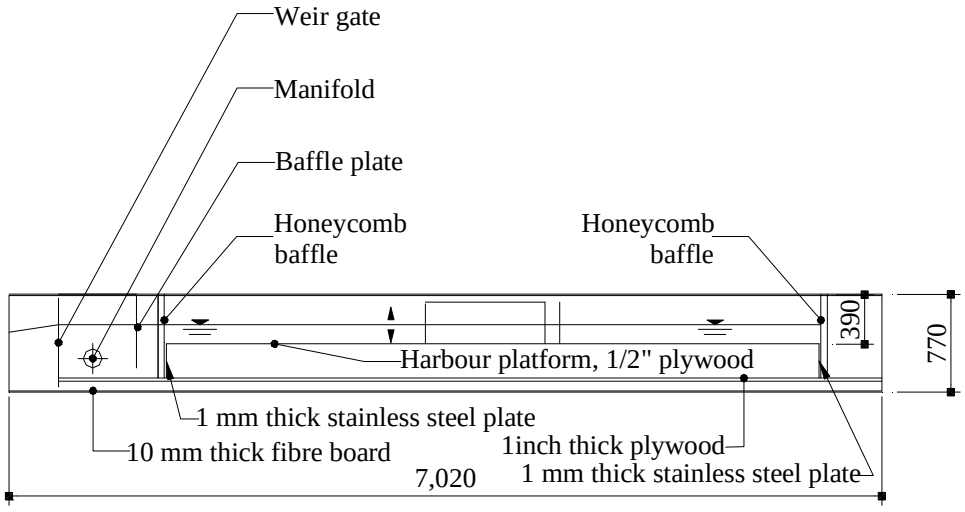

(b) Section through model harbour
Dimensions are in millimetres

Figure 6.3 - Schematic illustration of the laboratory tidal basin and model harbour configuration

accommodated another pipe, was designed for future extension of the laboratory in order to generate currents. Despite the fact it did not play a role in original design of the basin for current study, it was assumed that it partly absorbed the tidal motions before they were reflected by the end wall and again on the way back to the basin. Although using honeycomb baffles improved the flow state and reduced the turbulence, further modifications were needed to provide a uniform flow in the basin. These modifications have been demonstrated in Section 6.6. The schematic illustration of the experimental layout has been given in figure (6.3).

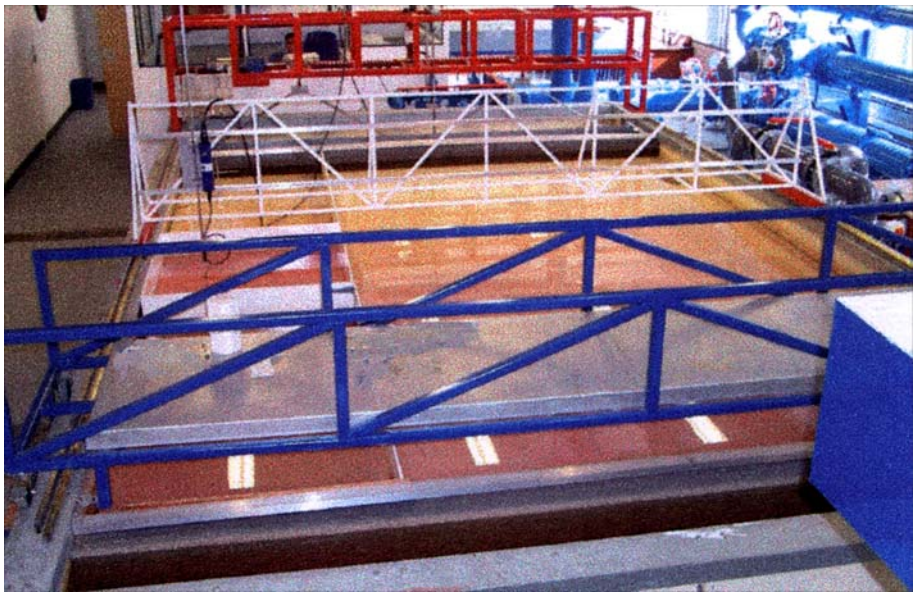

Picture (6.1) - General view of the tidal basin and model harbour

A bridge across the tank facilitated the accessibility of every location of the tidal tank for positioning the measurement instruments and providing the possibility of closer observations without disturbance and interruption during the experiments. Another bridge across the basin provided supports for accurate positioning and holding the velocity meters, wave meters and conductivity probe. Both bridges were movable along the basin and the supports on the second bridge were movable across the basin which facilitated positioning the probes in every point in the basin. Picture (6.1) shows the general view of the tidal basin and model harbour.

6.4.2 Weir Drive Mechanism

Constant amplitude and constant period model tides were reproduced in the tidal tank by means of a vertically oscillating weir, located just inside the tidal tank, adjacent and parallel to the inlet pipe. Although the weir gate drive and control

system demonstrated herein are different from what has previously been used and described in the literature, an overflow weir for tide generation has been used in a number of studies: Falconer (1982), Jiang and Falconer (1983), Nece (1984) and Nece and Falconer (1989a). Falconer and Chapman (1996) have described the design of a similar type of tide generator.

A computerised position control servo loop system was used for driving and controlling the tide generator, which was designed to have a maximum range of 200 mm. The system involved using a variable speed DC motor driving jactuators equipped with a reduction gear drive, a KBRG-240D four-quadrant motor speed controller, position control comparator board, and a Solatron type ACR 100 displacement transducer with maximum range of 200 mm providing the feedback.

The motor was a Baldor 0.75 hp DC type with maximum speed of 1750 rev/min. Each of the two Duff Norton metric jactuators (CE 2500-275), had a capacity of one tonne, 20 mm diameter, 5 mm pitch, standard gear worm ratio of 5:1, and 0.5 maximum hp. The drive from the motor was transferred by a shaft to the jactuators through universal joints, which gave flexibility to any possible misalignment of the drive shaft. Picture (6.2) shows the weir gate and its components. The KBRG is a full-wave regenerative-type control, capable of operating the DC motor in a bi-directional mode. It provides four-quadrant operation which allows forward and reverse torque in both speed directions.

The position control board consisted of a comparator circuit with opto-isolator, AC signal conditioner for displacement transducer, and an emergency stop relay. A digital to analogue output card and an analogue to digital card converted the data to be sent and received by the computer.

The control principle used with the equipment is that a DC voltage was produced by the PC, which was proportional to the movement required by the weir. The position of the weir at any instant was given by $y = f(t)$, where y is the weir position and t is time, and the velocity of the weir was given by the differential of this expression with respect to time. The command signal was updated in the step increments of 0.2 sec. This proceeded by receiving the command signal form the system controller software. The voltage from the PC was used as the command signal for input for comparator circuit. A second voltage for input to the comparator circuit was derived from the displacement transducer and its signal conditioner.

(a) Weir gate and manifold area

(b) Weir gate in operation

(c) Weir gate drive mechanism

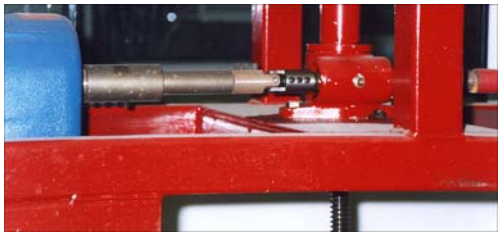

(d) Universal joint

(e) Safety switches

Picture (6.2) - Weir gate, drive and components

This signal was proportional to the position of the weir gate and served as the feedback input to the comparator circuit. The comparator circuit then produced an output, which was proportional to difference between the command signal and feedback signal. This signal after suitable amplification was fed to the input of the KBRG velocity controller, which controlled the speed and direction of rotation of the DC motor and hence the position of the actuators. The output voltage from the comparator circuit must be in the range -10<V<10, where the absolute value of 10 volts gives the maximum motor speed in either directions.

The Rossi Motoriduttori reduction gear drive had a scaling factor equal to 12.7. So the drive from the motor was scaled by 12.7 and transferred to the jactuators through the shaft, which in turn drove the weir gate. One turn of worm gear actuators gave one millimetre rise of lifting screw. Thus the harmonic motion of the weir produced an oscillatory water surface within the tank which gave rise to very nearly sinusoidal model tides. Full details of measurement procedures and determination of time relationships between weir crest elevation and tidal curve phase angles have been demonstrated in Chapter Seven.

6.4.2.1 Weir Gate Servo Loop Control Mechanism

The comparator circuit, which is a servo loop controller, compares the command signal received from the computer with the feedback signal from the transducer, and provides the appropriate voltage. This voltage is the required voltage to compensate the difference between the command signal (i.e. expected weir gate position), and the feedback signal (i.e. actual weir gate position), in each interval of updating the command signal. The output voltage from comparator circuit further is amplified by a gain amplifier, which is tuned to provide the right proportional gain and then it is further passed through an opto-isolator circuit, before it is received by the full-wave four-quadrant motor drive. The KBRG motor drive then controls the speed of the motor dependent upon the received voltage. The Tacho generator has a velocity feed back to the speed controller to ensure the accuracy and efficiency of the motor drive controller. Safety switches override the control system and shut down the KBRG controller and consequently stop the weir gate if the weir gate exceeds and overshoots the designed maximum range of movements either side of the mean level position. The command signal is generated digitally in the computer. A digital to analogue card converts the command signal before it is sent to the comparator

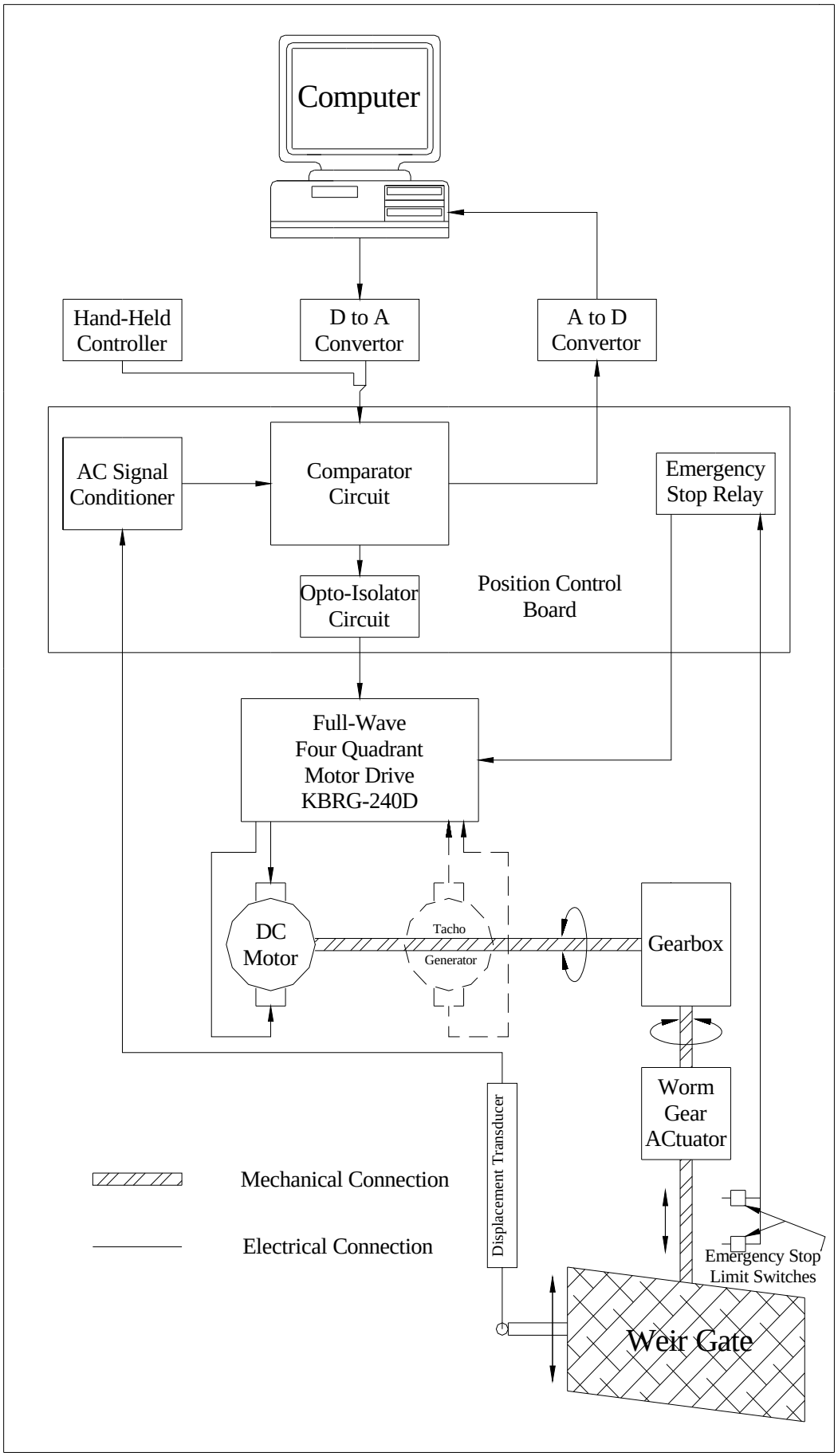

Figure 6.4 - Schematic diagram of weir gate control system

circuit. The feedback from transducer received by the AC signal conditioner is also passed for monitoring purposes to the PC through an analogue to digital card. This feedback signal provides the information of actual weir gate elevation and, together with the command signal, is displayed on the monitor and is recorded through a data-logging software. During the experiments the water elevation and conductivity data were also transferred to the PC through the analogue to digital card, where they were displayed and recorded together with the weir gate elevation data. Data-logging systems are described in Chapter Seven. Figure (6.4) illustrates the schematic diagram of weir gate control system.

The tidal characteristics are fed into the PC by specifying low and high weir gate level, corresponding to the low and high water level, and period. A cyclic variation on the weir movement to simulate the effect of a spring-neap cycle can easily be imposed and more complex tidal situations can be modelled by establishing a suitable function or by specifying a table of discrete values corresponding to the step intervals over the tidal cycle.

6.5 DESIGN OF THE MODEL HARBOUR

The model tidal ranges, mean water depths and planform area had scaled dimensions typical of many existing small harbours in Puget Sound, Washington, USA, with the idealised prototype harbour having dimensions and experiencing tidal conditions similar to many of those harbours sited in the region. Basins considered are essentially enclosed, relatively shallow, typically protected on the seaward side by breakwaters and have relatively small navigation entrances and have no significant fresh water inflow, so that tidal currents are dictated primarily by entrance configuration and basin planform geometry.

The prototype harbour was therefore assumed to have a planform dimension of 432 m × 432 m, a single asymmetric entrance of 48 m width, horizontal bottom and vertical walls, varying mean water depth of 6-10 m, and was assumed to experience repetitive sinusoidal, semi-diurnal tides of period 12.4 hr and range of 4.0 m. The laboratory tests outlined herein utilised vertically distorted models with a 10:1 and 20:1 distortion ratio and both homogenous and density stratified fluids. As it was mentioned in previous sections of this chapter such models do not scale diffusion-dispersion processes, however, the assumption inherently made in this study is that the dominant mode of water exchange is through advective transport. This

assumption has been made in a number of specific model studies of the tidal exchange characteristics in various harbour investigations, particularly where tidal currents have been known to govern the flow field features (Nece and Richey, 1972). Numerical model simulations of similar prototype conditions have indicated that diffusion-dispersion processes are small in comparison with advective transport for such harbour dimensions and tidal conditions (Falconer, 1980b).

Nece (1992) has mentioned that roughness-scaling requirements for these types of harbours can be relaxed. As marina basins are small and internal flows depend almost entirely on the planform geometry and bathymetry of the harbour, bottom roughness scaling essential to larger estuary models is not needed. Because the tidal currents are indeed quite strong in the basins modelled, it is safe to ignore Coriolis as well as wind and wave effects, and because the basins are relatively short and deep, the absence of a friction calibration is not viewed as a major concern (Nece et al, 1976), so the effects of wind action, short period surface waves and the earth's rotation have also been neglected in the laboratory studies. Similar laboratory models had been used in a number of studies conducted by Falconer and Mardapitta-Hadjipandeli (1987), Nece and Falconer (1989b), Falconer and Yu (1991) and Falconer and Li (1994).

The idealised rectangular model harbour was constructed on a level platform covering the full working area of the basin. The harbour platform was constructed of $^1/_2$ inch thick plywood. The harbour constructed of $^1/_2$ inch thick plywood, had a horizontal base, four vertical 330 mm high sidewalls and a single asymmetric entrance. The entrance barriers were made of PVC plastic, which were in varying heights ranging from 60 to 200 mm. In each set of the experiments, barriers were placed and sealed at the entrance. The model harbour was positioned at one side of the tidal tank and received long-shore currents, with the harbour bed being raised above the floor of the tidal tank to give the correct depth in the model at the mean water level. The harbour platform was screwed to aluminium channel support beams which were placed along the basin. The beams were raised to the elevation needed for providing correct mean depth in model by using height adjustment screws, which were bolted to them, and rectangular box levelling supports. The breakwater was extended along the whole length of the basin and to the honeycomb baffles. Picture (6.3) shows the location of the harbour in the tidal basin.

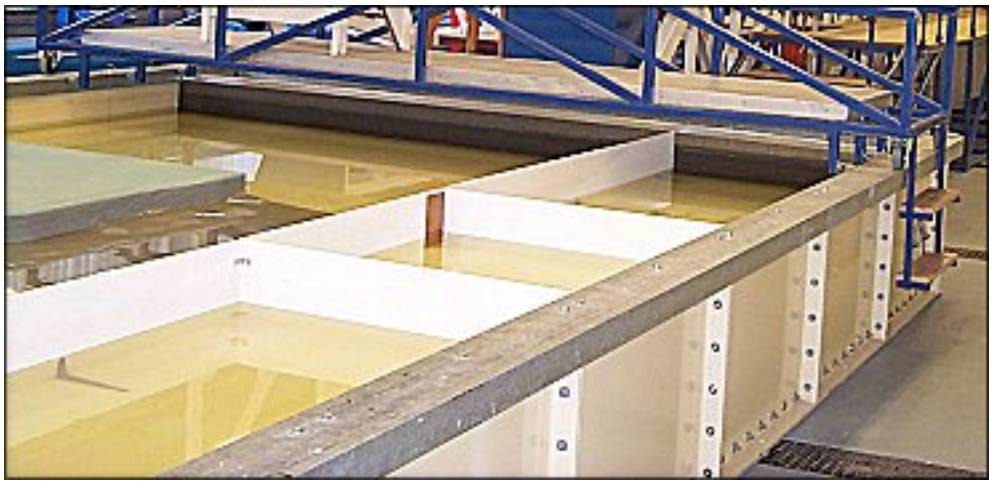

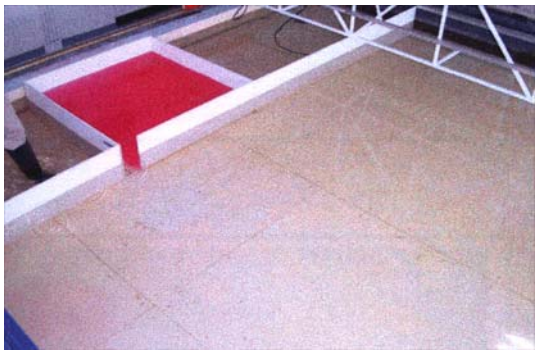

Picture (6.3) - Model harbour location in the tidal basin

As has been discussed in this chapter, in modelling most free surface flows, the flow Reynolds number (representing proper viscosity scaling) and the Froude number (representing gravity scaling) cannot be satisfied simultaneously for coastal and estuarine models. The usual practice to overcome this dilemma is to ensure that the model-scale flow, like the full-scale flow, is fully turbulent. This requirement implies that viscosity does not influence the results, and it thereby relaxes strict adherence to Reynolds number similitude and therefore a central similitude requirement is equality of Froude number in model and prototype, because waves and tidally induced circulations in coastal regions, harbours, and estuaries are dominated by gravity and inertia forces.

Using horizontal and vertical length scales of 400 and 40 respectively, for the distortion ratio of 10 and, 400 and 20 for the distortion ratio of 20, the scaled laboratory model harbour had a planform dimension of 1080 mm × 1080 mm, mean depths of 150, 200 and 250 mm for various test arrangements, and an entrance width of 120 mm. Idealised model harbour dimensions are summarised in Table (6.2).

Table (6.2) - Model harbour dimensions

Model Type	Horizontal Scale X_r	Vertical Scale Z_r	Model Length (mm)	Model Width (mm)	Entrance Width (mm)	Mean Depth (mm)
1	400	40	1080	1080	120	150, 250
2		20				200

Likewise, using a Froude law scaling relationship for dynamic similarity, the corresponding velocity and time scales for the distortion ratio of 10 were 6.325 and 63.25 respectively, and 4.472 and 89.44 for the distortion ratio of 20 in the same order, resulting in a model tidal period of 708 sec and 500 sec and ranges of 100 mm and 200 mm for the distortion ratios of 10 and 20 respectively. These figures have been tabulated in Table (6.3) for convenience and further reference.

Dimensions and geometric features of the laboratory model harbour also had been previously observed by numerical modelling considerations and by the objective of fitting several different grid sizes perfectly into square harbour shape and across the asymmetric entrance. Numerical model studies of the laboratory basin were undertaken using three different grid sizes, including 12, 6 and 4 cm (Falconer and Yu, 1991).

Table (6.3) - Summary of the scale ratios employed for the laboratory tests

Model Type	Horizontal scale X_r	Vertical scale Z_r	Distortion ratio G	Tidal Range (mm)	Velocity Scale V_r	Time Scale t_r	Model period (sec) T
1	400	40	10	100	6.325	63.25	708
2	400	20	20	200	4.472	89.44	500

6.6 OPERATION AND SET-UP OF THE TIDAL BASIN

To obtain an indication of the path-lines in the basin, a simple visual method was used. Initially the tidal generator was run for two complete tidal cycles so that a tidally averaged steady circulation developed. Plastic fishing floats, weighted at the bottom to maintain a vertical orientation, were used and individual floats could be inserted at any location and at any time of a tidal cycle. Plastic fishing floats inserted

at the same time at three points which divided the width of the basin into four equal parts. Floats were tracked visually and remaining in the same pathline and moving along with the same speed as other floats was a confirmation of uniform flow, and a verification that flows were only in the longitudinal direction of the basin and no cross flows were influencing the direction and speed of the movements of floats. It should be mentioned that here the less restricted definition of uniform flow applies, according to which flow is said to be uniform if it does not change in the direction of the flow (Henderson, 1966).

To obtain the best uniform delivery of water through the original manifold (i.e. the unwrapped pipe with equally distributed holes along the pipe in three rows; top, bottom, and the side facing the working area of the basin), different sets of configuration adjustment of open and plugged holes were examined by using plastic plugs. The measure was obtaining the best possible uniform flow in the basin using the visual method described herein. By using the visual method and dye injection two major circulations were observed, one in the working area of the basin circulating the basin in anti-clockwise direction and the other one in the manifold area also with an anti-clockwise circulation pattern. Figure (6.5) illustrates these circulations and relatively still zones. The original non-uniform delivery of water through manifold was assumed to be attributed to few reasons such as different discharge coefficients of each hole which could also accordingly affect the unequal head loss rate through the pipe. The other reason was assumed to be the possible very little mis-alignment of the pipe due to displacements caused during fitting and gluing the pipe to the inlet pipe and the end wall of the manifold area. However, because the main goal of these tests were to ensure a uniform delivery of flow in the basin, it did not seem necessary to confirm and measure the degree of influence of the reasons mentioned, as long as the modifications applied, provided the undisturbed uniform flow in the basin. The best set of the configuration for the plugs was confirmed by the visual method and by measuring the flow velocity at 9 points which divided the basin area into 16 equal squares (Fig. 6.5). This configuration was maintained and the pipe was wrapped with 2 layers of 8 mm thick synthetic fibre, which as a filter material damped the disturbance of water. The whole pipe was then wrapped by stainless steel perforated sheet forming a cylinder around the pipe. This modification together with using the honeycomb baffles provided a reasonable flow in the basin. Nevertheless the circulations in the working and manifold area, with weaker

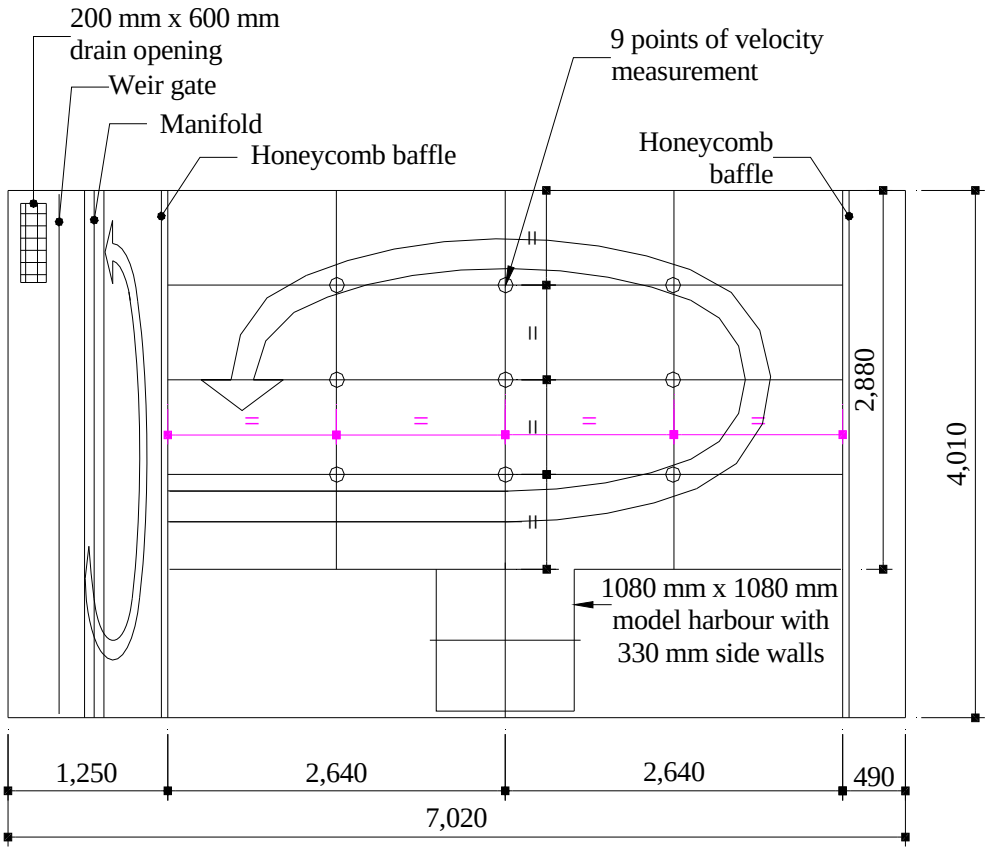

(a) Circulation pattern in the tidal basin and manifold area in flood tide

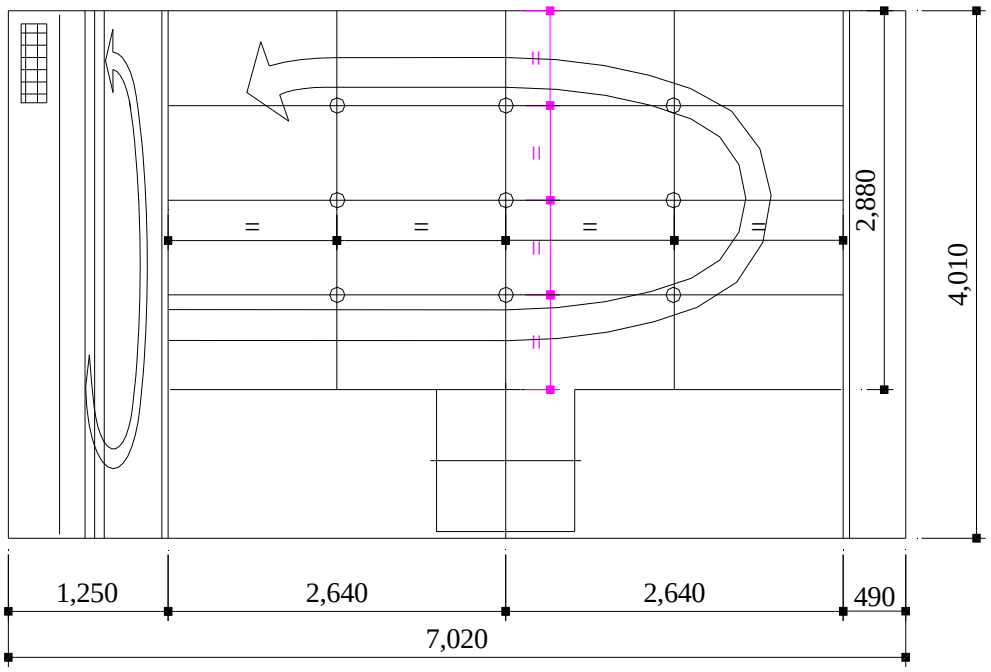

(b) Circulation pattern in the tidal basin and manifold area in ebb tide

Dimensions are in millimetres

Figure 6.5 - Flow patterns in the tidal basin before modifications

circulation however, were observable. The circulation in the manifold area was also assumed to be partly due to a vertical disturbance acting across the depth and also the interaction of flow with the expected nearly still water below the platform of the harbour.

The solution to improve the flow in the basin involved using two 1 mm thick stainless steel plates (Fig. 6.3), which were placed at the beginning and end side of the working area, adjacent to the honeycomb baffles, across the basin and just below the elevation of main platform of the basin (i.e. harbour platform which was raised to provide the correct depth of mean water). This stopped the inflow to interact with the nearly still water under the platform and reduced the vertical disturbances caused by this interaction.

The other modification was using a baffle plate across the manifold area between the honeycomb baffle and inlet pipe, which was movable along this distance with the closest possible distance from honeycomb baffle equal to 175 mm and the farthest equal to 350 mm. In this study the nearest position to the honeycomb baffle was found to be the most efficient. The purpose of using the baffle plate was to stop the interaction of water circumnavigating the manifold with the flow in the working area of the basin. The baffle plate kept the possible disturbance of the water in the manifold area behind the plate, and water flowed underneath the plate, to push the ambient water between the plate and honeycomb baffle to the working area of the basin. This provided an undisturbed uniform flow in the working area of the basin, which formed the designed oscillatory water surface within the tank. The use of the baffle plate improved the flow state significantly. After the modifications were made, in the visual test, fishing floats moved with the flow in their original path-line in flood and ebb tides and no misalignment was observed. Picture (6.4) shows the baffle plate.

Furthermore to obtain an indication of the depth mean velocity fields in the basin and use a more accurate measure to examine the flow pattern, velocity was measured at 9 points in the basin (Fig. 6.5). The results showed that the velocities had the same magnitude for similarly located points along the basin and flow direction (i.e. the points with equal distance from the boundaries; upstream and downstream). The velocities had very low magnitudes in the range of absolute maximum value of 1-1.5 cm/s in the direction of flow, and the cross-flow velocity magnitudes were very nearly equal to zero. The entrance of the harbour was closed

and sealed during these tests, so that no disturbance was caused by the existence of the harbour and water flowed along the sidewalls and the breakwater.

Picture (6.4) - Baffle plate

6.7 SUMMARY

Aimed primarily at obtaining laboratory data to verify and enhance the predictive capability of the numerical model, the hydraulic model harbour was sized so that it also was considered, to some extent and with limitations, as a process physical model using conventional Froude law scaling with length ratios within ranges commonly used in practice in typically distorted models. The design of the laboratory tidal basin and model harbour was explained, and the modifications made to the original design to improve the flow in the basin were demonstrated. The results from visual method and velocity measurements confirmed the existence of a uniform flow in the basin, and provided a good level of confidence to conduct the tests in the model harbour.

CHAPTER SEVEN

PHYSICAL MODEL STUDIES

INSTRUMENTATION, TEST ARRANGEMENTS, DATA ACQUISITION AND SIGNAL PROCESSING

"The success of any physical investigation depends on the judicious selection of what is to be observed as of primary importance, combined with a voluntary abstraction of the mind from those features which, however attractive they may appear, we are not yet sufficiently advanced in science to investigate with profit."

J. Clerk Maxwell (Langhaar, 1951)

7.1 INTRODUCTION

Velocity components in three directions, water surface elevation and salinity have been the elements of the data acquisition for the laboratory tests in the present study.

Instantaneous values of velocity components in three directions at pre-set locations and depths have been measured by Nortek acoustic Doppler velocimeters (ADVs; ADVLab). HR Wallingford wave probe monitors were used for the measurement of instantaneous water levels at the water surface of the same locations as velocity measurements were undertaken. For the data of the salinity, the instantaneous conductivity was measured by a Jenway conductivity meter, model 4320, at preset locations and depths.

The ADV velocity meters, wave probe monitors and conductivity meter have been described and the accuracy of the ADVs is discussed in some detail followed by a review on the sources of the noise and spikes in ADVs. The calibration procedure includes the instrument calibration and the calibration of the recorded readings which has been presented for each instrument.

Tests have been conducted for fresh and saline water conditions to investigate the hydrodynamics of the harbour under tidal circulations and the influence of salinity and stratification on the flow characteristics. It was thought that the hydrodynamics of the harbour would also be affected by the presence of a barrier in the entrance resembling a barrage. Therefore a variety of barrier heights were applied and the experiments were undertaken for each set. The influence of the distortion ratio on the hydrodynamics, circulation and the stratification in the model harbour was investigated by the simulation of two tidal ranges corresponding to different distortion ratios.

The software for ADVs provided by Nortek was used for measuring the velocity components. For measuring the water surface elevation and conductivity, GENIE data acquisition and control software was adapted and used.

The data collected by the ADVs and the conductivity meter were significantly noisy. Therefore, a signal-processing procedure was carried out to minimise the noise in the data. The literature for denoising and despiking the ADV data has been reviewed in some detail. For despiking and denoising the velocity data a linear correlation algorithm was established, whereby a Wiener filter was designed and adapted for the temporal correlation of the signals. For the conductivity a moving average procedure was carried out as the data did not suffer from spikes and exhibited almost a constant band of noisy fluctuations. The water elevation time series showed reasonably clean signal and no filtering procedure was carried out.

As in many experimental programmes, the number of points to be measured and the duration of the experiments are chosen with the economic considerations, an interpolation method for producing the missing data has been provided. This method may be deployed for increasing the sampling frequency and can also be extended to produce data for the spatial domain (for the locations which are not included in the measurements). Moreover, it may be incorporated for smoothing the numerical simulation outputs as a post-processing tool.

7.2 INSTRUMENTATION

The instruments used for the current research work are described in the following sections. Picture (7.1) shows the instruments in operation.

7.2.1 *ADV Velocity-meter*

The ADV is a remote-sensing, three-dimensional velocity sensor, originally developed and tested for use in physical model facilities (Kraus et al., 1994). Its operation is based on the Doppler shift effect. Velocimeters use acoustic sensing techniques to measure flow in a remote sampling volume. The measured flow is practically undisturbed by the presence of the probe.

A Velocimeter consists of three modules: the measuring probe, the conditioning module with cable (Pic. 7.2a), and the processing module. Picture (7.2) shows the three types of the ADV velocimeters used in the present study. The down-looking probe is suitable for most situations with the exception of locations near the surface, the side-looking probe is capable of measuring the velocities near the walls, and the up-looking probe facilitates measuring the velocity of the locations near the water surface.

The acoustic sensor consists of one transmit-transducer and three receive-transducers (Pic. 7.2e). The three 10-MHz receive-transducers are mounted on short arms on a circle around the 10-MHz transmit-transducer at 120° azimuth intervals. The sampling volume is located away from the sensor to provide undisturbed measurements. The acoustic beams are slanted at 30° from the axis of the transmit-transducer so that the receive-beams intercept the transmit beam at a point located at 5-6 cm below the sensor, which ensures nonintrusive flow measurements. The exact position is encoded in a probe-specific configuration file that is read by the data acquisition software. The software automatically uses this data in reporting the distance from the sampling volume to the nearest boundary (Nortek AS, 1997a). The interception of these four beams, together with the width of the transmit pulse, define the sampling volume. This volume is 3-9 mm long and approximately 6 mm in diameter. All three receivers must be submerged to ensure correct three-dimensional velocity measurements. The high-frequency cable is connected to the ADV processor, which consists of a PC-card.

(a) - Three ADVs, wave probe monitor and conductivity meter in operation

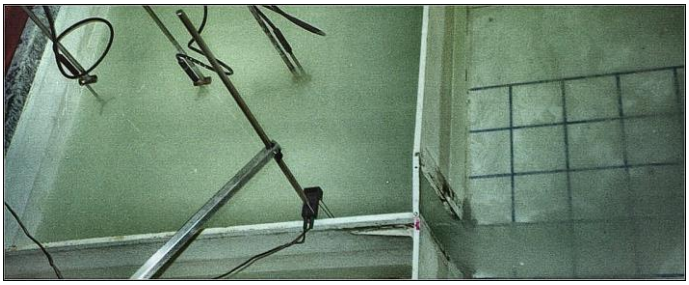

(b) - Saline water flooding out in the ebb tide

(c) - From the left: 3D down-looking, side-looking and up-looking ADVs

(d) - Wave probe

(e) - Conductivity meter probe

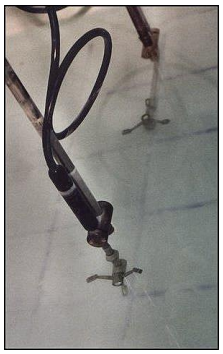

(f) - ADV probes

Picture (7.1) - 3D ADV velocimeters, wave probe monitor and conductivity-meter

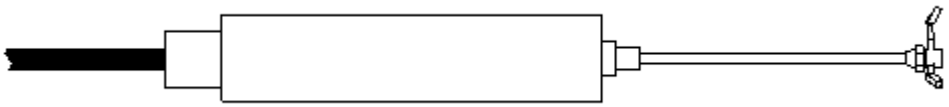

(a) - Parts of a velocimeter probe. From left to right: cable, conditioning module, measuring probe

(b) - Down-looking probe

(c) - Side-looking probe

(d) - Up-looking probe

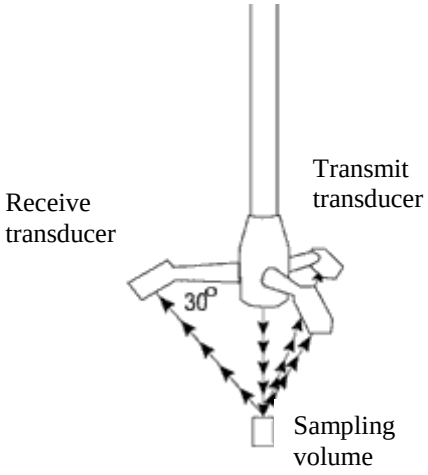

(e) - Details of a standard down-looking probe

Picture (7.2) - 3D ADV probes: (a) - Parts of a probe, (b) - Down-looking probe, (c) - Side-looking probe, (d) - Up-looking probe, (e) - Details of a down-looking probe

The performance characteristics of ADVs according to Nortek AS (1997a) are as follows:

1. Acoustic frequency: 10 MHz;
2. Velocity range: ±3, 10, 30, 100, or ±250 cm/s, which is a nominal value as the exact maximum velocity is different along the axis normal to the transmitting transducer and the plane parallel to its face.
3. Velocity resolution: 0.1 mm/s;

4. Velocity bias: ±0.5%, with no measurable zero-offset in the horizontal direction;
5. Random noise: approximately 1% of velocity range at 25 Hz;
6. Sample reporting rate: programmable from 0.1 to 25 Hz;
7. Sampling volume: less than 0.25 cm^3;
8. Minimum distance from sampling volume to boundary: 5 mm. Positioning the probe in the vicinity of the surface or a solid boundary is within an accuracy of 2-3 mm.

The nominal velocity was set to ±3 cm/s. The maximum vertical velocity, V_z, for a down-looking probe for example, was ±10 cm/s towards the transmit-transducer and ±30 cm/s in the plane perpendicular to the axis of the transducer (horizontal velocity components for a down-looking probe; V_x and V_y).

According to the Nortek AS (1997a) ADV specifications, the statistical uncertainty of the velocity measurements due to the Doppler noise is approximately proportional to the maximum velocity range that the ADV can measure. It is recommended that the velocity range of the ADV be set to the minimum value that covers the range of velocities expected in a given flow.

A velocimeter transmits acoustic pings into the water along the transmit-beam, at a high rate, typically many hundreds per second. The ping rate is fixed within each velocimeter according to its acoustic frequency and velocity range. The sampling rate, or the rate at which the velocimeter reports data, is much smaller than the ping rate to allow each measurement to average multiple pings. As the pulses propagate through the water column, a fraction of the acoustic energy is scattered back by small particles suspended in the water. The phase data from successive coherent acoustic returns are converted into velocity estimates using a pulse-pair processing technique (Miller and Rochwarger, 1972). The phase data are then converted into speed using the Doppler relation. The scattering strength is determined by the concentration and size of the particles suspended in the water. In natural bodies of water the natural occurrence of particles is sufficient for proper operation. In model tanks with running water microscopic bubbles in the water column tend to act as natural seeding. In clean, quiescent water, seeding materials must be added to ensure sufficient scattering strength. Recommended seeding level is 10-50 grams per cubic metre (Nortek AS, 1997a). Non-soluble seeding material from Nortek was used for the present experiments.

7.2.1.1 Accuracy of the ADV Velocimeters

Because positive phase angles greater than 180° cannot be distinguished from negative phase angles between –180° and 0°, if the phase angle is greater than 180° it will be seen as a negative phase angle between –180° and 0°, and will be incorrectly interpreted as a negative velocity. Similarly, phase angles less than –180° are interpreted as positive phase angles and positive velocities. As a result, when the flow velocity approaches the limits of the measurement range, it is possible for the probe to report velocities that alternate from large positive to large negative values and vice-versa. This behaviour is known as aliasing, and erroneous velocities reported by the probe when operating in this range are called velocity ambiguities (Wahl, 2000).

Velocity ambiguities sometimes occur in two situations where they are not expected. Firstly, large velocity components directed towards or away from the transmitting transducer of an ADV can cause over-ranging even when the total velocity magnitude is well below the nominal range setting of the probe. This is due to the geometric arrangement of the transmitting and receiving acoustic transducers, which causes the velocity range normal to the transmitting transducer face to be about one third of the range in the plane parallel to the transducer face. The stated nominal range setting is most closely associated with flow in the plane parallel to the transmitting transducer face. Secondly, the range setting of an ADV probe can sometimes change during the boundary-adjustment phase of configuring the probe at the start of each measurement. This occurs when the probe detects nearby acoustic boundaries that might cause interference with operation of the probe. To overcome this interference, the lag-times of the acoustic signals transmitted by the ADV are reduced, causing a reduction of the velocity range that may lead to over-ranging of the probe (Wahl, 2000).

Voulgaris and Trowbridge (1998) evaluated the accuracy of the acoustic Doppler velocimeter. Simultaneous measurements of open-channel flow were undertaken in a 17-metre flume using an ADV and a laser Doppler velocimeter. Flow velocity records obtained by both instruments were used for estimating the true flow characteristics and the noise variances encountered during the experiments. They concluded that the ADV is suitable for accurate measurements of mean flow even at positions close to the boundary.

To validate the use of acoustic Doppler velocimeters (ADVs) for the measurement of turbulent flows, Khorsandi et al. (2012) conducted experiments in an axisymmetric turbulent jet and in approximately homogenous isotropic turbulence with zero mean flow. The experiments showed that the horizontal RMS velocities measured by the ADV were overestimated compared to flying hot-film anemometry measurements and the accepted values in the literature. However, the vertical component of the RMS velocity agreed well with those of other studies. The results also showed no clear relationship between the Doppler noise and the mean flow. In addition, subtracting the Doppler noise, measured for a given mean velocity, from the measured RMS velocities, at the same mean velocity, did not significantly decrease the RMS velocities. Snyder and Castro (1999) verified the usability of the ADV in a stratified tank.

The errors encountered may be combinations of bias and short-term uncertainty, which have different ramifications for the results of data collection:

- Bias is the error that remains after taking long-term averages.
- Short-term uncertainty is the random error of individual measurements, which can be removed by averaging.

Velocimeter's long-term accuracy depends on the geometry of its probes and the stability of its internal oscillators. A factory-calibrated ADV velocimeter should have a scale-factor bias that is less than 1% of the measured velocity. The analysis conducted by Voulgaris and Trowbridge (1998) showed that the ADV sensor can measure mean velocity within 1% of the estimated true value. Mean velocities can be measured at distances less than 1 cm from the boundary. A velocimeter will retain this accuracy as long as its probe remains unbent. Bias increases near the extremes of velocity range because velocities that would be measured beyond the extremes wrap around to the opposite end of the range. This bias can be avoided by keeping the maximum observed speed towards the middle of the maximum range.

Small short-term uncertainty comes from collecting acoustic echoes with exceedingly high correlation. However, because sources of decorrelation can be both internal and external, noise level of a probe is not entirely intrinsic to the probe itself, but it depends also on the environment in which it is measuring. Primary external sources of decorrelation include mean speed, turbulence and non-uniformity in the scatterers.

7.2.1.2 Sources of the Noise and Spikes

Voulgaris and Trowbridge (1998) divided the source of the noise in ADV velocity records into three categories:

1. Sampling errors related to the electronic circuitry of the sensor and the accuracy of the ADV's analogue to digital board in resolving the changes in phase. This error is independent of the flow and depends on the pulse length, which is set by the velocity range of the ADV. The error in flow measurements due to this noise term depends on sensor velocity range setting and ranges from ± 0.95 to ± 3.0 mm/s.
2. Doppler noise, which is an intrinsic feature of all Doppler backscatter systems and is flow-related. This noise dominates at rapid flows and is caused by turbulence and particle scattering, beam divergence, and the finite residence time of the particles in the sampling volume.
3. The error attributable to mean velocity gradients in the sampling volume. This error becomes important in flows with sharp velocity gradients, such as boundary layers.

The most significant source of noise in ADV measurements is the Doppler noise, which is inherent to the technique (Garbini et al., 1982; Lohrmann et al., 1994). Doppler noise is white noise, which does not influence the mean velocity. Hurther and Lemmin (2001) characterised the Doppler noise as having a flat spectrum over the frequency domain, unbiased and therefore not affecting the mean velocity, statistically independent of the true velocity fluctuations and true Doppler frequency, and having statistically independent noise from one receiver to the next.

The main source of Doppler noise is the random target distribution in the sampling volume, which induces an instantaneous Lagrangian deviation of the target's position from the mean position determined by the spatially averaged velocity. This creates instantaneous random Doppler-phase noise that is added to the spatially averaged Doppler phase (Doroudian et al., 2010).

Nikora and Goring (1998) concluded that:

1. Both the spectra and the probability distributions indicate that as a first approximation, the Doppler noise is Gaussian white noise;
2. The horizontal noise components are both approximately of the same energy level and have significantly more energy than the vertical component;

3. The velocity range has a significant effect on the noise;
4. The cross-correlation functions between noise components indicate that the cross-correlations are absolute maximum at zero time-lag. If the orthogonal noise components were independent, one would expect the cross-correlations to be zero. In fact, they are not independent but are linear functions of the three direct, along-beam, noise components.

Assuming the correlation between the velocity and the noise to be zero, Nikora and Goring (1998) subtracted the measured noise from the measured velocity to estimate the true velocity. Lemmin and Lhermitte (1999) challenged this method, remarking that the Doppler noise should be an increasing function of the mean velocity of the flow. In contrast to Doppler noise, random spikes are not inherent to the measurement technique and occur mostly in poor measurement environments (Doroudian et al., 2010).

To study the effect of the sampling frequency of the ADV on the turbulence statistics, McLelland and Nicholas (2000) estimated the contribution of noise to the velocity variance at various sampling frequencies at different mean velocities and depths in a channel flow. They showed that although higher sampling frequencies can characterise a larger range of turbulence frequencies, the total noise in the velocity variance increases at higher sampling rates.

In many velocimeter measurements, velocity spikes are the dominant source of error. Spikes can be disproportionate sources of error because they can have large values compared with the mean velocity. Large spikes can be removed from the data, but it appears that even despiked data have higher noise levels than comparable data without spikes. The source for spikes is not well understood. Spikes may occur as a result of the environment itself, but it is clear that the velocimeter hardware and algorithms are a primary source of spikes.

Wahl (2003) considered that spikes in ADV time series may be caused by many factors, including high turbulence intensities, aerated flows that have undesirable acoustic properties, and phase difference ambiguities that occur when velocities exceed the upper limits of ADV probe velocity ranges. Spikes may also be introduced into the data when obstacles such as solid particles or air bubbles block the sound path between the emitter and the receiver (Doroudian et al., 2010).

Parsheh et al. (2010) showed that power spectral density is significantly susceptible to the presence of spikes, and an improvement in the quality of the

contaminated time series is directly reflected in the spectra. By removing the spikes they recovered the low-frequency region of the spectra which is the region with the highest energy content. The high-frequency region cannot be accurately recovered due to the steps introduced in the time series by the application of the last valid data point for signal reconstruction. Yin et al. (2001) considered turbulent velocity fluctuations as a random process, described with a Gaussian probability distribution.

7.2.2 *Wave Probe Monitors*

The water surface elevation was measured in the model harbour using HR Wallingford wave probe monitors. The instrument works on the principle of measuring the current flowing in an immersed probe, which consists of a pair of parallel stainless steel wires, 1.5 mm in diameter and spaced 12.5 mm apart. The maximum measurable wave height for the standard shallow water probe of 300 mm long is 280 mm (HR Wallingford, 1994). The probe is energised with a high frequency square wave voltage to avoid polarisation effects at the wire surfaces. The wires dip into the water and the current that flows between them is sensed by an electronic circuit providing an output voltage proportional to the instantaneous depth of immersion, i.e. wave height, and can be used to drive a high speed chart recorder and/or a data logger. The voltage output range is ±10 volts. However, the measured voltage is alternating and so the signal is fed to a precision rectifier and envelope detection circuit to produce a D.C. voltage which is proportional to the wave height. The associated wave monitor module carries the energisation and sensing circuits and means for compensating for the resistance of the probe connecting cable. It is powered from a separate power supply module, A.C. mains operated.

7.2.3 *Conductivity Meter*

A model 4320 conductivity meter from Jenway was used to measure the conductivity of saline water in the model harbour. The instrument is a laboratory unit available with the graphics mode liquid crystal display which enables a menu-based approach to each analysis and the selection of the relevant operating mode. The conductivity meter incorporates analogue and digital interfacing capability. A conductivity electrode enables the measurements.

The specifications of the conductivity meter are as follows (Jenway Ltd., 1996):

Conductivity:

- Ranges: 0 to 19.99 S, 0 to 1.999 S,
  0 to 199.9 mS, 0 to 19.99 mS, 0 to 1.999 mS,
  0 to 199.9 µS, 0 to 19.99 µS, 0 to 1.999 µS;
- Resolution: 0.01 S/0.001 S,
  0.1 mS/0.01 mS/0.001 mS,
  0.1 µS/0.01 µS,
  corresponding to the first, second and third set of ranges;
- Accuracy: ±0.5% ±2 digits.

1. Salinity:
   - Range: 0 to 99.9;
   - Resolution: 0.1;
   - Accuracy: ±1 of reading for the range of 0 to 35, and ±3 of reading for the range of 35 to 99.9.
2. Temperature:
   - Range: -10 to +105 °C;
   - Resolution: 0.1 °C;
   - Accuracy: ±0.5 °C.

7.3 CALIBRATION

The calibration of the experimental instruments and the data logger readings are presented in separate sections for each instrument and according to the corresponding data acquisition system utilised.

7.3.1 *ADV Velocimeters*

Velocimeter calibration factors are determined by the speed of sound and by the angles between the transmit- and receive-transducers. To ensure that the correct speed of sound is used, the water temperature and salinity concentration values were entered in the data acquisition software. The calibration angles are measured at the factory and need only be changed when a new probe is installed. Maintenance calibration is not required unless the probe is physically damaged.

7.3.2 *Wave Probe Monitors*

The output voltage is calibrated in terms of wave height by varying the depth of immersion of the probe in still water by a measured amount, and noting the change in output signal. Once the calibration has been set and established, the only further adjustment needed may be to trim the set datum. The conductivity of the water changes with temperature (2% per 1°C approximately), and it is also dependent on the concentration of dissolved salts in the hydraulic model. The wave probe monitors used in the present study were designed for fresh water only.

For the calibration of the wave probe monitors the aforementioned procedure was undertaken. For obtaining the actual water elevation, the calibration was performed to adjust the water elevation with the readings from the wave monitor data logger. The final values were calculated, programmed and graphed against the readings of data logger with a correlation of R^2 =1. This procedure was repeated for each set of the measurements.

7.3.3 *Conductivity Meter*

The Model 4320 conductivity meter offers three methods of calibration determined by the level of accuracy required as follows (Jenway Ltd., 1996):

- With known cell constant;
- With standard solution;
- With standard solutions.

While the standard solution method provides a higher level of accuracy than the known cell constant method, the standard solutions method provides the highest level of confidence for the accuracy. For the present studies the calibration has been performed using the standard solution method. 0.745 grams of dried A.R. grade potassium chloride (KCl), dissolved in 1 litre deionised water was used for the calibration, which produces a 0.01N solution with a conductivity of 1413µS at 25°C.

Firstly by adding specific amounts of salt to the water taken from the basin, the increased volume of saline water and the weight of samples were measured. The concentration of salt (g/l), with the consideration of the initial salinity of the basin, was then calculated and graphed against the amount of the added salt to the water samples at 25°C (Fig. 7.1). The density of the saline water against the concentration was also calculated and is graphed in figure (7.2).

The conductivity and salt content readings for calibration solution were 1.413 mS and 0.8 g/l respectively. Measurements were performed on the salt from Fisher Scientific. After the instrumental calibration, salt was added to the water taken from the basin with the steps of 1 gram, and the corresponding conductivity was measured and the readings from the conductivity meter for salt content were tabulated accordingly. The salinity concentration, obtained from the relevant relationship derived in the first step, was calculated and graphed versus conductivity and vice-versa. Finally the conductivity of the saline water was calculated and graphed with respect to the added salt to the water from the basin. By weighing the sample-bottles for a specific volume of saline water, the density variation of the saline water was also graphed against the conductivity. The relative density of the tap water was calculated equal to 0.9984 at 24 °C.

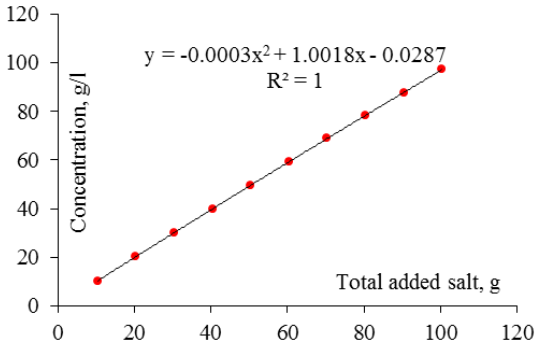

Figure (7.1)
Concentration of saline water versus the added salt to the water

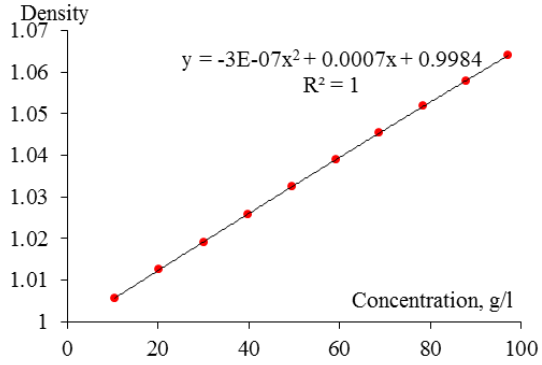

Figure (7.2)
Density of saline water versus the concentration of salt

Table (7.1) – Test sets

	Experiment Conditions			
Barrier Height (mm)	Fresh Water		Saline Water	
200	TR = 100	TR = 200	TR = 100	TR = 200
100	TR = 100	TR = 200		
90	TR = 100			
60	TR = 100			
0	TR = 100			

For the calibration of the conductivity meter readings during the experiments, samples were taken from the model harbour, and the conductivity of the samples was measured. A graph was then produced to show the variation of the measured conductivities of the samples against the readings. The trend-line equation of the graph was used to convert the readings to calibrated conductivity presented as the results of measurements.

7.4 TEST ARRANGEMENTS

To investigate the hydrodynamics of the model harbour under long-shore currents, tidal conditions were applied to the laboratory model. A barrier was placed in the entrance to explore the circulation characteristics due to the presence of a barrage. The effect of salinity and stratification on the flow characteristics was simulated by filling the model harbour with saline water up to the height of the barrier and same tides as the fresh water condition were imposed. Tidal conditions were initiated from the low water level in order to minimise the effects of transient surface disturbances within the saline water. Water temperatures ranged between 18°C and 20°C. The actual measured tides were found to be very nearly sinusoidal in form.

The experimental sets were divided into two conditions of fresh water (FW) and saline water (SW). The barrier heights were chosen equal to 0 (BH = 0, i.e. no barrier), 60, 90, 100, and 200 mm.

To account for the influence of distortion ratio on the hydrodynamics, circulation and the stratification in the model harbour, two tidal ranges of 100 (TR = 100) and 200 (TR = 200) mm corresponding to different distortion ratios were simulated.

The experimental sets were therefore categorised as tabulated in Table (7.1). The measurements were taken at locations which were chosen in a mesh of 12×12 cm grids, as illustrated and labelled in figure (7.3). The depth of the measurement locations is shown in figure (7.4) for velocity and salinity measurements.

The water elevation locations are addressed according to the labelling system presented in figure (7.3). Figure (7.5) demonstrates the location of measured values for each set of the measurements and provides a summary of the location and vertical layers for each corresponding set of the measurements.

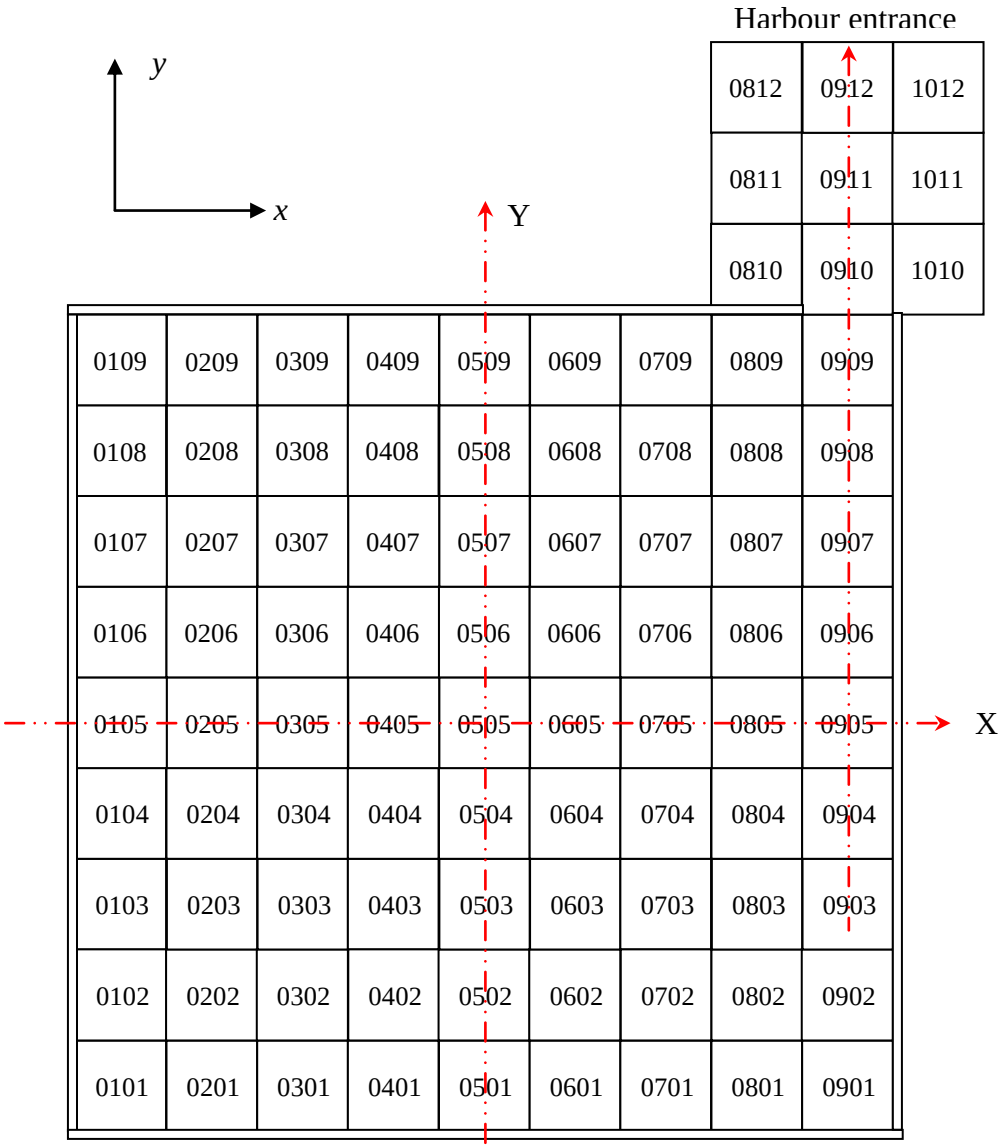

Figure (7.3) – Address label of the experimental cells for measurements of the model harbour in plan

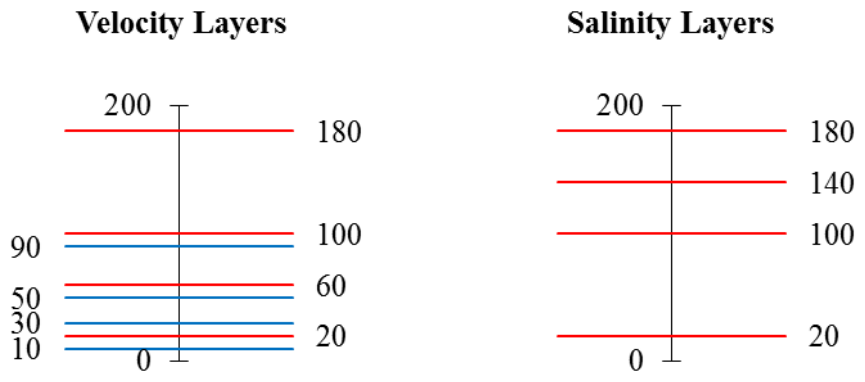

Figure (7.4) – Velocity and salinity measured layers: blue lines refer to measurements with barrier heights up to 100 mm (BH = 0, 60, 90 and 100), and red lines refer to measurements with barrier height of 200 mm (BH = 200)

(a)

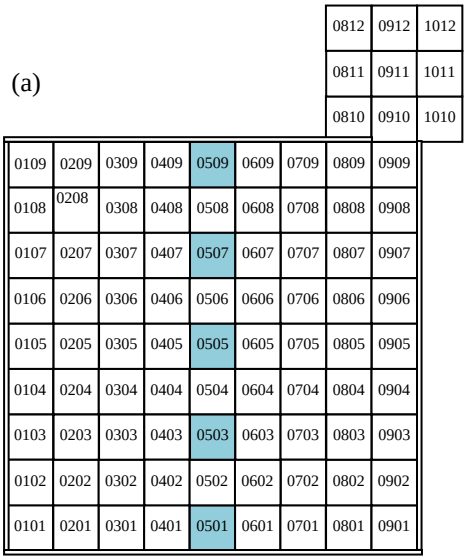

Velocity and water elevation measurement locations for tidal range of 100 mm and no barrier
(TR = 100: BH = 0)

Velocity measurements at layers 1, 5, and 9 cm above bed

(b)

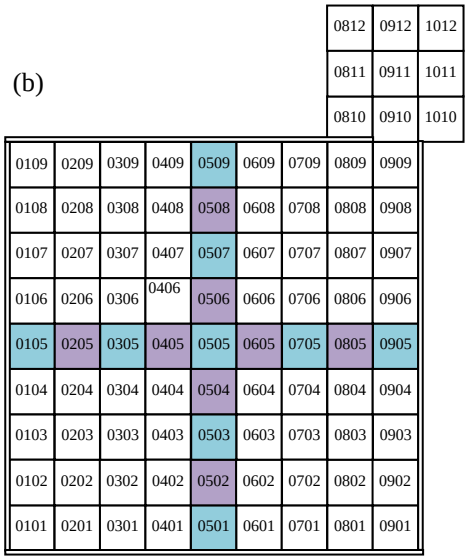

Velocity and water elevation measurement locations for tidal range of 100 mm and barrier heights of 60 and 90 mm
(TR = 100: BH = 60; BH = 90)

Velocity measurements at layers 1, 5, and 9 cm above bed for aqua cells and at layers 1 and 9 cm above bed for purple cells
Water elevation measurements for aqua cell locations

(c)

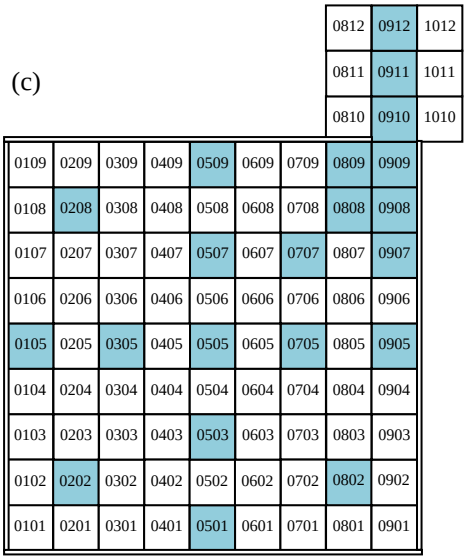

Velocity and water elevation measurement locations for tidal range of 100 and 200 mm and barrier height of 100 and 200 mm
(TR = 100: BH = 100; BH = 200)
(TR = 200: BH = 100; BH = 200)

Velocity measurements at layers 1, 3, 5, and 9 cm above bed

(d)

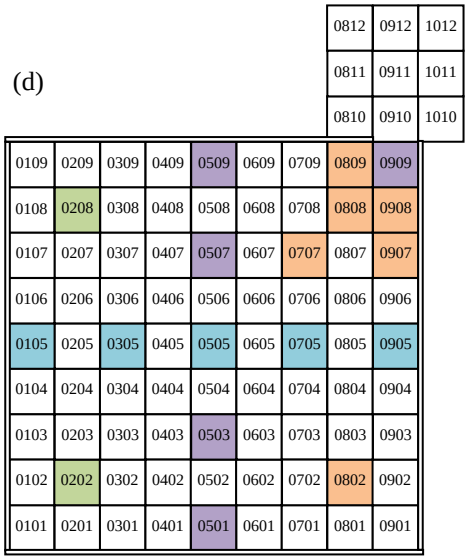

Salinity measurement locations for tidal range of 100 and 200 mm and barrier height of 200 mm
(BH = 200: TR = 100; TR = 200)

Salinity measurements at layers 2, 10, 14, and 18 cm above bed for aqua cells, at layers 10, 14, and 18 for purple cells, at layers 2, 10, and 18 cm above bed for olive cells and at layers 10 and 18 cm above bed for orange cells

Figure (7.5) – Cell locations for different experimental sets and the summary of test arrangements

7.5 DATA ACQUISITION

In the present study only the mean values of the velocity, water elevation and salinity due to conductivity have been measured. The measurement of the turbulent, fluctuating components or their mean values have not been in the scope of the physical model studies. The measurement of mean values is quite sufficient for most practical applications (Schlichting, 1979).

7.5.1 *ADV Data Acquisition and Processing Software*

The processing module of ADVs performs the digital signal processing required to measure Doppler shifts. In the laboratory velocimeters, this computationally intensive task is implemented on a PC-board that fits any IBM-compatible computer with full-sized slots. Three velocimeters were controlled by one computer. The standard data acquisition software supplied with the velocimeters provides real-time display of data in graphical and tabular form. The data were recorded to disk in highly compressed binary files which then were converted to ASCII format with the data conversion programs supplied with the system. The ASCII velocity data generated by the post-processing ADV software from the binary files, were further processed to consider the probe direction during the experiments.

The signal-to-noise ratio, SNR, parameter indicates the relative density of acoustic scatterers in the flow and the resulting strength of the signal received compared to the noise level of the instrument. The acoustic Doppler velocimeter is based on the Doppler principle. First, a short acoustic pulse of known frequency is transmitted along the vertical axis. The echo from the water is received in three small transducer elements, amplified in the conditioning module and digitised in the processing board. The frequency shift between the transmit-pulse and the received echo is proportional to the water velocity. To ensure proper operation, the echo must be strong enough to allow accurate calculation of the frequency shift. If the echo is weak, the calculation will be statistically noisy and the velocity data will show significant short-term variability. The strength of the echo is quantified in terms of a SNR expressed in dB for each receiving-beam. ADV manufacturers recommend an SNR value of at least 5 when measuring mean flow velocities (Nortek AS, 1997a). The correlation parameter, COR, is an indicator of the relative consistency of the behaviour of the scatterers in the sampling volume during the sampling period.

ADVs collect data at a higher sampling rate than the sample reporting rate, and the COR parameter indicates the consistency of the multiple measurements that take place within each sampling period. The value varies from 0 to 100, and ADV manufacturers have recommended filtering to remove any samples with correlation values below 70. The values for SNR and correlation refer to the beams of ADV and not to *x*, *y* and *z* directions. Wahl (2000) introduced the WinADV program designed for post-processing of real time data files recorded by SonTek and Nortek ADVs.

7.5.2 *GENIE Data Acquisition and Control Software*

GENIE (ADVANTECH, 1995) provides an icon-based system for designing real-time automation and control strategies, system monitor displays, and dynamic operator displays. It enables graphically creating, simulating, and running real-time data acquisition and process control strategies. A strategy is defined as one or more tasks, where a task is a collection of blocks and display items that are related to each other. The software was used for water elevation and salinity measurements. GENIE consists of three modules. These are the strategy editor, display editor, and runtime modules. The strategy editor is an icon-based designing environment that provides, through the use of a toolbox, the building blocks that allow the control process to be designed, arranged, and viewed. Blocks are connected together and used to communicate with the I/O hardware to control and monitor the process. Display items are connected to the strategy in order to display process events and allow supervisory control during GENIE runtime. The display editor is used to create the operator display panel for the process, allowing a dynamic interface with the running strategy. The runtime module provides a real-time, multitasking environment that combines the logical flow of a previously defined strategy with any number of display items in the operator panel. Runtime executes the strategy in real-time, based upon data received from I/O devices or by manual operator entry. Through the runtime module, the process can be monitored and controlled, and the data can be logged to a disk, and manipulated by standard or user-defined functions.

7.6 SIGNAL PROCESSING AND DIGITAL FILTERING

When a signal is corrupted by the addition of noise, it is possible, to a certain extent, to reconstruct the original signal with an appropriate digital filter. The

average strength of the noise is constant and independent of the magnitude of the signal. The effect of the noise on the relative error of a series of measurements becomes greater as the quantity being measured decreases in magnitude. The noise level, also called the noise floor, is its most fundamental measure of measurement uncertainty.

Velocimeter uncertainty is a random white noise. This means that each velocity estimate is independent of the next, and it means that the noise has no preferred frequency. The noise level varies widely according to the characteristics of the velocimeter, its set up, the characteristics of the flow, and the acoustic scattering environment. The velocity noise level limits the frequency range, over which useful data can be obtained. However, the velocity spikes are the major source of error as they can have large values compared with the mean velocity and are more difficult to be detected, removed and replaced by clean signal.

The conductivity data also suffer from very noisy signals. However, the nature of the noise for the conductivity data is such that the signal fluctuates around a mean value with almost a constant band of fluctuations, therefore the filtering process is less complicated.

7.6.1 *Denoising and Despiking Techniques for ADV Velocimeters*

Yin et al. (2001) introduced a method, which analyses a time series of velocity signals in order to obtain a time series of a moving averaged velocity. Moving average algorithm is not constructive when the filter passes through peaks that are narrow compared to the filter width. A better procedure is to perform a least squares fit of a small set of consecutive data points to a polynomial and take the calculated central point of the fitted polynomial curve as the new smoothed data point. The smoothing effect of the latter algorithm is not as sharp as in the case of the moving average and the loss and/or distortion of vital information is comparatively limited. However, for both algorithms part of the original information is lost or distorted.

To reduce the effect of noise resulting from random spikes, several post-processing techniques have been proposed. The iterative phase-space thresholding method of Goring and Nikora (2002) was based on the assumption that good data can be found within a cluster and points located outside the cluster are spikes. Spike detection was based on the postulate that under normal flow conditions the instantaneous acceleration in a stream must be of the same order or less than the

acceleration of gravity g. To replace the spikes, a polynomial fitted to good data on either side of the spike event, then interpolated across the event, was recommended by the authors. They mentioned that if the data sequence were undergoing a sustained change in velocity (e.g., over a tidal cycle or during a change in river flow), then the phase-space method would not work unless these long-scale fluctuations were removed by high-pass filtering. They also pointed out that for some records the choice of thresholds is very difficult and subjective.

These techniques also include the despiking filters of Cea et al. (2007) and Parsheh et al. (2010). The latter reasoned that the phase-space thresholding despiking method (Goring and Nikora, 2002; Wahl, 2003) erroneously also removes some valid data points in the vicinity of the spikes. They modified the phase-space-thresholding despiking method so that the data points near the peak of the probability density function (PDF) were not affected by the despiking method, as these points are not spurious. Furthermore, the modified method replaces the spikes by the last valid data point instead of leaving a gap in the time series. It was shown that the modified method improved the spectrum over all frequencies compared to the original despiking method. Spike-removal, however, depends on the flow conditions and caution should be taken when proposing universal guidelines (Doroudian et al., 2010). Chanson et al. (2008) used an ADV for high-frequency velocity measurements in a small estuary. They showed that conventional despiking methods such as the phase-space thresholding method (Goring and Nikora, 2002) were not sufficient.

Doroudian et al. (2010) combined a spike-removal procedure on the beam velocities with a noise-reduction method on the flow velocities to improve turbulence measurements, and compared the results with those obtained from ADVP (acoustic Doppler velocity profiler) measurements under the same conditions. They applied the despiking method to the bistatic velocities before the orthogonal velocities were calculated. It was shown that spikes were best removed from ADV beam velocity data before calculating flow velocities, thereby correcting all three flow velocity components at the source. The noise reduction method is based on the decorrelation of the Doppler noise terms contained in two vertical velocities redundantly sampled in the same volume. It has been pointed out by most authors, however, that spike detection and spike replacement techniques in three receiver ADV data still remain

an arbitrary procedure and that none of the currently available methods gives totally satisfactory results (Doroudian et al., 2010).

Parsheh et al. (2010) proposed a method for reconstructing contaminated time series which integrates two previously developed techniques for detecting and replacing spurious spikes. The spikes are first detected using a modified version of the universal phase-space-thresholding technique and subsequently replaced by the last valid data points. The accuracy of the approach is evaluated by applying it to identify and remove spikes and reconstruct the spectra of two clean data sets which are artificially contaminated with random spikes. The results show that the power spectra of the reconstructed time series contain a filtered white noise caused by the steps in the reconstruction technique using the last valid data point.

7.6.2 *Fourier Transform, Discrete and Fast Fourier Transforms*

An integral transform is a transformation in the form of an integral that produces from given functions new functions depending on a different variable. If $f(x)$ is absolutely integrable on the *x*-axis and piecewise continuous on every finite interval, then the Fourier transform $\hat{f}(w)$ of $f(x)$ given by equation (7.1) exists (Kreyszig, 2011).

$$\hat{f}(w)=\frac{1}{\sqrt{2\pi}}\int_{-\infty}^{\infty} f(x)e^{-i\omega x}\,\mathrm{d}x \tag{7.1}$$

$$f(x)=\frac{1}{\sqrt{2\pi}}\int_{-\infty}^{\infty} \hat{f}(w)e^{i\omega x}\,\mathrm{d}w \tag{7.2}$$

Representation (7.2) of $f(x)$ is the inverse Fourier transform of $\hat{f}(w)$ and a superposition of sinusoidal oscillations of all possible frequencies, called a spectral representation. In (7.2), the spectral density, $\hat{f}(w)$, measures the intensity of $f(x)$ in the frequency interval between *w* and $w+\Delta w$ (Δw small, fixed). In connection with vibrations, the integral $\int_{-\infty}^{+\infty}\left|\hat{f}(w)\right|^2\mathrm{d}w$ can be interpreted as the total energy of the physical system. Hence an integral of $\left|\hat{f}(w)\right|^2$ from *a* to *b* gives the contribution of the frequencies *w* between *a* and *b* to the total energy.

When a function $f(x)$ is given in terms of values at finitely equally spaced many points, as they occur in time series analysis and simulation problems, the

Fourier analysis deals with sampled values rather than with functions, and the Fourier transform can be replaced by the discrete Fourier transform (DFT). Considering $f(x)$ to be periodic, for simplicity of period 2π, and assuming that *N* measurements of $f(x)$ are taken over the interval $0 \le x \le 2\pi$ at regularly spaced points of,

$$x_k = \frac{2\pi k}{N}, \quad k = 0,1,\ldots,N-1, \tag{7.3}$$

the discrete Fourier transform (DFT) of a given signal $\boldsymbol{f} = [f_0 \ldots f_{n-1}]^T$, is then the frequency spectrum of the signal, and is represented by the vector $\hat{\boldsymbol{f}} = \lfloor \hat{f}_0 \ldots \hat{f}_{n-1} \rfloor$ with components as in equation (7.4):

$$\hat{f}_n = \sum_{k=0}^{N-1} f_k \, e^{-inx_k}, \qquad f_k = f(x_k), \qquad n = 0, \ldots, N-1. \tag{7.4}$$

In vector notation, $\hat{\boldsymbol{f}} = \overline{\boldsymbol{F}}_N \boldsymbol{f}$, where the $N \times N$ Fourier matrix $\overline{\boldsymbol{F}}_N = [e_{nk}]$ has the entries as the equation (7.5):

$$e_{nk} = e^{-inx_k} = e^{-2\pi ink/N} = w^{nk}, \quad w = w_N = e^{-2\pi i/N}, \quad n,k = 0,\ldots,N-1 \tag{7.5}$$

The components $\hat{f}_n$ of $\hat{\boldsymbol{f}}$, give a resolution of the 2π-periodic function $f(x)$ into simple complex harmonics. Only *n*'s that are much smaller than *N*/2, should be used to avoid aliasing. The fast Fourier transform (FFT) is a computational method for the DFT that needs only $O(N)\log_2 N$ operations instead of $O(N^2)$, making it a practical tool for large *N*.

7.6.3 *Wiener Smoothing Filter*

The Wiener smoothing filter is an LMMSE (Linear Minimum Mean Square Error) estimator. To estimate a parameter φ based on the data vector $\boldsymbol{x}$ defined as equation (7.6), LMMSE is the best estimator in the sense that among all classes of linear estimators of the form of the equation (7.7), it minimises the Bayesian mean square error (MSE) defined in equation (7.8) and only relies on the correlation between random variables (Kay, 1993).

$$\boldsymbol{x} = [x[0], x[1], \ldots, x[N-1]]^T \tag{7.6}$$

$$\hat{\varphi} = \sum_{n=0}^{N-1} a_n \, x[n] \tag{7.7}$$

$$\mathrm{Bmse}\left(\hat{\varphi}\right)=\mathrm{E}\left[\left(\varphi-\hat{\varphi}\right)^2\right] \tag{7.8}$$

For the noise reduction of the velocity signals, the variable ***v*** which is the true velocity vector, should be estimated based on the noisy recorded signal ***x*** = ***v*** + ***n***, where ***n*** is Doppler noise which is believed to be a Gaussian white noise (Nikora and Goring, 1998).

7.6.3.1 Exploiting Correlations in Time

Wiener smoothing filter finds coefficients $w_{i,j}$ to best estimate:

$$\hat{v}_i=\sum_{j=0}^{N-1} w_{i,j}\, v_j \tag{7.9}$$

such that for each $i\in\{0,\ldots,N-1\}$ the Bayesian mean square error is minimised:

$$\mathrm{Bmse}\left(\hat{v}_i\right)=\mathrm{E}\left[\left(v_i-\hat{v}_i\right)^2\right] \tag{7.10}$$

In the vector form $\hat{\boldsymbol{v}}=\overline{\boldsymbol{W}}\,\boldsymbol{x}$, where $\overline{\boldsymbol{W}}$ is an $N\times N$ matrix. Assuming Doppler noise ***n*** and the true velocity signal ***v*** are uncorrelated, solving for $\overline{W}$ to minimize equation (7.10), reduces to:

$$\overline{\boldsymbol{W}}=\overline{\boldsymbol{R}}_{vv}\left(\overline{\boldsymbol{R}}_{vv}+\overline{\boldsymbol{R}}_{nn}\right)^{-1} \tag{7.11}$$

where $\overline{\boldsymbol{R}}_{vv}$ and $\overline{\boldsymbol{R}}_{nn}$ denote autocorrelation matrices for true velocity and Doppler noise respectively (Kay, 1993). Equation (7.11) can be rewritten as follows:

$$\overline{\boldsymbol{W}}=\left(\overline{\boldsymbol{R}}_{xx}-\overline{\boldsymbol{R}}_{nn}\right)\overline{\boldsymbol{R}}_{xx}^{-1} \tag{7.12}$$

7.6.3.1.1 Autocorrelation Matrices

In the case that velocity signal ***v*** and the additive noise ***n*** are considered wide sense stationary signals, all the matrices would be Symmetric Toeplitz matrices. Hence, $\overline{\boldsymbol{R}}_{xx}$ can be approximated using samples of recorded data as follows:

$$\begin{aligned}\overline{\boldsymbol{R}}_{xx}(i,j)=\overline{\boldsymbol{R}}_{xx}\left(|i-j|\right)&=\mathrm{E}\left[\left(x_i-\overline{\mathrm{E}}_x\right)\cdot\left(x_j-\overline{\mathrm{E}}_x\right)\right]\\&=\frac{1}{N-|i-j|}\sum_{k=0}^{N-1-|i-j|}\left(x_k-\overline{\mathrm{E}}_x\right)\cdot\left(x_{k+|i-j|}-\overline{\mathrm{E}}_x\right)\end{aligned} \tag{7.13}$$

Assumption of Doppler noise as white Gaussian noise, imposes ***n*** to be wide sense stationary signal, and results $\overline{\boldsymbol{R}}_{nn}$ a diagonal matrix with diagonal elements of noise variance σ_n^2. To approximate the noise variance, the DFT of the signal ***x*** was calculated. Based on that, the higher frequencies only contain white noise, as the

velocity signal is wrapped around lower frequencies, and using the fact that white noise is spread almost equally over the spectrum, an approximate σ_n^2 may be calculated. To compute the noise power for each point a high-pass filter was designed to reject the main signal and only let part of white noise go through. Figure (7.6) shows the frequency spectrum of a point, for which it is expected that for the frequencies more than 0.2 Hz the signal only contains additive white Gaussian noise. Therefore the power of the signal for frequencies more than 0.2 Hz is calculated and is extended for the whole frequency spectrum.

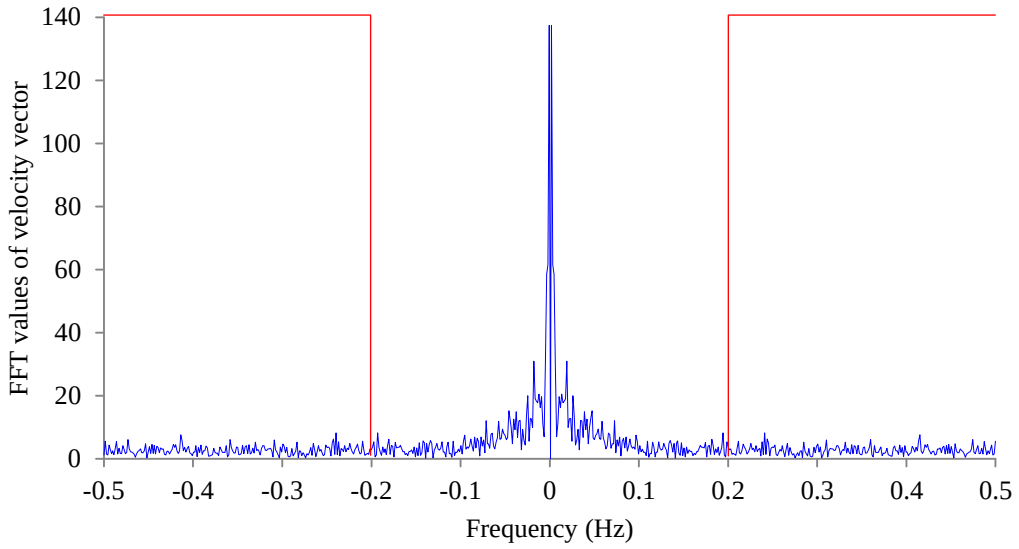

Figure (7.6) – Frequency spectrum for *u*-component of velocity data recorded at point (0507) at 100 mm above bed for saline water condition with the tidal range of 100 mm

7.6.3.1.2 Fourier Transform Interpretation

In the smoothing problem in which the sequence $\boldsymbol{v}_n$ is to be estimated based on $\{\ldots, x[-1], x[0], x[1], \ldots\}$ or $x[k]$ for all k, corresponding to infinite impulse response non-causal filtering, the smoothing estimator takes form of the equation (7.14).

$$\hat{v}_n = \sum_{k=-\infty}^{\infty} w_{k,n}\, x_k = \sum_{k=-\infty}^{\infty} w\left(|n-k|\right) x_k = w_n * x_n \tag{7.14}$$

where * denotes convolution. The coefficients w_n in equation (7.14) are solved as:

$$\sum_{k=-\infty}^{\infty} w\left(|n-k|\right) \boldsymbol{R}_{xx}(k) = w_n * \boldsymbol{R}_{xx}(n) = \boldsymbol{R}_{vv}(n) \tag{7.15}$$

Denoting the frequency response of the infinite Wiener smoother by *H(f)*, the Fourier transform of equation (7.15) results as follows:

$$H(f)=\frac{P_{vv}(f)}{P_{xx}(f)}=\frac{P_{vv}(f)}{P_{vv}(f)+P_{nn}(f)}=\frac{\frac{P_{vv}(f)}{P_{nn}(f)}}{\frac{P_{vv}(f)}{P_{nn}(f)}+1} \tag{7.16}$$

Hence, the Wiener smoother filter emphasises portions of the frequency spectrum of the data where SNR is high and attenuates those where it is low. To clarify this, Wiener smoothing frequency response is $H(f)\approx 0$ for low local SNR, defined as $\eta(f)=P_{vv}(f)/P_{nn}(f)$, and $H(f)\approx 1$ for high local SNR.

7.6.3.2 Velocity Filtered Results

Wiener filter with a window size of 5 samples has been applied to *u*, *v* and *w* components of the noisy velocity vector collected in the model harbour at point (0503) and at 10 cm above bed for the tidal range of 100 mm and saline water condition. For the *u*-velocity the estimated σ_n^2 equals 0.0062, which corresponds to estimated SNR = 14.83 dB.

The filter coefficients are calculated as follows:

$$\boldsymbol{h}=[h[-2],h[-1],h[0],h[1],h[2]]=[0.0616,0.1410,0.4804,0.1410,0.0616] \tag{7.17}$$

which are symmetric with respect to the central point and emphasise higher correlations as expected. The filtering then proceeds as follows:

$$\hat{v}_i=\sum_{j=i-2}^{j=i+2} h_{j-i}\, v_j \tag{7.18}$$

The filtered data for the *u*, *v* and *w* components of velocity are plotted in figure (7.7). The spikes are more influenced than the noisy signal as was expected.

7.6.3.3 Exploiting Correlations in Space

The same notion can be used to take advantage of correlation of velocity samples located in different positions in the grid and/or along different depths.

In this case the parameter to be estimated is, for example, $v(p_1,i)$ based on collected noisy random signal $\{x(p_1,i),x(p_2,i),\ldots,x(p_n,i)\}$ where $(p_\cdot,i)$ denote the position and time indices respectively. The symmetric matrix $\overline{\boldsymbol{R}}_{xx}$ then becomes as follows:

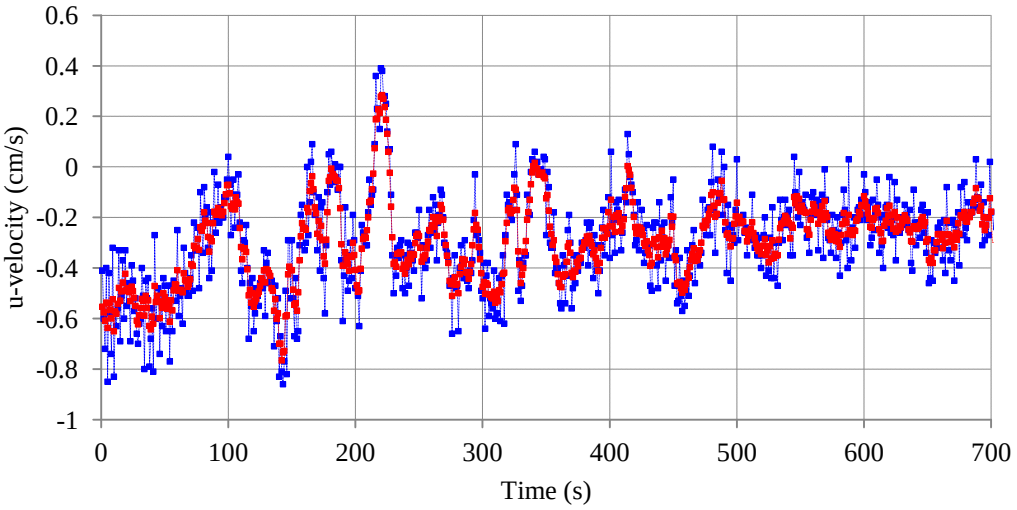

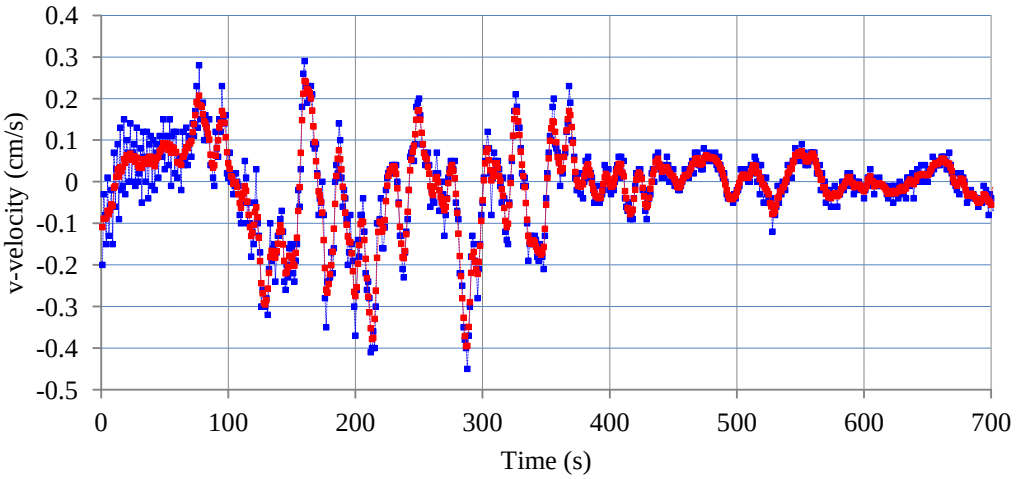

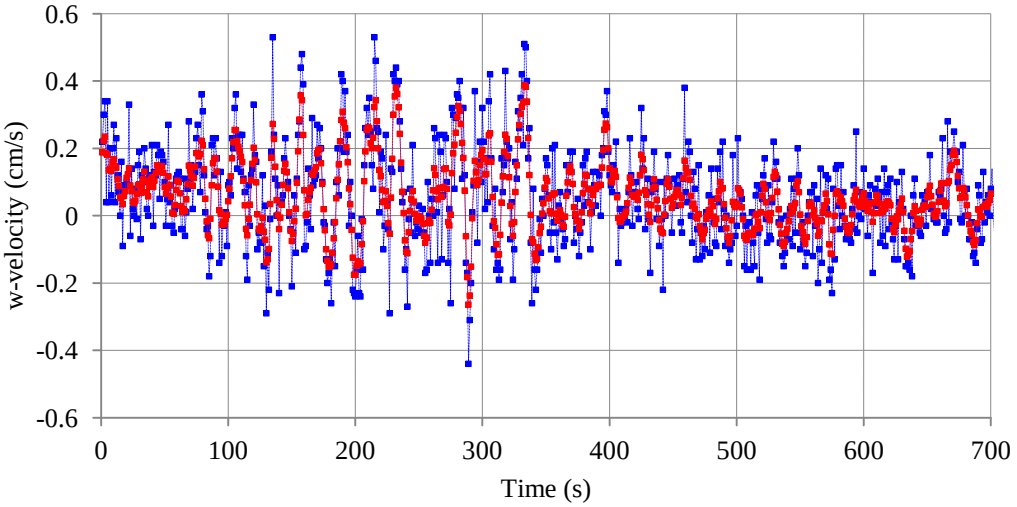

Figure (7.7) – Noisy (blue) and filtered (red) velocity time series for point (0503) at layer 100 mm above bed for saline water condition with the tidal range of 100 mm

$$\begin{aligned}\overline{\boldsymbol{R}}_{xx}(p_m, p_n) &= \overline{\boldsymbol{R}}_{xx}(|m-n|) = \mathrm{E}\left[\left(x(p_m,.)-\overline{\mathrm{E}}_{x(p_l,.)}\right)\cdot\left(x(p_n,.)-\overline{\mathrm{E}}_{x(p_l,.)}\right)\right] \\ &= \frac{1}{N-|m-n|}\sum_{l=0}^{N-1-|m-n|}\left(x(p_l,.)-\overline{\mathrm{E}}_{x(p_l,.)}\right)\cdot\left(x\left(p_{l+|m-n|},.\right)-\overline{\mathrm{E}}_{x(p_l,.)}\right)\end{aligned} \tag{7.19}$$

Again correlation matrix $\overline{\boldsymbol{R}}_{nn}$ is diagonal.

Accordingly, the best linear estimate $\hat{v} = [v(p_1,i), v(p_2,i), \ldots, v(p_n,i)]$ based on noisy data $x = [x(p_1,i), x(p_2,i), \ldots, x(p_n,i)]$ for each and every time instance *i* is computed as follows:

$$\hat{\boldsymbol{v}} = \left(\overline{\boldsymbol{R}}_{xx} - \overline{\boldsymbol{R}}_{nn}\right)\boldsymbol{R}_{xx}^{-1}\,\boldsymbol{x} \tag{7.20}$$

LMMSE estimator relies on the correlation between random variables, and uncorrelated parameters cannot be linearly estimated. Therefore, to achieve a more effective noise reduction, the elements of vector ***x*** should be chosen such that they establish a strong correlation. The methodology can be expanded to two, three, and four dimensions to include the integrated one-, two- and three-dimensional spatial and temporal correlations.

7.6.3.4 Interpolation

Wiener filter also may be used to interpolate missing data points by computing the correlation coefficients between the existing and missing data, either to obtain a higher frequency for a quantity which has been recorded with a low frequency (e.g. velocity) or to estimate a variable in a different place in space (e.g. velocity at a different depth) where no measurements have been taken.

In the following, the performance of a Wiener interpolation filter is examined. For a set of data points and for a window length (2*w* + 1), the correlation between all odd time indexed and even time indexed velocity points are calculated to obtain interpolation coefficients. Then assuming, for example, even time indexed data points are missing, they are estimated as follows:

$$\hat{v}_{2k} = \sum_{i=-w}^{i=+w} h_{2k,\,2k+i}\; v_{2k+i} \tag{7.21}$$

and vector ***h*** is calculated as follows:

$$\boldsymbol{h} = \overline{\boldsymbol{R}}_{oo}^{-1}\,\boldsymbol{R}_{eo} \tag{7.22}$$

in which $\overline{\boldsymbol{R}}_{oo}$ is the correlation matrix of odd time indexed velocity points and $\boldsymbol{R}_{eo}$ is the vector of correlation between odd and even indexed velocity points. Using this

strategy of interpolation, the sampling frequency for the point (0505) at layer 10 cm above bed was increased to 2 Hz from recorded data of 1 Hz. Signal to noise ratio, based on the definition given in equation (7.23), for the interpolated signal was calculated about 10.96 dB. This means that the interpolation error variance is about 0.1 signal power. Figure (7.8) shows the interpolated signal.

$$\mathrm{SNR} = \frac{\mathrm{var}\left(\boldsymbol{x}_{\mathrm{e}} - \hat{\boldsymbol{x}}_{\mathrm{e}}\right)}{\mathrm{var}\left(\boldsymbol{x}_{\mathrm{e}}\right)} \tag{7.23}$$

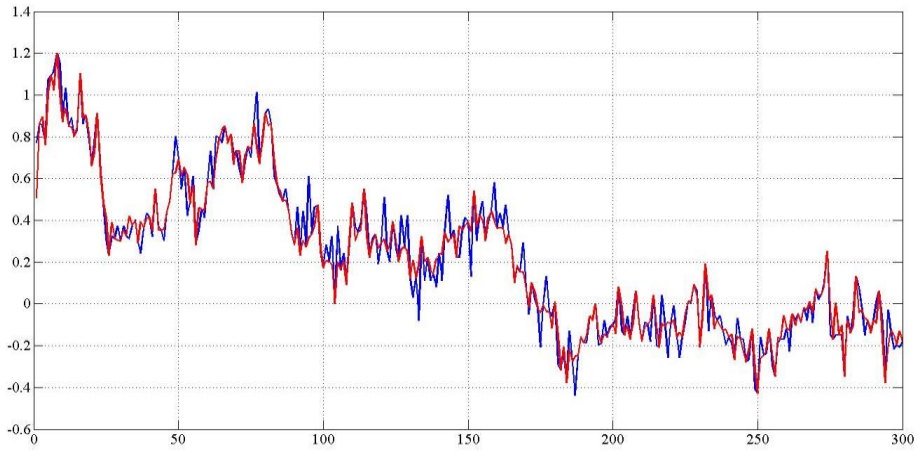

Figure (7.8) – Interpolated data (red) based on the recorded samples (blue) for point (0505) at a depth of 2 cm above bed for tidal range of 100 mm and saline water condition

7.6.4 *Salinity Time Series*

The salinity recorded data were very noisy. However the signal magnitudes fluctuate around the mean value with almost uniform amplitude of fluctuations (Fig. 7.9). A backward moving average strategy has been adapted for the signals of conductivity recorded with a sampling frequency of 5 Hz. Before the tidal water flushes into the harbour, it is expected that the salinity remains almost constant as no forcing influences the water inside the harbour, and only the slight local movements due to stirring the water may produce small motions which will not change the salinity pattern. Therefore the span for the moving average algorithm was chosen such that for each set of data the first part shows uniform behaviour. The result for point (0705) at layer 180 mm above bed, which exhibits the most salinity exchange, is plotted for the tidal range of 100 mm in figure (7.9).

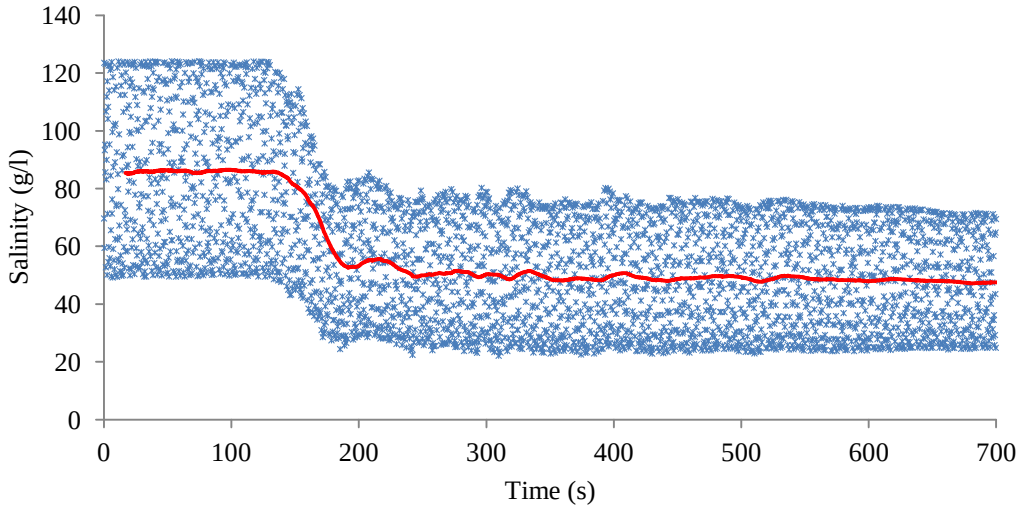

Figure (7.9) – Moving average curve of the noisy salinity samples collected for point (0705) at 180 mm above bed for the tidal range of 100 mm

7.7 SUMMARY

Instantaneous values of velocity components in three directions, water elevations and conductivity were measured at pre-set depths and locations. The instrumentation and the calibration procedure have been described. Tests have been conducted for fresh and saline water conditions, various barrier heights, tidal ranges and mean water depths. The ADV data acquisition and control software was sued for the procedure of measuring the velocity components. For measuring the water surface elevation and conductivity, GENIE data acquisition and control software was adapted and used.

For despiking and denoising the velocity data a linear correlation algorithm was established and a Wiener filter was designed and adapted for the temporal correlation of the signals, which successfully lowered the noise level and removed the spikes where the stationary assumption of the statistical characteristics of flow was valid. The filter can be extended to the spatial domain by establishing one-, two- or three-dimensional correlations. An interpolation method for producing the missing data has been provided which may be deployed for increasing the sampling frequency or producing data for the spatial domain. For conductivity a moving average strategy has been deployed.

CHAPTER EIGHT

PHYSICAL MODEL STUDIES

LABORATORY TESTS RESULTS, COMPARISONS AND DISCUSSIONS

"Experimenting with models seems to afford a ready means of investigating and determining beforehand the effects of any proposed estuary or harbour works; a means, after what I have seen, I should feel it madness to neglect before entering upon any costly undertaking." *Osborne Reynolds* (Langhaar, 1951)

8.1 INTRODUCTION

This chapter presents the laboratory results of the measurements taken in the model harbour. Test arrangements, signal processing and filtering of the recorded data have been presented in Chapter Seven. The presentation of the results, comparisons and discussions is divided into three parts:

- Velocity measurements
- Water elevation measurements
- Salinity measurements

The velocity measurements are presented for time series, horizontal profiles, horizontal flow patterns and comparison profiles for different barrier heights. The water elevation measurements are plotted for time series, and the salinity measurements are presented for time series and horizontal and vertical profiles.

8.2 VELOCITY MEASUREMENTS RESULTS

Time series of some selected velocity measurements are presented. The horizontal profiles show variation of the dominant velocity components along the axes X and Y, and the axis of the harbour entrance (Fig. 7.3). Horizontal flow patterns for four layers demonstrate the general circulations inside the harbour. The horizontal profiles are also graphed for different barrier heights.

8.2.1 *Velocity Time Series*

The velocity time series of *u* and *v* components are presented for 6 points inside the model harbour for the barrier height of 100 mm (BH = 100) and the tidal ranges of 100 mm (TR = 100) and 200 mm (TR = 200) for fresh water (FW) condition in figure (8.1). The schematic location of these points is shown in the figure description. For point P0202 the negative *u* velocities have the largest values at layer 1 cm (L1), near the bottom, and at the top layer (L9). The positive *v* velocity component exhibits large values at layer L1, and almost similar trend for the top layer with larger values. The *w* velocity component (not shown) has very small magnitudes for all layers indicating weak vertical circulations. Velocity time series for point P0208 show almost similar trend for all layers with very small *w* (not shown), and positive *u* and *v* velocity components forming a clockwise circulation in the harbour.

Point P0802 is a point of relatively smaller velocity magnitudes with rather similar trends for all layers and nearly zero velocities for the ebb tide. This point also obeys the same clockwise flow circulation in the harbour. Almost same trend of the velocity time series can be seen for point P0808 for all layers with positive *u* and negative *v* velocity magnitudes and small vertical components, confirming the same clockwise circulation inside the harbour. These results are in agreement with the findings of Falconer (1980a) who reported the observation of one gyre in the experimental and numerical studies of the same harbour configuration.

Points P0503 and P0507 located along Y axis at the left and the right of the centre of the harbour and at an equal distance from it exhibit larger values for *u* velocities and smaller values for *v* velocities with almost symmetrical values for both components that confirms the general clockwise circulation in the harbour.

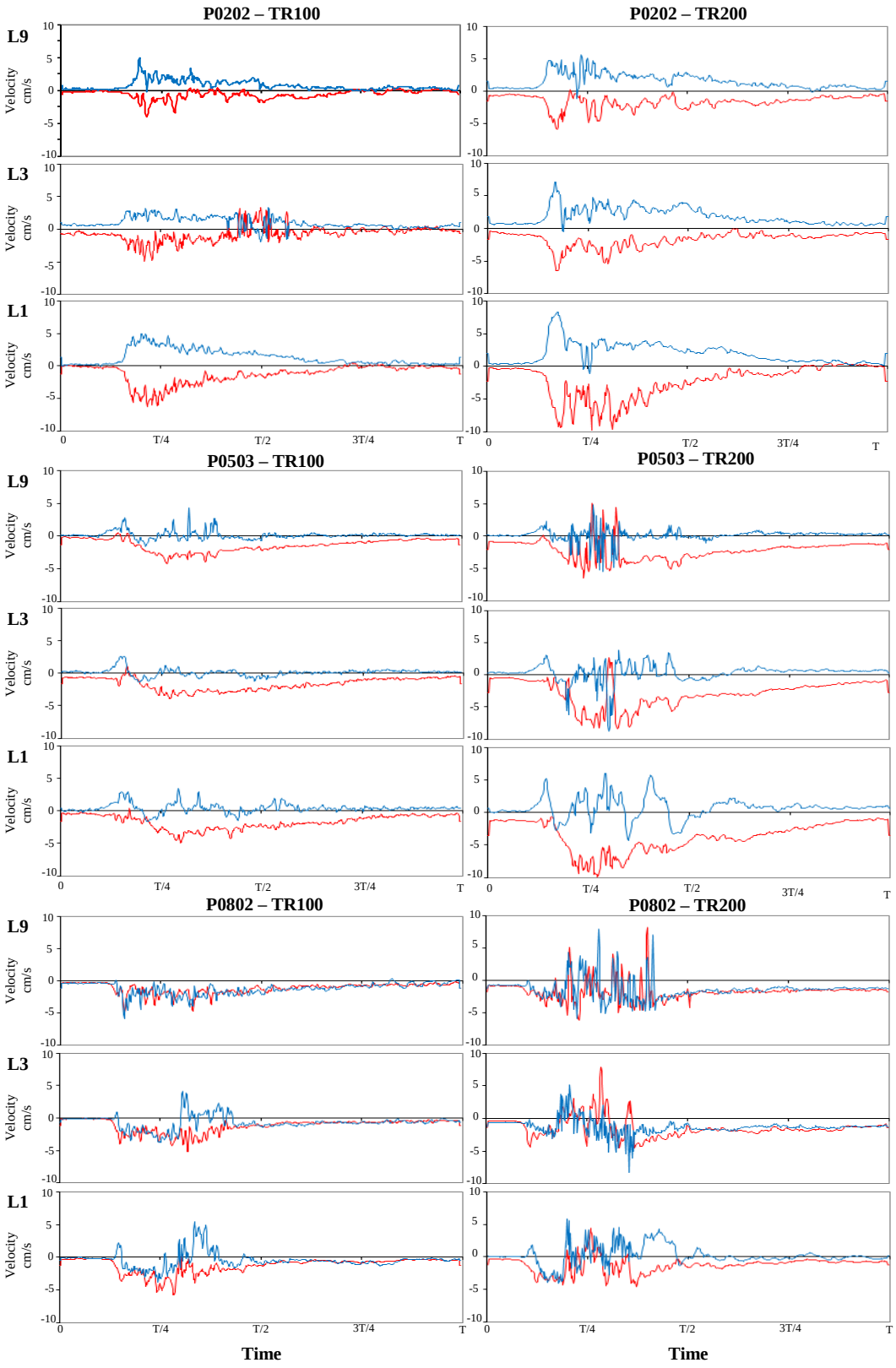

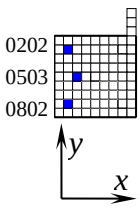

Figure (8.1a) - Velocity time series for points P0202, P0503 and P0802, BH = 100, TR = 100 and TR = 200, FW, layers L1, L3 and L9 for *u* (red) and *v* (blue) components

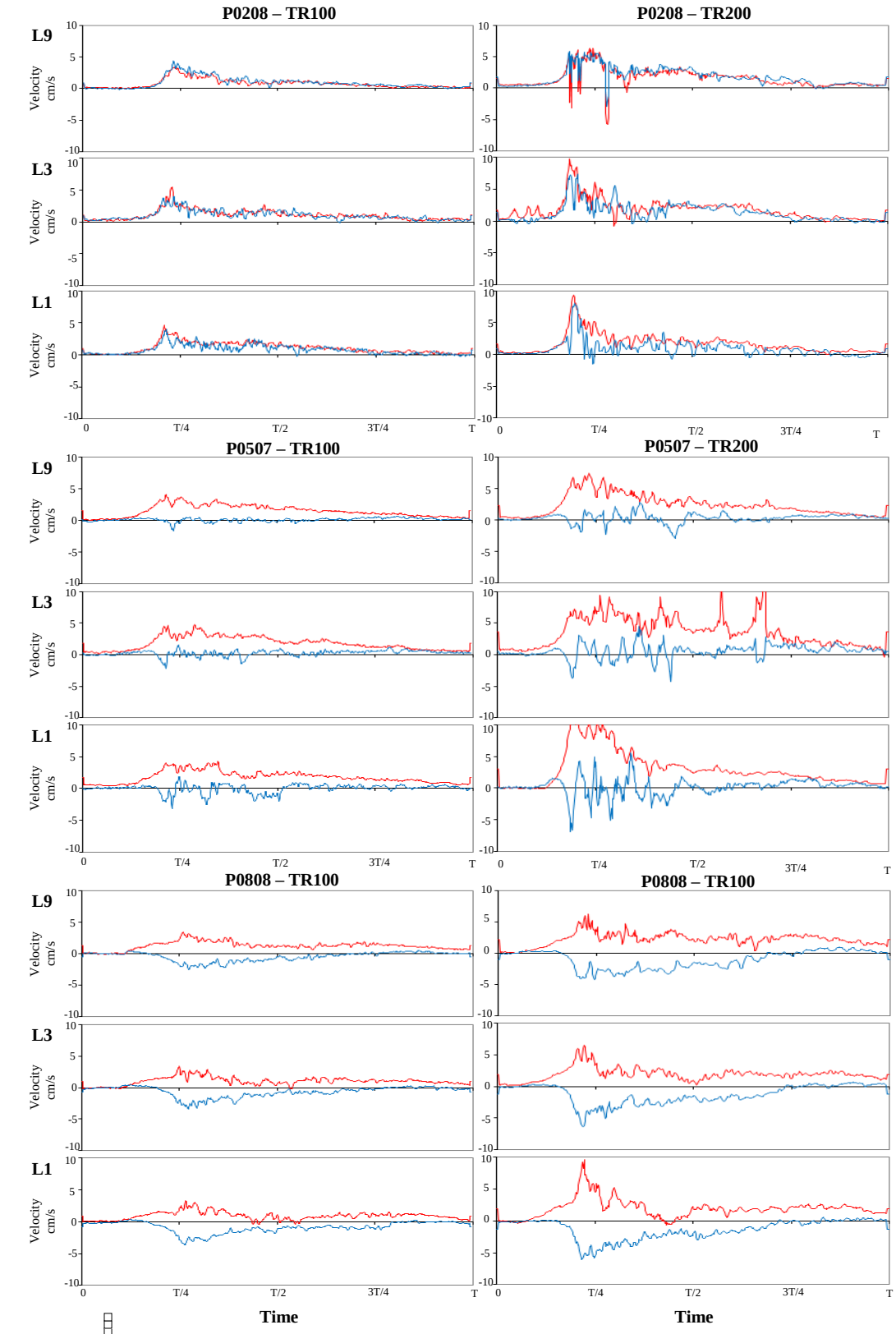

Figure (8.1b) - Velocity time series for points P0208, P0507 and P0808, BH = 100, TR = 100 and TR = 200, FW, layers L1, L3 and L9 for *u* (red) and *v* (blue) components

For points P0305 and P0705 (not shown) the flow patterns are the same as the general clockwise circulation pattern of the flow in the harbour. For point P0908 (not shown) the velocity values rise from the bottom towards the water surface where large noticeable *v* values are present. For point P0909 (not shown) located at the neighbouring point of the entrance, however, the measurements do not show large velocity values. This is thought to be due to the presence of the barrier which is closely located to this point and limits the water motion.

Velocity time series for the tidal range of 200 mm (TR = 200) follow the same patterns as was discussed for the tidal range of 100 mm, but with larger velocity magnitudes. The only remarkable comment is for point P0909, for which, due to the stronger forcing, the *v* velocity component rises noticeably during the ebb tide.

For the barrier height of 200 mm (BH = 200) the time series of *u* and *v* velocity components of point P0705 are illustrated for the fresh and saline water conditions and tidal ranges of 100 and 200 mm (TR = 100 and TR = 200) in figure (8.2). For fresh water condition (FW) and tidal range of 100 mm (TR = 100) the general circulation pattern of the harbour is present. The tidal range of 200 mm (TR = 200) shows same flow regime with larger magnitudes. The flushing in the harbour occurs after the water elevation in the basin rises to the top of the barrier which happens after the mid-flood tide, the reason for the flat part of the graphs for this tidal range. For the saline water condition the water motion is suppressed resulting in lower magnitudes for velocity components for lower layers. For the upper layers, however, the increase of velocity magnitudes is noticeable.

For point P0507 (not shown) the same general circulation pattern is present for lower layers, and for the upper layers water flows towards the entrance. The velocity magnitudes for point P0905 (not shown) increase from the bottom towards the surface but for the saline water condition the increase of the surface layer velocities happens with quite less magnitudes. For point P0909 (not shown) a relatively large positive *v* velocity for the ebb tide exists which is expected.

8.2.2 *Velocity Horizontal Profiles*

The profiles of the velocity components have been graphed along the centreline axes of the harbour with the axes intersecting at the harbour centre, and the axis passing through the harbour entrance. The axes are shown in figure (7.3).

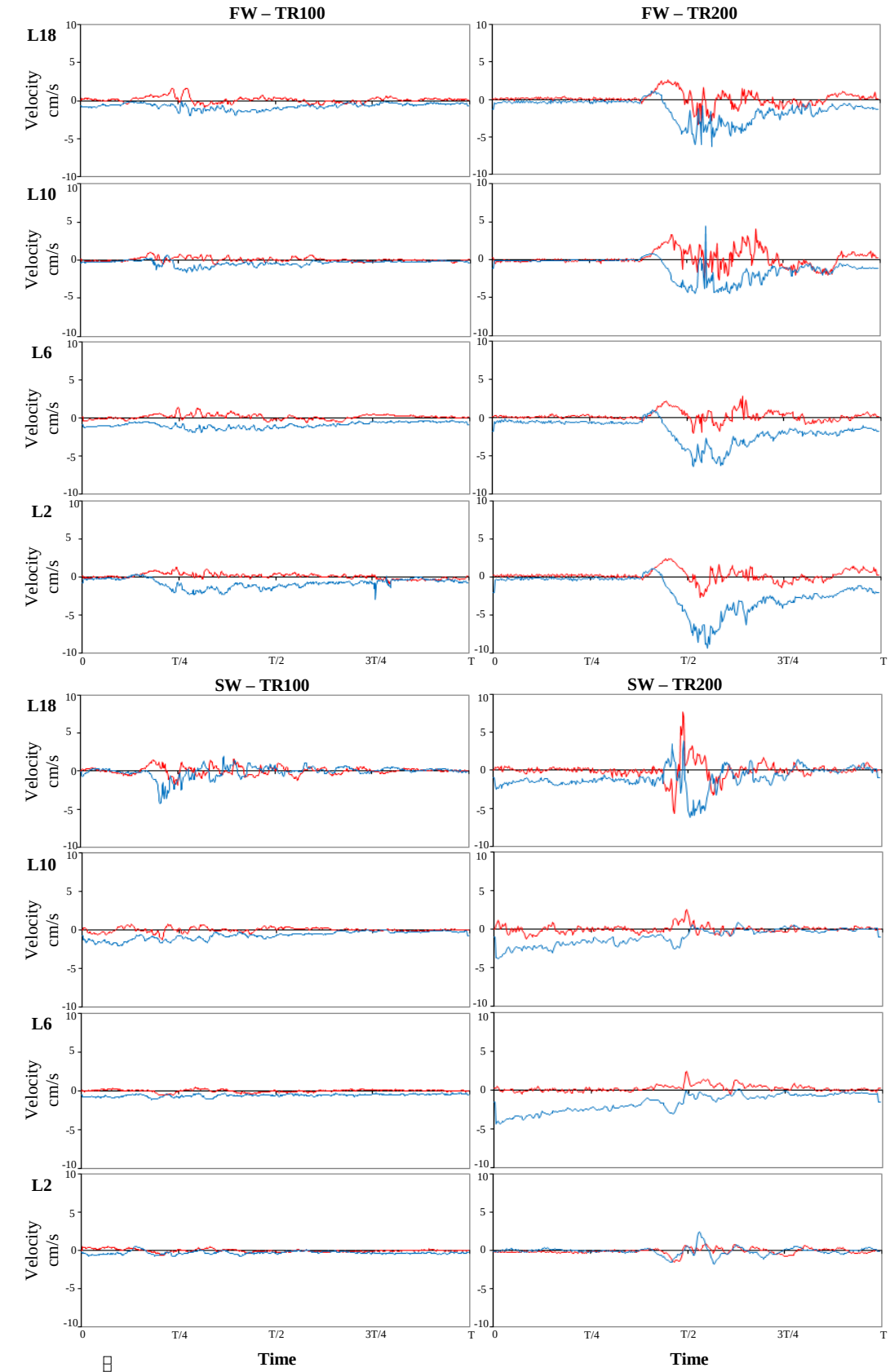

Figure (8.2) - Velocity time series for point P0705, BH = 200, TR = 100 and TR = 200, FW and SW, and layers L2, L6, L10 and L18 for *u* (red) and *v* (blue) components

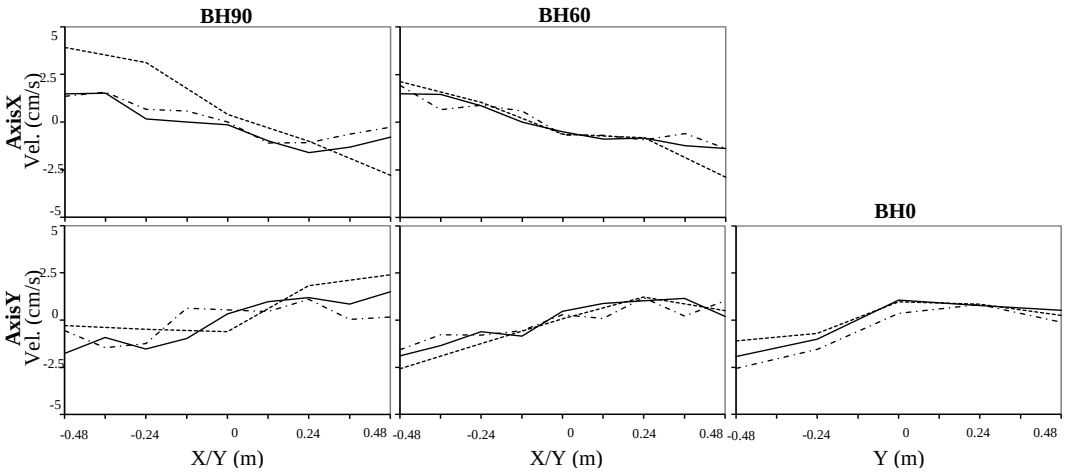

Figure (8.3) - Velocity horizontal profiles for X (*v*) and Y (*u*) axes, BH = 0, BH = 60 and BH = 90, TR = 100 and layers L1 (solid), L5 (dash) and L9 (dash-dot) at mid-flood tide (T/4)

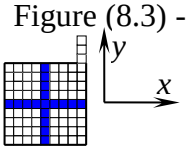

The horizontal profiles of the centreline axes X (*v* velocity) and Y (*u* velocity) are shown for the dominant velocity components for different layers of velocity measurements and for test cases with no barrier and barrier heights of 60 and 90 mm (BH = 0, BH = 60 and BH = 90) at mid-flood tide (T/4) in figure (8.3). The profiles show that the circulation near the wall on the opposite side to the entrance is stronger than the wall where the entrance is located, with the exception of Y axis for BH = 90. Also, for the barriers of the height of 60 and 90 mm (BH = 60 and BH = 90) the circulations show stronger intensities crossing the X axis at layer L5. For mid-ebb tide (not shown) circulations are weaker when compared to mid-flood tide.

For the barrier height of 100 mm (BH = 100) the velocity horizontal profiles of centreline axes X (*v* velocity), Y (*u* velocity) and the axis of harbour entrance (*v* velocity) are presented for two tidal ranges of 100 and 200 mm (TR = 100 and TR = 200) in figure (8.4) at time T/4 and for fresh water condition. The measurements for the barrier height of 200 mm (BH = 200) and tidal range of 100 mm (TR = 100) for both fresh and saline water conditions (FW and SW) have also been profiled along the axes X (*v*), Y (*u*) and the axis of harbour entrance (*v*) in figure (8.4) at time T/4. The horizontal profiles for the same test arrangements but with the tidal range of 200 mm (TR = 200) are also graphed in figure (8.4) for mid-ebb tide (3T/4).

In these profiles the same circulation pattern may be seen. The salinity suppresses the circulation intensity across the water depth with the exception of the top layer. For the barrier of 100 mm (BH = 100) the circulation is weaker at layer L5,

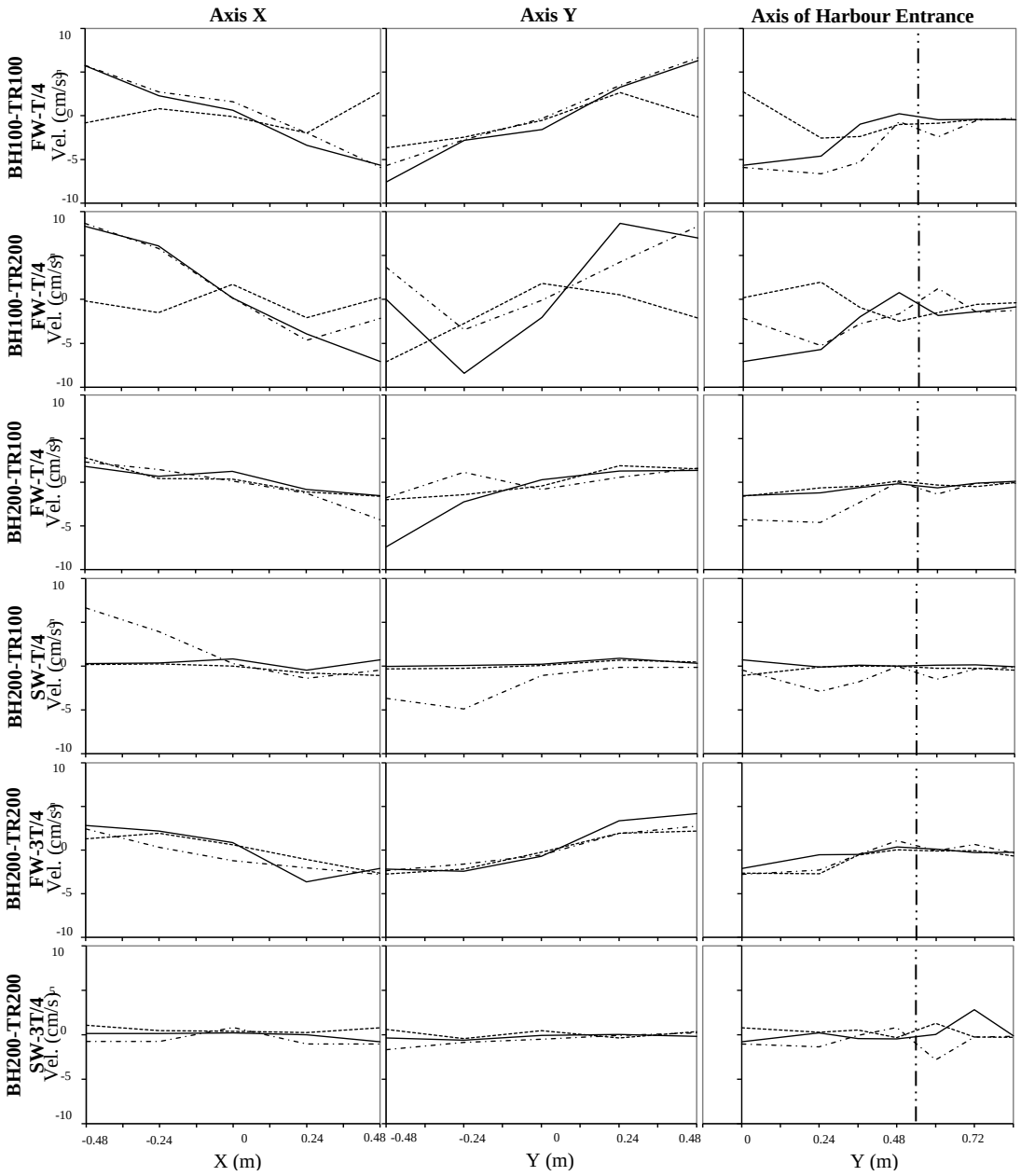

Figure (8.4) - Velocity horizontal profiles for X (*v*), Y (*u*) and harbour entrance (*v*) axes. The barrier heights, tidal ranges and the corresponding times are specified for each graph. BH = 100: L1 (solid), L5 (dash), L9 (dash-dot); BH = 200: L2 (solid), L10 (dash), L18 (dash-dot). The vertical (dash-double dot) line on third column shows the harbour edge.

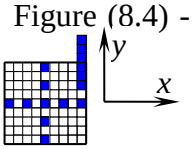

and obviously the tidal range of 200 mm (TR = 200) gives rise to velocity magnitudes. The ebb tide exhibits smaller velocity values and the points outside the harbour follow the general flow pattern in the basin. For the barrier height of 200 mm (BH = 200), tidal range of 100 mm (TR = 100) and the fresh water condition, stronger circulation shows near the bed crossing the Y axis. Larger flushing is apparent at the top layer near the entrance which is expected. Again the salinity

suppresses the flow motion with the exception of the top layer where the velocity magnitudes increase with salinity. For the same barrier height (BH = 200), the tidal range of 200 mm and fresh water condition at the mid-flood tide the circulations are very weak (not shown), and stronger circulations are present at the mid-ebb tide. The negligible velocity values of the mid-flood tide are due to the water level in this case which only reaches the tip of the barrier at time T/4. For this case apart from slight circulation at the top layer with the presence of salinity, for the lower layers the saline water substantially suppresses water motion.

8.2.3 *Horizontal Velocity Flow Patterns*

Velocity flow patterns are demonstrated to give a clearer picture of water circulations in the harbour in horizontal layers of the flow. Horizontal flow patterns have been graphed for layers at 1, 3, 5 and 9 cm (L1, L3, L5 and L9) above the bed for the barrier height of 100 mm (BH = 100) and both tidal ranges of 100 and 200 mm (TR = 100 and TR = 200). For the barrier of 200 mm (BH = 200) and for both fresh and saline water conditions (FW and SW) and tidal ranges of 100 and 200 mm (TR = 100 and TR = 200) the horizontal flow patterns correspond to layers at 2, 6, 10 and 18 cm (L2, L6, L10 and L18) above the bed. The graphs are demonstrated in figures (8.5a) and (8.5b) for mid-flood (T/4) and mid-ebb (3T/4) tides respectively.

The general circulation discussed in previous sections is clearly present in the horizontal flow patterns. The circulations are stronger in the mid-flood tide than the mid-ebb tide for all configurations except for one of the test arrangements which is addressed in next paragraphs. For the barrier height of 100 mm (BH = 100) and the tidal range of 100 mm (TR = 100) at layer L5 a sharp flow shows along the X axis in the middle of harbour, which changes its direction for the tidal range of 200 mm (TR = 200) initiating just inside the harbour near the entrance. For the barrier height of 200 mm (BH = 200), the tidal range of 100 mm (TR = 100) and fresh water condition (FW) a bottom layer flow is present from the corner on the opposite side of the entrance towards the corner on the other end of the diagonal axis of the harbour. The salinity suppresses the velocity magnitudes with the exception of the top layer where the velocity values are increased. For the same barrier height and the tidal range of 200 mm the saline water strengthens the circulation for the mid-flood tide but for the mid-ebb tide the fresh water exhibits stronger circulation than time T/4. Among all cases, this is the only situation that the circulation is stronger for the mid-ebb tide.

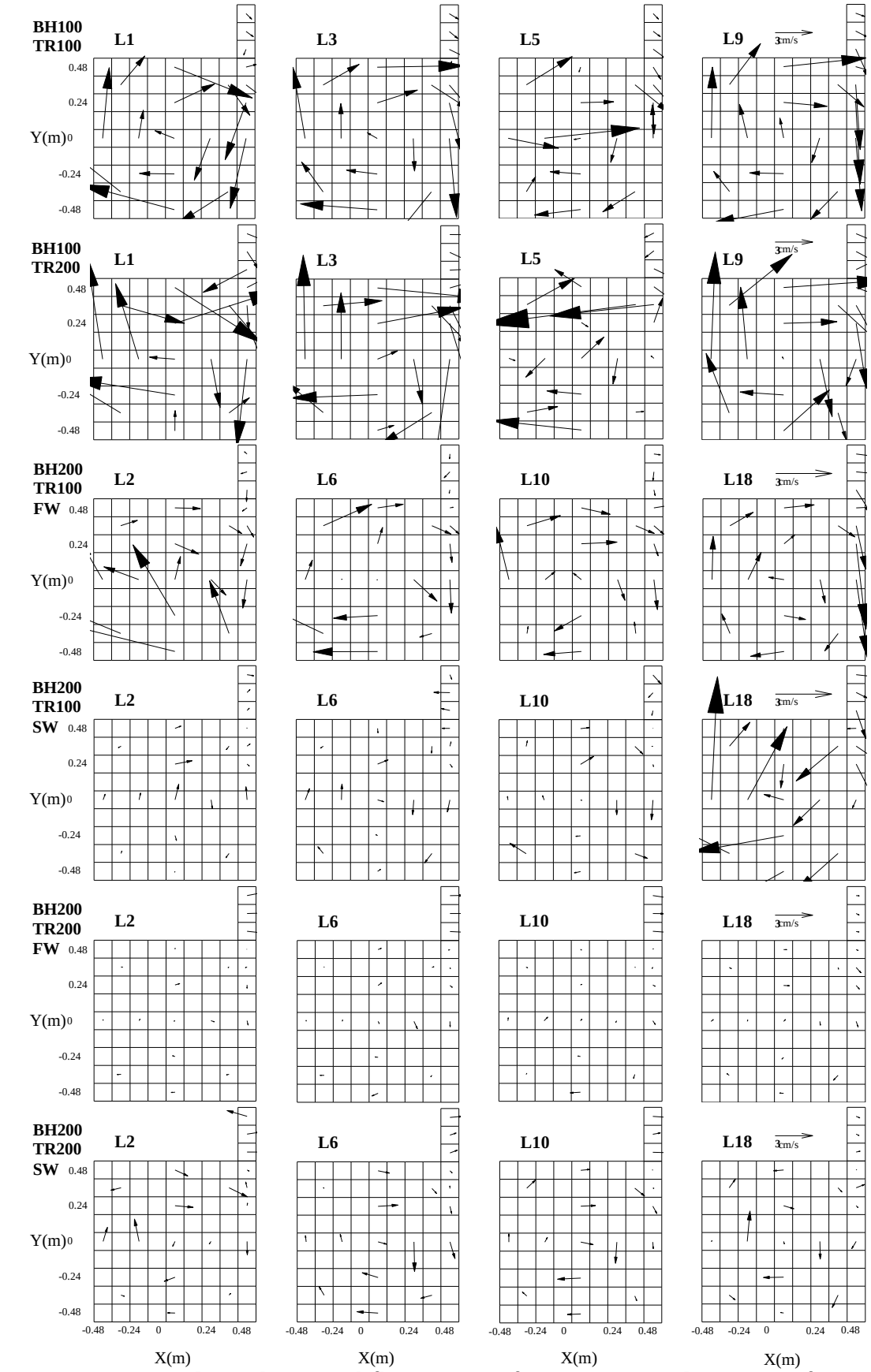

Figure (8.5a) - Velocity horizontal flow patterns for TR = 100 and TR = 200 for BH = 100, FW at layers L1, L3, L5 and L9, and for BH = 200, FW and SW at layers L2, L6, L10 and L18 at time T/4

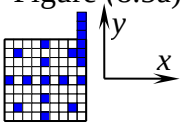

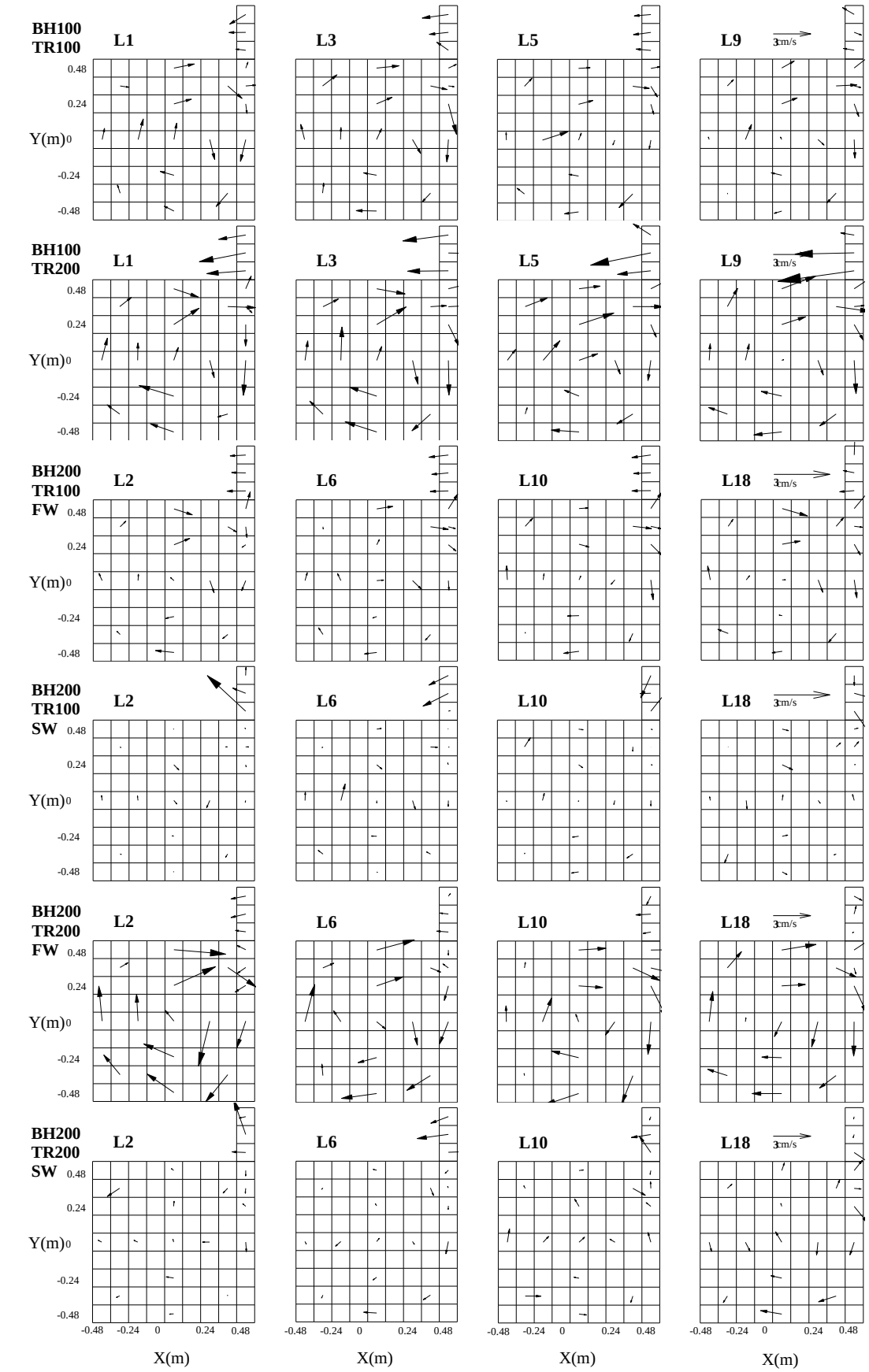

Figure (8.5b) - Velocity horizontal flow patterns for TR = 100 and TR = 200 for BH = 100, FW at layers L1, L3, L5 and L9, and for BH = 200, FW and SW at layers L2, L6, L10 and L18 at time 3T/4

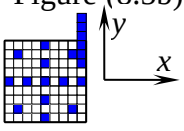

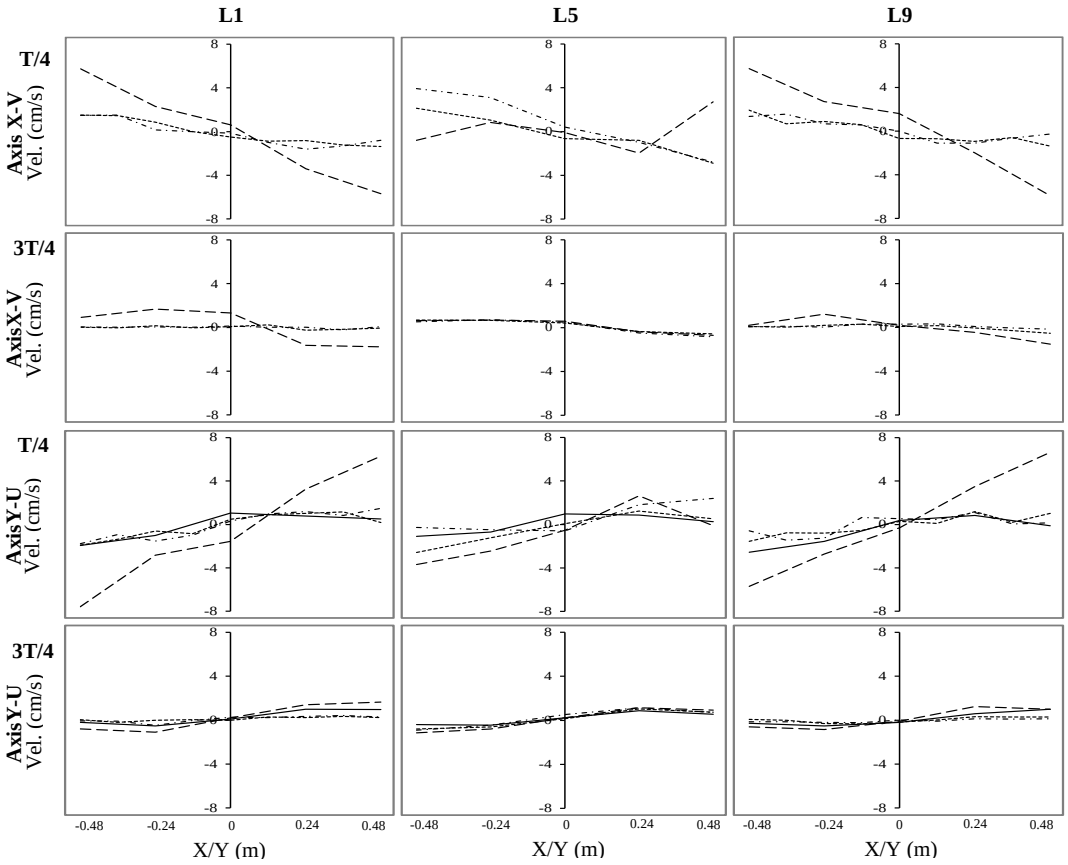

Figure (8.6) - Velocity horizontal profiles for TR = 100 and layers L1, L5 and L9 for axis X (*v*) and Y (*u*) at times T/4 and 3T/4, BH = 0 (solid), BH = 60 (dash), BH = 90 (dash-dot) and BH = 100 (long dash)

8.2.4 *Comparison Horizontal Profiles for Different Barrier Heights*

The horizontal profiles for layers 1, 5 and 9 cm (L1, L5 and L9) above bed for the tidal range of 100 mm (TR = 100) at times T/4 and 3T/4, and the cases of barrier heights of 60, 90 and 100 mm (BH = 60, BH = 90 and BH =100) have been demonstrated for axis X (*v* velocity) in figure (8.6). The same profiles for the cases of no barrier (BH = 0) and barrier heights of 60, 90 and 100 mm for axis Y (*u* velocity) are also presented in the figure (8.6). The profiles generally show that the velocity magnitudes are larger for the barrier height of 100 mm (BH = 100) which is due to the smaller area for the discharge of the water flushing into or from the basin.

8.3 WATER ELEVATION MEASUREMENTS RESULTS

Tidal water surface varies smoothly over the tidal period and the records show no noise during the measurements. Times series of surface variations for point P0505

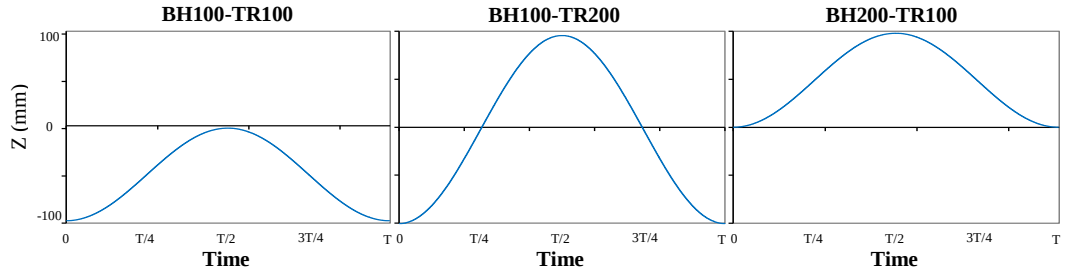

Figure (8.7) – Water elevation time series for point P0505, BH = 100 and BH = 200, TR = 100 and TR = 200, for fresh water condition

are presented in figure (8.7). The graphs show the water elevation time series for the test arrangements of barrier 100 and 200 mm (BH = 100 and BH =200) with tidal ranges of 100 and 200 mm (TR = 100 and TR = 200), and for fresh water condition.

8.4 SALINITY MEASUREMENTS RESULTS

For the salinity measured values in the harbour the time series of some selected experimental points and the horizontal and vertical profiles for the axes X, Y and the axis of harbour entrance are presented.

8.4.1 *Salinity Time Series*

The salinity time series are presented for 4 points and all the layers that the conductivity has been measured, for two tidal ranges of 100 and 200 mm (TR = 100 and TR = 200). The barrier height for both sets of measurements was equal to 200 mm (BH = 200). The results are shown in figure (8.8). The vertical axis of the graphs which shows the salinity is in the reverse direction. The graphs show that for the points near the walls and especially the walls farther from the entrance, where the main circulation occurs, the change of the salinity is more than the central points. The change of the salinity during the tidal cycle essentially affects the top layer of 180 mm above bed (L18) for the case of the tidal range of 100 mm (TR = 100). For the tidal range of 200 mm (TR = 200) the change of the salinity stretches to lower layers and again the points near the walls farther from the entrance experience more decrease of the salinity compared with the central points. The more decrease for the tidal cycle of 200 mm (TR = 200) is expected due to the more power of this tide. The constant value for the first part of the graphs is due to the time needed for the water to reach the tip of the barrier for the tidal cycle of 200 mm and also the time that the salinity probe needed to sense the change of the conductivity.

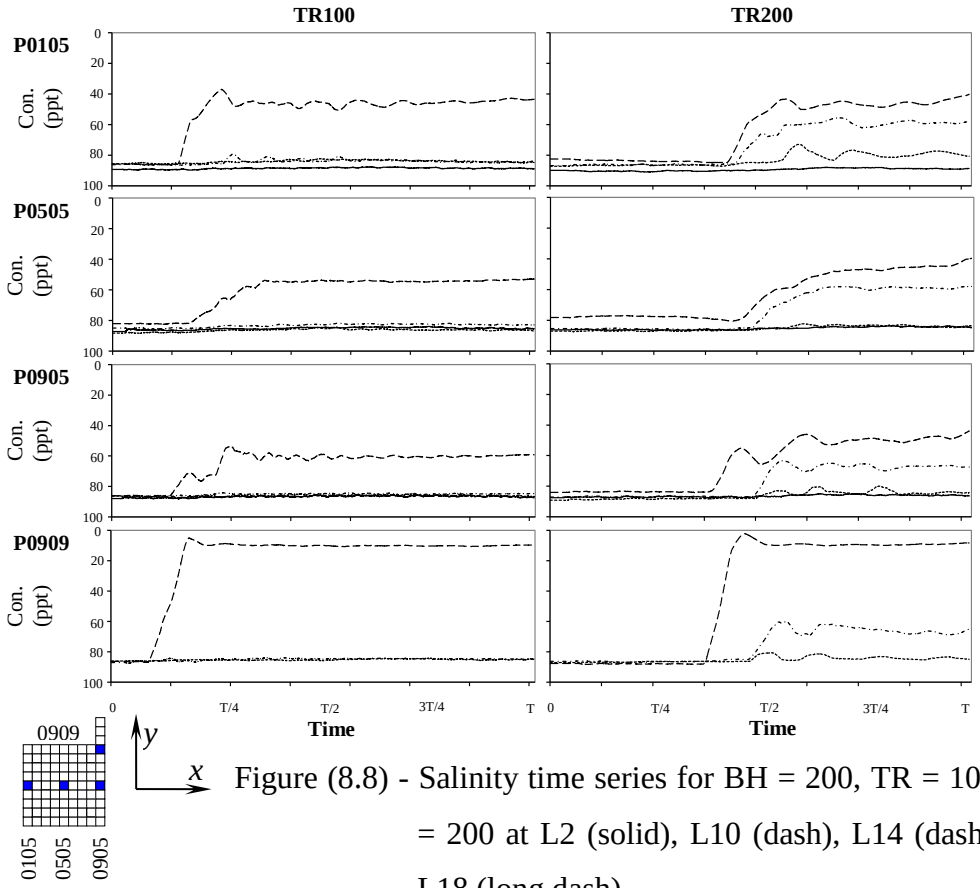

Figure (8.8) - Salinity time series for BH = 200, TR = 100 and TR = 200 at L2 (solid), L10 (dash), L14 (dash-dot) and L18 (long dash)

8.4.2 *Salinity Horizontal Profiles*

Salinity horizontal profiles for the axes X, Y and the axis of harbour entrance for the layers of 2, 10, 14 and 18 cm above bed (L2, L10, L14 and L18) are presented in figure (8.9) for two tidal ranges of 100 and 200 mm (TR = 100 and TR = 200). The graph shows the profiles at 4 times, T/4 to T. For both axes X and Y the far end of the axes show more decrease of the top layer salinity than the end near to the entrance. For the tidal range of 100 mm (TR = 100) the decrease of salinity only happens for the top layer whilst for the tidal range of 200 mm (TR = 200) this stretches to lower layers.

8.4.3 *Salinity Vertical Profiles*

Salinity vertical profiles have been presented for the same configuration of the salinity horizontal profiles in figure (8.10).

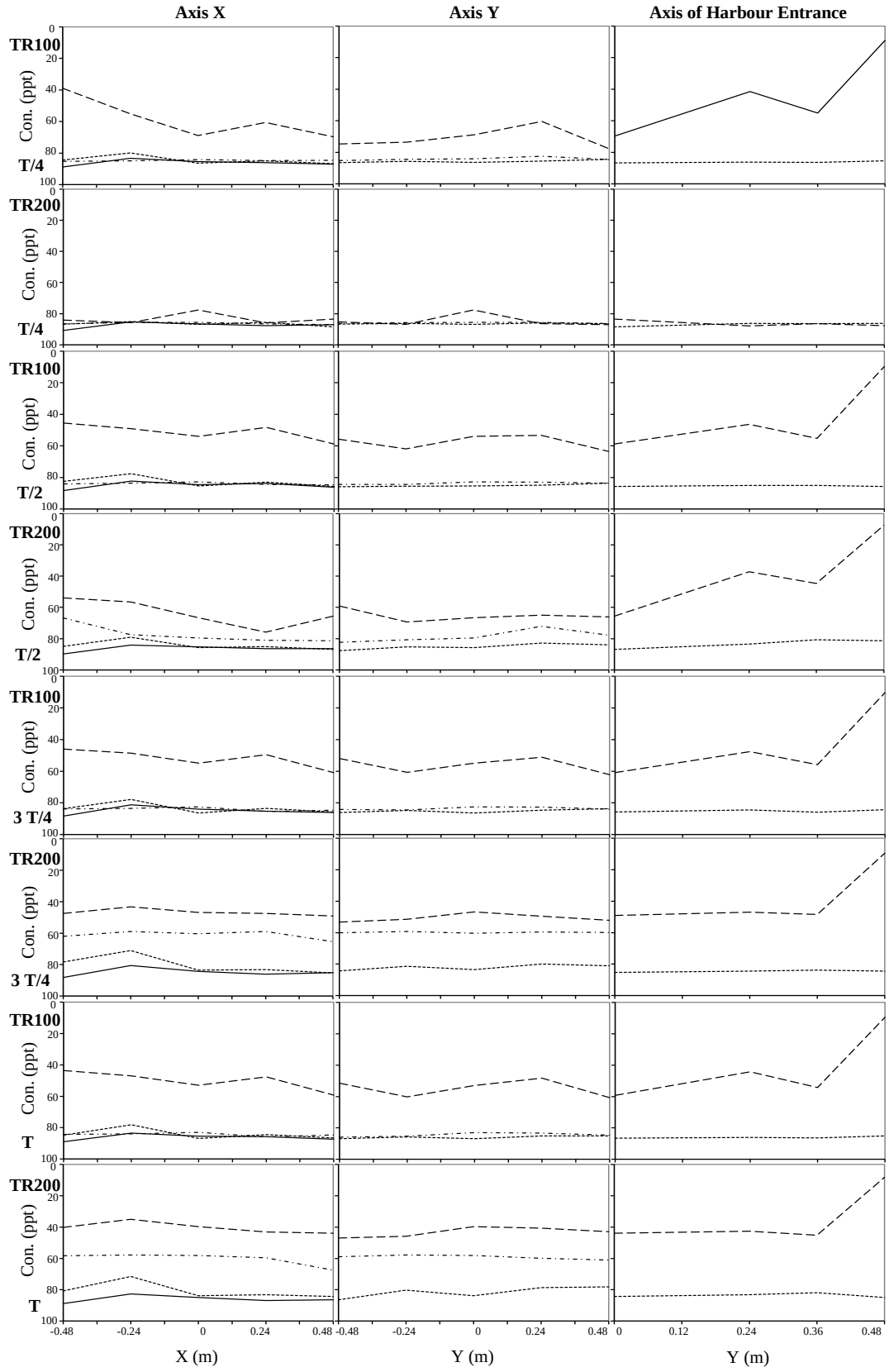

Figure (8.9) – Salinity profiles along axes X, Y and harbour entrance for BH = 200, TR = 100 and TR = 200, for layers L2 (solid), L10 (dash), L14 (dash-dot) and L18 (long dash)

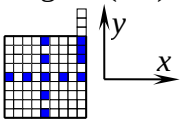

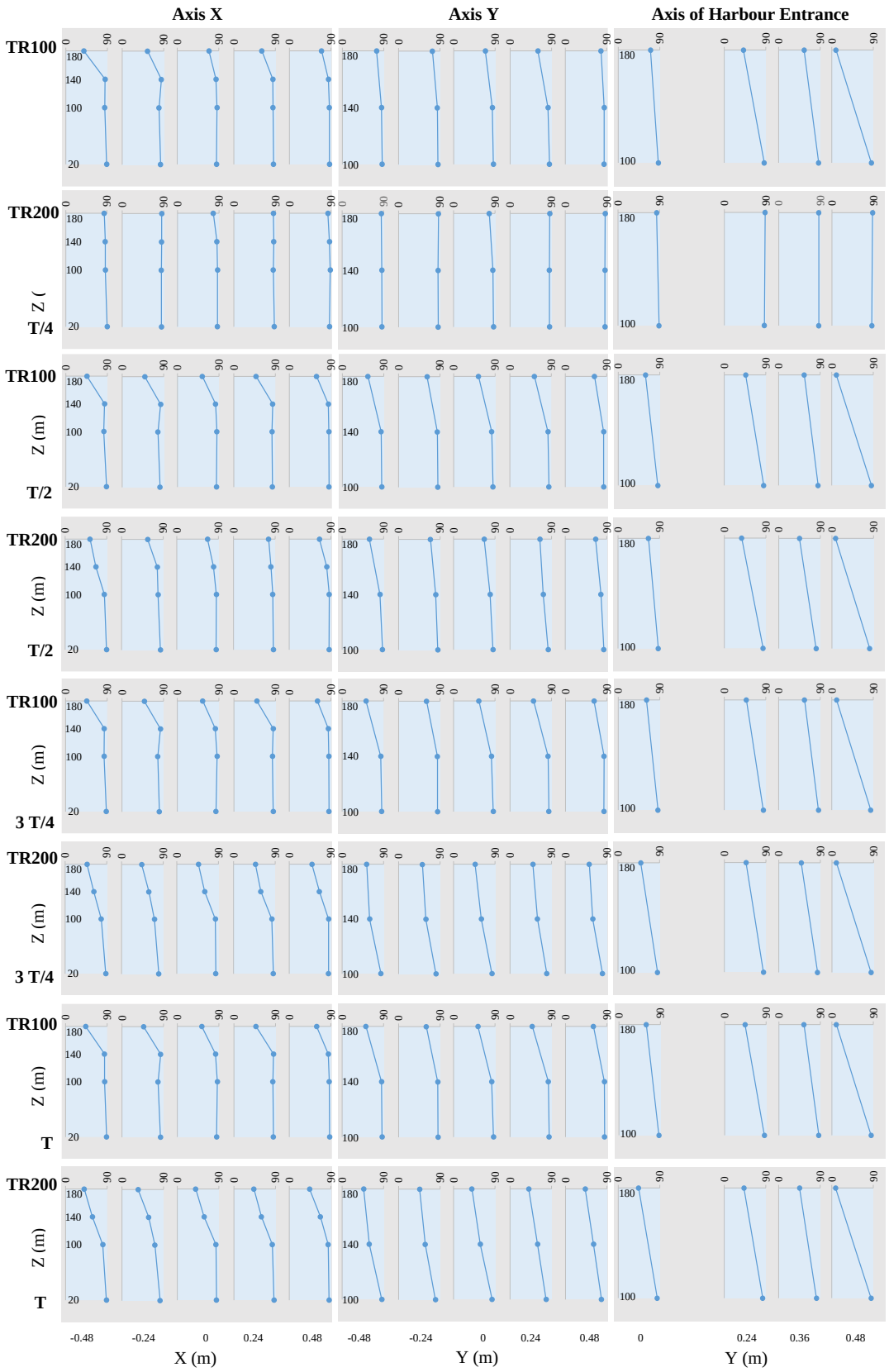

Figure (8.10) – Salinity vertical profiles along axes X, Y and harbour entrance for BH = 200, TR = 100 and TR = 200; top horizontal axes show the concentration values (g/l).

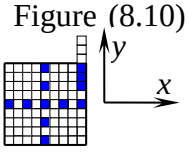

8.5 SUMMARY

Time series of velocity components, water elevations and salinity concentrations are presented for various test arrangements. Horizontal profiles of the dominant velocity components and salinity along the centreline axes of the harbour, and the axis of harbour entrance are graphed. The vertical profiles of salinity are also illustrated along centreline axes of the harbour and the axis of the harbour entrance. The horizontal flow patterns demonstrate the circulations in the harbour.

The time series of velocities show a clockwise circulation in the harbour. The *w* velocity component is very small for all layers indicating weak vertical circulations. Although the vertical velocity flow patterns show some kind of local vertical eddies but they do not present a clear structure of vertical circulation, which may be partly due to the lack of adequate points of recorded velocities in each cross section. However the velocity magnitudes are larger for barrier height of 100 mm in the flood-tide compared to the barrier height of 200 mm for the axis of harbour entrance.

For the point near the entrance the measurements do not show large velocity values, which is due to the close boundaries limiting the water motion. Velocity time series for the larger tidal range exhibit larger velocity magnitudes. The barrier height of 200 mm exhibits lower velocity magnitudes. The horizontal profiles for mid-flood tide show stronger flow circulations compared to mid-ebb tide exhibiting low magnitudes for velocity component values. The comparison horizontal profiles for different barrier heights show that the velocity magnitudes are generally larger for the barrier height of 100 mm compared to cases with the barrier heights of 0, 60 and 90 mm, which is due to the smaller area for the discharge of the water flushing into or from the basin.

The tidal water surface varies smoothly over the tidal period and the records show no noise during the measurements. The times series of wave monitor probe show the water elevation variation as it is expected.

Salinity suppresses the circulation intensity across the water depth with the exception of the top layer where the velocity magnitudes are increased with salinity. This results in less mixing in the vertical direction and stronger flushing on the surface. The graphs show that for the points near the walls and especially the farther walls to the entrance, where the main circulation occurs, the change of the salinity is

more than the central points. The change of the salinity during the tidal cycle essentially affects the top layer for the tidal range of 100 mm. For the tidal range of 200 mm the change of the salinity also stretches to the lower layers. Salinity distributions also confirmed the influence of the circumnavigating flood tide jet, with the variations generally increasing radially outwards from the harbour centre indicating the occurrence of the maximum flushing around the harbour, and the highest salinity concentrations near the centre.

CHAPTER NINE

NUMERICAL MODELLING

APPLICATION TO THE MODEL HARBOUR AND COMPARISONS WITH THE EXPERIMENTAL RESULTS

"By a model is meant a mathematical construct which, with the addition of certain verbal interpretations, describes observed phenomena. The justification of such a mathematical construct is solely and precisely that it is expected to work."

von Neumann (O'Connor and Robertson, 1999)

9.1 INTRODUCTION

This chapter is dedicated to the application of the numerical model to the model harbour and presentation of the results. The chapter comprises four parts:

- Validation of the three-dimensional numerical model
- A mesh convergence study for the three-dimensional applications
- An investigation for studying the effect of distortion ratio on the results
- A study for analysing the influence of mean water depth and barrier height and variation of the salinity concentration on the hydrodynamics and stratification in the harbour. This study also provides simulated results of the salinity stratification in more realistic conditions and compares the hydrodynamics inside the harbour for saline or fresh water conditions in the harbour under fresh or saline water flushing respectively.

9.2 THREE-DIMENSIONAL MODEL VALIDATION

The validation process includes the calibration and the verification of the three-dimensional numerical model. The model has been calibrated by the experimental data of the two cases of fresh and saline water conditions. For the verification, the simulated results for the fresh and saline water conditions of two other cases have been compared with the corresponding experimental data.

It often happens that the mixing and flow of some areas within water bodies are separated from the adjacent areas by natural or manmade walls (e.g. break-waters in harbours). It is also most possible that in the numerical simulation of such water bodies and due to the computational time, the grid size is much larger than the thickness of such walls, barrages, barriers, etc. Therefore assuming the thickness of the wall equal to one grid size could cause serious inaccuracies, especially in the regions of discontinuity (e.g. in the entrance of a harbour), and provide unrealistic flow patterns. Using non-uniform grid near such boundaries -with the expense of reduction of the order of accuracy of scheme- is one solution. In this study to eliminate the effects of wide-crest overflow and to improve the accuracy of the predictions, for simulation of barriers, a zero-thickness wall with characteristics of a wall boundary is assumed to be placed at the entrance of the harbour.

9.2.1 *Model Calibration*

The numerical model has been calibrated for the fresh water condition with the experimental results of the test with barrier height of 100 mm (BH = 100) and tidal range of 100 mm (TR = 100). For the calibration of the saline water condition the laboratory measured data of the test with barrier height of 200 mm (BH = 200) and tidal range of 200 mm (TR = 200) was used. The saline water has 80 g/l salt content with a relative density of 1.052 where the relative density of fresh water was taken equal to 0.998. The surface roughness parameter and the bounds for the k and ε values were adjusted so that the best results were obtained compared to the experimental data. This setting was then maintained for the verification of the numerical model for both fresh and saline water conditions.

Although the bounds for k and ε values alter the turbulent eddy viscosity, but it was found that the more influential parameter in this study was the surface roughness, which was equal to k_s = 0.02 m where the closest agreements with the

measured values were obtained. It should be mentioned, however, that the predictions were not largely dependent on the calibration parameters, which is mainly due to the simple geometry and bathymetry and the uniform roughness of the model harbour.

The tidal flushing into the harbour exhibits a phase difference compared with the experimental data. To overcome this, the phase difference of the peak of the water elevation inside the harbour was compensated for the numerical model and this time difference was applied to the time that the predicted values are compared with the experimental data for all results.

9.2.2 *Model Verification*

For the verification of the numerical model, the simulated results for velocity, water elevation and salinity were compared with the experimental data. For both fresh and saline water conditions the comparisons were made for the case with the barrier height of 200 mm (BH = 200) and the tidal range of 100 mm (TR = 100).

9.2.2.1 Velocity Components

The simulated velocity values have been compared against the time series, the velocity profiles along X and Y axes and the axis of harbour entrance, and the velocity flow patterns inside the harbour of the measured values of the velocity components.

9.2.2.1.1 Velocity Time Series

Six points are chosen for time series comparisons of the velocity components. Four of these are the end points of the centreline axes of the harbour which are close to the walls and experience the strongest circulations. One is the central point of the harbour and the other one is the point located adjacent to the entrance just outside the harbour. The comparisons of the time series for the fresh and saline water conditions are presented in figure (9.1) for the dominant velocity for each point.

For the fresh water condition for the point (0501) the model slightly under-predicts the absolute *u*-velocity component. It is understood that the model slightly under-predicts the velocity components for the zones where the circulation is strong and that the under-prediction is associated with the dominant velocity component.

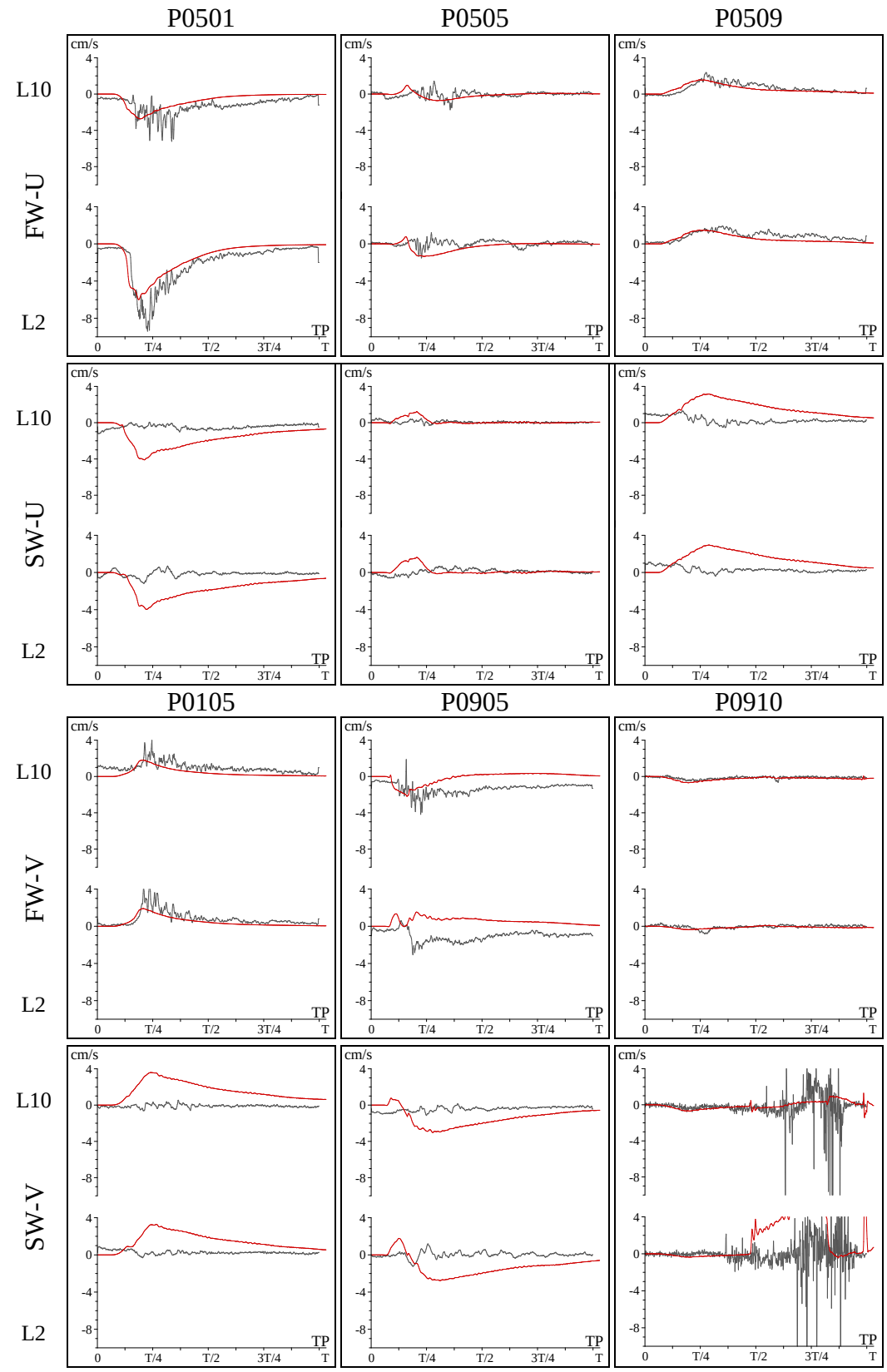

Figure (9.1) - Comparison of simulated (red) and measured (grey) velocity time series for the barrier height of 200 mm (BH = 200), tidal range of 100 mm (TR = 100) and fresh water condition (FW) for the dominant velocities of points P0501, P0505, P0509, P0105, P0905 and P0910

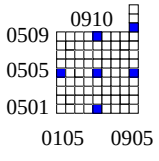

This under-prediction is due to the model calibration which has adjusted the model in favour of better predictions for the interior zones of the harbour. In other words the model calibration adjusted the model so that the absolute value of the dominant velocity component for the points located along the walls, which experience the strongest forcing due to the circulation, are under-predicted in favour of a better estimation for the interior points. The values of the experimental data show discrepancy from zero at time zero, which is thought might be due to the residual currents in the harbour from the previous experimental test. For the central point (0505) the simulated results do not show the variations present in the measured data. Again due to the location of the point (0509) the predicted absolute values of the *u*-velocity show very little underestimation compared with the measured values. Same reason applies to point (0905) for the *v*-velocity component for which the absolute value of the predictions shows an underestimation compared with experimental results. Although the model calibration in favour of interior zones resulted in lower predicted absolute values for dominant velocities in strong circulations, the general flow patterns exhibit closer agreement with the flow patterns of the laboratory data.

For the fresh water condition for point (0105) the *u*-velocity predictions are in good agreement with the measured values (not shown). It is thought that the oscillations in the laboratory data do not represent the real flow fluctuations and are mostly related to the data acquisition problems associated with the noisy samples. The filtering procedure has enhanced the data, but for the points where the stationary assumption of the statistical characteristics of the flow is not valid, the noise and the spikes are present. However the numerical model slightly under-predicts the absolute *v* values. Finally the point (0910), just outside the harbour and adjacent to the entrance, shows a generally good agreement with the time series of the measured velocity components.

The saline water suppresses the velocity magnitudes in the lower layers of the water column and increases the circulation forcing at the top layer. For the saline water condition due to the suppression of the velocities for the lower layers and the increase of the velocity values for the top layer, the under-prediction present in the fresh water condition for the near wall points have changed to an over-prediction for lower layers and a better agreement of the results for the top layer.

This over-prediction is present for the *u*-velocity component of the lower layers of point (0501). In the graphs of point (0505) the simulated values peak for the *u*-

velocity component which is not present in the laboratory data. For point (0509) the over-prediction of the lower layers for the absolute *u*-velocity and for point (0905) the over-prediction of the absolute *v*-velocity for all layers are present. For the point (0105) the simulated *v*-velocity values are over-predicted for the lower layers compared with the experimental data. Due to the high oscillations of the experimental data for point (0910) it is difficult to conclude about the comparisons of this point but the general agreement is good.

9.2.2.1.2 Velocity Profiles

The velocity profiles for fresh and saline water conditions with the barrier height of 200 mm (BH = 200) and tidal range of 100 mm (TR = 100) are graphed in figure (9.2). The profiles show the dominant velocity variations along the axes X, Y and the axis of harbour entrance. The dominant velocities are compared for two layers of 6 and 10 cm above bed at times T/4, T/2 and 3T/4.

The simulated velocity profiles of *u*-component for the Y axis show an under-prediction compared with the measured values, but the general trends are similar. The *v*-velocity predicted values along the X axis show discrepancies with the laboratory measured values but the general trend of the experimental and numerical results is similar. However, at times T/2 and 3T/4 the experimental values show the same trend as the time T/4, but the simulated results do not show much circulation. In fact the under-prediction has resulted in small velocities with weak circulations. For the entrance axis the measured values are almost negative but this is not in agreement with the predicted values for the interior part of the harbour. The under-prediction of the numerical model is also evident in the results.

The simulated saline water velocity profiles for *u*-component along the Y axis imply a circulation which is due to the over-prediction of the numerical model for the saline water condition. This circulation is not present for the experimental data. The model over-predicts the *v*-velocities.

9.2.2.1.3 Velocity Flow Patterns

To visualise the general circulations, the horizontal flow patterns of the simulated values and the experimental data are presented and compared. The flow patterns are shown in figure (9.3) for the fresh and saline water conditions with the barrier height of 200 mm (BH = 200) and the tidal range of 100 mm (TR = 100) for

three layers of 2 (L2), 10 (L10) and 18 (L18) cm above bed at mid-flood and mid-ebb tides. The reference vector is shown on the top of the page.

For the fresh condition the horizontal flow patterns show a generally good agreement with the flow patterns based on the measured values. The velocity magnitudes are generally under-predicted especially during the ebb tide. The results are in good agreement with the measured values for the time T/4. For the saline water condition the flow patterns are in general good agreement.

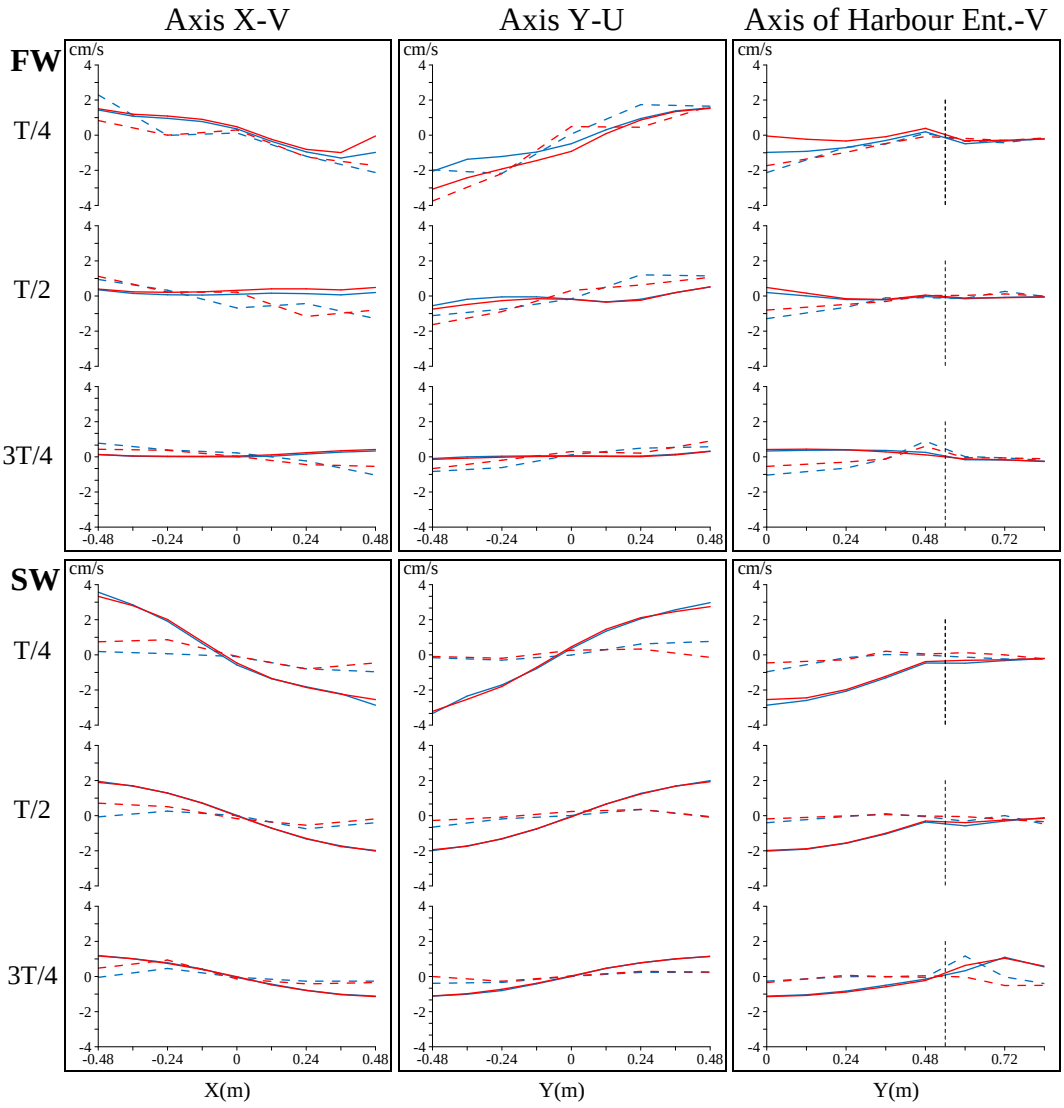

Figure (9.2) - Predicted (solid) and measured (dash) velocity profiles for fresh (FW) and saline (SW) water conditions along the axes X, Y and harbour entrance for their dominant velocity components at layers L6 (red) and L10 (blue) at times T/4, T/2 and 3T/4. Vertical (dash) lines of third column show the edge of harbour.

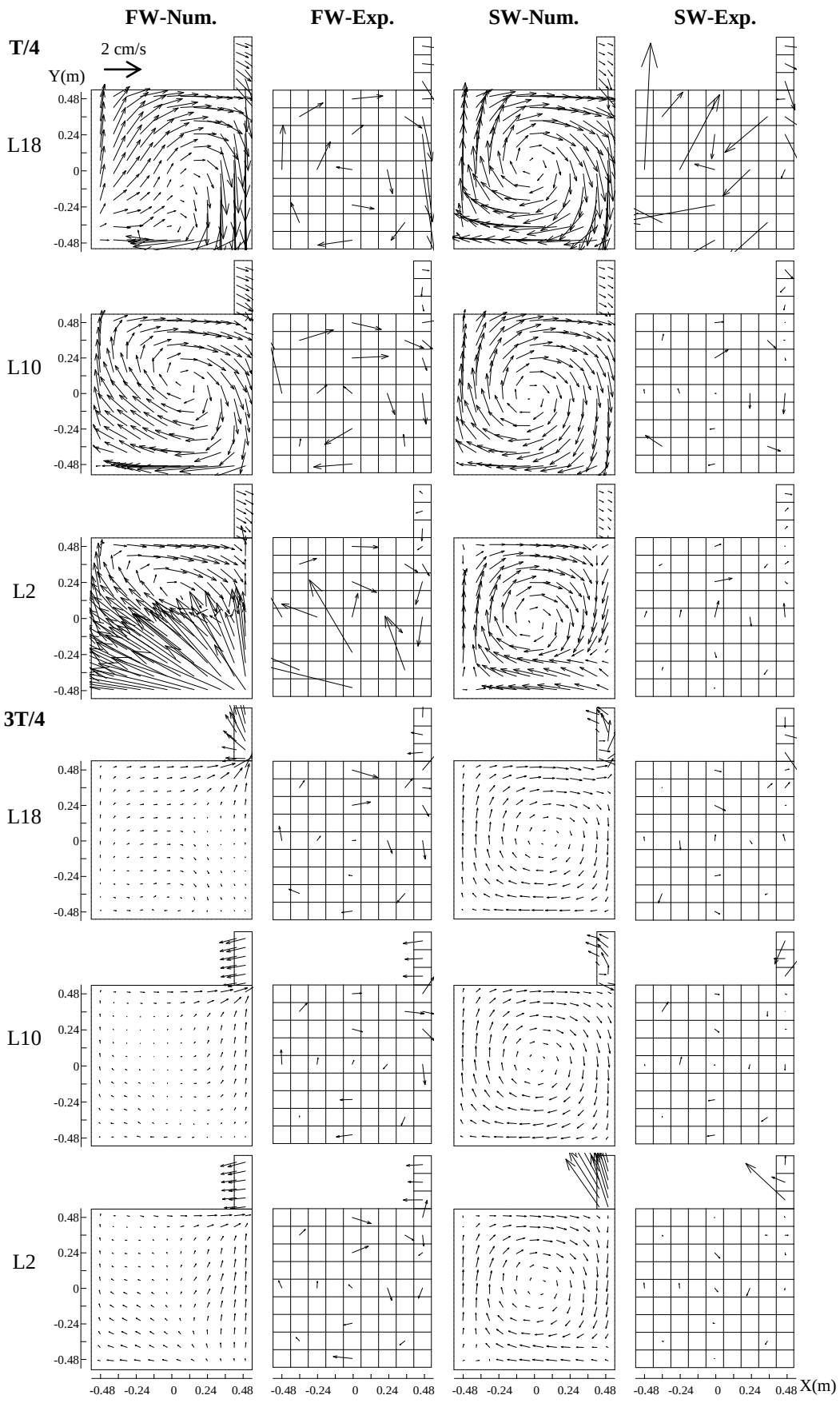

Figure (9.3) - Simulated and measured flow patterns for fresh (FW) and saline (SW) water conditions, BH = 200, TR = 100, for layers L2, L10 and L18 at T/4 and 3T/4

9.2.2.2 Water Elevation

For the water elevation the simulated time series of points P0501, P0505 and P0509 are compared against measured values in figure (9.4). The simulated water elevation time series show good agreements with the measured data.

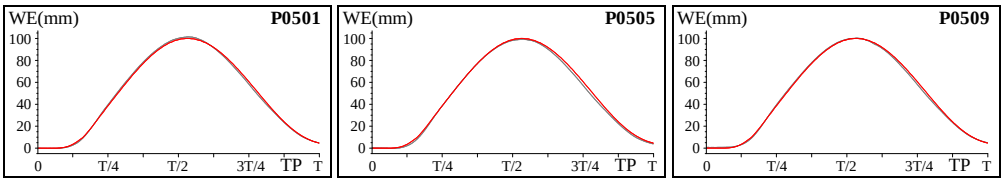

Figure (9.4) – Time series of simulated (red) and measured (grey) values of water elevation

9.2.2.3 Salinity

The time series of the simulated salinities for three points along the Y axis are compared with the laboratory measured values in figure (9.5) for two layers of 10 (L10) and 18 (L18) cm above bed which experience most variations during the tidal excursions. The salinity profiles along the three axes X, Y and the axis of harbour entrance are graphed in figure (9.6). These profiles are shown at mid-flood and mid-ebb tides at layers L10 and L18.

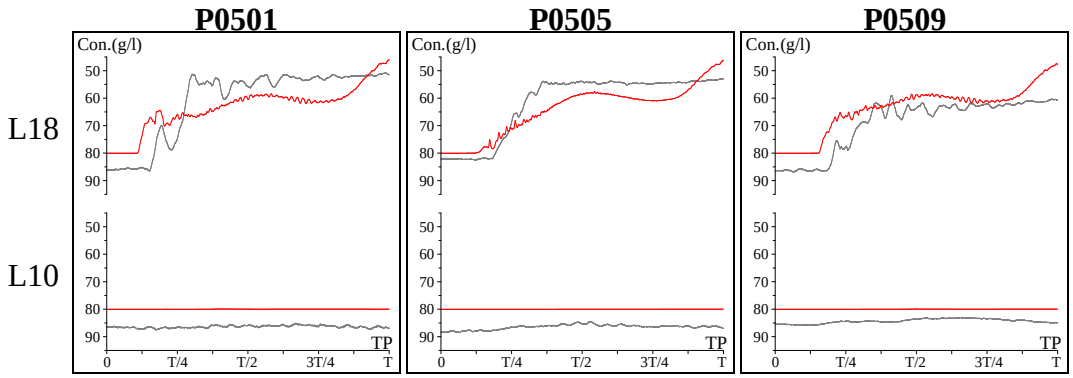

Figure (9.5) – Simulated (red) and measured (grey) time series of salinity values for L10 and L18

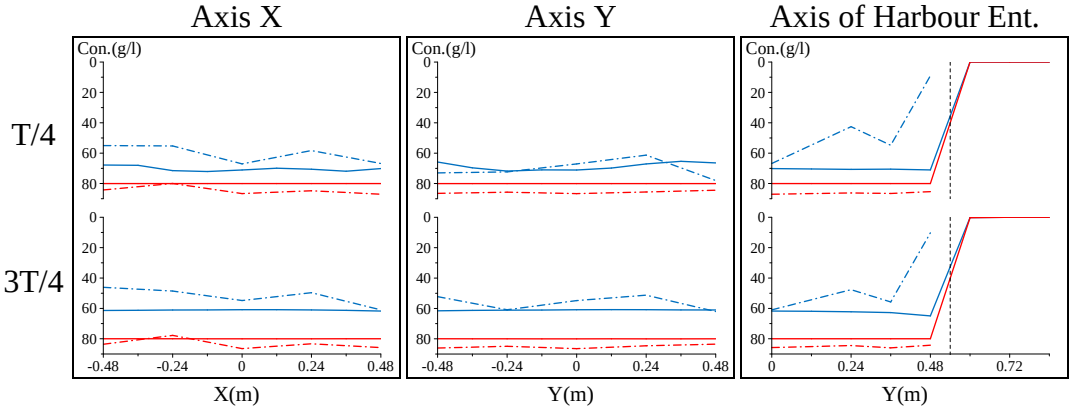

Figure (9.6) - Predicted (solid) and measured (dash) salinity profiles along X, Y and entrance axes at T/4 and 3T/4; L10 (red) and L18 (blue). Vertical (dash) lines show the edge of harbour.

Inspecting the salinity time series shows that the initial salinity of the laboratory measured values is more than the value of 80 g/l planned for the experiments, which may be due to the extra amount of salt added to the water or due to malfunctioning of the conductivity probe. For the numerical simulations, however, the salinity concentration has been taken equal to 80 g/l. Apart from the difference in the initial salt concentration values, the predictions are in good agreement with the laboratory data for layer L10 for all points. For the layer L18, points (0501) and (0505) are over-predicted and the comparisons for point (0509) show good agreements. The salinity profiles also show good agreements between the simulated and measured values for layer L10, but for layer L18 the simulated values are over-predicted. The numerical results exhibit almost constant values along the axes X and Y and do not show the local variations present in the experimental graphs.

9.3 MESH CONVERGENCE STUDY

In order to optimise the accuracy and economy a mesh convergence study has been carried out for the three-dimensional applications. The saline water condition with the barrier height of 200 mm and tidal range of 100 mm is simulated. The study is organised in two steps. In the first step, keeping the grid dimension constant in the horizontal plane and equal to $\Delta x = \Delta y = 3$ cm, the number of layers in the z-direction has been taken equal to 10, 15, 20 and 25, and the simulations have been carried out for each number of the layers. In the second step, keeping the number of layers equal to the number derived in the first step, the grid size in the horizontal plane has been taken equal to 2, 3 and 4 cm for different sets of the simulations. The results of the simulations are then plotted against the measured values and the comparisons have been made. The strategy is to determine the set of the simulations with the coarsest possible grid, while remaining insensitive to grid resolution and exhibiting close predictions compared to the measured values. The comparisons have been made for the velocity and salinity profiles. The predictions for the alternative number of layers and grid size for water elevations are almost the same.

9.3.1 *Velocity Components*

The velocity profiles are plotted for the u-velocity components along Y axis at mid-flood tide (T/4) in figure (9.7) for layers 6 (L6) and 10 (L10) cm above bed. It

can be seen that the numerical set-up of 25 layers shows divergence of the results. This analysis suggests that the choice of 20 layers for *z*-direction optimises accuracy and economy while providing the closest predictions to measured values. To analyse the effect of the horizontal grid dimensions, the inspection of velocity profiles (Fig. 9.7.b) suggests grids of 3 or 4 cm. Owing to the point that the grid size of 4 cm exhibits oscillations for the last part of the tidal range during the ebb tide, the grid size of 3 cm is recommended for the horizontal mesh.

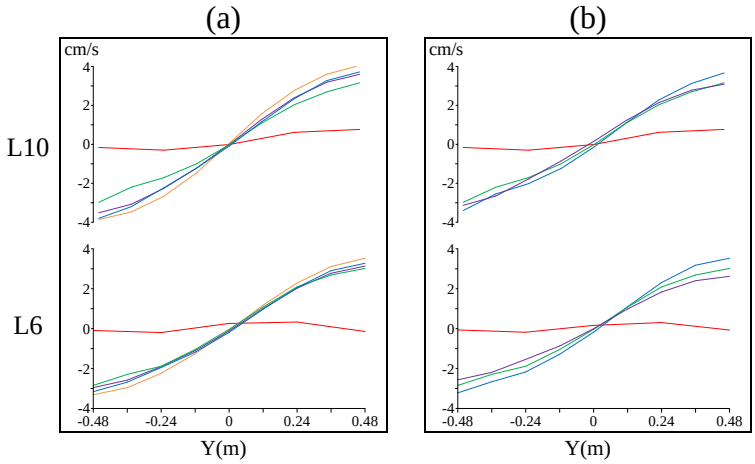

Figure (9.7) – Simulated profiles along axis Y for *u*-velocity component, (a) - variation of number of layers: n = 10 (orange), 15 (purple), 20 (green) and 25 (blue); (b) - variation of horizontal grid size: $\Delta x = \Delta y$ = 4 (purple), 3 (green) and 2 (blue) cm for layers L6 and L10 at T/4. Measured values are in red.

9.3.2 *Salinity*

The salinity profiles along Y axis are plotted for layers L10 and L18 at mid-flood tide (T/4) in figure (9.8). They also suggest the choice of 20 layers. Examining the predictions for the alternative horizontal grid size suggests a choice of 2 or 3 cm.

It can be concluded that the choice of 20 layers in the *z*-direction and a grid size of 3 cm in the horizontal plane provides a stable solution with computational time considerations while having the closest results to the experimental data.

9.4 DISTORTION STUDY

A study has been carried out to investigate the effect of distortion ratio on the hydrodynamics and stratification in the harbour. The results may be used for better interpretation of the predictions and also to provide a better understanding of the effects for the laboratory model experiments. The original configuration of the model

harbour has been maintained and two distortion ratios of 10 and 20 have been studied. The numerical set-ups then include the tidal range of 100 mm, barrier height of 100 mm with a mean water depth of 150 mm for the distortion ratio of 10, and the tidal range of 200 mm, barrier height of 200 mm with a mean water depth of 300 mm for the distortion ratio of 20. For both tests the salinity concentration has been taken equal to 80 g/l. The numerical details for the number of layers in the *z*-direction and the grid size in the horizontal plane derived in the previous section have been applied and the results have been plotted for the velocity (Fig. 9.9) and salinity (Fig. 9.10) along Y axis at mid-flood (T/4) and mid-ebb (3T/4) tides.

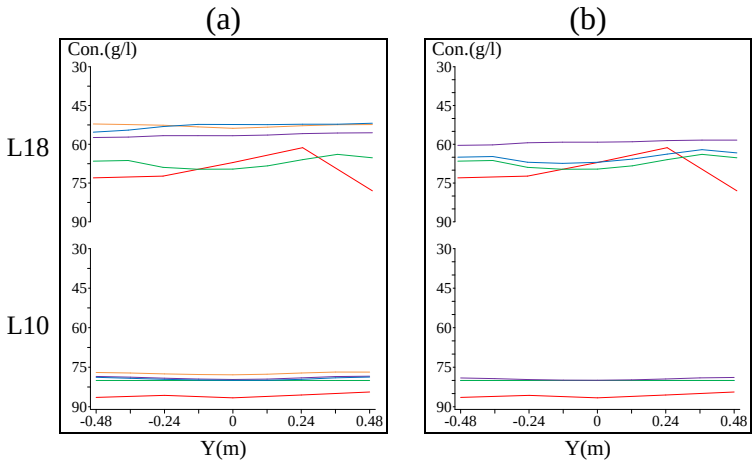

Figure (9.8) - Simulated horizontal salinity profiles along Y axis, (a) – variation of number of layers: *n* = 10 (orange), 15 (purple), 20 (green) and 25 (blue); (b) – variation of horizontal grid size: $\Delta x = \Delta y$ = 4 (purple), 3 (green) and 2 (blue) cm for layers L10 and L18 at T/4. Measured values are in red.

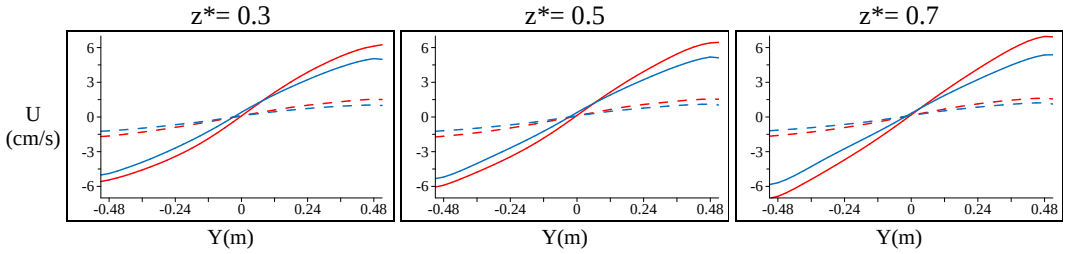

Figure (9.9) - Predicted values of *u*-velocity component for distortion ratios of 20 (red) and 10 (blue) at normalized elevations z^* and times T/4 (solid) and 3T/4 (dash) along Y axis

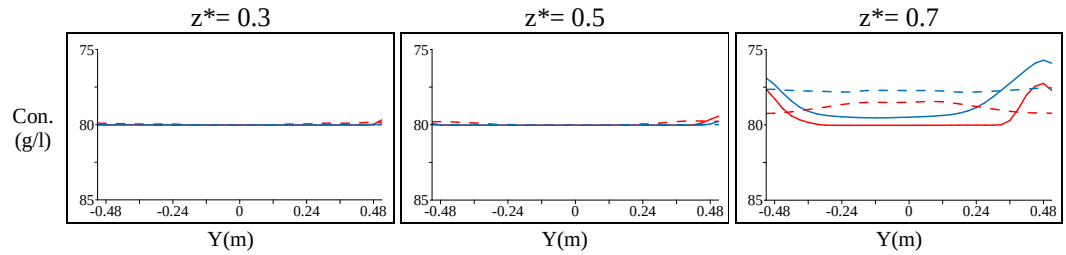

Figure (9.10) - Predicted values of salinity for distortion ratios of 20 (red) and 10 (blue) at normalized elevations z^* at times T/4 (solid) and 3T/4 (dash) along Y axis

The results are shown for the normalised depths of z^* equal to 0.3, 0.5 and 0.7, where the normalised depth z^* is defined as the ratio of the elevation of the point above bed to the barrier height (z/BH).

The velocity graphs do not show much difference for different tides, however, the velocities are larger for distortion ratio of 20 especially at mid-flood tide (T/4). No difference was detected for the water elevations, and the salinity graphs only show little difference for z^* equal to 0.7 where the higher distortion ratio results in lower change of salinity due to tidal excursions of fresh water flushing.

9.5 ENGINEERING ANALYSES

This section aims to analyse the effect of the mean water depth and the barrier height on the hydrodynamics of the harbour. Two different situations are considered; saline water inside the harbour and saline water flushing into the harbour. Although in some cases the harbour may be fed with the receiving water from an upstream river and therefore contain fresh water, but this situation does not remain so after the tidal excursions. The real situation most often is that the sea water flushes the saline water into the harbour and the fresh water flow from the upstream river is also fed. The latter has not been considered in the current study. The initial aim for the salinity measurements of the current research project was to investigate the stratification produced in the harbours with a barrage in the entrance and to study the hydrodynamics of such an impoundment to learn to what extent the stratification influences the hydrodynamics of the harbour. However a remaining question is to what extent the results would change if the real conditions were applied. For this analysis three cases are considered and for each case the simulations proceeded for different mean water depths and barrier heights. The three cases are as follows:

- Harbour filled with saline water with a concentration of salt equal to 80 g/l and the tidal flushing of fresh water (case I: saline, flushed by fresh);
- Harbour filled with fresh water and the saline water flushing into the harbour with a concentration of salt equal to 80 g/l (case II: fresh, flushed by saline);
- Harbour filled with fresh water and the saline water flushing into the harbour with a concentration of salt equal to 35 g/l (case III: fresh, flushed by weakly saline).

The summary of the simulations for each case are tabulated in Table (9.1).

Table (9.1) – Simulation sets for different mean water depths and barrier heights

Mean Water Depth (mm)	Barrier Height (mm)		
150 (LW)	100 (LB-LW)	150 (MB-LW)	190 (HB-LW)
200 (MW)	150 (LB-MW)	200 (MB-MW)	240 (HB-MW)
250 (HW)	200 (LB-HW)	250 (MB-HW)	290 (HB-HW)

For each case the lowest barrier has a height equal to the low tide water elevation and is labelled as (LB: low barrier), the barrier with the height of mean water depth of each case is referred as (MB: medium barrier) and the barrier with a height 10 mm below the high tide level is labelled as (HB: high barrier). The second abbreviations in the labels of the barriers refer to the corresponding mean water depths (LW: low mean water, MW: medium mean water and HW: high mean water). For all simulations a tidal range of 100 mm has been applied.

To study the results, the graphs are produced for the dominant velocities and the salinities along three axes X, Y and the axis of harbour entrance. The graphs for each axis show the results at mid-flood (T/4) and mid-ebb (3T/4) tides for different mean water depths and barrier heights and for three layers as follows:

- L^*_L (low layer) = LB/2, at the elevation of half of the lowest barrier height
- L^*_M (medium layer) = LB, at the elevation of the top of the lowest barrier
- L^*_H (high layer) = at the elevation of the mean water level

9.5.1 *Velocity Components*

The graphs for axes X (*v*-velocity component) and Y (*u*-velocity component) and the axis of harbour entrance (*v*-velocity component) are presented in figures (9.11), (9.12) and (9.13) respectively. At mid-flood tide due to the lower level of water in the basin than the crest of the barrier with the height equal to mean water depth (MB) no circulation is present in the harbour for the case of medium barrier (MB).

In the ebb tide, the velocities exhibit smaller values due to the opposite directions of the discharge from the harbour and the circulation present in the harbour. Inspection of the *u*-velocity component for X axis (not shown) shows that in

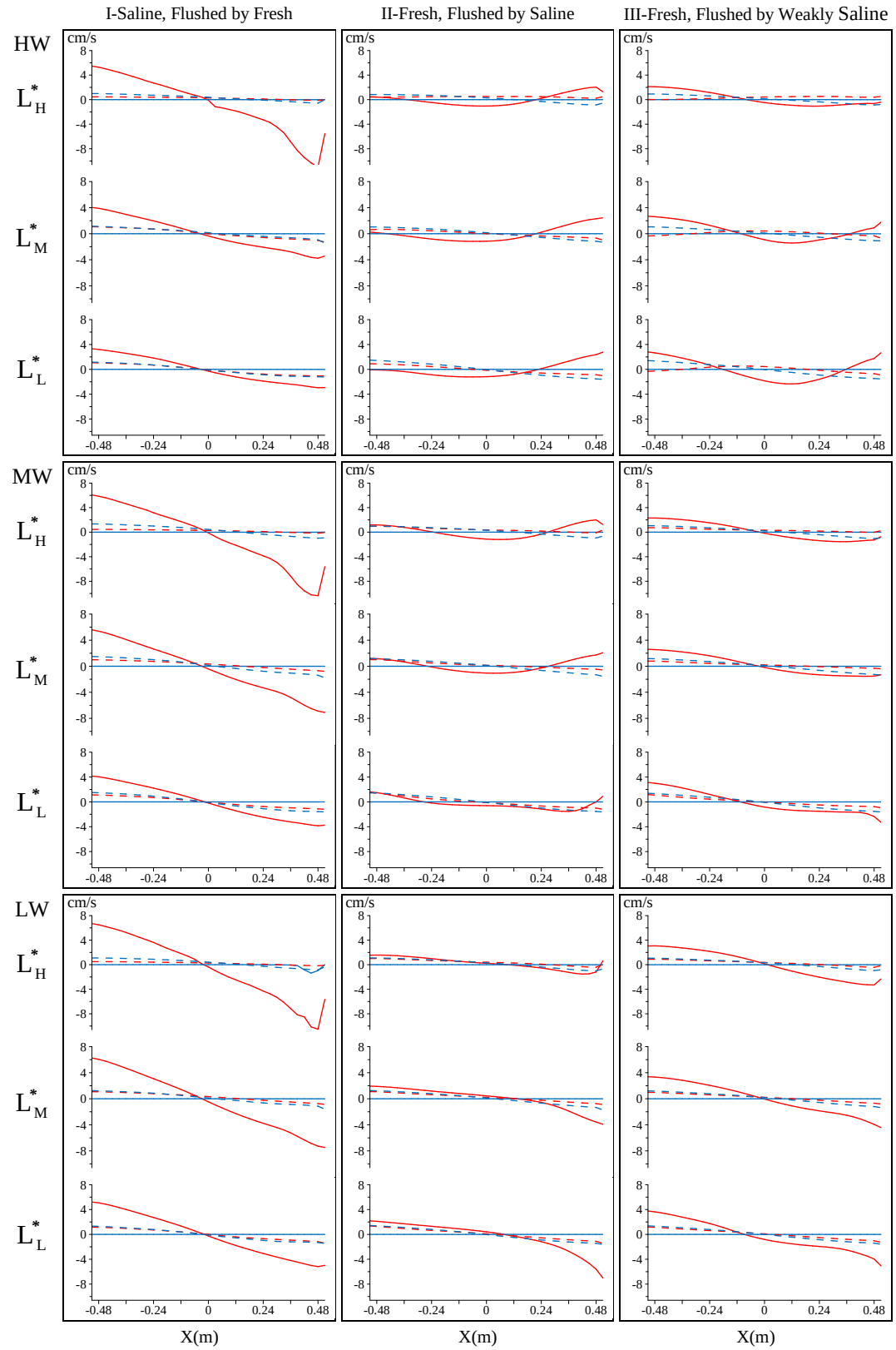

Figure (9.11) - Simulated *v*-components along X axis for cases (I, II, III), mean water depths (LW, MW, HW), barrier heights (LB: red and MB: blue), layers (L^*_L , L^*_M , L^*_H) at times T/4 (solid) and 3T/4 (dash)

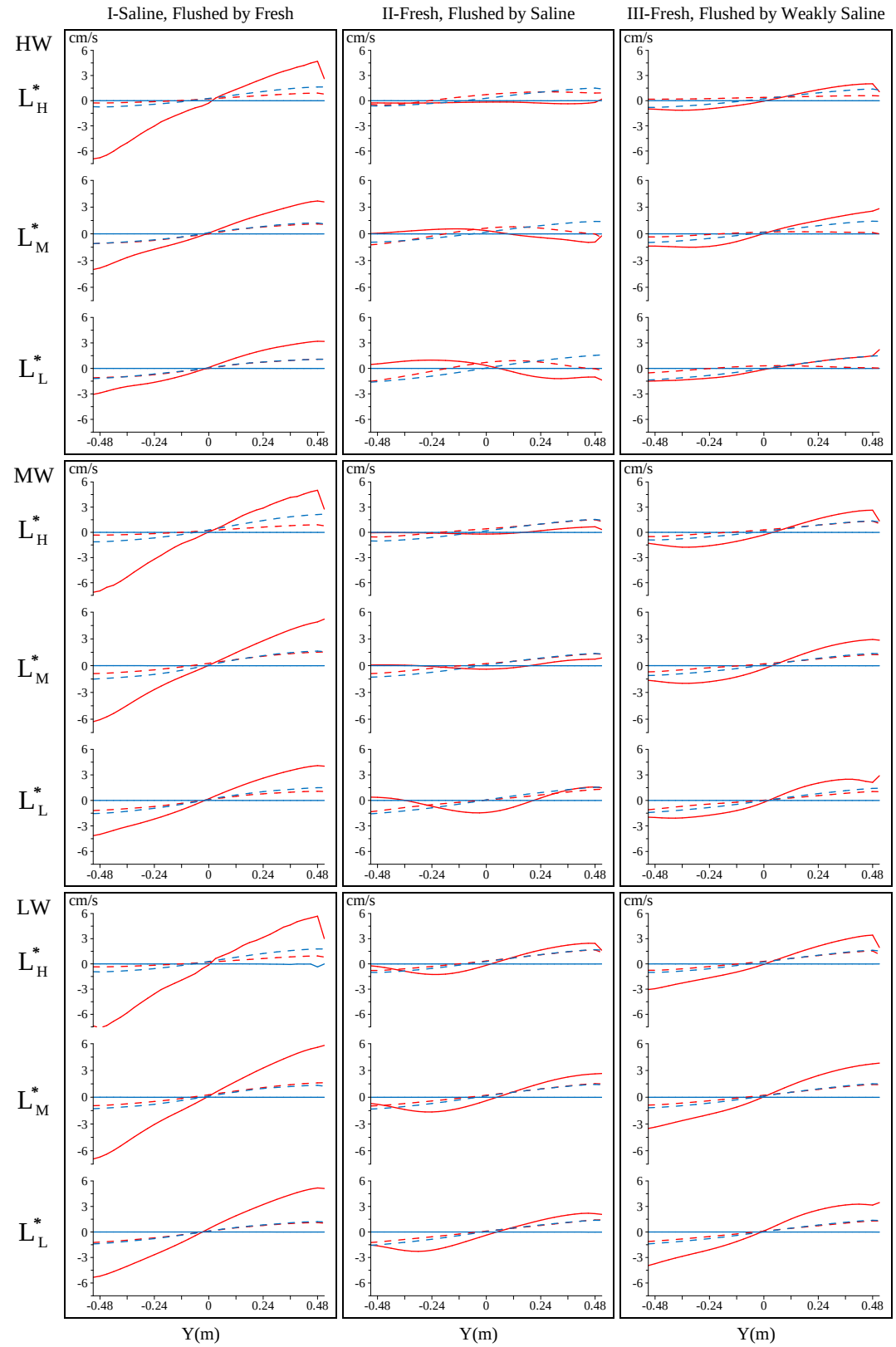

Figure (9.12) - Simulated *u*-components along Y axis for cases (I, II, III), mean water depths (LW, MW, HW), barrier heights (LB: red and MB: blue), layers (L^*_L , L^*_M , L^*_H) at times T/4 (solid) and 3T/4 (dash)

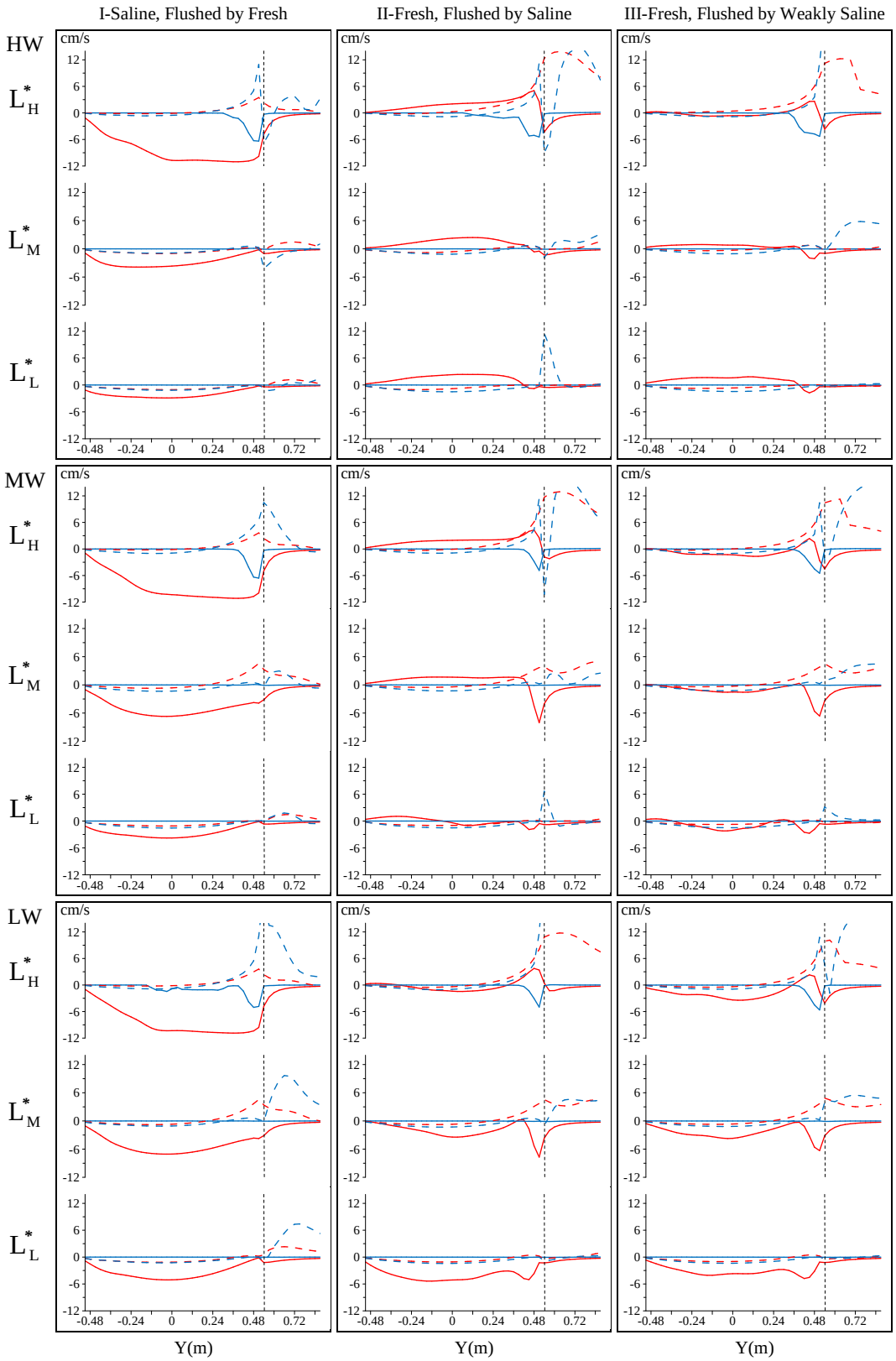

Figure (9.13) - Simulated *v*-components along axis of harbour entrance for cases (I, II, III), mean water depths (LW, MW, HW), barrier heights (LB: red and MB: blue), layers (L^*_L , L^*_M , L^*_H) at times T/4 (solid) and 3T/4 (dash). Vertical (dash) lines show the edge of harbour.

general for cases (II) and (III) the reduction of the velocities with the increase of barrier height is more evident for larger mean water depths and this intensifies for the denser flushing water (case II). This does not equally apply to *v* velocities and the differences are small, showing that the changes are less effective for the dominant velocities, however the circulations experience variations. For the *v* velocities along X axis for case (I) and for all mean water depths, the velocity magnitudes are slightly more for the upper layers, which slightly increase with the increase of the barrier height. For case (II), however, for LW the flushing of denser saline water flows underneath and produces a circulation near the bed where the velocities exhibit slightly larger magnitudes for lower layers, but for MW and HW the velocity magnitudes do not present tangible differences for different layers. For case (III) the velocities are with slightly larger magnitudes for lower layers. For the taller barrier the velocities show very little increase. The velocities generally have the largest magnitudes for case (I) and the smallest for case (II) with the higher concentration of flushing saline water. With the increase of mean water depth the circulations weaken and the velocities show very little decrease for different cases and mean water depths. It is evident that for case (II) the circulation centre has shifted towards the entrance from the centre of the harbour for case (I). *w* velocities for axis X (not shown) for all cases and mean water depths are larger in lower layers in flood tide. They increase with the increase of mean water depth but do not exhibit tangible differences with the variation of the barrier height, but the vertical flow structure exhibits different patterns.

The dominant velocity of axis Y (*u*-velocity), exhibits larger values for the top layers at the flood tide in case (I), where a slight increase of the velocity may be seen for the taller barrier in the ebb tide. For cases (II) and (III), however, the velocity of the lower layers is slightly larger, for which the difference increases with the increase of the mean water depth for case (II). The influence of the barrier height is such that the velocities are slightly larger for the taller barrier. The velocities experience a decrease with the increase of mean water depth for all cases, and generally the velocities of case (I) exhibit the largest values while those of case (II) are the smallest. For the *v* velocities of axis Y (not shown), generally, the velocities of case (II) are the largest and those of case (I) the smallest. The *w* velocities (not shown) are larger for lower layers and increase with the increase of mean water depth. The overall *w* velocities are the largest for case (III) and the smallest for case (I).

For the entrance axis, the *u* velocities (not shown) exhibit larger values for upper layers for case (I), but for cases (II) and (III) the middle layers show larger values. The *v* velocities of this axis for case (I) have larger values for upper layers, but for case (II) the larger values are present in lower layers for LW, while for MW and HW they are larger for upper layers. For case (III) there is not much difference for different layers for all mean water depths. The variation of mean water depth does not show a clear trend of the change for the *u* and *v* velocities. The *v* velocities are generally larger in case (I). The *w* velocities (not shown) are present in lower layers of water column and they are much stronger in cases (II) and (III) such that the increase of the salinity concentration of flushing tide strengthens the vertical velocities.

9.5.2 *Salinity*

The salinity graphs with the same configuration as velocities are presented in figures (9.14), (9.15) and (9.16) for axes X, Y and the axis of harbour entrance respectively. The concentration axis is in the reverse direction to show the high salinities in lower levels where they are usually located in stable stratifications.

For axis X and case (I), L^*_L does not face any changes with tidal excursions. For L^*_M only LB causes the salinity change which is limited to LW and MW and no change in salinity happens for HW. For L^*_H no changes happen for HB, but MB shows changes in the mid-ebb tide which reduces the salinity to values near zero for LW and HW but MW shows less reduction of the salinity, and LB exhibits values almost equal to zero. For case (II) and LW and for the barriers HB and MB the L^*_L graphs show zero salinity for mid-flood tide, but salinity increases for LB. In mid-ebb tide the salinity has its largest increase for LB and lesser increase for MB and a little for HB. For MW and HW the same trend applies but with less increase. L^*_M graphs present the same trend with lesser increase and for L^*_H only LB shows a slight growth. Generally with the increase of water depth the increase of salinity lessens. For case (III) the same trend of graphs as case (II) are evident but with lower values due to the lower concentration of salinity. The axis Y and entrance show the same trend. The area outside the harbour is not considered in the present analysis.

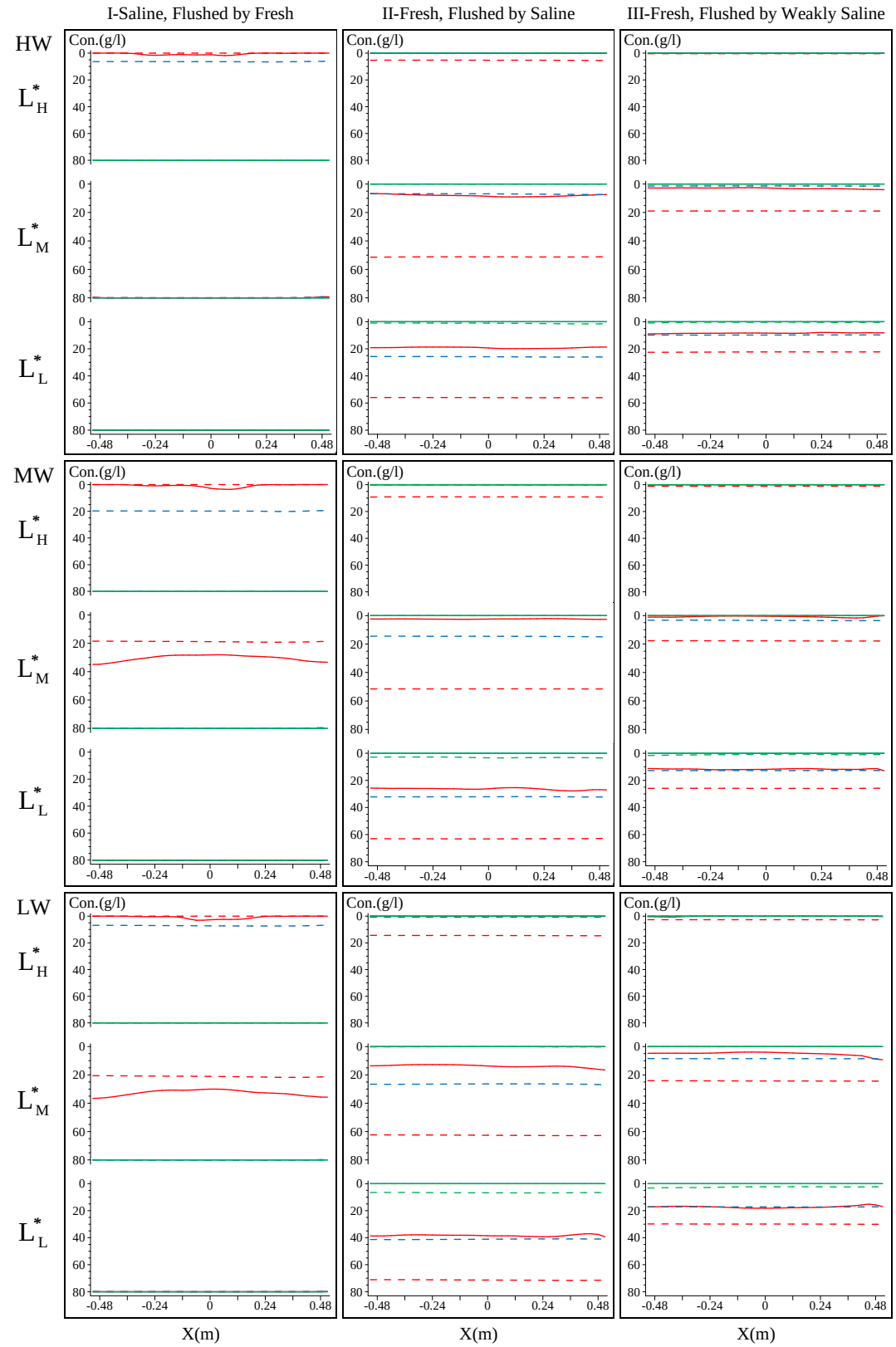

Figure (9.14) - Simulated salinities along X axis for cases (I, II, III), mean water depths (LW, MW, HW), barrier heights (LB: red, MB: blue, HB: green), layers (L^*_L , L^*_M , L^*_H) at times T/4 (solid) and 3T/4 (dash)

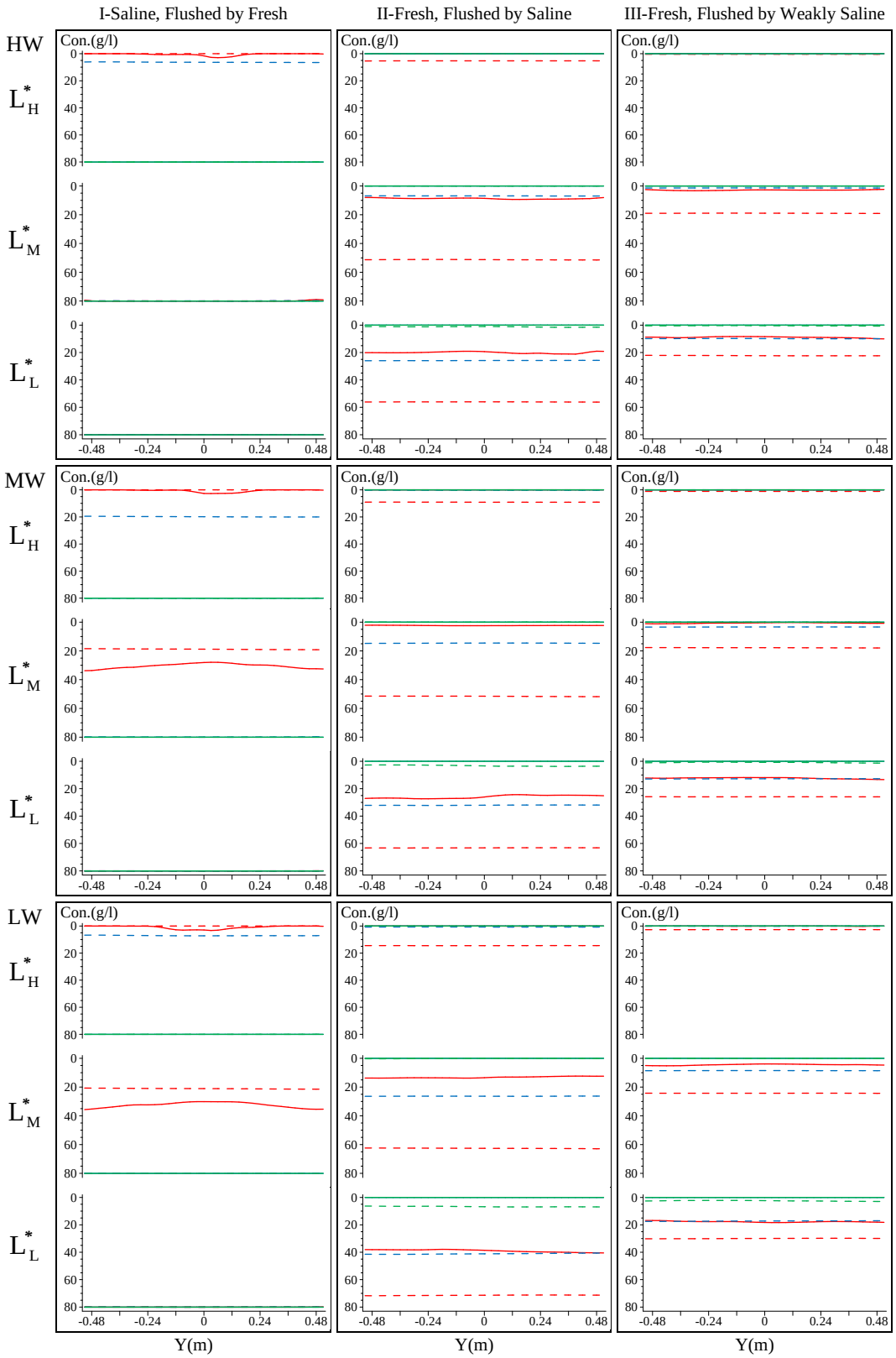

Figure (9.15) - Simulated salinities along Y axis for cases (I, II, III), mean water depths (LW, MW, HW), barrier heights (LB: red, MB: blue, HB: green), layers (L^*_L , L^*_M , L^*_H) at times T/4 (solid) and 3T/4 (dash)

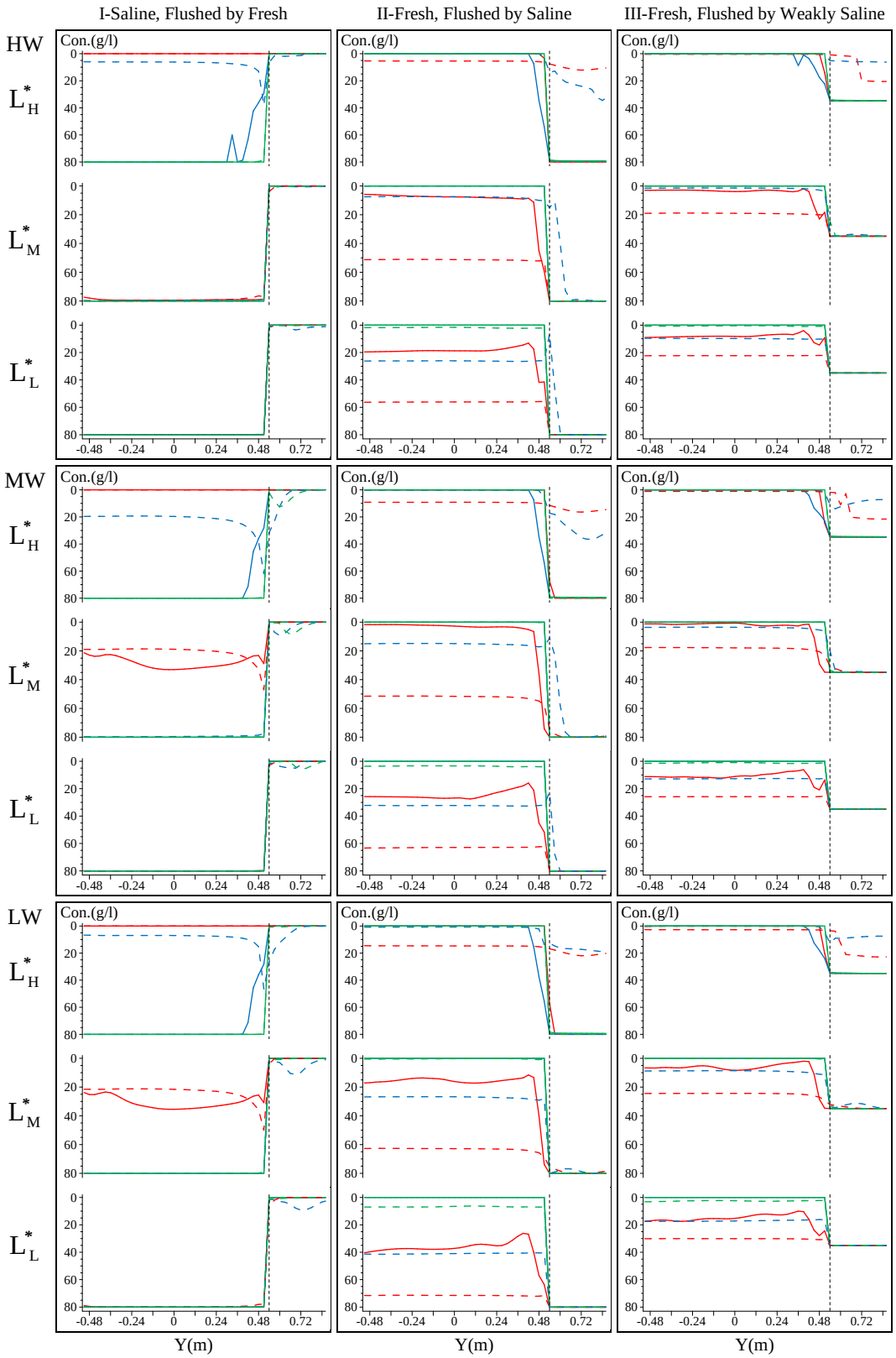

Figure (9.16) - Simulated salinities along axis of harbour entrance for cases (I, II, III), mean water depths (LW, MW, HW), barrier heights (LB: red, MB: blue, HB: green), layers (L^*_L, L^*_M, L^*_H) at times T/4 (solid) and 3T/4 (dash). Vertical (dash) lines show the edge of harbour.

In case (I) the fresh water circulation over the saline water impoundment, has little influence on lower layers and consequently the change of the salinity. The fresh water circulation, however, affects the upper layers and the salinity concentration lessens with the tidal excursions. In cases (II) and (III) a circulation initiates near the bed by the salinity intrusion from the flushing water resulting in the change of salinity in all layers, especially the lower layers, which amplifies with time. In general, with the increase of mean water depth and barrier height the change of salinity reduces.

Due to the density difference of the water in the basin and the harbour a current forms near the entrance. In case (I), the saline water of harbour produces a gravity current towards the outside before the ebb tide pushes the water outside the harbour. Figure (9.16) shows that for axis entrance during the ebb tide, where the fresh water of basin meets the nearly fresh water of harbour flushing out for case (I), the salinity change in harbour is with little variation, but for cases (II) and (III) the incoming saline water flows underneath and pushes the fresh ambient water to upper layers and the ebb tide therefore exhibits low values of salinity concentration, which results in the more concentrated saline water in the harbour over time with repetitive tidal excursions.

9.6 SUMMARY

The three-dimensional numerical model has been calibrated and verified against the experimental data. To eliminate the effects of wide-crest overflow and to improve the accuracy of the predictions, for simulation of barriers, a zero-thickness wall is assumed to be placed at the entrance of the harbour. For calibrating the numerical model the surface roughness and the bounds for the k and ε values were adjusted so that the best results were obtained compared to the experimental data.

The velocities and flow patterns are in good general agreement with the measured values. However, for the fresh water condition the model under-predicts the velocity components for the areas with strong circulation which is associated with the dominant velocity component. Although the calibration has resulted in prediction of lower absolute values for dominant components of the velocity in strong circulations, the general flow pattern for the velocities exhibits closer configuration with the laboratory data for the interior zones of the harbour. For the saline water condition due to the suppression of the velocities for the lower layers

and the increase of the velocity values for the top layer, the simulated results show an over-prediction in lower layers and a better agreement with the measured values for the top layer. The simulated water elevation time series show good agreements with the measured data. The salinity profiles also show good agreements between the simulated and measured values for lower layers but for the top layer the simulated values are over-predicted.

The grid sensitivity study showed that the choice of 20 layers in the *z*-direction and a grid size of 3 cm in horizontal plane provide a stable solution with computational time considerations while having the closest results to the experimental data. The results of the distortion study demonstrated for the normalised depths of z^* showed little alteration for different distortion ratios. However, higher distortion ratio results in lower change of salinity due to tidal excursions of fresh water flushing.

The effect of the mean water depth and the barrier height on the hydrodynamics of the harbour was investigated for two situations of saline water inside the harbour and saline water flushing into the harbour whereby three cases were considered. For the X axis, the changes are less effective for the dominant *v* velocity, and with the increase of mean water depth the circulations weaken and the velocities show very little decrease. For axis Y the dominant velocity *u*, exhibits larger values for taller barriers. The velocities experience a reduction with the increase of the mean water depth. Generally the velocities of case (I) exhibit the largest values while those of case (II) the smallest for the dominant velocity for both axes. The *w* velocities are larger for lower layers and grow with the increase of mean water depth. For cases (II) and (III) generally with the increase of water depth the increase of salinity over the tidal period lessens. For case (I) the fresh water circulation over the saline water impoundment has little influence on lower layers and affects the upper layers where the salinity concentration lessens by the tidal excursion. In cases (II) and (III) a circulation initiates near the bed by the salinity intrusion from the flushing water resulting in the change of salinity in all layers, especially the lower layers. In general, with the increase of mean water depth and barrier height the change of salinity reduces. For cases (II) and (III) the incoming saline water flows underneath and pushes the fresh ambient water to upper layers and the ebb tide, therefore, discharges less salinity resulting in higher salinity concentration in the harbour over time.

CHAPTER TEN

GENERAL CONCLUSIONS AND RECOMMENDATIONS FOR FURTHER RESEARCH

"As far as the laws of mathematics refer to reality, they are not certain;
and as far as they are certain, they do not refer to reality."
Albert Einstein (J.R. Newman, The World of Mathematics, New York, 1956)
(O'Connor and Robertson, 1999)

10.1 SUMMARY

The principal aim of this study was to achieve a better understanding of hydrodynamics of estuarine harbours, salt transport and stratification and their relation to harbour mixing. Despite the narrowness of estuaries compared to ocean geometry, the flow and mixing exhibit three-dimensional nature due to the complex bathymetry, inflow and outflow regime of the estuary, stochastic character, and stratification in such hydro-environments. To predict the flow field and the salinity distribution and profile in large water bodies, estuaries, harbours and barrages an arbitrary Lagrangian-Eulerian (ALE) three-dimensional hydrodynamic free-surface numerical model was developed, based on the conservative form of the time-dependent Reynolds-averaged Navier-Stokes equations. The model with non-hydrostatic pressure distribution is capable of simulating non-homogeneous variable-density stratified flows and problems involving complex bathymetry. The model also

may be deployed for the rigid-lid condition or may be switched to a laterally-averaged model. A structured non-orthogonal curvilinear staggered mesh for the computational domain has been employed. The discretisation of the flow and transport equations has been based on the finite volume method. A fractional-step (projection) method has been deployed for solving the set of the equations, by which the pressure gradient term was decoupled from the advection and diffusion. The fractional-step method combined with alternating direction implicit (ADI) method resulted in a locally one-dimensional (LOD) or fractional splitting approximation for the transport terms and two-dimensional solution to the Poisson equation. The solution of the species concentration equation was uncoupled from the solution of the momentum Poisson equation and was solved at each half-time-step prior to the solution of the Poisson equation. Accurate and computationally-efficient modelling of turbulent stratified flows is of great importance in both coastal and large-scale ocean circulation. The k-ε turbulence model still dominates a wide range of engineering applications due to its simplicity, fairly accurate results, and computational efficiency. For modelling turbulence, and to optimise accuracy and economy, the two-equation k-ε turbulence model with buoyancy terms has been included in the numerical model. The solution of the turbulence transport equations advanced at the beginning of each half-time-step and the computed eddy viscosities were used in the flow equations of the same half-time-step. The equations were discretised using a fifth-order-accurate upstream LOD scheme to obtain the face values for use in the advection terms. For the diffusive contribution of transport, the Crank-Nicolson method was deployed and for the pressure, the Poisson equation was solved using a central difference scheme which comprised a block tri-diagonal matrix. The block tri-diagonal matrix was solved by block forward and back substitution. The matrices were diagonally dominant and hence no pivoting was required, satisfying the boundedness requirement of the numerical scheme. The scheme is non-iterative and the momentum and Poisson equations were only solved once at each half-time-step. The θ scheme is used for the pressure in the domain and for the velocity on the free surface. For computing the derivatives and coefficients of unknown pressures an algorithm was introduced based on quantity and geometry matrices. The overall accuracy of the set of the equations is first order in time and second order in space.

A laboratory tidal basin was designed, set up and employed for instantaneous velocity, water surface elevation and salinity measurements of an idealised vertically distorted model harbour for fresh water and salinity stratified conditions with various barrier heights, tidal ranges and mean water depths. Constant amplitude and constant period sinusoidal model tides were reproduced in the tidal tank by means of a vertically oscillating weir. Aimed primarily at obtaining laboratory data to verify and enhance the predictive capability of the numerical model, the hydraulic model harbour was sized so that it also was considered, to some extent and with limitations, as a process physical model. For despiking and denoising the velocity data a linear correlation algorithm was established and a Wiener filter was designed and adapted for the temporal correlation of the signals, which successfully lowered the noise level and removed the spikes where the stationary assumption of the statistical characteristics of flow was valid. For the conductivity a moving average procedure was carried out as the data did not suffer from spikes and exhibited almost a constant band of noisy fluctuations. The water elevation data showed a reasonably clean signal and no filtering procedure was carried out.

10.2 DISCUSSION ON THREE-DIMENSIONAL MODELLING OF ESTUARINE HARBOURS

The measurements show a horizontal clockwise circulation in the harbour and weak vertical circulations. The water motion near the entrance is limited due to the closed boundaries. Velocities exhibit larger magnitudes for the larger tidal range, and the barrier height of 200 mm exhibits lower velocity magnitudes compared with the barrier height of 100 mm. The velocity profiles for mid-flood tide show stronger circulations compared to mid-ebb tide. The velocity magnitudes are generally larger for the barrier height of 100 mm compared to the barrier heights of 0, 60 and 90 mm, which is due to the smaller area for the discharge of the water flushing into or from the basin. Tidal water surface varies smoothly over the tidal period as it is expected. Salinity suppresses the circulation intensity across the water depth with the exception of the top layer where the velocity magnitudes are increased with salinity. This is caused by less mixing in vertical direction and stronger flushing on the surface. For the points around the harbour where the main circulation occurs, the change of the salinity is more than the central points. The change of the salinity essentially affects

the top layer for the tidal range of 100 mm, while for the tidal range of 200 mm stretches to the lower layers.

The advection terms play a crucial role for the equations of motion, transport of salinity and the transport of turbulence model parameters. The key role of the advection in the evolution of stratification in such environmental regions and estuarine harbours and barrages emphasises the special treatment of this term in the hydraulic and numerical modelling. Therefore, six new explicit schemes were introduced for advection. All schemes make use of the upwind quantities, which ensures the fulfilment of the transportiveness requirement. Three of these process the advection by the locally-one-dimensional (LOD) method, and the other three handle the advection by a two-dimensional approach. A von Neumann stability analysis was carried out for the proposed scheme, showing stable solutions for Courant numbers below 1. For monotone behaviour of the solution, a limiter was used and its influence on the scheme was demonstrated. A small-amplitude standing wave sloshing in a confined container, a small amplitude progressive wave simulating a flap-type wave-maker, and a solitary wave propagating in constant water depth have been simulated to evaluate the free surface predictions. The results show the capability of the model in simulating free surface flows and non-linear terms in Navier-Stokes equations. To optimise the accuracy and computational time a grid sensitivity study was carried out to obtain the criteria for mesh generation, for two- and three-dimensional problems.

The three-dimensional numerical model was calibrated and verified against the experimental data. To eliminate the effects of wide-crest overflow and to improve the accuracy of the predictions, for simulation of barriers, a zero-thickness wall was assumed to be placed at the entrance of the harbour. For calibrating the numerical model the surface roughness parameter and the bounds for the k and ε values were adjusted so that the best results were obtained compared to the experimental data. The velocities and flow patterns are in generally good agreement with the measured values. For the fresh water condition, however, the model under-predicts the dominant velocities for the areas with strong circulation. For the saline water condition the simulated results show an over-prediction in lower layers and good agreements with the measured values for the top layer. The water elevations show very close predictions compared with the measured data. The salinity simulated profiles show good agreements with the measured values for lower layers and an over-prediction for the top layer. A study was carried out to portray the deficiencies

of measured values due to vertical distortion used in the laboratory models and to address some of the discrepancies of numerically simulated values due to this distortion, with the results indicating little alteration for different distortion ratios. However, higher distortion ratio results in lower change of salinity due to tidal excursions of fresh water flushing.

The effect of the mean water depth and the barrier height on the hydrodynamics and stratification in the harbour was investigated for two situations of saline water inside the harbour and saline water flushing into the harbour. The analyses showed that the dominant velocities are increased with the increase of the barrier height. With the exception of the top layer of the axis of the harbour entrance, with the increase of mean water depth the circulations weaken and the dominant velocities show very little decrease. The *w* velocities are larger for lower layers and grow with the increase of mean water depth. The overall *w* velocities are larger for saline water flushing into the harbour than the saline water in the harbour and the increase of the salinity concentration of flushing tide strengthens the vertical velocities. Generally the dominant velocities of the harbour with saline water exhibit larger values than the harbour with saline water flushing into the harbour. When saline water flushes into the harbour, generally, with the increase of water depth the increase of salinity over the tidal period lessens. For a harbour with saline water the fresh water circulation over the saline water impoundment has little influence on lower layers and affects the upper layers where the salinity concentration lessens due to the tidal excursion. When saline water flushes into the harbour a circulation initiates near the bed by the salinity intrusion from the flushing water resulting in the change of salinity in all layers, especially the lower layers. In general, with the increase of mean water depth and barrier height the change of salinity reduces. For saline water flushing into the harbour the incoming saline water flows underneath and pushes the fresh ambient water to upper layers and the ebb tide, therefore, discharges less salinity resulting in higher salinity in the harbour over time.

10.3 ANSWERS TO RESEARCH QUESTIONS

The scope of the research was aimed to address the following questions:

1. What are the dominant processes that determine the transport and distribution of salt in harbours?

2. What are the interactive mechanisms of hydrodynamics, stratification and mixing in harbours?
3. How do the geometry and hydrodynamic forcing conditions influence the above mechanisms and the nature of stratification in harbours?
4. How accurately is a three-dimensional numerical model able to predict the hydrodynamics governing the harbour mixing and stratification?
5. What is the influence of stratification on flow and turbulence in harbours and barrages?

The answers to the above questions are outlined in the following paragraphs.

1. Advection plays the main role in the transport of salt and the evolution of stratification in harbours. This is affected by the tidal forcing, the barrier height and mean water depth, and the concentration of salinity.
2. Salinity suppresses the circulation intensity across the water depth with the exception of the top layer where the velocity magnitudes are increased with salinity. This is caused by less mixing in vertical direction and stronger flushing on the surface. For the points around the harbour where the main circulation occurs, the change of the salinity is more than the central points.
3. Velocities show larger magnitudes for larger tidal ranges. The dominant velocities are increased with the increase of the barrier height, but with the increase of mean water depth the circulations weaken and the dominant velocities decrease. The *w* velocities are larger for lower layers and grow with the increase of mean water depth. In general, with the increase of mean water depth and barrier height the change of salinity reduces. The change of the salinity stretches to lower layers with stronger tidal flushing. With a taller barrier the surface flushing intensifies, while the vertical circulation reduces.
4. The numerical model satisfactorily simulates the flow patterns. The model under-predicts the dominant velocities for the areas with strong circulation. Salinity exhibits an over-prediction for the top layer and good results for the lower layers. The water elevations show very good predictions.
5. Salinity suppresses the circulation intensity across the water depth resulting in less mixing in the vertical direction. Saline water flows underneath the ambient water and pushes the fresh water to upper layers resulting in higher salinity in the harbour over time.

10.4 CONCLUDING REMARKS

The concluding remarks are categorised in the following paragraphs.

- Numerical modelling
  - The results show the capability of the numerical model in simulating free surface flows and non-linear terms in Navier-Stokes equations.
  - The simulated velocities and flow patterns of the model harbour are in good general agreement with the measured values. For the fresh water the model under-predicts the dominant velocity components and for the saline water the simulations show an over-prediction in lower layers and good agreements for the top layer.
  - The water elevations of the model harbour show very close predictions to the measured data.
  - The salinity simulated profiles show good agreements with the measured values in the model harbour for lower layers and an over-prediction for the top layer.
  - A distortion study for the model harbour indicated little alteration for different distortion ratios, however, higher distortion ratio results in lower change of salinity due to tidal excursions of fresh water flushing.

  An investigation on the effects of the variations of the mean water depth and barrier height on the hydrodynamics of the model harbour showed that:
  - The dominant velocities are increased with the increase of the barrier height.
  - With the increase of mean water depth the circulations inside the harbour weaken and the dominant velocities slightly decrease.
  - The *w* velocities are larger for lower layers and grow with the increase of mean water depth.

- Stratification

  Physical and numerical modelling of the model harbour showed that:
  - Salinity suppresses the circulation intensity with the exception of the top layer where the velocity magnitudes are increased, caused by less mixing in vertical direction and stronger flushing on the surface.
  - For the points around the harbour where the main circulation occurs, the change of the salinity is more than the central points.

- Generally the dominant velocities along the axes of the harbour with saline water exhibit larger values than the harbour with saline water flushing into the harbour.
- The fresh water circulation over the saline water impoundment has little influence on lower layers and affects the upper layers.
- For saline water flushing into the harbour a circulation initiates near the bed resulting in the change of salinity in all layers, especially the lower layers.
- In general, with the increase of mean water depth and barrier height the change of salinity reduces.
- The incoming saline water flows underneath the ambient water resulting in higher salinity concentration in the harbour over time.

10.5 RECOMMENDATIONS FOR FURTHER RESEARCH

The recommendations for further research are categorised as follows:

- Numerical Modelling
  - For stratified flows, a coordinate system with a dividing plane located immediately above the region of larger density gradients may be used to enhance the predictions of the interface location for stably stratified flows.
- Physical Modelling
  - It is recommended that the vertical velocities across the depth of water column be measured in more locations to give a better picture of vertical circulations under variable conditions.
- Comparisons with field data
  - Investigation of the field data from real estuaries, harbours and barrages is recommended to assess the results of the present numerical modelling with field data.
  - Due to the distortion, the mixing in the model would be too slow vertically and too fast transversely; therefore, the horizontal and vertical profiles of salinity distribution and consequently the structure of the stratification could differ from the real stratified estuaries and harbours, hence the numerical conclusions for real-scale problems are of great importance.

- Turbulent stratified flows
  - Understanding the profile of variations of Richardson number in the water bodies of interest of this research project may result in more accurate predictions of the flow field in the absence of strong circulations where the prediction of the flow pattern and local circulations are governed by small values.
  - It is recommended that a formulated relation between harbour mixing and stratification be more precisely investigated.
- Signal processing
  - It is recommended that the validity of the proposed interpolation method for increasing the sampling frequency of the measured data as well as producing data for the spatial domain be examined.
  - The effectiveness and accuracy of the proposed interpolation method for smoothing the numerical simulation outputs to be assessed as a post-processing tool.
  - The correlation used for the filter for the temporal domain can be extended for the spatial domain.
  - For the regions where the stationary assumption of the statistical characteristics of flow is not valid, a block-adaptive Wiener filter may be utilised or a Kalman filter deployed to include the non-stationary random signals.
- New features
  - The study of the effect of wave-current interaction on hydrodynamics and mixing in stratified coastal waters, and harbours is of great importance.
  - It is recommended to investigate the flushing rate and the water quality processes so that to obtain the geometrically and dynamically limitations for adequate circulation and flushing in harbours and barrage schemes, while satisfying to the extent possible the economic considerations.

REFERENCES

Abbott, M.B., 1979, "Computational Hydraulics, Elements of the Theory of Free Surface Flows", Pitman, London.

Abbott, M.B., 1989, "Review of Recent Developments in Coastal Modelling", *Proceedings of the International Conference on Hydraulic and Environmental Modelling of Coastal, Estuarine and River Waters*, Bradford, UK, pp. 3-19.

Abbott, M.B., 1993, "The Dynamic Environment: An Introduction", in *Coastal, Estuarial and Harbour Engineers' Reference Book*, M.B. Abbott and W.A. Price, Eds., Chapman & Hall, London.

Abbott, M.B., 1997, "Range of Tidal Flow Modelling", *Journal of Hydraulic Engineering*, ASCE, Vol. 123, No. 4, pp. 257-277.

Abbott, M.B., and Basco, D.R., 1989, "Computational Fluid Dynamics, An Introduction for Engineers", Longman Scientific & Technical, Essex, England.

ADVANTECH, 1995, "GENIE Reference Manual", Version 2.0, American Advantech Corporation, USA.

Ai, C., Jin, S., and Lv, B., 2011, "A New Fully Non-Hydrostatic 3D Free Surface Flow Model for Water Wave Motions", *Int. J. Numer. Meth. Fluids*, Vol. 66, pp. 1354-1370.

Alahyari, A.A., and Longmire, E.K., 1996, "Development and Structure of a Gravity Current Head", *Experiments in Fluids*, Vol. 20, pp. 410-416.

Aldridge, J.N., and Davies, A.M., 1993, "A High Resolution Three-Dimensional Hydrodynamic Tidal Model of the Eastern Irish Sea", *J. Physical Oceanography*, Vol. 23, pp. 207-224.

Alfrink, B.J., and van Rijn, L.C., 1983, "Two-Equation Turbulence Model for Flow in Trenches", *Journal of Hydraulic Engineering, ASCE*, Vol. 109, No.3.

Allen, G.P., Salomon, J.C., Bassoullet, P., Du Penhoat, Y., and De Grandpré, C., 1980, "Effects of Tides on Mixing and Suspended Sediment Transport in Macrotidal Estuaries", *Sedimentary Geology*, Vol. 26, pp. 69-90.

Allen, J.R.L., 1971, "Mixing at Turbidity Current Heads, and its Geologic Implications", *J. Sediment. Petrol.*, Vol. 41, pp. 97-113.

Allen, J.R.L., 1982, "Sedimentary Structures: Their Character and Physical Basis", Elsevier, Amsterdam, 1256 pp.

Amsden, A.A., 1970, "A Simplified MAC Technique for Incompressible Fluid Flow Calculations", *J. Comp. Phys*., Vol. 6, pp. 322-325.

Anthonio, S.L., and Hall, K.R., 2006, "High-Order Compact Numerical Schemes for Non-Hydrostatic Free Surface Flows", *Int. J. Numer. Meth. Fluids*, Vol. 52, pp. 1315-1337.

Armfield, S., and Street, R., 2002, "An Analysis and Comparison of the Time Accuracy of Fractional-Step Methods for the Navier-Stokes Equations on Staggered Grids", *Int. J. Numer. Meth. Fluids*, Vol. 38, pp. 255-282.

Armfield, S., and Street, R., 2003, "The Pressure Accuracy of Fractional-Step Methods for the Navier-Stokes Equations on Staggered Grids", *ANZIAM Journal*, Vol. 44 (E), pp. C20-C39.

ASCE Task Committee on Turbulence Models in Hydraulic Computations, 1988, "Turbulence Modelling of Surface water Flow and Transport: Part I", *Journal of Hydraulic Engineering*, ASCE, Vol. 114, No. 9, pp. 970-991.

ASCE, 2000, "Hydraulic Modelling, Concepts and Practice", *ASCE Manuals and Reports on Engineering Practice*, No. 97, ASCE, Reston, USA.

Bahari, A.M., and Hejazi, K., 2009, "Development and Investigation of a Non-Isotropic k-ε Turbulence Model for Horizontal Gravity Currents Applications", *Proceedings of the 7th IASME/WSEAS International Conference on Fluid Mechanics and Aerodynamics (FMA '09)*, S.H. Sohrab, H.J. Catrakis, and N. Kobasko, Eds., pp. 150-156.

Bai, Y., and Cheung, K.F., 2013, "Depth-Integrated Free-Surface Flow with Parameterized Non-Hydrostatic Pressure", *Int. J. Numer. Meth. Fluids*, Vol. 71, pp. 403-421.

Barenblatt, G.I., and Chorin, A.J., 1997, "New Perspectives in Turbulence", *Berkeley Mathematics Newsletter*, Vol. V, No. 1.

Barron, C.N., Kara, A.B., Martin, P.J., Rhodes, R.C., and Smedstad, L.F., 2006, "Formulation, Implementation and Examination of Vertical Coordinate Choices in the Global Navy Coastal Ocean Model (NCOM)", *Ocean Model.*, 11, pp. 347-375.

Basara, B., and Younis, B.A., 1995, "Prediction of Turbulent Flows in Dredged Trenches", *Journal of Hydraulic Research*, Vol. 33, No. 6, pp. 813-824.

Batten, P., Ingram, D.M., Saunders, R., and Causon, D.M., 1996, "A Time-Splitting Approach to Solving the Navier-Stokes Equations", *Computers and Fluids*, Vol. 25, No.4, pp. 421-431.

Bell, J.B., Colella, P., and Glaz, H.M., 1989, "A Second-Order Projection Method for the Incompressible Navier-Stokes Equations", *Journal of Computational Physics*, Vol. 85, pp. 257-283.

Benjamin, T.B., 1968, "Gravity Currents and Related Phenomena", *J. Fluid Mech.*, Vol. 31, Part 2, pp. 209-248.

Birman, V.K., and Meiburg, E., 2006, "High-Resolution Simulations of Gravity Currents", *J. of the Braz. Soc. of Mech. Sci. & Eng.*, Vol. XXVIII, No. 2, pp. 169-173.

Birman, V.K., Martin, J.E., and Meiburg, E., 2005, "The Non-Boussinesq Lock-Exchange Problem, Part 2: High-Resolution Simulations", *J. Fluid Mech.*, Vol. 537, pp. 125-144.

Blasco, J., Codina, R., and Huerta, A., 1998, "A Fractional-Step Method for the Incompressible Navier-Stokes Equations Related to a Predictor-Multicorrector Algorithm", *International Journal for Numerical Methods in Fluids*, Vol. 28, pp. 1391-1419.

Blumberg, A. F., and Mellor, G. L., 1980, "A Coastal Ocean Numerical Model", *Proc. Int. Symp. on Math. Modelling of Estuarine Phys.*, J. Sundermann and K.P. Holz, Eds., pp. 202-219.

Blumberg, A.F., and Mellor, G.L., 1987, "A Description of a Three-Dimensional Coastal Ocean Circulation Model", in *Three-Dimensional Coastal Ocean Models*, N.S. Heaps, Ed., in Coastal and Estuarine Studies, Vol. 4, American Geophysical Union, Washington, DC, pp. 1-16.

Blumberg, A.F., Galperin, B., and O'Connor, D.J., 1992, "Modelling Vertical Structure of Open-Channel Flows", *J. of Hydraulic Engineering*, ASCE, Vol. 118, No. 8, pp. 1119-1134.

Bombardelli, F.A., Cantero, M.I., Buscaglia, G.C., and García, M.H., 2004, "Comparative Study of Convergence of CFD Commercial Codes when Simulating Dense Underflows", *Mec´anica Computacional*, Vol. XXIII, pp. 1187-1199.

Boñgolan-Walsh, V.P., Duan, J., Fischer, P., Özgökmen, T.M., and Iliescu, T., 2007, "Impact of Boundary Conditions on Entrainment and Transport in Gravity Currents", *Applied Mathematical Modelling*, Vol. 31, pp. 1338-1350.

Bowden, K.F., 1983, "Physical Oceanography of Coastal Waters", Ellis Horwood, Chichester, UK.

Bradshaw, P., 1978, "Introduction", in *Turbulence*, P. Bradshaw (Ed.), Springer-Verlag, Berlin.

Bredberg, J., 2001, "On Two-Equation Eddy-Viscosity Models", Internal Report 01/8, Department of Thermo and Fluid Dynamics, Chalmers University of Technology, Göteborg, Sweden, 41 pp.

Britter, R.E., and Simpson, J.E., 1978, "Experiments on the Dynamics of a Gravity Current Head", *J. Fluid Mech.*, Vol. 88, pp. 223-240.

Brown, D.L., 2001, "Accuracy of Projection Methods for the Incompressible Navier-Stokes Equations", *Workshop of Numerical Simulation of Incompressible Flows*, California, U.S. Department of Energy.

Brown, D.L., Cortez, R., and Minion, M.L., 2001, "Accurate Projection Methods for the Incompressible Navier-Stokes Equations", *Journal of Computational Physics*, Vol. 168, pp. 464-499.

Brown, M.A., 1999, "The Effect of Uphill Slopes on Mixing in Turbulent Gravity Currents", in *Mixing and Dispersion in Stably Stratified Flows, Proceedings of the Institute of Mathematics & its Applications Conference Series, New Series, No. 68*, P.A. Davies, Ed., Oxford University Press, Oxford.

Bruneau, C.H., Fabrie, P., and Rasetarinera, P., 1997, "An Accurate Finite Difference Scheme for Solving Convection-Dominated Diffusion Equations", *Int. J. Numer. Meth. Fluids*, Vol. 24, pp. 169-183.

Burchard, H., and Bolding, K., 2002, "GETM, A General Estuarine Transport Model: Scientific Documentation", European Commission, Joint Research Centre, Institute for Environment and Sustainability, Italy, 157 pp.

Burchard, H., Craig, P.D., Gemmrich, J.R., van Haren, H., **Mathieu, P.-P., Meier, H.E.M., Nimmo Smith, W.A.M., Prandke, H., Rippeth, T.P., Skyllingstad, E.D., Smyth, W.D., Welsh, D.J.S., and Wijesekera, H.W.**, 2008, "Observational and Numerical Modelling Methods for Quantifying

Coastal Ocean Turbulence and Mixing", *Progress in Oceanography*, Vol. 76, pp. 399-442.

Burt, N., and Rees, A., 2001, "Guidelines for the Assessment and Planning of Estuarine Barrages", Thomas Telford, London.

Cancino, L., and Neves, R., 1999, "Hydrodynamic and Sediment Suspension Modelling in Estuarine Systems, Part I: Description of the Numerical Models", *Journal of Marine Systems*, Vol. 22, pp. 105-116.

Castro Díaz, M.J., Garcia-Rodriguez, J.A., Macías, J., Parés, C., and Vázquez-Cendón, E., 2004, "A Two-Layer Finite Volume Model for Flows Through Channels with Irregular Geometry: Computation of Maximal Exchange Solutions, Application to the Strait of Gibraltar", *Commun. Nonlinear Sci. Numer. Simulat.*, Vol. 9, pp. 241-249.

Castro, M.J., Jose, A., Rodriguez, G., Gonzalez-Vida, J.M., Macias, J., and Pares, C., 2007, "Improved FVM for Two-Layer Shallow-Water Models: Application to the Strait of Gibraltar", *Advances in Engineering Software*, Vol. 38, No. 6, pp. 386-398.

Casulli, V., 1999, "A Semi-Implicit Finite Difference Method for Non-Hydrostatic, Free-Surface Flows", *Int. J. Numer. Meth. Fluids*, Vol. 30, pp. 425-440.

Casulli, V., and Cattani, E., 1994, "Stability, Accuracy and Efficiency of a Semi-Implicit Method for Three-Dimensional Shallow Water Flow", *Computers & Mathematics with Applications*, Vol. 27, pp. 99-112.

Casulli, V., and Cheng, R.T., 1992, "Semi-Implicit Finite Difference Methods for Three-Dimensional Shallow Water Flow", *Int. J. Numer. Meth. Fluids*, Vol. 15, pp. 629-648.

Casulli, V., and Stelling, G.S., 1998, "Numerical Simulation of 3D Quasi-Hydrostatic, Free-Surface Flows", *Journal of Hydraulic Engineering*, Vol. 124, No. 7, pp. 678-686.

Casulli, V., and Walters, R.A., 2000, "An Unstructured Grid, Three-Dimensional Model Based on the Shallow Water Equations", *Int. J. Numer. Meth. Fluids*, Vol. 32, pp. 331-348.

Casulli, V., and Zanolli, P., 2002, "Semi-Implicit Numerical Modelling of Non-hydrostatic Free-Surface Flows for Environmental Problems", *Mathematical and Computer Modelling*, Vol. 36, pp. 1131-1149.

Cea, L., Puertas, J., and Pena, L., 2007, "Velocity Measurements on Highly Turbulent Free Surface Flow Using ADV", *Exp. Fluids*, Vol. 42, No. 3, pp. 333-348.

Chan, R.K.C., 1975, "A Generalized Arbitrary Lagrangian-Eulerian Method for Incompressible Flows with Sharp Interface", *Journal of Computational Physics*, Vol. 17, pp.311-331.

Chang, W., Giraldo, F., and Perot, B., 2002, "Analysis of an Exact Fractional Step Method", *Journal of Computational Physics*, Vol. 179, pp. 1-17.

Chanson, H., Aoki, S.-i., and Maruyama, M., 2002, "Unsteady Two-Dimensional Orifice Flow: A Large-Size Experimental Investigation", *Journal of Hydraulic Research, IAHR*, Vol. 40, No. 1, pp. 63-71.

Chanson, H., Trevethan, M., and Aoki, S.-i., 2008, "Acoustic Doppler Velocimetry (ADV) in Small Estuary: Field Experience and Signal Post-Processing", *Flow Measurement and Instrumentation*, Vol. 19, pp. 307-313.

Chen, C., Liu, H., and Beardsley, R.C., 2003, "An Unstructured Grid, Finite Volume, Three-Dimensional, Primitive Equations Ocean Model: Application to Coastal Ocean and Estuaries", *J. Atmos. Oceanic Technol.*, Vol. 20, pp. 159-186.

Chen, G.Q., and Lee, J.H.W., 1998, "Turbulent Gravity Current of Lock Release Type: A Numerical Study", *Proceedings of the Second International Symposium on Environmental Hydraulics*, Hong Kong, pp. 449-454.

Chen, S.-C., and Peng, S.-H., 2006, "Two-dimensional Numerical Model of Two-Layer Shallow Water Equations for Confluence Simulation", *Advances in Water Resources*, Vol. 29, No. 11, pp. 1608-1617.

Chen, XJ., 2003, "A Fully Hydrodynamic Model for Three-Dimensional, Free-Surface Flows", *Int. J. Numer. Meth. Fluids*, Vol. 42, pp. 929-952.

Cheong, H.-B., and Han, Y.-H., 1997, "Numerical Study of Two-Dimensional Gravity Currents on a Slope", *Journal of Oceanography*, Vol. 53, pp.179-192.

Chiang, C.M., 1989, "The Applied Dynamics of Ocean Surface Waves", Advanced Series on Ocean Engineering, Vol. 1, World Scientific, Singapore.

Choi, D.Y., and Wu, C.H., 2006, "A New Efficient 3D Non-Hydrostatic Free Surface Flow Model for Simulating Water Wave Motions", *Ocean Engineering*, Vol. 33 (5–6), pp. 587-609.

Choi, H.G., Choi, H., and Yoo, J.Y., 1997, "A Fractional Four-Step Finite Element Formulation of the Unsteady Incompressible Navier-Stokes Equations Using SUPG and Linear Equal-Order Element Methods", *Computer Methods in Applied Mechanics and Engineering*, Vol. 143, pp. 333-348.

Chorin, A.J., 1968, "Numerical Solution of the Navier-Stokes Equations", *Mathematics of Computation*, Vol. 22, pp. 745-762.

Chou, P.C., and Pagano, N.J., 1967, "Elasticity", D. Van Nostrand Company, Princeton.

Chow, V.T., 1959, "Open-Channel Hydraulics", McGraw-Hill Book Company, New York.

Coates, M.J., Guo, Y., and Davies, P.A., 2001, "Laboratory Model Studies of Flushing of Trapped Salt Water from a Blocked Tidal Estuary", *J. Hydraul. Res.*, Vol. 39, No. 6, pp. 601-609.

Cuthbertson, A.J.S., Davies, P.A., and Guo, Y., 2006, "Model Study of the Influence of Submerged Tidal Barriers on Estuarine Mixing and Exchange Processes", *Journal of Hydraulic Engineering*, ASCE, Vol. 132, No. 10, pp. 1033-1043.

D'Alessio, S.J.D., Moodie, T.B., Pascal, J.P., and Swaters, G.E., 1996, "Gravity Currents Produced by Sudden Release of a Fixed Volume of Heavy Fluid", *Studies in Applied Mathematics*, Vol. 96, pp. 359-385.

Dalrymple, R.A., 1985, "Introduction to Physical Models in Coastal Engineering", in *Physical Modelling in Coastal Engineering*, R.A. Dalrymple, Ed., A.A. Balkema, Rotterdam, pp. 3-9.

Dalrymple, R.A., 1989, "Physical Modelling of Littoral Processes", in *Recent Advances in Hydraulic Physical Modelling*, R. Martins, Ed., Kluwer Academic Publishers, Netherlands, pp. 567-588.

Daubert, O., and Cahouet, J., 1984, "Approche Numérique de la Houle pas les Équations de Navier Stokes", *Annales des Ponts et Chaussées*, No. 32, 4e Trimestre, pp. 2-24.

Daubert, O., Hauguel, A., and Cahouet, J., 1982, "Waterwaves Calculation by Navier-Stokes Equations", Report, Laboratoire National d'Hydraulique, EDF, France.

Daugherty, R.L., 1961, "Fluid Properties" in *Handbook of Fluid Dynamics*, V.L. Streeter, Ed., McGraw-Hill Book Company, New York.

Davidson, L., 1990, "Second-Order Corrections of the k-ε Model to Account for Non-Isotropic Effects Due to Buoyancy", *Int. J. Heat Mass Transfer*, Vol. 33, No. 12, pp. 2599-2608.

Davies, A.M., and Jones, J.E., 1990, "On the Numerical Solution of the Turbulence Energy Equations for Wave and Tidal Flows", *Int. J. Numer. Meth. Fluids*, Vol. 11, pp. 1-25.

de Nijs, M.A.J., 2012, "On Sedimentation Processes in a Stratified Estuarine System", Ipskamp Drukkers B.V.

de Nijs, M.A.J., and Pietrzak, J.D., 2011, "An Explanation for Salinity and SPM-Induced Vertical Counter-Gradient Buoyancy Fluxes", *Ocean Dynamics*, Vol. 61, No. 4, pp. 497-524.

de Nijs, M.A.J., and Pietrzak, J.D., 2012a, "On Total Turbulent Energy and the Passive and Active Role of Buoyancy in Turbulent Momentum and Mass Transfer", *Ocean Dynamics*, Vol. 62, No. 6, pp. 849-865.

de Nijs, M.A.J., and Pietrzak, J.D., 2012b, "Saltwater Intrusion and ETM Dynamics in a Tidally-Energetic Stratified Estuary", *Ocean Modelling*, Vol. 49-50, pp. 60-85.

de Nijs, M.A.J., Pietrzak, J.D., and Winterwerp, J.C., 2010, "Advection of the Salt Wedge and Evolution of the Internal Flow Structure in the Rotterdam Waterway", *Journal of Physical Oceanography*, Vol. 41, pp. 3-27.

de Nijs, M.A.J., Winterwerp, J.C., and Pietrzak, J.D., 2009, "On Harbour Siltation in the Fresh-Salt Water Mixing Region", *Continental Shelf Research*, Vol. 29, pp. 175-193.

Dean, R.G., and Dalrymple, R.A., 1991, "Water Wave Mechanics for Engineers and Scientists", Academic Series on Ocean Engineering, Vol. 2, World Scientific, Singapore.

Delft Hydraulics, 2006, "Delft3D-FLOW User Manual, Version 3.13", Delft, Netherlands.

Delft Hydraulics, 2013, "Delft3D-FLOW User Manual, Version 3.15.30059", Delft, Netherlands.

Deponti, A., Pennati, V., and De Biase, L., 2006, "A Fully 3D Finite Volume Method for Incompressible Navier-Stokes Equations", *Int. J. Numer. Meth. Fluids*, Vol. 52, pp. 617-638.

DHI, 2009a, "MIKE 3 Flow Model, Hydrodynamic Module, Scientific Documentation", Denmark.

DHI, 2009b, "MIKE 21 & MIKE 3 Flow Model FM, Hydrodynamic and Transport Module, Scientific Documentation", Denmark.

Dingemans, M.W., 1997, "Water Wave Propagation over Uneven Bottoms, Part 1 - Linear Wave Propagation", Advanced Series on Ocean Engineering, Vol. 13, World Scientific, Singapore.

Dombroski, D.E., and Crimaldi, J.P., 2007, "The Accuracy of Acoustic Doppler Velocimetry Measurements in Turbulent Boundary Layer Flows over a Smooth Bed", *Limnol. Oceanogr.: Methods*, Vol. 5, pp. 23-33.

Doroudian, B., Bagherimiyab, F., and Lemmin, U., 2010, "Improving the Accuracy of Four-Receiver Acoustic Doppler Velocimeter (ADV) Measurements in Turbulent Boundary Layer Flows", *Limnol. Oceanogr.: Methods*, Vol. 8, pp. 575-591.

Drago, M., and Iovenitti, L., 2000, "σ-Coordinates Hydrodynamic Numerical Model for Coastal and Ocean Three-Dimensional Circulation", *Ocean Engineering*, Vol. 27, pp. 1065-1085.

Dronkers, J.J., 1964, "Tidal Computations in Rivers and Coastal Waters", North Holland Publishing Co., Amsterdam.

Dwoyer, D.L., Hussaini, M.Y., and Voigt, R.G., 1985, "Theoretical Approaches to Turbulence", Springer-Verlag, New York.

E., W., and Liu, J.-G., 1995, "Projection Method I: Convergence and Numerical Boundary Layers", *SIAM Journal of Numerical Analysis*, Vol. 32, No. 4, pp. 1017-1057.

Eagleson, P.S., and Dean, R.G., 1966, "Small Amplitude Wave Theory", in *Estuary and Coastline Hydrodynamics*, A.T. Ippen, Ed., McGraw-Hill Book Company, New York.

Falconer, R.A., 1976, "Mathematical Modelling of Jet-Forced Circulation in Reservoirs and Harbours", PhD Thesis, Imperial College, London.

Falconer, R.A., 1980a, "Modelling of Planform Influence on Circulation in Harbours", *Proceedings of Seventeenth Coastal Engineering Conference*, pp. 2726-2744.

Falconer, R.A., 1980b, "Numerical Modelling of Tidal Circulation in Harbours", *Journal of the Waterway, Port, Coastal and Ocean Division*, Vol. 106, No. WW1, ASCE, pp. 31-48.

Falconer, R.A., 1982, "Application of Numerical and Physical Models in Harbour Design", *Dock and Harbour Authority*, Vol. LXIII, No.737, pp. 34-37.

Falconer, R.A., 1984, "Temperature Distributions in Tidal Flow Field", *Journal of Environmental Engineering, ASCE*, Vol. 110, No. 6.

Falconer, R.A., 1993, "An Introduction to Nearly Horizontal Flows", in *Coastal, Estuarial and Harbour Engineers' Reference Book*, M.B. Abbott and W.A. Price, Eds., Chapman & Hall, London.

Falconer, R.A., and Chapman, B.C., 1996, "Design and Operation of a Laboratory Tidal Basin for Model Harbour Studies", *Dock and Harbour Authority*, Vol. 76, No. 864, pp. 175-179.

Falconer, R.A., and Chen, Y., 1996, "Modelling Sediment Transport and Water Quality Processes on Tidal Floodplains", in *Floodplain Processes*, M.G. Anderson, D.E. Walling and P.D. Bates, Eds., John Wiley & Sons, Chichester, UK.

Falconer, R.A., and Li, G., 1994, "Numerical Modelling of Tidal Eddies in Coastal Basins with Narrow Entrances Using the k-ε Turbulence Model", in *Mixing and Transport in the Environmental*, K.J. Beven, P.C. Chatwin and J.H. Millbank, Eds., John Wiley & Sons, London, pp. 325-350.

Falconer, R.A., and Mardapitta-Hadjipandeli, L., 1987, "Numerical and Physical Modelling of Tidal Flows and Flushing in Coastal Basins", *Proceedings of XXII IAHR Congress*, pp. 288-294.

Falconer, R.A., and Yu, G., 1991, "Effects of Depth, Bed Slope and Scaling on Tidal Currents and Exchange in a Laboratory Model Harbour", *Proceedings of Institution of Civil Engineers, Part2, Research and Theory*, Vol. 91, pp. 561-576.

Fernholz, H.-H., 1978, "External Flows", in *Turbulence*, P. Bradshaw, Ed., Springer-Verlag, Berlin.

Fischer, H.B., 1976, "Mixing and Dispersion in Estuaries, Annual Review of Fluid Dynamics", Annual Reviews, Inc., Palo Alto, USA, pp. 107-133.

Fischer, H.B., List, E.J., Koh, R.C.Y., Imberger, J., and Brooks, N.H., 1979, "Mixing in Inland and Coastal Waters", Academic Press, New York.

Fletcher, C.A.J., 1991, "Computational Techniques for Fluid Dynamics, Vol. II: Specific Techniques for Different Flow Categories", 2nd ed., Springer-Verlag, Berlin.

Floryan, J.M., and Rasmussen, H., 1989, "Numerical Methods for Viscous Flows with Moving Boundaries", *Applied Mechanics Reviews*, Vol. 42, pp. 323-341.

Flow Science, Inc., 2008, "FLOW-3D User Manual", Version 9.3, USA.

Fluent Inc., 2006, "FLUENT 6.3 User's Guide", USA.

Flynn, M.R., and Sutherland, B.R., 2004, "Intrusive Gravity Currents and Internal Gravity Wave Generation in Stratified Fluid", *J. Fluid Mech.*, Vol. 514, pp. 355-383.

Fossati, M., and Piedra-Cueva, I., 2013, "A 3D Hydrodynamic Numerical Model of the Rio de la Plata and Montevideo's Coastal Zone", *Applied Mathematical Modelling*, Vol. 37, pp. 1310-1332.

French, R.H., 1986, "Open-Channel Hydraulics", McGraw-Hill Book Company, New York.

Fringer, O.B., Gerritsen, M., and Street, R.L., 2006, "An Unstructured-Grid, Finite-Volume, Nonhydrostatic, Parallel Coastal Ocean Simulator", *Ocean Modelling*, Vol. 14, pp. 139-173.

Fromm, J.E., 1968, "A Method for Reducing Dispersion in Convective Difference Schemes", *Journal of Computational Physics*, Vol. 3, pp. 176-189.

Garbini, J.L., Forster, F.K., and Jorgensen, J.E., 1982, "Measurement of Fluid Turbulence Based on Pulsed Ultrasound Techniques, Part 1. Analysis" *J. Fluid Mech.*, Vol. 118, pp. 445-470.

García-Navarro, P., Brufau, P., and Burguete, J., 2002, "Recent Advances in Computational Hydraulics", *proceedings of the 5th International Conference on Hydroinformatics, Volume One: Model Development and Data Management*, Cardiff, Keynote Address, pp. 15-24.

Garcla, M.H., and Parsons, J.D., 1996, "Mixing at the Front of Gravity Currents", *Dynamics of Atmospheres and Oceans*, Vol. 24, pp. 197-205.

Gatski, T.B., and Speziale, C.G., 1993, "On Explicit Algebraic Stress Models for Complex Turbulent Flows", *J. Fluid Mech.*, Vol. 254, pp. 59-78.

Geyer, W.R., Trowbridge, J.H., and Bowen, M.M., 2000, "The Dynamics of a Partially Mixed Estuary", *Journal of Physical Oceanography*, pp. 2035-2048.

Girimaji, S.S., 1996, "Fully Explicit and Self-Consistent Algebraic Reynolds Stress Model", *Theor. Comput. Fluid Dyn.*, Vol. 8, pp. 387-402.

Gladstone, C., Ritchie, L.J., Sparks, R.S.J., and Woods, A.W., 2004, "An Experimental Investigation of Density-Stratified Inertial Gravity Currents", *Sedimentology*, Vol. 51, pp. 767-789.

Godunov, S.K., 1959, "Finite Difference Method for Numerical Computation of Discontinuous Solutions of the Equations of Fluid Dynamics", *Matematicheskij Sbornik*, Vol. 47, pp. 271-306.

Golub, G.H., and Van Loan, C.F., 1989, "Matrix Computations", 2nd ed., The Johns Hopkins University Press, USA.

Goring, D.G., and Nikora, V.I., 2002, "Despiking Acoustic Doppler Velocimeter Data", *J. Hydraul. Eng.*, ASCE, Vol. 128, No. 1, pp. 117-26.

Greenspan, D., and Casulli, V., 1988, "Numerical Analysis for Applied Mathematics, Science, and Engineering", Addison-Wesley Publishing Company, Inc., USA.

Gresho, P.M., 1990, "On the Theory of Semi-Implicit Projection Methods for Viscous Incompressible Flow and its Implementation via a Finite Element

Method that also Introduces a Nearly Consistent Mass Matrix, Part 1: Theory", *International Journal for Numerical Methods in Fluids*, Vol. 11, pp. 587-620.

Gresho, P.M., and Sani, R.L., 1987, "On Pressure Boundary Conditions for the Incompressible Navier-Stokes Equations", *Int. J. Numer. Meth. Fluids*, Vol. 7, pp. 1111-1145.

Guermond, J.L., Minev, P., and Shen, J., 2006, "An Overview of Projection Methods for Incompressible Flows", *Comput. Methods Appl. Mech. Engrg.*, Vol. 195, pp. 6011-6045.

Hacker, J., Linden, P.F., and Dalziel, S.B., 1996, "Mixing in Lock-Release Gravity Currents", *Dynamics of Atmospheres and Oceans*, Vol. 24, pp. 183-195.

Hadaeghi, M., and Hejazi, K., 2013, "2D Modelling of Vortex Transport in Viscous Fluid Flows Using a Nested Grid Method", *Proceedings of the 7th National Congress on Civil Engineering*, Iran, pp. 1-7.

Hallworth, M.A., Phillips, J.C., Huppert, H.E., and Sparks, R.S.J., 1993, "Entrainment in Turbulent Gravity Currents", *Nature*, Vol. 362, pp. 829-831.

Haney, R.L., 1991, "On the Pressure Gradient Force Over Steep Topography in σ Coordinate Ocean Models", *Journal of Physical Oceanography*, Vol. 21, pp. 610-619.

Haque, A., and Berlamont, J., 1998, "Modelling Density and Turbulence in Stratified Tidal Medium", *J. Hydraul. Eng.*, ASCE, Vol. 124, No. 2, pp. 135-145.

Harleman, D.R.F., 1961, "Stratified Flow" in *Handbook of Fluid Dynamics*, V.L. Streeter, Ed., McGraw-Hill Book Company, New York.

Harleman, D.R.F., 1966a, "Diffusion Processes in Stratified Flow", in *Estuary and Coastline Hydrodynamics*, A.T. Ippen, Ed., McGraw-Hill Book Company, New York.

Harleman, D.R.F., 1966b, "Pollution in Estuaries", in *Estuary and Coastline Hydrodynamics*, A.T. Ippen, Ed., McGraw-Hill Book Company, New York.

Harlow, F.H., and Welch, J.E., 1965, "Numerical Calculation of Time-Dependent Viscous Incompressible Flow of Fluid with Free Surface", *Physics of Fluids*, Vol. 8, pp. 2182-2189.

Hassan, W., Verwaest, T., and Willems, M., 2012, "Physical Modelling of Waves Inside the New Harbour of Ostend", *Coastlab12, Book of Abstracts of the 4th International Conference of the Application of Physical Modelling to Port and Coastal Protection*, P. Troch, V. Stratigaki and S. De Roo, Eds., Ghent, Belgium, pp. 121-122.

Hejazi, K., 2005, "3D Numerical Modelling of Flow and Turbulence in Oceanic Water Bodies Using an ALE Projection Method", *1st Conference on Numerical Modelling in Civil Engineering, K.N. Toosi University of Tech.*, Tehran, pp. 47-99.

Hejazi, K., Sami, S., and Soltanpour, M., 2014a, "Fully Coupled Numerical Modelling of Wave-Current-Mud Interaction by Finite Volume Method", *to appear in the Proceedings of the 11th International Conference on Hydroscience & Engineering (ICHE 2014)*, Hamburg.

Hejazi, K., Sami, S., Soltanpour, M., and Samsami, F., 2014b, "Numerical Modelling of Irregular Wave on Mud Layer Using Spectral Method", *to appear in the Proceedings of the 34th International Conference on Coastal Engineering (ICCE 2014)*, Seoul.

Hejazi, K., Soltanpour, M., and Sami, S., 2013, "Numerical Modelling of Wave-Mud Interaction Using Projection Method", *Ocean Dynamics*, Vol. 63, Issue 9-10, pp. 1093-1111.

Henderson, F.M., 1966, "Open Channel Flow", Macmillan, New York.

Henkes, R.A.W.M., and LeQuere, P., 1996, "Three Dimensional Transition of Natural-Convection Flows", *Journal of Fluid Mechanics*, Vol. 319, pp. 281-303.

Henriksen, M.O., and Holmen, J., 2002, "Algebraic Splitting for Incompressible Navier-Stokes Equations", *Journal of Computational Physics*, Vol. 175, pp. 438-453.

Herzfeld, M., 2009, "Improving Stability of Regional Numerical Ocean Models, *Ocean Dynamics*, Vol. 59, pp. 21- 46.

Hinze, J.O., 1975, "Turbulence", 2nd ed., McGraw-Hill Book Company, New York.

Hirsch, C., 1988, "Numerical Computation of Internal and External Flows; Volume 1, Fundamentals of Numerical Discretisation", John Wiley & Sons, Chichester, UK.

Hirsch, C., 1990, "Numerical Computation of Internal and External Flows; Volume 2, Computational Methods for Inviscid and Viscous Flows", John Wiley & Sons, Chichester, UK.

Hirt, C.W., 1970, "An Arbitrary Lagrangian-Eulerian Computing Technique", in *Proceedings of the Second International Conference on Numerical Methods in Fluid Dynamics*, Berkley, USA.

Hirt, C.W., Amsden A.A., and Cook J.L., 1974, "An Arbitrary Lagrangian-Eulerian Computing Method for All Speeds", *Journal of Computational Physics*, Vol. 14, pp. 227-253.

Hirt, C.W., and Nichols, B.D., 1981, "Volume of Fluid (VOF) Method for the Dynamics of Free Boundaries", *Journal of Computational Physics*, Vol. 39, pp. 201-225.

Hoffmann, K.A., and Chiang, S.T., 1993, "Computational Fluid Dynamics for Engineers", Vol. I, Engineering Education System, USA.

Holford, J.M., and Linden, P.F., 1999, "Turbulent Mixing in a Stratified Fluid", *Dynamics of Atmospheres and Oceans*, Vol. 30, pp. 173-198.

Horn, D.A., Imberger, J., and Ivey, G.N., 2001, "The Degeneration of Large-Scale Interfacial Gravity Waves in Lakes", *J. Fluid Mech.*, Vol. 434, pp. 181-207.

HR Wallingford, 1994, "Wave Probe Monitor, Operating Instructions", Issue 5, HR Wallingford Ltd., Wallingford.

HR Wallingford, 1979, "Saline Intrusion and Sediment Transport in the Rotterdam Waterways, Two-Layer Numerical Model Simulation Studies", Report No. EX 883, Hydraulics Research Station, Wallingford, UK.

HR Wallingford, 1999, "Guidelines for the Assessment and Planning of Estuarine Barrages", Report No. SR 491, HR Wallingford, UK.

Huang, W., and Spaulding, M., 1995, "3D Model of Estuarine Circulation and Water Quality Induced by Surface Discharges", *J. Hydraul. Eng.*, ASCE, Vol. 121, No. 4, pp. 300-311.

Hughes, S.A., 1993, "Physical Models and Laboratory Techniques in Coastal Engineering", *Advanced Series on Ocean Engineering*, Vol. 7, World Scientific, Singapore.

Huppert, H.E., 2006, "Gravity Currents: A Personal Perspective", *J. Fluid Mech.*, Vol. 554, pp. 299-322.

Huppert, H.E., and Simpson, J.E., 1980, "The Slumping of Gravity Currents", *J. Fluid Mech.*, Vol. 99, Part 4, pp. 785-799.

Hurther, D., and Lemmin, U., 2001, "A Correction Method for Turbulence Measurements with a 3D Acoustic Doppler Velocity Profiler" *J. Atmos. Oceanic Technol.*, Vol. 18, No. 3, pp. 446-458.

HydroQual, Inc., 2004, "A Primer for ECOMSED, Version 1.4, Users Manual", USA.

Iskandarani, M., Haidvogel, D.B., and Levin, J.C., 2003, "A Three-Dimensional Spectral Element Model for the Solution of the Hydrostatic Primitive Equations", *J. Comput. Phys.*, Vol. 186, pp. 397-425.

Jacobitz, F.G., 2000, "Scalar Transport and Mixing in Turbulent Stratified Shear Flow", *International Journal of Heat and Fluid Flow*, Vol. 21, pp. 535-541.

Jay, D.A., and Smith, J.D., 1990, "Circulation, Density Structure, and Neap-Spring Transitions in the Columbia River Estuary", *Prog. Oceanogr.*, Vol. 25, pp. 81-112.

Jenway Ltd., 1996, "Model 4320 Conductivity Meter Operating Manual", Jenway Ltd., England.

Jiang, J.X., and Falconer, R.A., 1983, "On the Tidal Exchange Characteristics of Model Rectangular Harbours", *Proceedings of Institution of Civil Engineers, Part2, Research and Theory*, Vol. 75, pp. 475-489.

Johansson, A., 2000, "Engineering Turbulence Models and Their Development, with Emphasis on Explicit Algebraic Reynolds Stress Models", in Theories of Turbulence, M. Oberlack and F.H. Busse, Eds., CISM International Centre for Mechanical Sciences, Vol. 442, pp. 253-300.

Jones, W.P., and Launder, B.E., 1972, "The Prediction of Laminarization with a Two-Equation Model of Turbulence", *Int. J. Heat and Mass Transfer*, Vol. 15, 301-314.

Jongen, T., and Gatski T.B., 1998, "General Explicit Algebraic Stress Relations and Best Approximation for Three-dimensional Flows", *Int. J. Eng. Sci.*, Vol. 36, pp. 739-763.

Kamphuis, J.W., 1991, "Physical Modelling", in *Handbook of Coastal and Ocean Engineering"*, J.B. Herbich, Ed., Vol. 2, Gulf Publishing Company, Houston, USA.

Kanarska, Y., Shchepetkin, A., and McWilliams, J.C., 2007, "Algorithm for Non-Hydrostatic Dynamics in the Regional Oceanic Modelling System", *Ocean Modelling*, Vol. 18, pp. 143-174.

Kanarska, Y.V., and Maderich, V.S., 2002, "Non-Hydrostatic Model for Stratified Flows with Free-Surface", *Applied Hydromechanics*, Vol. 4, No. 76, pp. 280-289.

Karelse, M., Vreugdenhil, C.B., Delvinge, G.A.L. and Breusers, H.N.C., 1974, "Momentum and Mass Transfer in Stratified Flows", Report on Literature Study, Report No. R 880, WL/Delft Hydraulics, Netherlands.

Karimi, M., Hejazi, K., and Mojabi, M., 2012, "Integrated Numerical Modelling of Oil Spills, Sedimentation and Transport of Oil in Sediment Laden Marine Waters", *Proceedings of the 10th International Conference on Coasts, Ports and Marine Structures (ICOPMAS 2012)*, Tehran, pp. 751-758.

Kawahara, M., Kobayashi, M., and Nakata, K., 1983, "Multiple Level Finite Element Analysis and its Applications to Tidal Current Flow in Tokyo Bay", *Appl. Math. Mod.*, Vol. 7, pp. 197-211.

Kay, S.M., 1993, "Fundamentals of Statistical Signal Processing, Estimation Theory", Vol. 1, Prentice Hall PTR, New Jersey.

Keulegan, G.H., 1966, "Model Laws for Coastal and Estuarine Models", in *Estuary and Coastline Hydrodynamics*, A.T. Ippen, Ed., McGraw-Hill Book Company, New York.

Khorsandi, B., Mydlarski, L., and Gaskin, S., 2012, "Noise in Turbulence Measurements Using Acoustic Doppler Velocimetry", *J. Hydraul. Eng., ASCE*, Vol. 138, No. 10, pp. 829-838.

Kim, C., and Lee, J., 1994, "A Three-Dimensional PC-Based Hydrodynamic Model Using an ADI Scheme", *Coastal Engineering*, Vol. 23, pp. 271-287.

Kim, J., and Moin, P., 1985, "Application of a Fractional-step Method to Incompressible Navier-Stokes Equations", *Journal of Computational Physics*, Vol. 59, pp. 308-323.

Kincaid, D., and Cheney, W., 1991, "Numerical Analysis", Brooks/Cole Publishing Company, USA.

Kneller, B.C., Bennett, S.J., and McCaffre, W.D., 1999, "Velocity Structure, Turbulence and Fluid Stresses in Experimental Gravity Currents", *Journal of Geophysical Research*, Vol. 104, No. C3, pp. 5381-5391.

Kneller, B.C., Bennett, S.J., and McCaffrey, W.D., 1997, "Velocity and Turbulence Structure of Density Currents and Internal Solitary Waves: Potential Sediment Transport and the Formation of Wave Ripples in Deep Water", *Sedimentary Geology*, Vol. 112, pp. 235-250.

Kobus, H., 1980, "Hydraulic Modelling", Bulletin No. 7, German Association for Water Research and Land Development.

Kocyigit, M., Falconer, R., and Lin, B., 2002, "Three-Dimensional Numerical Modelling of Free Surface Flows with Non-Hydrostatic Pressure", *Int. J. Numer. Meth. Fluids*, Vol. 40, pp. 1145-1162.

Komatsu, T., Ohgushi, K., and Asai, K., 1997, "Refined Numerical Scheme for Advective Transport in Diffusion Simulation", *Journal of Hydraulic Engineering, ASCE*, Vol. 123, No. 1, pp. 41-50.

Kranenburg, C., and Pietrzak, J.D., 1989, "Internal Lee Waves in Turbulent Two-Layer Flow", *J. Hydraul. Eng., ASCE*, Vol. 115, No. 10, pp. 1352-1370.

Kraus, N.C., Lohrmann, A., and Cabrera, R., 1994, "New Acoustic Meter for Measuring 3D Laboratory Flows", *J. Hydraul. Eng.*, Vol. 120, pp. 406-412.

Kreyszig, E., 2011, "Advanced Engineering Mathematics", 10th ed., John Wiley & Sons, Inc., USA.

Kun, Y., Yiping, H., Xueyi, Z., and Yuliang, L., 2000, "Study on Anisotropic Buoyant Turbulence Model", *Applied Mathematics and Mechanics*, Vol. 21, No. 1, pp. 43-48.

La Rocca, M., Adduce, C., Sciortino, G., and Bateman Pinzon, A., 2008, "Experimental and Numerical Simulation of Three-Dimensional Gravity Currents on Smooth and Rough Bottom", *Phys. Fluids*, Vol. 20, pp. 106603 (1-15).

La Rocca, M., and Bateman Pinzon, A., 2010, "Experimental and Theoretical Modelling of 3D Gravity Currents", in Numerical Simulations - Examples and Applications in Computational Fluid Dynamics, L. Angermann, Ed., pp. 281-310.

Langendoen, E.J., 1992, "Flow Patterns and Transport of Dissolved Matter in Tidal Harbours", Communications on Hydraulic and Geotechnical Engineering, Department of Civil Engineering, Delft University of Technology, Report 92-8.

Langhaar, H.L., 1951, "Dimensional Analysis and Theory of Models", John Wiley & Sons, New York.

Lapidus, L., and Pinder, G.F., 1982, "Numerical Solution of Partial Differential Equations in Science and Engineering", John Wiley & Sons, New York.

Launder, B.E., 1978, "Heat and Mass Transport", in *Turbulence*, P. Bradshaw, Ed., Springer-Verlag, Berlin.

Launder, B.E., and Spalding, D.B., 1972, "Lectures in Mathematical Models of Turbulence", Academic Press, London.

Lax, P.D., 1954, "Weak Solutions of Non-linear Hyperbolic Equations and Their Numerical Applications", *Communications on Pure and Applied Mathematics*, Vol. 7, pp. 159-193.

Le Méhauté, B., 1990, "Similitude", in *Ocean Engineering Science*, B. Le Méhauté, Ed., Vol. 9, Part B, John Wiley & Sons, New York, pp. 955-980.

Lee, H.G., and Kim, J., 2012, "A Comparison Study of the Boussinesq and the Variable Density Models on Buoyancy-Driven Flows", *J. Eng. Math.*, Vol. 75, pp. 15-27.

Lee, J.W., Teubner, M.D., Nixon, J.B., and Gill, P.M., 2006, "A 3-D Non-Hydrostatic Pressure Model for Small Amplitude Free Surface Flows", *Int. J. Numer. Meth. Fluids*, Vol. 50, pp. 649-672.

Lemmin, U., and Lhermitte, R., 1999, "Discussion of "ADV Measurements of Turbulence: Can We Improve Their Interpretation?" By V.I. Nikora and D.G. Goring" *J. Hydraul. Eng., ASCE*, Vol. 125, No. 9, pp. 987-988.

Leonard, B.P., 1979, "A Stable and Accurate Convective Modelling Procedure Based on Quadratic Upstream Interpolation", *Computer Methods in Applied Mechanics and Engineering*, Vol. 19, pp. 59-98.

Leonard, B.P., 1991, "The ULTIMATE Conservative Difference Scheme Applied to Unsteady One-Dimensional Advection", *Computer Methods in Applied Mechanics and Engineering*, Vol. 88, pp. 17-74.

Lesoinne, M., and Farhat, C., 1996, "Geometric Conservation Laws for Flow Problems with Moving Boundaries and Deformable Meshes, and Their Impact on Aeroelastic Computations" *Computer Methods in Applied Mechanics and Engineering*, Vol. 134, pp. 71-90.

Li, B., and Fleming, C., 2001, "Three-Dimensional Model of Navier-Stokes Equations for Water Waves", *ASCE Journal of Waterway, Port, Coastal, and Ocean Engineering*, Vol. 127, No. 1, pp. 16-25.

Li, C.W., and Zhu, B., 2002, "A Sigma Coordinate 3D k-ε Model for Turbulent Free Surface Flow Over a Submerged Structure", *Applied Mathematical Modelling*, Vol. 26, pp. 1139-1150.

Lin, B., and Falconer, R.A., 1996, "Numerical Modelling of Three-Dimensional Suspended Sediment for Estuarine and Coastal Waters", Journal of Hydraulic Research, Vol. 34, No.4, pp. 435-456.

Lin, B., and Falconer, R.A., 1997, "Three-Dimensional Layer-Integrated Modelling of Estuarine Flows with Flooding and Drying", *Estuarine, Coastal and Shelf Science*, Vol. 44, pp. 731-751.

Lin, P., and Li, C.W., 2002, "A σ-Coordinate Three-Dimensional Numerical Model for Surface Wave Propagation", *Int. J. Numer. Meth. Fluids*, Vol. 38, pp. 1045-1068.

Liu, W.-C., Hsu, M.-H., and Kuo, A.Y., 2002, "Application of Different Turbulence Closure Model for Stratified Tidal Flows and Salinity in an Estuarine System", *Mathematics and Computers in Simulation*, Vol. 59, pp. 437-451.

LNHE (Laboratoire National d'Hydraulique et Environnement), 2013, "TELEMAC Modelling System, TELEMAC-3D Software, Release 6.2, Operating Manual", Canada.

Lohrmann, A., Cabrera, R., and Kraus, N.C., 1994, "Acoustic Doppler Velocimeter (ADV) for Laboratory Use" *Proc. Symp. on Fundamentals and*

Advancements in Hydraulic Measurements and Experimentation, C. A. Pugh, Ed., ASCE, pp. 351-365.

Lowe, R.J., Rottman, J.W., and Linden, P.F., 2005, "The Non-Boussinesq Lock-Exchange Problem, Part 1: Theory and Experiments", *J. Fluid Mech.*, Vol. 537, pp. 101-124.

Luettich, R.A., Westerink, J.J., and Scheffner, N.W., 1991, "ADCIRC: An Advanced Three-Dimensional Circulation Model for Shelves, Coasts and Estuaries", Coast. Engrg. Res. Ct., US Army Engs. Wtrways. Experiment Station, Vicksburg, MS Report 1: Theory and Methodology of ADCIRC-2DDI and ADCIRC-3DL.

Lynch, D.R., and Werner, F.E., 1991, "Three-Dimensional Hydrodynamics on Finite Elements, Part II: Non-Linear Time-Stepping Model", *Int. J. Numer. Meth. Fluids*, Vol. 12, pp. 507-533.

Mahadevan, A., Oliger, J., and Street, R., 1996, "A Non-Hydrostatic Mesoscale Ocean Model, Part 1: Well Posedness and Scaling", *Journal of Physical Oceanography*, Vol. 26, No. 9, pp. 1868-1880.

Marshall, J., Hill, C., Perelman, L., and Adcroft, A., 1997, "Hydrostatic, Quasi-Hydrostatic, and Non-Hydrostatic Ocean Modelling", *Journal of Geophysical Research*, Vol. 102, No. C3, pp. 5733-5752.

Maskell, J.M., and Ng, B., 1999, "Impact of Tide-Overtopping Barrage on Water Quality and Subsequent Management", in *Environmental Hydraulics*, J.H.W. Lee, A.W. Jayawardena, and Z.Y. Wang, Eds., Balkema, Rotterdam, Netherlands, pp. 61-66.

Mayer, S., Garapon, A., and Sørensen, L.S., 1998, "A Fractional Step Method for Unsteady Free-Surface Flow with Applications to Non-Linear Wave Dynamics", *Int. J. Numer. Meth. Fluids*, Vol. 28, pp. 293-315.

McKee, S., Tome´, M.F., Ferreira, V.G., Cuminato, J.A., Castelo, A., Sousa, F.S., and Mangiavacchi, N., 2008, "Review: The MAC Method", *J. Computers & Fluids*, Vol. 37, pp. 907-930.

McLelland, S.J., and Nicholas, A.P., 2000, "A New Method for Evaluating Errors in High-Frequency ADV Measurements", Hydrological Processes, Vol. 14, pp. 351-366.

Mei, C.C., 1983, "The Applied Dynamics of Ocean Surface Waves", Wiley Inter-science, New York.

Mellor, G. L., and Yamada, T., 1982, "Development of Turbulence Closure Model for Geophysical Fluid Problems", *Reviews of Geophysics and Space Physics*, Vol. 20, No. 5, pp. 851-875.

Memarzadeh, R., and Hejazi, K., 2012, "ISPH Numerical Modelling of Nonlinear Wave Run-up on Steep Slopes", *Journal of the Persian Gulf (Marine Science)*, Vol. 3, No. 10, pp. 17-26.

Middleton, G.V., 1966a, "Experiments on Density and Turbidity Currents, I. Motion of the Head", *Can. J. Earth Sci.*, Vol. 3, pp. 523-546.

Middleton, G.V., 1966b, "Experiments on Density and Turbidity Currents, II. Uniform Flow of Density Currents", *Can. J. Earth Sci.*, Vol. 3, pp. 627-637.

Miller, K.S., and Rochwarger, M.M., 1972, "A Covariance Approach to Spectral Moment Estimation", *IEEE Trans. Inform. Theory*, IT-18, pp. 588-596.

Minev, P.D., 2001, "A Stabilized Incremental Projection Scheme for the Incompressible Navier-Stokes Equations", *International Journal for Numerical Methods in Fluids*, Vol. 36, pp. 441-464.

Mitchell, A.R., 1969, "Computational Methods in Partial Differential Equations", John Wiley & Sons, London.

Mojabi, M., and Hejazi, K., 2011, "A Numerical Study on Harbour Planform Effects on Cohesive Sediment Transport and Sedimentation", *Book of Abstracts, 11th International Conference on Cohesive Sediment Transport Processes (INTERCOH XI)*, Shanghai, pp. 157-158.

Mojabi, M., Hejazi, K., and Karimi, M., 2013, "Numerical Investigation of Effective Harbour Geometry Parameters on Sedimentation Inside Square Harbours", *Int. J. MAr. Sci. Eng.*, Vol. 3, No. 2, pp. 57-68.

Mojabi, S.M., Hejazi, K., and Mohammadi Aragh, M., 2011, "Numerical Modelling of Sediment Transport in Harbours and Study of Planform Effects on Sedimentation", *Proceedings of the 13th International Conference on Harbour, Maritime & Multimodal Logistics Modelling and Simulation (HMS 2011)*, A. Bruzzone, F. Longo, Y. Merkuryev, and M.A. Piera, Eds., pp. 13-18.

Monismith, S.G., and Fong, D.A., 1996, "A Simple Model of Mixing in Stratified Tidal Flows", *Journal of Geophysical Research*, Vol. 101, No. C12, pp. 28583-28595.

Muin, M., and Spaulding, M., 1997, "Three-Dimensional Boundary Fitted Circulation Model", *J. Hydraul. Eng.*, ASCE, Vol. 123, No. 1, pp. 2-12.

Namin, M.M., Lin, B., and Falconer, R.A., 2001, "An Implicit Numerical Algorithm for Solving Non-Hydrostatic Free-Surface Flow Problems", *Int. J. Numer. Meth. Fluids*, Vol. 35, pp. 341-356.

Nece, R.E., 1984, "Planform Effects on Tidal Flushing of Marinas", *Journal of Waterway, Port, Coastal & Ocean Engineering*, ASCE, Vol. 110, pp. 251-269.

Nece, R.E., 1992, "Physical Models", *Proceedings of the Institution of Civil Engineers, Water, Maritime and Energy*, Vol. 96, pp. 181-182.

Nece, R.E., and Falconer, R.A., 1989a, "Hydraulic Modelling of Tidal Circulation and Flushing in Coastal Basins", *Proceedings of Institution of Civil Engineers, Part 1, Design and Construction*, Vol. 86, pp. 913-935.

Nece, R.E., and Falconer, R.A., 1989b, "Modelling of Tide Induced Depth Averaged Velocity Distributions in a Square Harbour", *Proceedings of International Conference on Hydraulic and Environmental Modelling of Coastal, Estuarine and River Waters"*, pp. 56-66.

Nece, R.E., and Richey, E.P., 1972, "Flushing Characteristics of Small-Boat Marinas", *Proceedings of Thirteenth Coastal Engineering Conference*, Vol. III, pp. 2499-2512.

Nece, R.E., Falconer, R.A., and Tsutsumi, T., 1976, "Planform Influence on Flushing and Circulation in Small Harbours", *Proceedings of Fifteenth International Conference on Coastal Engineering, ASCE*, Vol. IV, pp. 3471-3486.

Nece, R.E., Richey, E.P., Rhee, J., and Smith, H.N., 1979, "Effects of Planform Geometry on Tidal Flushing and Mixing in Marinas", Technical Report No. 62, University of Washington, Seattle, USA.

Nece, R.E., Smith, H.N., and Richey, E.P., 1980, "Tidal Circulation and Flushing in Five Western Washington Marinas", Technical Report No. 63, University of Washington, Seattle, USA.

Nikora, V.I., and Goring, D.G., 1998, "ADV Measurements of Turbulence: Can We Improve Their Interpretation?", *J. Hydraul. Eng.*, ASCE, Vol. 124, No. 6, pp. 630-634.

Nomura, T., and Hughes, T.J.R., 1992, "An Arbitrary Lagrangian-Eulerian Finite Element Method for Interaction of Fluid and a Rigid Body". *Computer Methods in Applied Mechanics and Engineering*, Vol. 95, pp. 115-138.

NORTEK AS, 1997a, "ADV Operation Manual", NORTEK AS, Norway.

NORTEK AS, 1997b, "ADV Software Manual, Ver. 2.6", NORTEK AS, Norway.

Novak, P., and Cabelka, J., 1981, "Models in Hydraulic Engineering, Physical Principles and Design Applications", Pitman, Boston.

O'Connor, J.J., and Robertson, E.F., 1999, "Omar Khayyam", Web Site of the School of Mathematics and Statistics, University of St Andrews, Scotland.

Odd, N.V.M., and Rodger, J.G., 1978, "Vertical Mixing in Stratified Tidal Flows", *Journal of Hydraulic Division, ASCE*, Vol. 104 (HY3), pp. 337-351.

Ohle, N., Mai, S., and Zimmermann, C., 2000, "Comparison of Physical and Numerical Simulations of Currents", *Proc. of the 4th Int. Conf. on Hydroinformatics*, Iowa, USA, p. 75.

Olsen, N.R.B., 1997, "Computational Fluid Dynamics in Hydraulic and Sedimentation Engineering", Division of Hydraulic and Environmental Engineering, The Norwegian University of Science and Technology.

Ouillon, S., and Dartus, D., 1997, "Three-Dimensional Computation of Flow Around Groyne", "*Journal of Hydraulic Engineering", ASCE*, Vol. 123, No. 11, pp. 962-970.

Özgökmen, T., Fischer, P., Duan, J., and Iliescu, T., 2004, "Three-Dimensional Turbulent Bottom Density Currents from a High-Order Non-Hydrostatic Spectral Element Model", *Journal of Physical Oceanography*, Vol. 34, pp. 2006-2026.

Özgökmen, T.M., Iliescu, T., and Fischer, P.F., 2009, "Large Eddy Simulation of Stratified Mixing in a Three-Dimensional Lock-Exchange System", *Ocean Modelling*, Vol. 26, pp. 134-155.

Pandoe, W.W., and Edge, B.L., 2003, "Three-Dimensional Hydrodynamic Model, Study Cases for Quarter Annular and Idealized Ship Channel Problems", *Journal of Ocean Engineering*, Vol. 30, pp. 1117-1135.

Parsheh, M., Sotiropoulos, F., and Porté-Agel, F., 2010, "Estimation of Power Spectra of Acoustic-Doppler Velocimetry Data Contaminated with Intermittent Spikes", *J. Hydraul. Eng., ASCE*, Vol. 136, No. 6, pp. 368-378.

Patankar, S.V., 1980, "Numerical Heat Transfer and Fluid Flow", McGraw-Hill Book Company, New York.

Patankar, S.V., 1981, "A Calculation Procedure for Two-Dimensional Elliptic Situations", *Numerical Heat Transfer*, Vol. 4, pp. 409-425.

Patankar, S.V., and Baliga, B.R., 1978, "A New Finite-Difference Scheme for Parabolic Differential Equations", *Numerical Heat Transfer*, Vol. 1, pp. 27-37.

Patterson, M.D., Simpson, J.E., Dalziel, S.B., and Nikiforakis, N., 2005a, "Numerical Modelling of Two-Dimensional and Axisymmetric Gravity Currents", *Int. J. Numer. Meth. Fluids*, Vol. 47, No. 10-11, pp. 1221-1227.

Patterson, M.D., Simpson, J.E., Dalziel, S.B., and van Heijst, G.J.F., 2005b, "The Development of an Axisymmetric Gravity Current", *Proc. Mechanics of the 21st Century*, W. Gutkowski and T.A. Kowalewski, Eds., ICTAM 2004.

Pearce, B.R., and Cooper, C.K., 1981, "Numerical Circulation Model for Wind-Induced Flow", *Journal of Hydraulic Engineering*, ASCE, Vol. 107, No. 3, pp. 285-301.

Peng, S.-H., and Davidson, L., 2000, "New Two-Equation Eddy Viscosity Transport Model for Turbulent Flow Computation", *AIAA Journal*, Vol. 38, 1196-1205.

Peng, Y.-F., Mittal, R., Sau, A., and Hwang, R.R., 2010, "Nested Cartesian Grid Method in Incompressible Viscous Fluid Flow", *Journal of Computational Physics*, Vol. 229, pp. 7072-7101.

Perot, J.B., 1993, "An Analysis of the Fractional Step Method", *Journal of Computational Physics*, Vol. 108, pp. 51-58.

Perrels, P.A.J., and Karelse, M., 1982, "A Two-Dimensional Laterally Averaged Model for Salt Intrusion in Estuaries", Publication No. 262, Delft Hydraulics, Netherlands.

Pham, H., and Nguyen, T.D., 2012, "The Explicit Algebraic Reynolds Stress Models for Turbulent Flows", *Mechanical Engineering Research*, Vol. 2, No. 1, pp. 95-106.

Pope, S.B., 1975, "A More General Effective Viscosity Hypothesis", *J. Fluid Mech.*, Vol. 72, pp. 331-340.

Press, W.H., Flannery, B.P., Teukolsky, S.A., and Vetterling, W.T., 1986, "Numerical Recipes", Cambridge University Press, Cambridge.

Price, W.A., 1978, "Models - Can We Learn From the Past", *Proceedings of the 16th Coastal Engineering Conference, ASCE*, Vol. 1, pp. 25-36.

Puckett, E.G., Almgren, A.S., Bell, J.B., Marcus, D.L., and Rider, W.J., 1997, "A High-Order Projection Method for Tracking Fluid Interfaces in Variable Density Incompressible Flows", *Journal of Computational Physics*, Vol. 130, pp. 269-282.

Reid, R.O., 1957, "Modification of the Quadratic Bottom-Stress Law of Turbulent Channel Flow in the Presence of Surface Wind-Stress", Tech. Memo. No. 93, Beach Erosion Board, U.S. Dept. Army, Washington, D.C.

Reilly, N.P., 1993, "Barriers and Barrages", in *Coastal, Estuarial and Harbour Engineers' Reference Book*, M.B. Abbott and W.A. Price, Eds., Chapman & Hall, London.

Reynolds, A.J., 1974, "Turbulent Flows in Engineering", John Wiley & Sons, London.

Reynolds, W.C., 1976, "Computation of Turbulent Flows", *Annu. Rev. Fluid Mech.*, Vol. 8, pp. 183-208.

Riddle, A.M., and Lewis, R.E., 1999, "The Effect of the Tidal Barrage on the Flows and Mixing in the Tees Estuary", in *Mixing and Dispersion in Stably Stratified Flows, Proceedings of the Institute of Mathematics & its Applications Conference Series, New Series, No. 68*, P.A. Davies, Ed., Oxford University Press, Oxford.

Riley, J.J., and Lelon, M.-P., 2000, "Fluid Motions in the Presence of Strong Stable Stratification", *Annu. Rev. Fluid Mech.*, Vol. 32, pp. 613-657.

Roache, P.J., 1972, "Computational Fluid Dynamics", Hermosa Publishers, Albuquerque, New Mexico.

Rodi, W., 1976, "A New Algebraic Relation for Calculating the Reynolds Stresses", *ZAMM Journal of Applied Mathematics and Mechanics/ Z. Angew. Math. Mech.*, Vol. 56, pp. 219-221.

Rodi, W., 1984, "Turbulence Models and Their Application in Hydraulics", IAHR, Delft.

Rodi, W., 1987, "Examples of Calculation Methods for Flow and Mixing in Stratified Fluids", *Journal of Geophysical Research*, Vol. 92, No. C5, pp. 5305-5328.

Sankaranarayanan, S., and Ward, M.C., 2006, "Development and Application of a Three-Dimensional Orthogonal Coordinate Semi-Implicit Hydrodynamic Model", *Continental Shelf Research*, Vol. 26, pp. 1571-1594.

Sarhadi Zadeh, E., and Hejazi, K., 2010, "Modelling of Flow and Water Quality Processes of Oil Spills with Finite Volume Method", *Proceedings Earth and Space 2010: Engineering, Science, Construction, and Operations in*

Challenging Environments, G. Song and R.B. Malla, Eds., ASCE, pp. 2055-2062.

Sarhadi Zadeh, E., and Hejazi, K., 2012, "Eulerian Oil Spills Model Using Finite-Volume Method with Moving Boundary and Wet-Dry Fronts", *Modelling and Simulation in Engineering*, Vol. 2012, 7 pp.

Schlichting, H., 1979, "Boundary-Layer Theory", McGraw-Hill Book Company, New York

Schmitt, F.G., 2007, "About Boussinesq's Turbulent Viscosity Hypothesis: Historical Remarks and a Direct Evaluation of its Validity", *C. R. Mecanique*, Vol. 335, pp. 617-627.

Shams Nia, H., and Hejazi, K., 2012, "2DV Nonlinear *k-ε* Turbulence Modelling of Stratified Flows", *Journal of the Persian Gulf (Marine Science)*, Vol. 3, No. 10, pp. 7-16

Shapiro, A.H., 1961, "Basic Equations of Fluid Flow" in *Handbook of Fluid Dynamics*, V.L. Streeter, Ed., McGraw-Hill Book Company, New York.

Sharifian, M.K., and Hejazi, K., 2014, "Numerical Modelling of Saline Gravity Currents Using EARSM and Buoyant *k*-ε Turbulence Closures", *International Journal of Maritime Technology, IJMT*, Vol. 2, pp. 43-54.

Sharp, J.J., 1981, "Hydraulic Modelling", Butterworths, London.

Shchepetkin, A.F., and McWilliams, J.C., 2005, "The Regional Oceanic Modelling System (ROMS): A Split-Explicit, Free-Surface, Topography-Following-Coordinate, Oceanic Model", *Ocean Modell.*, Vol. 9, pp. 347-404.

Shen, H., 1991, "Numerical Analysis of Large-Scaled Flows and Mass Transport in Lakes", Doctoral Dissertation, Kyoto University, Japan.

Shen, H., Tsanis, I.K., and D'Andrea, M., 1995, "A Three-Dimensional Nested Hydrodynamic/Pollutant Transport Simulation Model for the Nearshore Areas of Lake Ontario" *J. Great Lakes Res.*, Vol. 21, No. 2, pp. 161-177.

Shin, J.O., Dalziel, S.B., and Linden, P.F., 2004, "Gravity Currents Produced by Lock Exchange", *J. Fluid Mech.*, Vol. 521, pp. 1-34.

Simpson, J.E., 1987, "Gravity Currents in the Environment and in the Laboratory", Wiley, New York, 244 pp.

Simpson, J.E., 1997, "Gravity Currents in the Environment and the Laboratory", 2nd ed., Cambridge University Press, Cambridge.

Simpson, J.E., and Britter, R.E., 1979, "The Dynamics of the Head of a Gravity Current Advancing over a Horizontal Surface", *J. Fluid Mech.*, Vol. 94, pp. 477-495.

Smith, G.D., 1985, "Numerical Solution of Partial Differential Equations: Finite Difference Methods", 3rd ed., Oxford University Press, Oxford.

Snyder, W.H., and Castro, I.P., 1999, "Acoustic Doppler Velocimeter Evaluation in Stratified Towing Tank", *J. Hydraul. Eng., ASCE*, Vol. 125, No. 6, pp. 595-603.

So, R.M.C., Jin, L.H., and Gatski, T.B., 2004a, "An Explicit Algebraic Reynolds Stress and Heat Flux Model for Incompressible Turbulence: Part I Non-Isothermal Flow", *Theoret. Comput. Fluid Dynamics*, Vol. 17, pp. 351-376.

So, R.M.C., Jin, L.H., and Gatski, T.B., 2004b, "An Explicit Algebraic Reynolds Stress and Heat Flux Model for Incompressible Turbulence: Part II Buoyant Flow", *Theoret. Comput. Fluid Dynamics*, Vol. 17, pp. 377-406.

So, R.M.C., Vimala, P., Jin, L.H., and Zhao, C.Y., 2002, "Accounting for Buoyancy Effects in the Explicit Algebraic Stress Model: Homogeneous Turbulent Shear Flows", *Theoret. Comput. Fluid Dynamics*, Vol. 15, pp. 283-302.

Song, Y.T., 1998, "A General Pressure Gradient Formulation for Ocean Models, Part I: Scheme Design and Diagnostic Analysis", *Monthly Weather Review*, Vol. 126, pp. 3212-3230.

Sorensen, R.M., 1997, "Basic Coastal Engineering", Kluwer Academic, New York.

Speziale, C.G., 1987, "On Nonlinear K-l and K-ε Models of Turbulence", *J. Fluid Mech.*, Vol. 178, pp. 459-475.

Speziale, C.G., Abid, R., and Anderson, E.C., 1992, "Critical Evaluation of Two-Equation Models for Near-Wall Turbulence", *AIAA Journal*, Vol. 30, 324-331.

Stansby, P.K., 1997, "Semi-Implicit Finite Volume Shallow-Water Flow and Solute Transport Solver with k-ε Turbulence Model" *Inter. Numer. Meth. Fluids*, Vol. 25, pp. 285-313.

Stansby, P.K., and Zhou, J.G., 1998, "Shallow-Water Flow Solver with Non-Hydrostatic Pressure: 2D Vertical Plane Problems", *Inter. Numer. Meth. Fluids*, Vol. 28, pp. 541-563.

Stelling, G., and van Kester, J.A.T.M., 1994, "On the Approximation of Horizontal Gradients in Sigma Coordinates for Bathymetry with Steep Bottom Slopes", *Int. J. Numer. Meth. Fluids*, Vol. 18, pp. 915-935.

Stelling, G., and Zijlema, M., 2003, "An Accurate and Efficient Finite-Difference Algorithm for Non-Hydrostatic Free-Surface Flow with Application to Wave Propagation", *Int. J. Numer. Meth. Fluids*, Vol. 43, pp. 1-23.

Stelling, G.S., and Busnelli, M.M., 2001, "Numerical Simulation of the Vertical Structure of Discontinuous Flows", *Int. J. Numer. Meth. Fluids*, Vol. 37, pp. 23-43.

Stoer, J., and Bulirsch, R., 1993, "Introduction to Numerical Analysis", 2nd ed., Springer-Verlag, New York.

Sung, J., Choi, H.G., and Yoo, J.Y., 1999, "Finite Element Simulation of Thin Liquid Film Flow and Heat Transfer Including a Hydraulic Jump", *International Journal for Numerical Methods in Engineering*, Vol. 46, pp. 83-101.

Sung, J., Choi, H.G., and Yoo, J.Y., 2000, "Time-Accurate Computation of Unsteady Free Surface Flows Using an ALE-Segregated Equal-Order FEM", *Computer Methods in Applied Mechanics and Engineering*, Vol. 190, pp. 1425-1440.

Svensson, U., 1978, "Mathematical Model of the Seasonal Thermocline", Report No. 1002, Dept. Water Resources Engineering, University of Lund, Sweden.

Tannehill, J.C., Anderson, D.A., and Pletcher, R.H., 1997, "Computational Fluid Mechanics and Heat Transfer", 2nd ed., Taylor & Francis, Washington, DC.

Taulbee, D.B., 1992, "An Improved Algebraic Reynolds Stress Model and Corresponding Nonlinear Stress Model", *Phys. Fluids A*, Vol. 4, No. 11, pp. 2555-2561.

Temam, R., 1969, "Sur l'Approximation de la Solution des Equations de Navier-Stokes par la Méthode des pas Fractionnaires", (I): *Archive for Rational Mechanics and Analysis*, Vol. 32, pp. 135-153; (II): *Archive for Rational Mechanics and Analysis*, Vol. 33, pp. 377-385.

Tennekes, H., and Lumley, J.L., 1972, "A First Course in Turbulence", MIT Press, USA.

Thé, J.L., Raithby, G.D., and Stubley, G.D., 1994, "Surface-Adaptive Finite-Volume Method for Solving Free Surface Flows", *Numerical Heat Transfer, Part B: Fundamentals"*, Vol. 26, pp. 367-380.

Tomoya, S., and Pun, K.L., 1992, "Multi-Level Model for Hydrodynamic Circulation and Dispersion Process in Bays", *Coastal Engineering in Japan*, Vol. 35, No. 1, pp. 49-66.

Tsanis, I.K., 1989, "Simulation of Wind-Induced Water Currents", *Journal of Hydraulic Engineering*, ASCE, Vol. 115, No. 8, pp. 1113-1134.

Twizell, E.H., 1984, "Computational Methods for Partial Differential Equations", Ellis Horwood Limited, Chichester.

Ungarish, M., 2009, "An Introduction to Gravity Currents and Intrusions", Chapman & Hall/CRC, Boca Raton, 489 pp.

Ushijima, S., 1998, "Three-Dimensional Arbitrary Lagrangian-Eulerian Numerical Prediction Method for Non-Linear Free Surface Oscillation", *Int. J. Numer. Meth. Fluids*, Vol. 26, pp. 605-623.

Vallentine, H.R., 1969, "Applied Hydrodynamics", Butterworths, London.

van Kan, J., 1986, "A Second-Order Accurate Pressure-Correction Scheme for Viscous Incompressible Flow", *SIAM J. Sci. Stat. Comput.*, Vol. 7, No. 3, pp. 870-891.

Venayagamoorthy, S.K., Kose, J.R., Ferziger, J.H., and Shih, L.H., 2003, "Testing of RANS Turbulence Models for Stratified Flows Based on DNS Data", *Centre for Turbulence Research, Annual Research Briefs*, pp. 127-138.

Verdier-Bonnet, C., Angot, P., Fraunie, P., and Coantic, M., 1999, "Three-Dimensional Modelling of Coastal Circulations with Different k-ε Closures", *Journal of Marine Systems*, Vol. 21, pp. 321-339.

Versteeg, H.K., and Malalasekera, W., 1995, "An Introduction to Computational Fluid Dynamics, The Finite Volume Method", Longman, England.

Vincent, S., and Caltagirone, J., 1999, "Efficient Solving Method for Unsteady Incompressible Interfacial Flow Problems", *International Journal for Numerical Methods in Fluids*, Vol. 30, pp. 795-811.

Violeau, D., 2009, "Explicit Algebraic Reynolds Stresses and Scalar Fluxes for Density-Stratified Shear Flows", *Physics of Fluids*, Vol. 21, pp. 035103 (1-19).

Viollet, P.L., 1990, "On the Modelling of Low Speed Variable Density and Reacting Flows with Complex Geometries", *Proceedings of 4th International Symposium on Refined Flow Modelling and Turbulence Measurements*, pp. 7-16.

Voulgaris, G., and Trowbridge, J.H., 1998, "Evaluation of the Acoustic Doppler Velocimeter (ADV) for Turbulence Measurements", *Journal of Atmospheric and Oceanic Technology*, Vol. 15, pp. 272-289.

Vreugdenhil, C.B., 1994, "Numerical Methods for Shallow-Water Flow", Kluwer Academic Publishers, Dordrecht.

Wahl, T.L., 2000, "Analyzing ADV Data Using WinADV", *Joint Conference on Water Resources Engineering and Water Resources Planning & Management 2000*, Minneapolis, R.H. Hotchkiss and M. Glade, Eds., pp. 1-10.

Wahl, T.L., 2003, "Despiking Acoustic Doppler Velocimeter Data", Discussion, *J. Hydraul. Eng.*, ASCE, Vol. 129, No. 6, pp. 484-487.

Walker, S.A., Hamill, G.A., and Johnston, H.T., 1999, "Development and Erosion of a Mixing Layer in a Stratified Flow", in *Mixing and Dispersion in Stably Stratified Flows, Proceedings of the Institute of Mathematics & its Applications Conference Series, New Series, No. 68*, P.A. Davies, Ed., Oxford University Press, Oxford.

Wallin, S., and Johansson, A.V., 2000, "An Explicit Algebraic Reynolds Stress Model for Incompressible and Compressible Turbulent Flows", *J. Fluid Mech.*, Vol. 403, pp. 89-132.

Walters, R.A., 2005, "A Semi-Implicit Finite Element Model for Non-Hydrostatic (Dispersive) Surface Waves", *Int. J. Numer. Meth. Fluids*, Vol. 49, pp. 721-737.

Wang, Y., and Hutter, K., 2001, "Comparisons of Numerical Methods with Respect to Convectively Dominated Problems", *Int. J. Numer. Meth. Fluids*, Vol. 37, pp. 721-745.

Weare, T.J., 1979, "Errors Arising from Irregular Boundaries in A.D.I. Solutions of the Shallow Water Equations", *International Journal for Numerical Methods in Engineering*, Vol. 14, pp. 921-931.

Wearing, M.J., 2000, "Modelling of Pollution Transport in Small Tidal Harbours", PhD Thesis, University of Salford, U.K.

White, B.L., and Helfrich, K.R., 2008, "Gravity Currents and Internal Waves in a Stratified Fluid", *J. Fluid Mech.*, Vol. 616, pp. 327-356.

Whyte, K., and Ali, K.H.M., 2003, "Experimental Investigation of the Expulsion of Seawater over Estuarial Barrages Using Baffles", *International Conference on Estuaries and Coasts*, China.

Wilcox, D.C., 1988, "Reassessment of the Scale-Determining Equation for Advanced Turbulence Models", *AIAA Journal*, Vol. 26, pp. 1299-1310.

Wilcox, D.C., 2006, "Turbulence Modelling for CFD", 3rd edition, DCW Industries, USA.

Wolf, J., 1983, "A Comparison of a Semi-Implicit with an Explicit Scheme in a Three Dimensional Hydrodynamic Model", *Continental Shelf Research*, Vol. 2, No. 4, pp. 215-229.

Xia, J., Falconer, R.A., and Lin, B., 2010, "Hydrodynamic Impact of a Tidal Barrage in the Severn Estuary, UK", *Renewable Energy*, Vol. 35, pp. 1455-1468.

Xing, J., and Davies, A.M., 1996, "Application of Turbulence Energy Models to the Computation of Tidal Currents and Mixing Intensities in Shelf Edge Regions", *J. of Physical Oceanography*, Vol. 26, No. 4, pp. 417-447.

Yalin, M.S., 1971, "Theory of Hydraulic Models", Macmillan Press, London.

Yanenko, N.N., 1971, "The Method of Fractional Steps: The Solution of Problems of Mathematical Physics in Several Variables", M. Holt (English Ed.), Springer-Verlag, Berlin, Translation of Russian Original Edition: "Metod drobnykh shagov resheniya rnnogomernykh zadach matematicheskoi fiziki", Nauka, Sibirskoe Otdelenie, Novosibirsk, 1967.

Yih, C.-S., 1980, "Stratified Flows", Academic Press, New York.

Yin, J., Lloyd, P.M., and Falconer, R.A., 2001, "Tidal Flow Local Mean Velocities in Noisy Signals", *Flow Measurement and Instrumentation*, Vol. 12, pp. 25-28.

Young, C.-C., Wu., C.H., Kuo, J.-T., and Liu, W.-C., 2007, "A Higher-Order σ-Coordinate Non-Hydrostatic Model for Nonlinear Surface Waves", *Ocean Engineering*, Vol. 34, pp. 1357-1370.

Yu, T.S., and Li, C.W., 1998, "Instantaneous Discharge of Buoyant Fluid in Cross-Flow", *Journal of Hydraulic Engineering, ASCE*, Vol. 124, No. 11, pp. 1161-1176.

Yuan, H., and Wu, C.H., 2004a, "A Two-Dimensional Vertical Non-Hydrostatic σ Model with an Implicit Method for Free-Surface Flows", *Int. J. Numer. Meth. Fluids*, Vol. 44, pp. 811-835.

Yuan, H., and Wu, C.H., 2004b, "An Implicit Three-Dimensional Fully Non-Hydrostatic Model for Free-Surface Flows", *Int. J. Numer. Meth. Fluids*, Vol. 46, pp. 709-733.

Yue, W., Lin, C.-L., and Patel, V.C., 2003, "Numerical Simulation of Unsteady Multidimensional Free Surface Motions by Level Set Method", *Int. J. Numer. Meth. Fluids*, Vol. 42, pp. 853-884.

Zalesak, S.T., 1979, "Fully Multi-Dimensional Flux Corrected Transport Algorithms for Fluid Flow", *Journal of Computational Physics*, Vol. 31, pp. 335-362.

Zhang, Q.Y., and Gin, K.Y.H., 2000, "Three-Dimensional Numerical Simulation for Tidal Motion in Singapore's Coastal Waters", *Coastal Engineering*, Vol. 39, pp.71-92.

Zhang, Y., and Baptista, A.M., 2008, "SELFE: A Semi-Implicit Eulerian-Lagrangian Finite-Element Model for Cross-Scale Ocean Circulation", *Ocean Modelling*, Vol. 21, pp. 71-96.

Zhang, Y.L., Baptista, A.M., and Myers, E.P., 2004, "A Cross-Scale Model for 3D Baroclinic Circulation in Estuary-Plume-Shelf Systems: I. Formulation and Skill Assessment", *Cont. Shelf Res.*, Vol. 24, pp. 2187-2214.

Zhong, L., and Li, M., 2006, "Tidal Energy Fluxes and Dissipation in the Chesapeake Bay", *Continental Shelf Research*, Vol. 26, No. 6, pp. 752-770.

Zhou, J.G., 1995, "Velocity-Depth Coupling in Shallow-Water Flows", *Journal of Hydraulic Engineering*, Vol. 121, No. 10, pp. 717-724.

Zhou, J.G., and Stansby, P.K., 1999, "An Arbitrary Lagrangian-Eulerian σ (ALES) Model with Non-Hydrostatic Pressure for Shallow Water Flows", *Journal of Computer Methods in Applied Mechanics and Engineering*, Vol. 178, pp. 199-214.

Zijlema, M., and Stelling, G.S., 2005, "Further Experiences with Computing Non-Hydrostatic Free-Surface Flows Involving Water Waves", *Int. J. Numer. Meth. Fluids*, Vol. 48, pp.169-197.